Inertial Alfvén Waves as a Possible Driver for Auroral Kilometric Radiation

by

Jose Mauricio Blanco Benavides

A thesis submitted in partial fulfillment of the requirements for the degree of

Doctor of Philosophy

Department of Physics
University of Alberta

Abstract

The inner magnetosphere hosts a variety of different plasma environments. The transition from one region to the next extends over considerable lengths where adjacent plasmas merge gradually. Plasma waves play an important role in coupling these regions by facilitating particle and energy flows necessary to maintain or restore a state of dynamic equilibrium. Most types of plasma waves undergo dispersion as they move through regions with changing properties, affecting energetic particle populations in the process.

In this thesis, the effects of Dispersive Alfvén Waves (DAW) on electron plasmas are investigated for different scenarios using numerical simulations. To this end, the Drift Kinetic (DK1D) Vlasov solver [Watt et al., 2004] has been extended to include inhomogeneous background plasma conditions while preserving self-consistency between field and particles. A density model has been added which consists of a mixture of two plasmas: an ionospheric contribution composed of singly ionized oxygen which decays quickly with altitude, and a magnetospheric hydrogen plasma that is assumed spatially uniform. The resulting density variation gives rise to a realistic temperature profile along geomagnetic field lines.

The occurrence of regular and inverse suprathermal electron energy dispersion reported by Cameron [2015] is addressed using a simpler version of the code valid for uniform plasmas. Regular energy dispersion is divided between cases with a single suprathermal component and those accompanied by a locally enhanced thermal population. Simulations reveal that the first kind of signatures form primarily under conditions of low wave phase speed and strong wave dispersion, ultimately producing electron acceleration to energies significantly higher than that predicted by Fermi-like interactions. Regular energy dispersion, on the other hand, shows evidence of an enhanced thermal population at larger wave phase speeds. The occurrence of high energy electron dispersion over Fermi-like electron energy dispersion is favored by a decrease of perpendicular

wavelength and an increase of the plasma temperature and wave amplitude. Recent observations of inverse electron energy dispersion by the Canadian ePOP micro-satellite are explained as being due to the relative motion of the satellite and the source of wave emission. It is demonstrated that, for a source moving in the cross-plane of the background magnetic field and emitting Alfvén waves parallel to the field, inverse electron energy dispersion will be observed by a satellite whose trajectory is also in the cross-plane of the background field.

The DK1D code is also used to determine the efficiency of electron trapping by Shear Alfvén Waves (SAW) in the magnetosphere. This process is shown to be limited by Landau damping at short perpendicular wavelengths. For the range of parameters considered, simulations reveal that waves do not survive to reach the inertial region. This strong influence of particle trapping and self-consistent Landau damping is an indication of possible over- or under-estimates of the energy gain of accelerated electrons in studies that disregard self-consistent wave-particle interactions.

Lastly, the efficiency of the Electron Cyclotron Instability (ECI) resulting from field-aligned electron acceleration by inertial Alfvén waves within and above the Ionospheric Alfvén Resonator (IAR) is investigated. Since the motion of these accelerated electrons preserves their magnetic moment the mirror force induces the formation of unstable horseshoe distributions. Electron distributions from simulation data are fitted to an analytical representation that enables the convective length associated with wave amplification of Auroral Kilometric Radiation (AKR) to be calculated. Simulation results show that AKR generation is most efficient where the ratio ω_{pe}/ω_{ce} is a minimum, and exclusively for electron number densities $\leq 10^5$ cm^{-3}, in accordance with observations. Enhanced efficiency of AKR generation can be obtained by increasing both the background plasma temperature and the perpendicular wavelength. At altitudes above the IAR, the interference of reflected and incident waves coincides with a sudden termination of the conditions for AKR amplification.

Preface

Appendix C of this thesis has been published as A. V. Artemyev, R. Rankin, and M. Blanco, "Electron trapping and acceleration by kinetic Alfvén waves in the inner magnetosphere", Journal of Geophysical Research: Space Physics, Vol. 120, 10305-10316, doi:10.1002/2015JA021781, 2015. I was responsible for deriving the two-fluid equations in the appendix of the paper and the expression for the effective potential in terms of the scalar potential through substitution of the vector potential from the wave equation. These equations indicate that electrons escape the wave at an altitude which depends on wave parameters, which motivated the analysis presented in the publication.

To

Segundo y María Ester.
Ceci, Cali, Yor, Rosi y Beto.
Virgil, Jason, Carlos, Gabriel, Javier, Ale, Fabián, Laura, Pablo, Priscila, Francisco, Fernando, Ema y Victoria.

Acknowledgements

I would like to thank my supervisor, Dr. Robert Rankin, for supporting me throughout so many years, despite multiple difficulties to complete this project. I am very grateful that Robert had the sensibility of letting me work on my own pace and with as little pressure as possible. Thanks also for stepping out and make an additional effort to support me financially when I had given up on finishing the program due to lack of funds to stay in Canada. I would also like to thank Dr. Clare Watt for providing the DK1D code utilized in this thesis. Clare developed the original formulation of the model during her tenure as a Research Associate at the University of Alberta. The availability of the DK1D model was what made the studies presented in the thesis possible.

Secondly, my appreciation goes to the other members of my thesis committee. Thanks to Dr. Richard Marchand and Dr. Richard Sydora for their availability, their kindness, and their understanding to discuss questions associated with my research, or other matters related to my program of studies itself.

There are three wonderful friends that have earned a special mention over these years. It is only fair that I acknowledge how much of this thesis has been possible due to their support. Thanks to Alison Muscat, who was always available to listen and help finding solutions to my academic struggles, so much as to let me borrow money to pay my tuition, even though I could not give her any guarantee that I could pay her back. She always made me look on the good side of everything, and her words of encouragement were key to my success.

Thanks to Claudio Norín, who has been a brother to me for most of my stay in Canada. To him I owe having a couch to sleep on when money was most scarce. His support has been constant and consistent, so much that to this day he lets me share his accommodation for a fare that is almost symbolic.

Last but not least, I want to express my sincere appreciation to Julie Kamal, who in times of struggle did her full-time job to help me fight away my feelings of discouragement. Without her continuous support the completion of this thesis would not have been possible.

Finalmente, quiero agradecer a mi familia. Aunque estando muy lejos, ellos me han proveído de su apoyo constante y sus oraciones. Gracias especialmente a Beto, quien sacrificó tiempo y recursos para completar trámites en mi representación. Y gracias a Cali por su inigualable aporte al hacerse cargo de mi deuda con la UCR.

Table of Contents

List of Tables

List of Figures

Chapter 1

Introduction

The objective of this thesis is to evaluate the possible association between *Auroral Kilometric Radiation* (AKR) with source in the Alfvénic acceleration region and the formation of unstable electron distributions driven by dispersive Alfvén waves at auroral latitudes where the convergent magnetic field favors the formation of horseshoe distributions. In order to accomplish that, computer simulations using a self-consistent Drift-Kinetic (DK1D) code [Watt et al., 2004] with a dipolar magnetic model were run to obtain numerical electron distributions under varying background plasma conditions and realistic parameters that determine the wave dispersion. Resulting unstable distributions are analyzed within the theoretical framework of the Electron Cyclotron Instability (ECI); the resonant curves are integrated to obtain estimations for frequency modes and damping rates.

Terrestrial radio emissions into space were first discovered by spacecraft in 1965 and studied ever since. Among these emissions, a rather broad frequency range from ~ 1 kHz to a few MHz show amplitudes that surpass the background level by several orders of magnitude; this component maximum power peaks within the $100 - 600$ kHz interval, which corresponds to wavelengths of around 1 km. For this reason, it is known as Auroral Kilometric Radiation (AKR) Paschmann et al. [2003]. AKR is the most powerful source of terrestrial radiation. It propagates mostly in the RX mode, and to less extent, in the LO and Z modes. Power emission ranges between 10^7 W during weak substorms to 10^9 W during strong substorms. Analogous emissions have been detected in the polar regions of other magnetized planets like Jupiter and Saturn. Wave amplification is driven by the so-called *Electron Cyclotron Instability* (ECI) [Chu, 2004], a process where the relativistic mass shift associated to the fast rotational motion of the non-thermal component of the electron distribution induces azimuthal bunching in phase-space; bunched electrons

may then amplify elliptically polarized free wave modes via coherent gyroresonant interaction. Azimuthal bunching causes coherent amplification at the expense of the free energy of the plasma, in the same way as a maser. The efficient generation of intense radiation is, however, conditioned to the absence or otherwise weak action of dissipation processes. Under such conditions, the plasma cannot dispose of the excess of energy, and it remains stored in the particle distribution [Treumann, 2006]. Optimal conditions for wave amplification at the source region include low density of the thermal plasma and a strongly magnetized environment. The former condition reduces wave energy loss due to Landau damping, as well as thermalization of the plasma due to collisions and long-range Coulomb interactions that tend to disorganize the coherent motion and cause shielding. The latter ensures gyromotion in the plane perpendicular to the magnetic field. Both these conditions are readily found in the near-Earth magnetospheric environment. The physical mechanism for plasma energization in this region is, however, not that trivial. The driving mechanism responsible for AKR is unstable horseshoe distributions in velocity or momentum phase space, which form in high latitude regions where the converging magnetic field presents strong gradients, and upward (downward) currents (electric fields) form as a product of magnetosphere-ionosphere coupling processes. An electric field oriented anti-parallel to the geomagnetic field ensures high emission rates of AKR through important modifications of the plasma properties: in combination with the magnetic mirror force, it accelerates ions upward, driving them into the magnetosphere; magnetospheric electrons, on the other hand, are accelerated downward by anti-parallel electric fields. The mirror force opposes electrons downward motion, with the result that only electrons with small pitch angle can reach low altitude. Ionospheric electrons are prevented from moving upward in the parallel electric field, with the net effect being that plasma within regions of the parallel potential drop is highly energetic and of low density, implying optimal conditions for the conversion of energy into radiation.

The magnetic-field-aligned electrostatic structures that develop in the upward current region are not the only source of field-aligned potential structures that can accelerate electrons. Parallel electric fields and associated upward currents can also appear as a consequence of the propagation of Shear Alfvén Waves (SAW) in regions where the perpendicular scale (relative to the geomagnetic field) of the waves is comparable to the ion acoustic gyroradius [Hasegawa, 1976] or the electron skin depth [Goertz and Boswell, 1979]. This effect has been widely studied in the context of electron acceleration in high altitude regions and is regarded as an important mechanism to enhance electron precipitation that generates auroras [Wygant et al., 2000; Watt and Rankin, 2009]. It is also speculated to energize plasmas capable of feeding the ECI that powers AKR [Su et al., 2007, 2008]. Evidence for this comes from the fact that AKR signatures

have recently been observed inside the Alfvénic acceleration region (Su et al. [2008]; Hanasz et al. [2008] and others), raising the possibility of an association with Inertial Alfvén Waves. To this date, the viability of parallel electric fields of Alfvénic origin as a possible driver of AKR has not been evaluated quantitatively, which motivates the studies presented here. Previous attempts to study this process [Su et al., 2007] have used a non-self-consistent approach that leaves out important physics, particularly the damping of waves. It will be demonstrated that with fewer assumptions, the self-consistent DK1D code predicts distribution functions that are highly favorable to the generation of AKR. The model includes wave growth and damping, and by the simple assumption of a constant electrostatic field along the magnetic field line, it relates the distribution function to the background plasma properties analytically.

The primary objective of this research is to establish whether there is a causal connection between AKR signals originated in the Alfvénic acceleration region and electron energization produced by the shear Alfvén propagation. In other words, to determine if modification of the plasma distribution function due to wave-particle interactions can generate unstable distributions, and determine the parameters and conditions with the right characteristics to explain observational results of AKR emissions. The SAW considered in this study are in the inertial regime, which corresponds to perpendicular wavelengths (with respect to the geomagnetic field) on the order of an electron skin depth c/ω_{pe} in the plasma. Ions are treated as a cold neutralizing background while the waves of interest have frequencies well below the ion gyro-frequency. The methodology consists of a self-consistent numerical Vlasov solver [Watt et al., 2004] that accounts for inhomogeneity in the magnetic field and kinetic wave dispersion. For this work, the DK1D code has been modified to include inhomogeneous conditions of electron density and temperature, while the self-consistency of the equilibrium distribution function is achieved by introducing an electrostatic potential into the spatial domain. This new formulation allows us to move up and down the spatial domain and study how the distribution function and wave fields at a given altitude are affected by different ambient plasma conditions along the geomagnetic field. It is shown that interaction of the inertial SAW with the electron plasma leads to the formation of horseshoe distributions that can be unstable to AKR if a gyroresonant interaction is established between the energetic plasma and the presence of free space modes. The relativistic condition for gyroresonance draws an ellipse whose location in phase space depends on the electron gyrofrequency and local wave propagation properties; by comparing unstable distributions obtained through simulation with the respective resonant surfaces, we intend to identify the parameters and locations along the magnetic field where the distributions are more unstable to AKR.

1.1 The magnetospheric environment

In the immediate neighborhood of the stars, high speed flows of ionized plasma and magnetic fields known as *solar wind* are continuously released as a byproduct of fusion reactions taking place in their core. For the case of our Sun, the solar corona temperature reaches $\sim 10^6$ K; the large thermal energy of the particles allows a significant fraction of electrons (1/2) and a small fraction of ions (1/100) to overcome the gravitational force and escape into interstellar space. The resulting charge imbalance establishes large electrostatic structures that help surface ions surpass the solar gravitational field [Parks, 2003]. Solar wind properties depend strongly on its heliocentric distance, but some of them, like the flow velocity and particle energies, reach an asymptotic value at long distances where the gravitational field is close to zero.

Table 1.1: Typical solar wind properties at 1 AU heliocentric distance (From Kivelson and Russel [1995])

Proton density (cm^{-3})	6.6
Electron density (cm^{-3})	7.1
He^{2+} density (cm^{-3})	0.25
Flow speed (km/s)	450
Proton temperature (K)	1.2×10^5
Electron temperature (K)	1.4×10^5
Magnetic field (nT)	7

Typical values of solar wind close to Earth are given in table 1.1. Despite these ultra-low densities and its collisionless nature (the mean free path between collisions is in the order of ~ 1 Au) [Kivelson and Russel, 1995], the solar wind has essential effects in driving solar-planetary interactions. Solar wind flows slowly erode the atmosphere of unmagnetized bodies until total depletion, and reshape the magnetic field on magnetized planets into a raindrop-like shape; compressed on the dayside and extended on the nightside regions. Since these effects are driven by the dynamic pressure of the solar wind, one can think of planets as streaming supersonically inside a nonviscous, conducting plasma fluid.

The frontier between the terrestrial environment and outer space is ultimately determined by the surface where pressure effects produced by momentum flux carried by the solar wind balances the magnetic stresses of Earths magnetic field, and thermal pressure of the plasma enclosed by it. This frontier is known as the *magnetopause*, and the cavity contained by the geomagnetic field is the *magnetosphere*. From the divergence-less nature of magnetic fields in general, it follows that advected interplanetary magnetic field lines

transported within the solar wind cannot just traverse the geomagnetic field. Furthermore, since both solar wind and magnetospheric plasmas are highly magnetized, neither can the solar wind plasma move through the magnetopause. Instead, magnetic field lines bend over, and solar wind particles are deflected around the Earth; the solar winds momentum flux and built up magnetic pressure pushes and deforms the geomagnetic field, compressing it on the sunward direction (stagnant point is $\sim 10\ R_E$), and stretching it at nightside into a long *magnetotail* ($\sim 10^2 - 10^3\ R_E$). Along the magnetopause, differences between the magnetic field configuration in the solar wind and magnetospheric regions produce current sheets that flow according to Ampére's law. Close to Earth, the solar wind speed is an order of magnitude higher than both the sound (60 km/s) and Alfvén (40 km/s) speeds. Therefore, before reaching the magnetopause, a standing *Bow Shock* forms in the shape of a hyperbolic surface beyond which the solar plasma is thermalized to subsonic velocities and higher densities. The region between the Bow Shock and the magnetopause is known as *the Magnetosheath*.

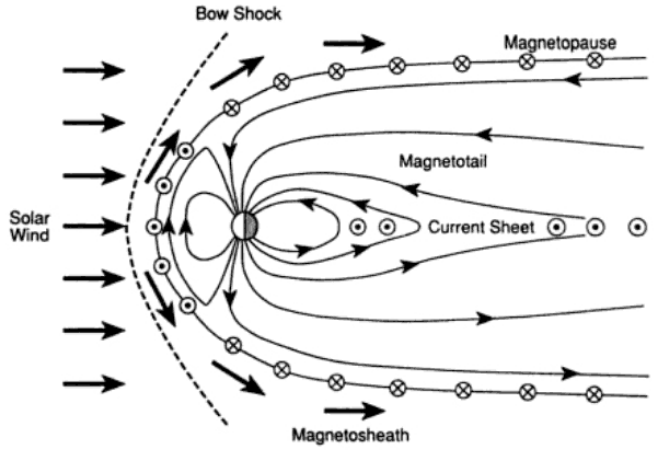

Figure 1.1: A noon-midnight representation of the magnetospheric environment upon interaction with the solar wind at times of southward IMF. Dotted (crossed) circles show currents flowing outside (inside) the page. (From Kivelson and Russel [1995])

Even though particle momentum of the solar wind is most responsible for shaping the magnetospheric region, the advection of interplanetary magnetic field (IMF) lines have a tremendous impact in the state of dynamic equilibrium shown in Figure 1.1, by effectively driving the convection processes that take place in the outer magnetosphere through reconnection of field lines in various sections of the magnetopause. Magnetic reconnection takes place at regions of finite conductivity and low plasma speed where magnetic field lines of markedly different orientation converge. At the point where this superposition of fields is close to zero, the magnetic stress is too low and fails to maintain the local

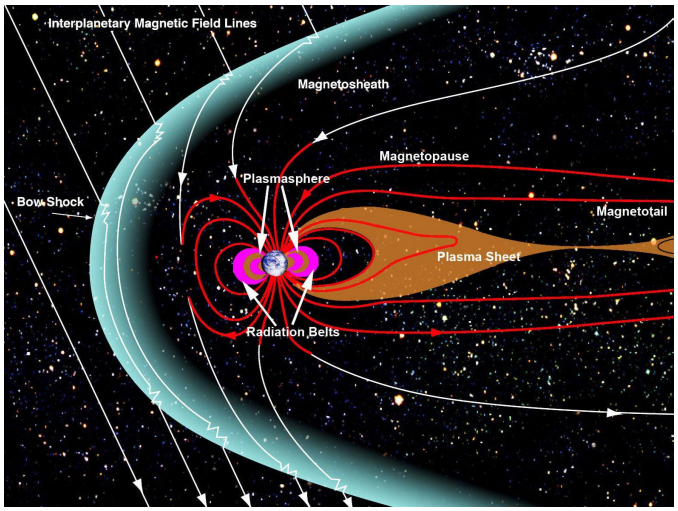

Figure 1.2: Another representation of the magnetosphere showing dayside reconnection. Red lines belong to the geomagnetic field, white lines are part of the solar wind. Advection of solar wind magnetic fields against the Earths field leads to reconnection. (From `https://www.nasa.gov/mission_pages/sunearth/science/magnetosphere2.html`)

plasma magnetized, so in that region particles can move freely across field lines, enabling mass interchange between the Magnetosphere and Magnetosheath regions. At the noon point of the Magnetopause, for example, when the IMF is predominantly southward, magnetic pressure builds up by the constant advection of solar wind, effectively pushing the magnetosphere towards the Earth. This magnetospheric compression causes the density of geomagnetic field lines to increase, eventually restoring the equilibrium. There is convection of both solar and geomagnetic field lines with opposite orientation that, when converging to the same point, tend to cancel each other out. Since field lines never end, a solar magnetic line diffusing into the null point breaks and reconnects with a geomagnetic field line, turning into a single line that traverses the Earth's core and extends into open space on both north and south sides (see Figure 1.2). This topologically modified line is then advected tailward as it is dragged by its ends in outer space by the solar wind while carrying a mixture of solar and terrestrial plasmas; this warm plasma fills a section of the Magnetotail composed with high latitude magnetic lines called *Plasma Mantle*. As the solar wind continues flowing and stretching these open field lines anti-earthward, the magnetic pressure of new reconnected lines will eventually drive them to lower latitudes into the *Tail Lobes*, where additional plasma from the ionosphere contributes to creating higher density (still $< 10^{-1}$ cm^{-3}) and lower temperature conditions. Eventually, at distances in the order of hundreds of Earth radii, the north and south arms of the magnetic line will collapse again at low latitudes, causing them to break and reconnect into

a single closed magnetospheric line and a free magnetic field line to be incorporated to the solar wind. During this process of magnetotail reconnection, inflows of lobe particles are energized to form ion and electron beams streaming earthward along the recently closed geomagnetic field lines. A fraction of particles constituting these beams bounces back due to the mirror force as tailward beams [Kivelson and Russel, 1995]. These counterstreaming beams are unstable to several wave modes, so eventually, the streaming particles are thermalized and deposited towards lower latitudes. The region containing these beams of fast particles ($\sim 10^2$ km/s) is known as the *Plasma Sheet Boundary Layer* (PSBL); and the hotter ($T_i = 2 - 20$ keV, $T_e \sim 0.4 - 4$ keV), denser ($\sim 0.1 - 1$ cm^3) region of thermalized plasma is the *Plasma Sheet* [Paschmann et al., 2003].

Both the PSBL and plasma sheet are connected to the ionosphere at high latitudes in the nightside auroral region, where geomagnetic field lines converge into the Earth surface. At lower latitudes, on the other hand, a toroidal region, the *plasmashpere*, stands between them, constrained inside dipolar field lines up to altitudes of $\sim 5 - 6$ Earth radii. Its outer boundary features strong gradients of increasing temperature and decreasing density as one moves towards the plasma sheet. The plasmasphere is filled with cold (~ 1 eV) plasma of ionospheric origin, with densities one or two orders higher than the plasma sheet [Paschmann et al., 2003]. As opposed to the outer regions of the magnetosphere, where the solar wind and reconnection processes dominate plasma dynamics, the plasma flow in this region is driven by the Earth rotation.

Coexisting approximately in the same region as the plasmasphere are the *Radiation Belts*, where trapped high energy particles (> 1 MeV) bounce back and forth along magnetic field lines up to a latitude that depends on the value of their magnetic moment, while drifting around the Earth by the action of the gradient and curvature drifts that result from the geomagnetic field inhomogeneity. The drifting of particles with energies between 20 and 300 keV is responsible for most of the *ring current* [Kivelson and Russel, 1995].

1.2 Auroral plasma region

The existence of magnetic field-aligned electric fields appears somewhat counter-intuitive considering the high conductivity of plasma in Earth's magnetosphere. At high latitudes, however, observations reveal that the right conditions exist to allow the formation of field-aligned electrostatic and electromagnetic structures. The associated field-aligned potential drops develop in field-aligned currents imposed by magnetosphere-ionosphere coupling processes. Such currents are carried mainly by magnetospheric electrons that stream freely down magnetic field lines toward the ionosphere. As they move into regions

of stronger magnetic field, those electrons with pitch angles outside the loss cone are mirrored back toward the magnetosphere. At sufficiently low altitude, perhaps extending up to an R_e or so, insufficient electrons exist within the loss cone, and in this situation, it is thought that electrostatic potential drops develop; they accelerate electrons within the loss cone to form aurora. Figure 1.3 includes in situ data corresponding to a pass of the NASA FAST spacecraft as it moves over the nightside auroral oval towards the pole, overviewing in its path upward current (purple), downward current (green) and Alfvénic acceleration (red) regions. From inspection of the first panel, there is an apparent correlation between upward (downward) current regions and the negative (positive) gradient of the background magnetic perturbation. The two regions that concern us are the upward current and the Alfvénic acceleration regions.

1.2.1 Upward current region

The upward current region between 16:44:30 UT and 16:46:30 UT in Figure 1.3 shows several characteristic features of plasmas in this region. From the electron energy spectrogram (third panel), the relatively narrow energy peak (of the order of several keV) defines a high energy band of current-carrying electrons of magnetospheric origin that have survived the mirror force and are accelerated by a potential drop located above the observation point. Typical of this type of structure, the peak in energy detected by the satellite increases as it moves towards the center of the upward current region, and decreases once it passes the center; this is why this region is commonly known as an *inverted V*. The electron pitch angle spectrogram (fourth panel) covers most of the spectrum almost homogeneously, although the low-density up-going electron flow indicates that this region is dominated by precipitating electrons. The ion energy spectra in the fifth panel shows evidence of a thermal ion plasma, while on the sixth panel enhancements in the density of particles with pitch angles close to 135 and 225 degrees can be seen; these enhancements are known as *ion conics*, and correspond to ions that are heated transversely by electromagnetic ion cyclotron (EMIC) waves [Paschmann et al., 2003].

1.2.2 The Auroral Density Cavity

The upward current region changes drastically when the FAST satellite happens to cross through a potential drop. Figure 1.4 shows data from another pass of the spacecraft. According to Ergun et al. [1998], the DC-active intervals in panel (a) of Figure 1.4 indicate the satellite is crossing a region with parallel electric fields. During this interval, the thermal component practically disappears for both electrons and ions (see panels (f)

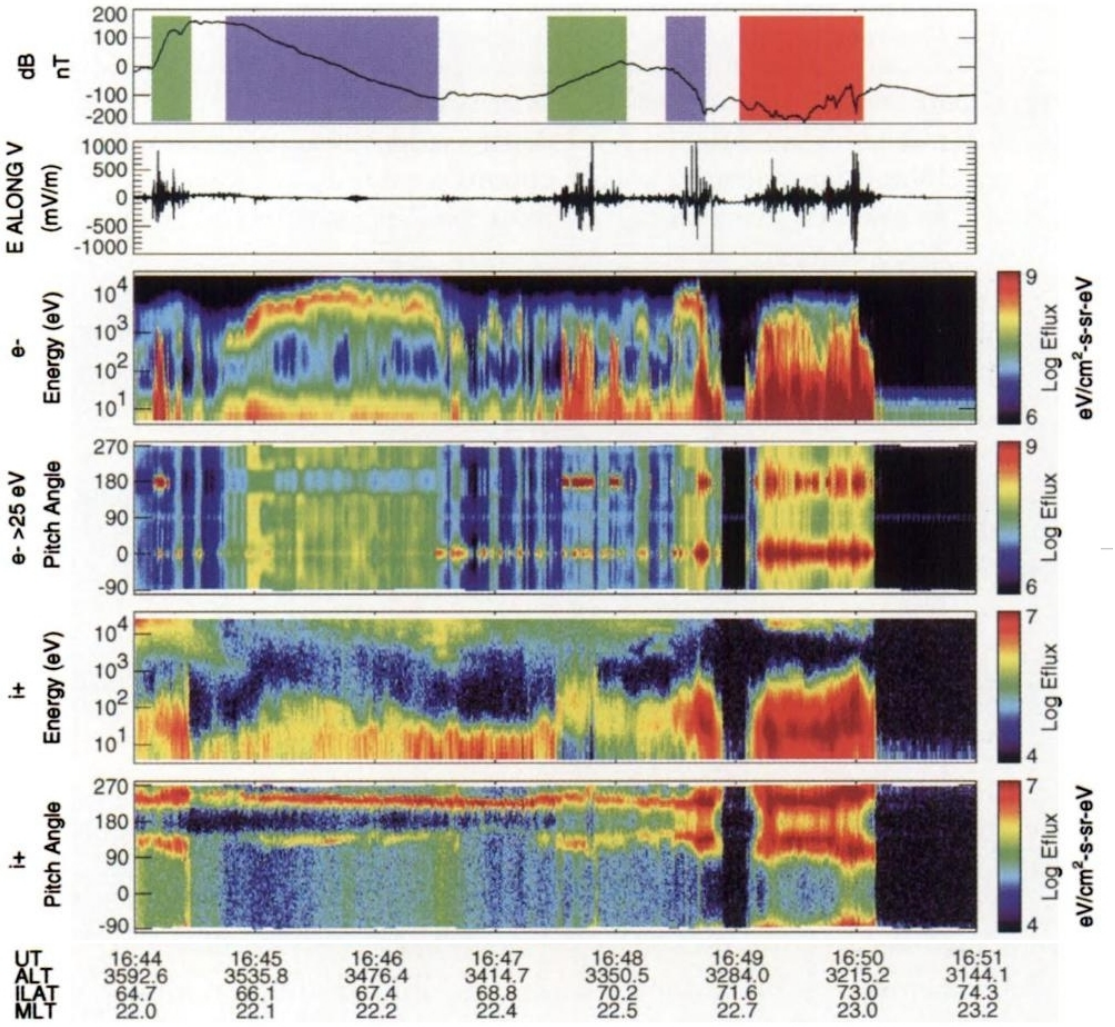

Figure 1.3: *In situ* data for an auroral pass by the FAST spacecraft, as it moves poleward in the nightside auroral oval. First panel plots the magnetic field perturbation relative to the IGRF magnetic field model. Second panel shows DC electric field perturbations. The next four panels show electron and ion energy and pitch angle distributions. (From Paschmann et al. [2003])

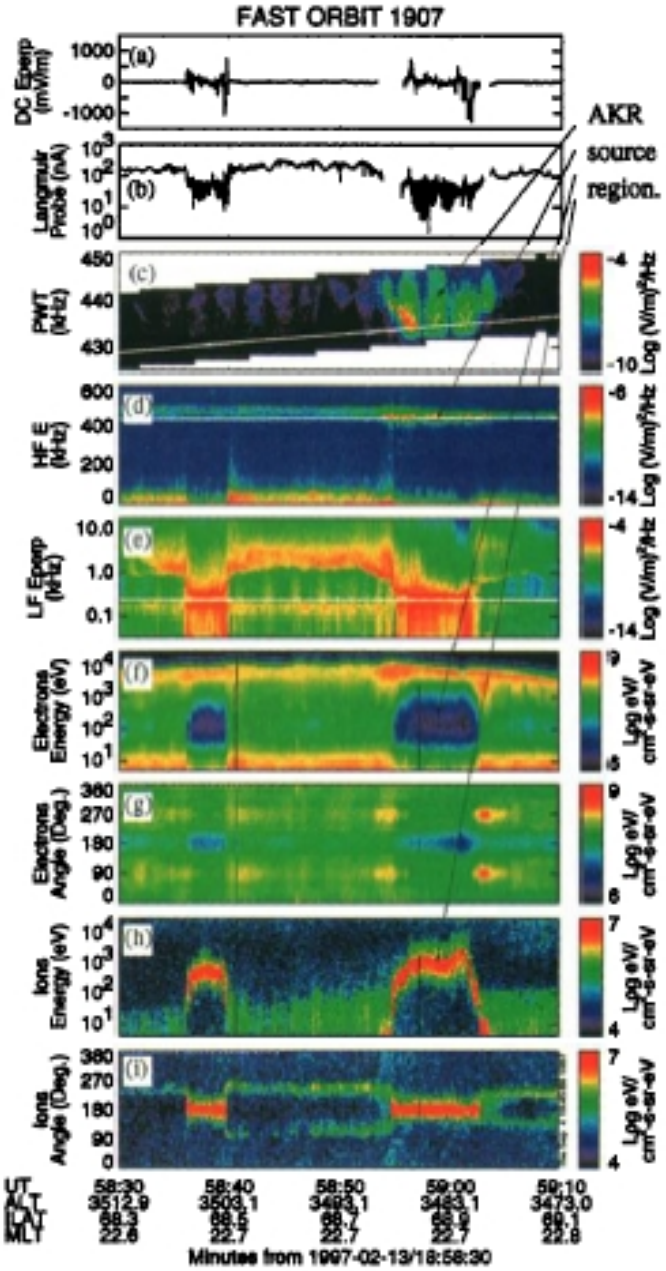

Figure 1.4: ((a) DC electric field. (b) The Langmuir probe current. A 2 nA current corresponds to $\sim$ 1 cm^3 cold plasma or $\sim$ 0.1 cm^3 warm plasma. (c) Wave power as measured by the Plasma Wave Tracker. The white line indicates the electron cyclotron frequency. (d) High frequency electric field power. The white line indicates the electron cyclotron frequency. (e) Low frequency, perpendicular wave power. (f) Electron energy flux distribution. (g) Electron pitch angle distribution. (h) Ion energy flux distribution. (i) Ion pitch angle distribution. (From Ergun et al. [1998])

and (h)), and all that is left are upward ion and downward electron beams. The pitch angle distribution for electrons looks very isotropic except at 180^o. Ion conics, in this case, turn into ion beams of energy $\sim$ 1 keV directed upwards. All these features are consistent with the presence of an electric field directed upwards. The region inside the upward current density containing parallel electric fields, low-density plasma, and ion and electron beams is known as the *auroral density cavity*. Panel (c) shows a strong enhancement of emission power as the second density cavity is crossed (from 18:58:55 UT to 18:59:30 UT approximately). The emission power is enhanced for frequencies approaching the electron cyclotron frequency, which is what is expected for AKR.

Electron distributions at the AKR source region (not included in Ergun et al. [1998]) have also been reported. Figure 1.5a shows a phase space diagram of the electron "horseshoe" distribution taken by FAST at a time of strong wave emissions below the electron cyclotron frequency. Positive parallel velocity indicates down-going electron motion, and negative parallel velocity corresponds to the up-going motion of electrons along the magnetic field line. The region of energies below 1 keV is omitted since most of it consists of photoelectrons [Ergun et al., 2000]. The diagram shown in Figure 1.5b illustrates the energy flow in the cycle of formation and diffusion of the horseshoe distribution; (1) low energy particles are energized in the presence of the parallel potential and stream downwards, (2) these electrons move to regions of stronger magnetic intensity since their associated magnetic moment must remain constant. Their perpendicular kinetic energy must increase at the expense of parallel momentum, thus moving them away from the horizontal axis, (3) AKR is produced through the resonant interaction of the free wave modes in the plasma with the unstable distribution, thermalizing the distribution in the process.

1.2.3 Alfvénic acceleration region

At latitudes slightly equatorward of the polar cap boundary (the boundary between open and closed geomagnetic field lines), there is a region where SAWs are observed and where Alfvénic wave activity becomes especially intense; it is commonly referred to as the Alfvénic acceleration region. In the context of Figure 1.3, the FAST satellite crosses the Alfvénic acceleration region between 16:49 and 16:50 UT approximately (red shadowed section in the first panel). This section of the satellite trajectory reveals plasma with energy extending to several keV, with a broad spectrum of energies for both electrons and ions. It is in stark contrast to the spectrum associated with an inverted-V. The electron pitch angle distribution in the fourth panel shows electron beams in both the upward and downward directions, while the ion pitch angle distribution (sixth panel) shows enhanced

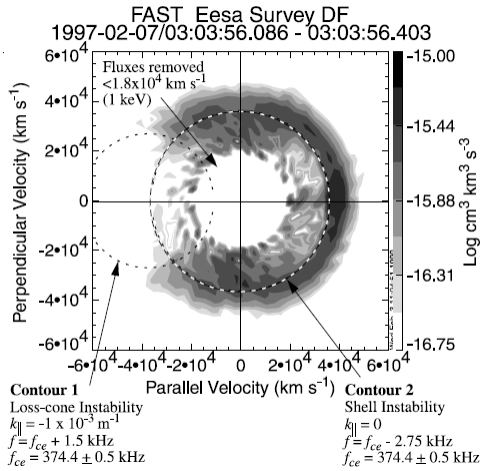

(a) Electron velocity distribution obtained by the FAST spacecraft inside the auroral cavity. (From Ergun et al. [2000])

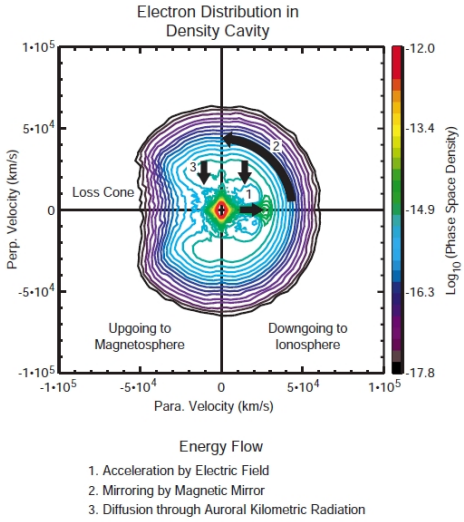

(b) A schematic of energy flow in a horseshoe distribution. (From Strangeway et al. [2001])

Figure 1.5: Horseshoe distribution

conics. In the acceleration region, background plasma conditions are dependent on the magnetospheric-ionospheric coupling processes continually taking place, which implies that dayside activity can be noticeably different from nightside activity. The higher energy levels of the background plasma in the region of Alfvénic activity are related to the presence of a warmer magnetospheric plasma that is injected in the process of reconnection. According to Paschmann et al. [2003], Alfvén waves are generated as a relaxing mechanism that allows the mixture of magnetospheric and ionospheric plasma to reach a convective equilibrium; some of the energy is converted into electron acceleration, which in turn excites higher energy waves that enhance ion conics.

From all the physical processes that can take place in the Alfvénic acceleration region, we are interested in those producing downward electron beams that evolve into horseshoe distributions. At high altitudes where the MHD approximation holds, no wave mode can generate beams. At lower altitudes, however, where the wavelength perpendicular scale becomes comparable to the motion scale for the particles, wave dispersion properties change considerably and become highly dependent on the background plasma properties. At this level, SAWs couple with the background plasma to become Dispersive Alfvén Waves (DAWs) that sustain magnetic field-aligned electric field components capable of producing electron acceleration. DAWs are further classified into Kinetic Alfvén Waves (KAWs) that propagate at high altitudes where the plasma is warm, and the background magnetic intensity is small (so the thermal speed, v_{te} is higher than the Alfvén speed v_A.

See section 2.4.2), and Inertial Alfvén Waves (IAWs) that are common at lower altitudes where the plasma is colder and the Alfvén speed takes higher values ($v_A > v_{te}$).

Most of the *in situ* measurements obtained from the Alfvénic acceleration region were gathered by the Polar, Freja and FAST spacecrafts at altitudes corresponding to the inertial regime (although Polar also samples the kinetic domain at a higher altitude as well). An approximation of the dispersion relation for IAW is given by [Stasiewicz et al., 2000]

$$\left(\frac{\omega}{k_{\parallel} v_A}\right)^2 = \frac{1}{1 + (k_{\perp}\lambda_e)^2}, \tag{1.1}$$

where $\lambda_e = c/\omega_{pe}$ is the electron inertial length. The electric to magnetic field ratio is

$$\frac{E_{\perp}}{B_{\perp}} = v_A \sqrt{1 + (k_{\perp}\lambda_e)^2} \tag{1.2}$$

and a parallel electric field such that

$$\frac{E_{\parallel}}{E_{\perp}} = \frac{k_{\parallel} k_{\perp} \lambda_e^2}{1 + (k_{\perp}\lambda_e)^2}. \tag{1.3}$$

Alfvénic activity recorded by the above-mentioned spacecrafts is usually identified through the ratio of the perpendicular electric to the perpendicular magnetic field amplitude. If we imagine that the wavelength associated with $k_{\perp}$ changes along the field line proportionally with the local radius of the magnetic flux tube, we find that the quantity $k_{\perp}\lambda_e$ scales as $\sqrt{B/n}$. Lysak and Song [2000] found that for the dipolar approximation for the magnetic intensity and an exponentially decaying model for the density, the electric field parallel component found with equation (1.3) takes its maximum value at altitudes that match the region of auroral acceleration, suggesting that inertial effects play an important role in electron acceleration. Measurements at different altitudes from Freja [Louarn et al., 1994] (600-1750 km), FAST [Chaston et al., 1999, 2000] (350-4180 km) and Polar [Wygant et al., 2000, 2002] (4-6 R_e geocentric) have detected high amplitude electromagnetic signals ($\sim 10^2$ mV/m, $\sim 10^1 nT$) associated with local density depletions ($\sim 10\%$) and strong Poynting fluxes ($\sim 10^{-3} - 10^{-2}$ W/m^2). These Poynting fluxes are predominantly downwards but often accompanied by a smaller upward Poynting flux component and field-aligned counter-streaming electron fluxes, which is consistent with the propagation of IAW and ionosphere-reflected IAW. By applying the Poynting flux theorem in the MHD limit, Wygant et al. [2000] mapped high altitude Poynting flux data to 100 km altitude and found that the mapped values are too high as compared to typical ones, which suggests that a considerable amount of Poynting flux

energy is dissipated in its transit to the ionosphere as Joule heating and plasma acceleration. Numerical simulations of IAWs propagating in both uniform and non-uniform background magnetic field lines [Watt and Rankin, 2009] subsequently revealed that energy in the form of Poynting flux could travel with little loss in regions where $v_{te} > v_A$ due to nonlinear trapping of electrons into the wave potential. Once the wave reaches the inertial regime, the parallel component of the electric field decreases in magnitude, allowing energetic electrons to escape and sink the energy of the wave. This process is a key ingredient in the study of how horseshoe distributions form, as will be discussed later.

The data shown in Figure 1.6, which corresponds to a dayside oval crossing of the FAST satellite illustrates many of the features just described. The field amplitudes for the first and second panel indicate $E_\perp/B_\perp \sim 5000$ km/s. The third panel shows significant density depletions associated with some of the higher amplitude perturbations. The fourth panel shows mostly downward Poynting flux, and the integrated electron flux is always directed downwards. The sixth panel shows evidence of so-called *electron bursts*, which correspond to a few broadband enhancements of electron differential energy flux with energies up to ~ 100 eV. The electron pitch angle distribution in the seventh panel shows that these electron bursts are moving downwards; their signature is strongly correlated with the most important depletions of low energy plasmas (see the third panel). The ion spectrum shows that there is an important contribution of magnetosheath particles [Chaston et al., 2000].

By comparing the features of Alfvénic acceleration in the dayside oval with electron acceleration in the auroral cavity inside an inverted-V potential drop, we see a few common elements which can lead to AKR emission; these are parallel electric fields, downward electron acceleration, and density depletion. However, there are also striking differences that work against high efficiency for AKR generation in the Alfvénic region; first, the associated electric fields are short lived as opposed to the inverted-V electrostatic potentials, which translates into much less energy to build unstable distributions; and second, the energized distributions are broadband, as opposed to beam-like. The bottom line is that the process of AKR generation (if any) is expected to be much less efficient than the one taking place in the auroral cavity. This efficiency is intrinsically bound to background plasma properties like plasma temperature and the perpendicular wavelength scale. The purpose of the studies presented here is to quantify the efficiency of AKR generation by IAW.

The formation of unstable distributions from electron bursts has been reported in Su et al. [2008], and their findings are shown here in Figure 1.7. According to the publication, such unstable distributions are more likely to be found in the nightside

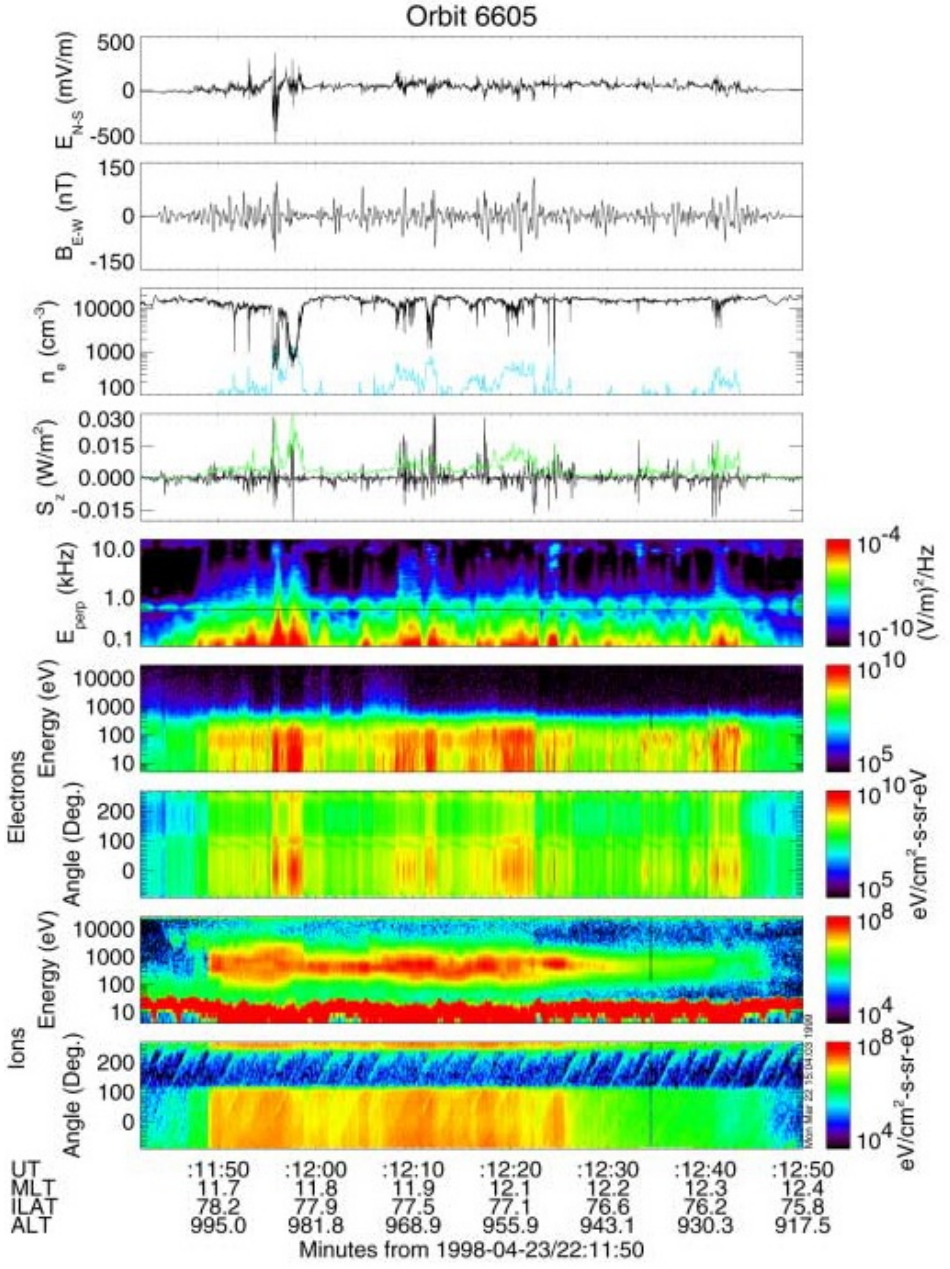

Figure 1.6: Data for NASA FAST satellite cusp crossing at an altitude of 1000 km. 1^{st} panel: N-S electric field component. 2^{nd} panel: E-W magnetic component. 3^{rd} panel: electron density (black) and hot electron density (blue). 4^{th} panel: field aligned downward poynting flux (black) and integrated electron energy flux ($\times 5$) (green). 5^{th} panel: spectrum of electric field fluctuations. The remaining panels show electron and ion energy and pitch angle fluxes. (From Chaston et al. [2000])

auroral region, since lower rates of ionization in the ionosphere (compared to the dayside auroral region) yields lower plasma densities. For the cases studied by Su et al. [2008], the ratio of the plasma frequency to the electron cyclotron frequency ranges from 0.15 to 0.5, which is at least one order of magnitude higher than for the intense AKR observed in upward current regions. The efficiency of the electron-cyclotron maser instability is given by the condition $(\omega_{pe}/\omega_{ce})^2 \ll 1$ [Treumann, 2006]. Under this condition, the generation of AKR as a result of Alfvénic activity is expected to be much less intense than the AKR originating in the auroral density cavity.

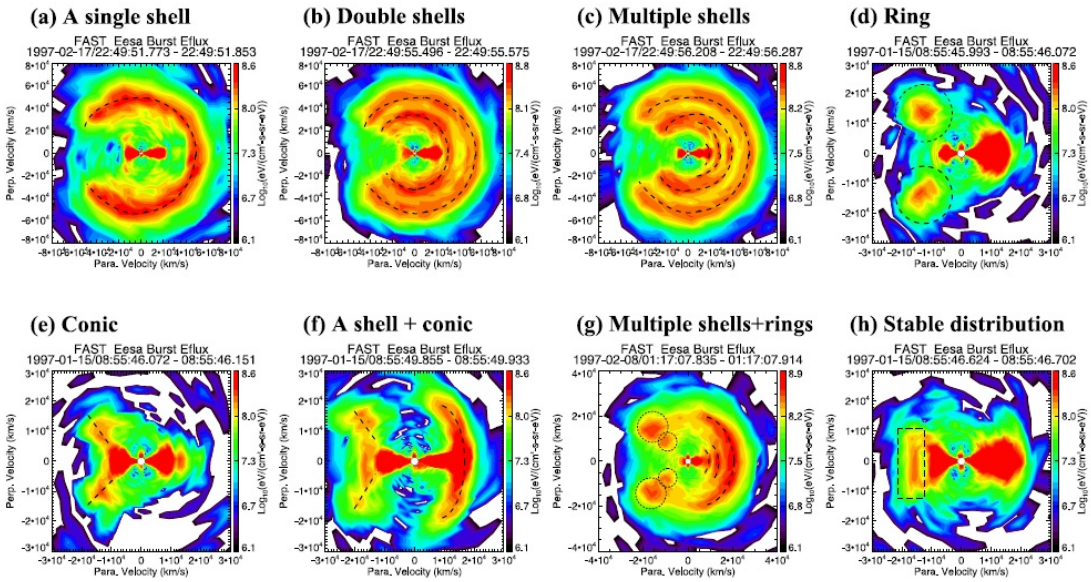

Figure 1.7: Electron velocity distributions observed by the NASA FAST spacecraft during electron burst events. Dashed lines remark each specific distribution type. (From Su et al. [2008])

Chapter 2

Basic plasma physics

2.1 Plasma definition

The term *plasma* is used to address a quasineutral mixture of ionized atoms or molecules and electrons that present collective behavior. Plasma substances rank fourth in a hierarchy that characterizes matter by the strength of molecular bonds of their constituent molecules, and for that reason is considered the *fourth state of matter*.

Atomic interactions result in *bond energies* that create molecules and tend to organize them and keep them together. These potential bonds continuously compete against the thermal kinetic energy of the molecules; the relative strength of these energies ultimately establishes an equilibrium that determines the *state* of matter. By increasing the temperature, one effectively increases the particles kinetic energy, which eventually leads to a *change of phase*: a solid becomes liquid; a liquid becomes gas. The processes of melting and evaporation occur at a constant temperature and only after a certain amount of energy called *latent heat* has been transferred into the substance. On the other hand, molecular bonds are absent in gaseous substances, and interactions are practically limited to direct collisions. Further heating of the gaseous substance increases the strength and frequency of molecular collisions; strong collisions will provide electrons with enough kinetic energy to surpass the binding forces and escape the atom, thereby inducing ionization. The transition from neutral to ionized gas does not require any latent heat; it occurs gradually as the temperature increases.

Ionization changes the behavior of the gas, relative to its neutral state. While in a neutral medium trajectories are dictated by collisions, in the ionized medium they are driven by long-range Coulomb interactions and electromagnetic fields. The above brings *collective effects* into the picture: charged particles interact with many other charged

particles simultaneously, and the seemingly erratic molecular movement of the neutral gas turns into a more *ordered* motion dictated by Maxwell's equations. One of such effects has to do with the fact that internal fields resulting from charge imbalance tend to be canceled by the rapid movement of the electrons as they move to the regions of higher potential. This process is known as *shielding* and is the reason behind the apparent *quasineutrality* of macroscopic plasmas. At sufficiently short scales, however, quasineutrality breaks down; instead, mobile electrons (and not so mobile ions) are continually moving to nullify any external or self-consistent electric fields, their high inertia makes them overshoot their position of equilibrium.

2.1.1 Plasma characterization

From the discussion above one can see that the *plasma* concept is somehow more blurred than the simple conceptual definition given in the first line of this section. Both the ionization degree and shielding concepts hint at the existence of time and spatial scales for the system to be considered as plasma.

Debye length

It is clear that, as one considers shorter spatial scales in a region with nonzero charge distribution, the shielding effect eventually fails and an increasingly stronger electric potential is measured. For larger scales, on the other hand, the collective behavior of the surrounding charges enhances the local shielding. To estimate this effect, one can imagine introducing some positive charge Q inside a region of plasma constituted by electrons and ions; the charge will attract the surrounding electrons and repel the ions. The resulting potential due to the charge Q of the new configuration is, to first order approximation, equal to its original coulomb potential in the absence of plasma, times an inverse exponential term that represents the attenuation due to the shielding of the neighboring charges as the distance r increases [Bittencourt, 2004]:

$$\phi_D = \frac{1}{4\pi\epsilon_0}\frac{Q}{r}\exp\left(-\frac{r}{\lambda_D}\right). \tag{2.1}$$

The parameter λ_D is known as the *Debye length*, which depends on the temperature T and density n_e of the plasma,

$$\lambda_D = \sqrt{\frac{\epsilon_0 k_B T}{n_e e^2}}, \tag{2.2}$$

where $\epsilon_0 = 8.85 \times 10^{-12}\, C^2/Nm^2$ is the *free space permittivity*, $k_B = 1.38 \times 10^{-23}\, J/K$ is the *Boltzmann constant*, $e = 1.602 \times 10^{-19} C$ is the elementary charge. Notice that the

presence of the exponential term in (2.1) indicates a strong attenuation of the resulting electric potential for distances higher than the Debye length. At lower distances, on the other hand, shielding is not as effective and there is charge imbalance. This argument defines a criterion for the definition of plasma, in terms of the characteristic scale L,

$$\lambda_D \ll L. \tag{2.3}$$

Plasma frequency

The spatial scale, represented by the Debye length, together with the mean energy of the distribution (represented by the *thermal velocity*), determine a time scale through the relationship

$$\lambda_D \omega_p = v_t, \tag{2.4}$$

where the *plasma frequency* is given by

$$\omega_{pe} = \sqrt{\frac{n_e e^2}{m_e \epsilon_0}}. \tag{2.5}$$

The plasma frequency can be derived by considering a slab of single ionized ion-electron pairs initially in equilibrium. If the electrons are all moved slightly relative to the ions and then left free, they will establish oscillations with frequency ω_{pe} around the ions [Nicholson, 1983].

Neutral particles are invisible to long-range interactions, causing direct collisions that disturb the collective motion of charged particles. A useful criterion to determinate a plasma reads:

$$\omega_{pe} \tau_c \gg 1, \tag{2.6}$$

where τ_c is the average collision time between charged particles and neutrals. Figure 2.1 shows typical ranges of λ_D and ω_p for different plasma environments.

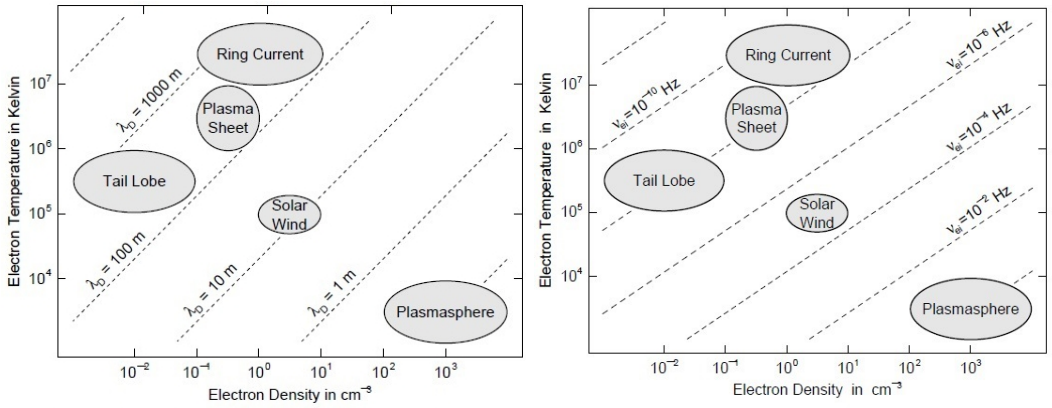

(a) Debye length

(b) Collision frequency

Figure 2.1: Ranges of typical parameters for several geophysical plasmas. (From Baumjohann and Treumann [1997])

2.2 Single charged particle motion

The motion of charged particles in plasmas is intrinsically nonlinear, in that said charge carriers are themselves a source of electromagnetic radiation. As the electric and magnetic fields at a given moment in time drive the motion of the plasma, the redistribution of particles causes reconfiguration of the fields, which will now affect the particles according to the new configuration. This process continuously repeats itself indefinitely. On the other hand, when the mean free path between collisions is long, and when the time scale is short enough as to let the particles to be affected by the external fields within this free path, it is possible to obtain tractable solutions for the trajectories of individual particles.

The nonrelativistic motion equation for a charged particle in the presence of electric and magnetic fields is:

$$m\frac{d\mathbf{v}}{dt} = q\left(\mathbf{E} + \mathbf{v} \times \mathbf{B}\right). \tag{2.7}$$

Next, the dynamics of particle motion is addressed for some illustrative configurations of the external fields.

Electric field

Consider first a charged particle in the presence of an external electric field, and zero magnetic field. From 2.7, it is clear that the particle accelerates in the direction of the electric field if the sign of the charge is positive, and in the opposite direction if the charge

is negative. The component of velocity perpendicular to the field remains invariant.

Constant magnetic field

Regardless of its configuration, magnetostatic forces do not exert work on charged particles. Notice that the dot product of the velocity times the motion equation in the absence of electric field leads to a statement of conservation of kinetic energy:

$$\mathbf{v} \cdot \left(m \frac{d\mathbf{v}}{dt} \right) = \frac{d(1/2mv^2)}{dt} = 0, \tag{2.8}$$

since the term $\mathbf{v} \cdot \mathbf{v} \times \mathbf{B}$ is identically zero. If the field is not just constant but also homogeneous, the cross product $\mathbf{v} \times \mathbf{B}$ also proves the invariance of the velocity component parallel to the field. For this reason, it is convenient to consider the parallel and perpendicular motions separately. The projected motion along the magnetic field in this case is just constant velocity motion. As for the transverse motion, one can write, since $\mathbf{B}$ is constant:

$$\begin{aligned} m\frac{d\mathbf{v}_\perp}{dt} &= q\frac{d\mathbf{r}_\perp}{dt} \times \mathbf{B}, \\ \frac{d}{dt}\Big[m\mathbf{v}_\perp &= q\mathbf{r}_\perp \times \mathbf{B} \Big]. \end{aligned} \tag{2.9}$$

The expression in squared parenthesis gives $\mathbf{v}_\perp$ in a form that characterizes circular motion:

$$\mathbf{v}_\perp = \mathbf{\Omega_c} \times \mathbf{r}_\perp, \tag{2.10}$$

with angular, or *cyclotron* frequency:

$$\mathbf{\Omega_c} = -\frac{q\mathbf{B}}{m}. \tag{2.11}$$

From (2.10), one obtains the radius $r_c = r_\perp$ of the circular perpendicular trajectory:

$$r_c = \frac{v_\perp}{\Omega_c} = \frac{mv_\perp}{|q|B}. \tag{2.12}$$

Furthermore, the orbital trajectory of the charged particle can be regarded as a circuit with current given by the particles charge divided by the period of gyration. Associated to said current, the magnitude of the magnetic moment $\mu = IA$ can be obtained:

$$\mu = \frac{|q|\Omega_c}{2\pi}\pi r_c^2 = \frac{1}{2}|q|\Omega_c r_c^2, \tag{2.13}$$

which, in terms of the magnetic intensity and the perpendicular velocity through the relations (2.12) and (2.11) becomes,

$$\mu = \frac{\frac{1}{2}mv_{\perp}^2}{B}. \tag{2.14}$$

The total particle trajectory draws a *helix*; the charge moves at constant velocity in the parallel direction while circling the magnetic field line. The frequency of the rotational motion is often so high that the exact position of the particle is of little practical importance. In such cases one considers the trajectory of the *gyrocenter*, which is defined as the particles average position over the time it takes to complete one gyration:

$$\mathbf{r_g}(t) = \int_t^{t+\tau} dt'\, v(t'), \tag{2.15}$$

where $\tau = \frac{2\pi}{\Omega_c}$.

2.2.1 Particle drifts

Perhaps the most immediate application of gyromotion leads to the concept of *particle drift*. For instance, consider the case of an electric field $\mathbf{E}_\perp$ directed somewhere in the plane normal to $\mathbf{B}$. The motion perpendicular to the magnetic field looks like

$$m\frac{d\mathbf{v}_\perp}{dt} = q\left(\mathbf{E}_\perp + \mathbf{v}_\perp \times \mathbf{B}\right). \tag{2.16}$$

It is convenient to observe the motion from a different reference frame which moves with constant velocity, $\mathbf{v_E}$, such that we can write $\mathbf{v}_\perp(t) = \mathbf{u}_\perp(t) + \mathbf{v_E}$. Then we get

$$m\frac{d\mathbf{u}_\perp}{dt} = q\left(\mathbf{E}_\perp + \mathbf{u}_\perp \times \mathbf{B} + \mathbf{v_E} \times \mathbf{B}\right). \tag{2.17}$$

This equation asserts that there is a reference frame from which the first and third terms on the right-hand-side cancel out, and all the observer sees is the circular motion described in the previous case. The relative velocity of this frame is given by

$$\mathbf{v_E} = \frac{\mathbf{E}_\perp \times \mathbf{B}}{B^2}. \tag{2.18}$$

Note that this can also be expressed in terms of the electric force as $\mathbf{v_E} = \mathbf{F_E} \times \mathbf{B}/(qB^2)$. In general, the presence of additional forces perpendicular to the magnetic field, as well as nonuniformities or gradients on the magnetic field, modify the helical motion and cause additional drifts. Table 2.1 summarizes the particle drifts for some special cases.

A general expression for the average motion due to an arbitrary force $\mathbf{F}$ is the following:

$$\mathbf{v_F} = \frac{1}{\Omega_C}\left(\frac{\mathbf{F}}{m} \times \frac{\mathbf{B}}{B}\right). \tag{2.19}$$

Table 2.1: Guiding center drifts and their resulting currents. (From Baumjohann and Treumann [1997])

$E \times B$ drift	$\mathbf{v_E} = \dfrac{\mathbf{E} \times \mathbf{B}}{B^2}$	
Polarization drift	$\mathbf{v_P} = \dfrac{1}{\Omega_c B}\dfrac{d\mathbf{E}}{dt}$	$\mathbf{j_P} = \dfrac{n_e(m_i + m_e)}{B^2}\dfrac{d\mathbf{E}}{dt}$
Gradient drift	$\mathbf{v}_\nabla = \dfrac{K_\perp}{2qB^3}(\mathbf{B} \times \nabla B)$	$\mathbf{j}_\nabla = \dfrac{n_e(\mu_i + \mu_e)}{B^2}(\mathbf{B} \times \nabla B)$
Curvature drift	$\mathbf{v_C} = \dfrac{mv_\parallel^2}{qr_cB^2}(\mathbf{r_c} \times \mathbf{B})$	$\mathbf{j_C} = \dfrac{2n_e(K_{i\parallel} + K_{e\parallel})}{(r_cB)^2}(\mathbf{r_c} \times \mathbf{B})$

Here $K = 1/2mv^2$, and the subindices e and i refer to *electrons* and *ions* respectively.

2.2.2 Magnetic mirror force

To illustrate this effect, consider the particle motion in a magnetostatic setup that is axially symmetric to the $\hat{\mathbf{z}}$ direction, and which intensifies *weakly* with increasing z; the following expression describes this field [Bittencourt, 2004]:

$$\mathbf{B}(r, \theta, z) = B_0\hat{\mathbf{z}} + (\mathbf{r} \cdot \nabla)\mathbf{B}, \tag{2.20}$$

assuming that the second term is small when compared to B_0. If we substitute (2.20) into (2.7), subtract the zero-order motion, and eliminate second and higher order terms, we obtain

$$m\left(\frac{d\delta\mathbf{v}}{dt}\right) = q(\delta\mathbf{v} \times \mathbf{B_0}) + q\mathbf{v_0} \times [\mathbf{r_0} \cdot (\nabla\mathbf{B})], \tag{2.21}$$

where r_0 and v_0 represent the circular motion or zero-order trajectory. The first term on the right hand side consists of small oscillations which add to zero when averaged over one period of gyration. As for the second term, notice that $\mathbf{r_0} \cdot (\nabla\mathbf{B}) = r_0\partial\mathbf{B}/\partial r$.

On the other hand, recall that $\hat{\mathbf{v}}_\mathbf{0} = -\hat{\theta}$ for ions and $\hat{\mathbf{v}}_\mathbf{0} = \hat{\theta}$ for electrons. Thus, the second term of the right hand side can be written as two components, one parallel and one perpendicular to the magnetic field orientation, given by

$$\mathbf{F}_\parallel = 2\mu \frac{\partial B_r}{\partial r}\hat{\mathbf{z}} \tag{2.22}$$

and

$$\mathbf{F}_\perp = -2\mu \frac{\partial B_z}{\partial r}\hat{\mathbf{r}} \tag{2.23}$$

respectively. Notice also that the quantity $|q|r_0 v_0 = mv_0^2/(2B_0) = \mu$ after substituting r_0 according to equation (2.12). The perpendicular force causes a gradient drift as indicated in table 2.1. As for the parallel force, we are interested in its average value over a gyration period

$$\left\langle F_\parallel \right\rangle = 2\mu \left(\frac{1}{2\pi} \oint d\theta \frac{\partial B_r}{\partial r} \right). \tag{2.24}$$

Consider the condition of divergentless magnetic field in cylindrical coordinates

$$\nabla \cdot \mathbf{B} = \frac{1}{r}\frac{\partial}{\partial r}(rB_r) + \frac{1}{r}\frac{\partial B_\theta}{\partial \theta} + \frac{\partial B_z}{\partial z} = 0. \tag{2.25}$$

By expanding the first term, and assuming a weak variation such that $\partial B_r/\partial r \simeq B_r/r$, we can write

$$\frac{\partial B_r}{\partial r} = -\frac{1}{2}\left(\frac{1}{r}\frac{\partial B_\theta}{\partial \theta} + \frac{\partial B_z}{\partial z} \right). \tag{2.26}$$

Average of the first term in the right hand side of (2.26) over one gyration is identically zero, as it can be noticed from the fact that it consists of a closed path integral of a derivative with respect to θ. To evaluate the second term, one assumes that the variation is approximately constant over the gyration. Furthermore, one uses the fact that $B_z \simeq B$. After these considerations we have

$$\left\langle \frac{\partial B_r}{\partial r} \right\rangle = -\frac{1}{2}\frac{\partial B}{\partial z}, \tag{2.27}$$

and (2.22) takes the rather simple form

$$\langle \mathbf{F}_\parallel \rangle = \mu \frac{\partial B}{\partial z}(-\hat{\mathbf{z}}). \tag{2.28}$$

This equation indicates that charged particles decelerate (accelerate) as they move into regions of higher (lower) magnetic intensity. The parallel force is commonly known as

mirror force since it can cause charged particles to reflect into regions of lower magnetic field.

2.2.3 Invariance of the magnetic moment

An important simplification in the study of particle trajectories arises as a consequence of kinetic energy conservation of charged particles when affected by the mirror force. Consider the parallel movement as described by equation (2.28), which multiplied by $v_\parallel = dz/dt$ becomes

$$m_s v_\parallel \frac{dv_\parallel}{dt} = -|\mu| \frac{\partial B}{\partial z} \frac{\partial z}{\partial t} \tag{2.29}$$

$$\frac{d(\frac{1}{2} m_s v_\parallel^2)}{dt} = -\frac{\frac{1}{2} m_s v_\perp^2}{2B} \frac{dB}{dz} \tag{2.30}$$

$$\frac{dK_\parallel}{dt} = -\frac{K_\perp}{B} \frac{dB}{dt}. \tag{2.31}$$

On the other hand, consider also the following statement of energy conservation:

$$\frac{dK}{dt} = \frac{dK_\parallel}{dt} + \frac{dK_\perp}{dt} = 0, \tag{2.32}$$

from which $dK_\parallel/dt = -dK_\perp/dt$ follows. By substituting the parallel kinetic energy term into (2.29), we obtain

$$\frac{1}{K_\perp} \frac{dK_\perp}{dt} - \frac{1}{B} \frac{dB}{dt} = 0. \tag{2.33}$$

The last equation can also be written as

$$\frac{d}{dt} \left[\ln(K_\perp) - \ln(B) \right] = 0, \tag{2.34}$$

which is equivalent to the condition

$$\frac{K_\perp}{B} = const. \tag{2.35}$$

2.2.4 Particle motion in the geomagnetic field

Even though orbital theory does not provide an accurate description of most plasma phenomena, some principles of single particle motion have been found useful to depict the large-scale steady motion of plasma within the inner magnetosphere. In this region, the magnetic configuration is often described as a dipole field with magnetic moment

$M_E = 8.3 \times 10^{22}$ Am^2. The vector that represents this dipole is tilted 11.5^o relative to the Earth's spin axis. Regarding a modified spherical coordinate system $(r, \phi, \lambda = \theta - \pi/2)$, oriented such that the $\hat{\mathbf{z}}$ axis goes along the magnetic moment direction, the geomagnetic field is expressed as

$$\mathbf{B_G}(r, \lambda) = \frac{\mu_0 M_E}{4\pi r^3} \left(2 \sin\lambda(-\hat{\mathbf{r}}) + \cos\lambda\hat{\lambda} \right). \tag{2.36}$$

A relationship describing the shape of magnetic field lines is found through the condition

$$d\mathbf{s} \times \mathbf{B_G} = 0, \tag{2.37}$$

where $d\mathbf{s} = dr\hat{\mathbf{r}} + rd\lambda\hat{\lambda}$ represents an arc element along the field line. This leads to

$$r(\lambda) = R_E L \cos^2\lambda, \tag{2.38}$$

where $R_E \simeq 6370$ km and L is the so-called *L-shell* or McIllwain parameter, which indicates the geocentric distance of the field line intersection with the equatorial plane in units of Earth radius. Substitution of equation (2.38) into (2.36) allows to express the geomagnetic field magnitude in terms of latitude for a given field line L

$$B(\lambda, L) = \frac{B_E}{L^3} \frac{\sqrt{1 + 3\sin^2\lambda}}{\cos^6\lambda}, \tag{2.39}$$

where $B_E = \mu_0 M_E/(4\pi R_E^3) = 3.11 \times 10^{-5}$ T. Furthermore, by taking $r = R_E$ in (2.38) one obtains the latitude at which any given field line intersects the Earths surface

$$\lambda_E = \arccos\sqrt{L^{-1}}. \tag{2.40}$$

Figure 2.2 presents a schematic of the typical motion of charged particles within the geomagnetic field. According to the ideas presented in the previous subsections, these particles draw helicoidal trajectories around magnetic field lines. As they move to higher latitudes where field lines converge, the mirror force causes deceleration in the direction parallel to the magnetic field and, if the force is strong enough, it will induce particle reflection and trapping, forcing bounce motion between certain latitudes known as *mirror points*. For a particle moving about some given field line, the mirror points are determined solely by the particles *pitch angle*:

$$\alpha = \arctan\left(\frac{v_\perp}{v_\parallel} \right). \tag{2.41}$$

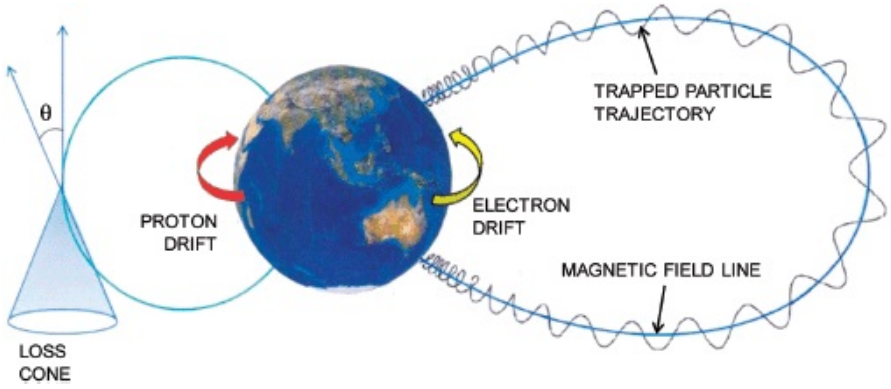

Figure 2.2: Typical trajectory for particles trapped in the geomagnetic field. Notice that the equatorial loss cone has been labeled as θ. (From `https://download.e-bookshelf.de/download/0003/9138/32/L-X-0003913832-0002397570.XHTML/index.xhtml`)

Alternatively, the bouncing motion can be explained through conservation of magnetic momentum. According to equation (2.35), as the particle moves towards higher latitudes into regions of stronger magnetic intensity, its perpendicular kinetic energy must also increase to maintain μ constant. Due to energy conservation, an increase of $K_\perp$ comes at the expense of $K_\parallel$. Trapped particles will reflect at a location where $K_\parallel$ becomes zero, i.e., its pitch angle reaches $\pi/2$ radians. For a particle located at latitude λ, the pitch angle required to reach the mirror point B_m is given by the condition

$$\frac{mv^2 \sin^2 \alpha(\lambda)}{2B(\lambda)} = \frac{mv^2 \sin^2 \frac{\pi}{2}}{2B_m}, \tag{2.42}$$

$$\alpha(\lambda) = \arcsin \sqrt{\frac{B(\lambda)}{B_m}}. \tag{2.43}$$

Not all particles lingering in the inner magnetosphere are trapped. At altitudes of approximately 100 km from Earth's surface, the adiabatic motion described above is interrupted by collisions and particles are lost to the atmosphere. For simplicity, consider the population of escapees as the particles that reach the latitude λ_E defined by equation (2.40). From (2.43) it follows that precipitating particles have pitch angles equal to or less than the following threshold limit, known as the *loss cone*.

$$\alpha_l(\lambda) = \arcsin \sqrt{\frac{B(\lambda)}{B(\lambda_E)}}. \tag{2.44}$$

Notice that the loss cone at a given latitude is uniquely determined by the ratio of magnetic intensities between the point where the loss cone is being measured and the

surface of the Earth. For instance, the equatorial ($\lambda = 0$) loss cone takes the value (see Figure 2.2)

$$\alpha_{l,eq} = \arcsin^2\left(\frac{\cos^6\lambda_E}{\sqrt{1+3\sin^2\lambda_E}}\right) = \arcsin^2\left(\frac{1}{\sqrt{4L^6-3L^5}}\right). \tag{2.45}$$

Besides its bouncing motion in between poles, plasma particles also drift as a consequence of the inhomogeneous nature of the geomagnetic field. Both gradient and curvature drifts (see table 2.1) induce westward motion for positively charged particles and eastward flow for negative ones. The resulting current flows westward around the Earth and is known as the *ring current*. Within the plasmasphere, a $E \times B$ drift occurs due to the induced corotation of the plasma with the Earth as a result of collisional coupling with the atmosphere [Gurnett and Bhattacharjee, 2005]; however, this drifting motion does not cause charge separation.

2.3 Elements of plasma kinetic theory

Plasmas, like gases, are systems composed by very large numbers of particles. As with gaseous systems, any practical attempt to describe the macroscopic state of a plasma has to be based on statistical principles. A key element on this formulation is the concept of *distribution function*; a mathematical entity that contains all the physical information of the system in terms of space phase coordinates and time. The distribution function $f_s(\mathbf{r}, \mathbf{v}, t)$ represents the density of particles of species s in the immediate neighborhood of the phase-space location $(\mathbf{r}, \mathbf{v})$ (Notice that in this context, the phase-space coordinates $\mathbf{r}$ and $\mathbf{v}$ constitute a set of 6 orthogonal coordinates, often known as μ-space). By definition, integration over the velocity space gives the particle density as a function of the position:

$$n_s(\mathbf{r}, t) = \int_v d^3v\, f_s(\mathbf{r}, \mathbf{v}, t). \tag{2.46}$$

In general, notice that $f_s(\mathbf{r}, \mathbf{v}, t)$ bins particles into groups that share the same dynamical state. For one of such conglomerates, the total amount of certain property, say $\chi(\mathbf{r}, \mathbf{v}, t)$, inside a phase-space volume $d^3r d^3v$ around $(\mathbf{r}, \mathbf{v})$, is given by the quantity $\chi(\mathbf{r}, \mathbf{v}, t) f_s(\mathbf{r}, \mathbf{v}, t) d^3r d^3v$. Therefore, the macroscopic average $\langle \chi(\mathbf{r}, \mathbf{v}, t) \rangle$ can be conveniently expressed in terms of the weighted sum over the velocity space, divided by the number of particles within the spatial volume element, $n_s(\mathbf{r}, t) d^3r$,

$$\langle \chi_s(\mathbf{r}, t) \rangle = \frac{1}{n_s(\mathbf{r}, t)} \int_v d^3v\, \chi(\mathbf{r}, \mathbf{v}, t) f_s(\mathbf{r}, \mathbf{v}, t). \tag{2.47}$$

Equation (2.47) provides a systematic tool to define macroscopic properties from the microscopic state represented by the distribution function. For instance, the average velocity $\mathbf{u_s}(\mathbf{r}, t)$ describing the macroscopic drift of the bulk plasma is obtained by setting $\chi = \mathbf{v}$ in equation (2.47):

$$\mathbf{u_s}(\mathbf{r}, t) = \frac{1}{n_s(\mathbf{r}, t)} \int_v d^3v \, \mathbf{v} f_s(\mathbf{r}, \mathbf{v}, t). \tag{2.48}$$

In general, these macroscopic properties are defined as a function of the so-called *moments of the distribution function.* The moment of order k is expressed as

$$\mathbf{M}^{(k)} = \int_v d^3v \, \mathbf{v}^k \, f_s. \tag{2.49}$$

The amount $\mathbf{\Gamma_s}(\mathbf{r}, t) = n_s \mathbf{u_s}(\mathbf{r}, t)$ is known as the *particle flux density*, each of its components is equal to the number of particles crossing the location $\mathbf{r}$ per unit time. Notice that both the particle density and particle flux correspond to the zeroth and first moments of the distribution, respectively. Other physical quantities are associated to higher order moments: the momentum flow dyad is given by the second moment as $\mathbf{\Pi} = m_s M^{(2)}$, while the total energy flux triad $\mathbf{E} = m_s M^{(3)}$. In the special case when $\mathbf{u_s} = 0$, the former reduces to the pressure tensor, while the second becomes the thermal energy flux tensor [Bittencourt, 2004].

2.3.1 The Boltzmann equation and the Vlasov equation

Another advantage of having particles sorted together in phase-space bins is that it becomes easier to track the distributions time evolution. Consider one such group of particles inside an infinitesimal phase-space volume element $d^3r d^3v$. The subsequent motion of these particles is identical since they have the same initial position and velocity. After some time, these particles will have moved to a different location within phase-space, but the number of particles remains invariant. Although microscopically the phase-space volume will deform in time due to slight differences in position and velocity between particles within the infinitesimal volume, it can be demonstrated [Bittencourt, 2004; Baumjohann and Treumann, 1997] that macroscopically these variations are negligible. This leads to the following statement of conservation:

$$\frac{D}{Dt} f_s(\mathbf{r}, \mathbf{v}, t) = \frac{\partial}{\partial t} f_s(\mathbf{r}, \mathbf{v}, t) + \mathbf{v} \cdot \nabla_{\mathbf{r}} f_s(\mathbf{r}, \mathbf{v}, t) + \mathbf{a} \cdot \nabla_{\mathbf{v}} f_s(\mathbf{r}, \mathbf{v}, t) = 0. \tag{2.50}$$

Furthermore, a more careful treatment [Nicholson, 1983] of the time derivative of the

density of states in the Γ-space asserts that the variation of the density of the number of states is identically zero; this result is known as *Liouville's theorem.*

The invariance expressed in equation (2.50) could be thwarted if collisions in the system occur frequently. Inclusion of a source term associated to the effect of collisions results in the so called *Boltzmann equation*:

$$\frac{\partial}{\partial t} f_s(\mathbf{r},\mathbf{v},t) + \mathbf{v}\cdot\nabla_{\mathbf{r}} f_s(\mathbf{r},\mathbf{v},t) + \frac{q_s}{m_s}\left(\mathbf{E}+\mathbf{v}\times\mathbf{B}\right)\cdot\nabla_{\mathbf{v}} f_s(\mathbf{r},\mathbf{v},t) = \left.\frac{\delta}{\delta t} f_s(\mathbf{r},\mathbf{v},t)\right|_c \quad (2.51)$$

2.3.2 Fluid equations

The Boltzmann equation expresses the conservation of the number of particles within the volume $d^3r d^3v$. Likewise, a statement of conservation for the macroscopic property $\chi(\mathbf{v})$ is obtained by simple integration of the Boltzmann equation in the following fashion

$$\int_v d^3v\, \chi(\mathbf{v}) \left(\frac{D f_s(\mathbf{r},\mathbf{v},t)}{Dt} = \left.\frac{\delta f_s(\mathbf{r},\mathbf{v},t)}{\delta t}\right|_c \right) \quad (2.52)$$

provided that $f_s(\mathbf{r},\mathbf{v},t)$ has compact support in velocity space. Thus, by setting $\chi = m_s$, $\chi = m_s\mathbf{v}$, and $\chi = 1/2 m_s v^2$; one obtains equations for mass, momentum, and energy conservation, respectively. On the other hand, it is impossible to obtain a closed system of equations using this method exclusively, as the integration of the k-th moment returns its conservation in terms of the moment $k+1$. An important part on setting a fluid theory consists of truncating the number of conservation laws up to a certain moment k and setting a separate condition defining the higher order moment involved. The choice of such a closure condition will naturally cause the fluid theory to be valid within the range of systems where the condition is valid. There are several plasma fluid formulations in the literature, suitable to describe plasmas with different properties. We do not include their derivation here due to space limitations, but we use the magnetohydrodynamic approximation in section 2.4.1, and the *two-fluid* approximation in section 2.4.2.

2.3.3 Linear Kinetic Theory

The fluid description of plasmas is appropriate in cases where the distribution is close to a thermodynamical and Coulomb collisional equilibrium. To describe the dynamics of non-equilibrium systems, variations of the distribution function must be accounted for explicitely. Within the treatment of collisionless plasmas, the complete set of equations is composed by the Vlasov equation in terms of the self-consistent electric and magnetic fields; the Maxwells equations; and the definition of the charge and current densities in

terms of the distribution function:

$$\rho = \sum_s q_s \int_v d^3v\, f(v), \tag{2.53}$$

$$\mathbf{j} = \sum_s q_s \int_v d^3v\, \mathbf{v} f(v). \tag{2.54}$$

Later on in section 2.4.3 we use this approach to derive solutions of the dispersion equation valid for the same approximations as the DK1D algorithm and prove that obtained solutions coincide with the general solution found in Lysak and Lotko [1996] when $T_i \to 0$.

A different approach, which has been widely used to analyze wave propagation and dispersion in magnetized plasmas, consists of considering the plasma as a dielectric medium. Under this premise, $\mathbf{j}$ is treated as a displacement current. Ampere's equation has the form

$$\nabla \times \mathbf{B} = \mu_0 \frac{\partial \mathbf{D}}{\partial t} = \frac{1}{c^2} \frac{\partial \mathbf{K} \cdot \mathbf{E}}{\partial t}, \tag{2.55}$$

where $\mathbf{D} = \epsilon_0 \mathbf{K} \cdot \mathbf{E}$ is the electric displacement vector and $\mathbf{K}$ is the *effective dielectric tensor*.

We consider wave solutions with space-time variations of the form $\exp[i(\mathbf{k} \cdot \mathbf{r} - \omega t)]$. Thus Ampere and Faraday's equations become, respectively

$$\mathbf{k} \times \mathbf{B} = -\frac{\omega}{c^2} \mathbf{K} \cdot \mathbf{E} \tag{2.56}$$

and

$$\mathbf{B} = \frac{\mathbf{k} \times \mathbf{E}}{\omega}. \tag{2.57}$$

Substitution of (2.57) into (2.56) leads to the relation

$$\mathbf{k} \times \mathbf{k} \times \mathbf{E} + \left(\frac{\omega}{c}\right) \mathbf{K} \cdot \mathbf{E} = 0. \tag{2.58}$$

Finally, evaluate the triple product on the left hand side, $\mathbf{a} \times \mathbf{b} \times \mathbf{c} = \mathbf{b}(\mathbf{a} \cdot \mathbf{c}) - \mathbf{c}(\mathbf{a} \cdot \mathbf{b})$, and introduce the index of refraction, $\mathbf{n} = c\mathbf{k}/\omega$, to obtain a general form of the dispersion equation:

$$\left(\mathbf{nn} - n^2 \mathbf{I} + \mathbf{K}\right) \cdot \mathbf{E} = 0. \tag{2.59}$$

Here $\mathbf{I}$ represents the unit dyad. Nontrivial wave solutions can be found by setting the

determinant of the expression in between parenthesis to zero.

2.4 Alfvén waves in magnetized plasma

2.4.1 Ideal MHD waves

Consider wave propagation within a conducting, nonviscuous and compressible plasma with density $\rho_0 = (m_i + m_e)n_0 \simeq m_i n_0$ embedded in an uniform background magnetic field $\mathbf{B_0} = B_0\hat{\mathbf{z}}$. The normal wave modes are determined by the following physical relations:

- Continuity equation

$$\frac{\partial \rho}{\partial t} + \nabla \cdot (\rho \mathbf{v}) = 0. \tag{2.60}$$

- Momentum conservation

$$\rho \frac{D\mathbf{v}}{Dt} = -\nabla p + \mathbf{J} \times \mathbf{B}. \tag{2.61}$$

- The adiabatic energy approximation, $p\rho^\gamma = \text{const}$, can be written as

$$\nabla p = c_s^2 \nabla \rho, \tag{2.62}$$

  where $c_s = \sqrt{\gamma p/\rho} = \sqrt{\gamma k_B T/m_i}$ is the adiabatic sound speed.

- Low-frequency Ampere law

$$\nabla \times \mathbf{B} = \mu_0 \mathbf{J}. \tag{2.63}$$

- Faraday law

$$\nabla \times \mathbf{E} = -\frac{\partial \mathbf{B}}{\partial t}. \tag{2.64}$$

- Ohm's law for ideal MHD

$$\mathbf{E} + \mathbf{v} \times \mathbf{B} = 0. \tag{2.65}$$

From this system, equations (2.61), (2.62), and (2.63) can be combined in the form [Bittencourt, 2004]

$$\rho\frac{D\mathbf{v}}{Dt} + c_s^2\nabla\rho + \mathbf{B}\times\frac{(\nabla\times\mathbf{B})}{\mu_0} = 0. \tag{2.66}$$

Similarly, we can dispense of the electric field by combining equations (2.64) and (2.65):

$$\frac{\partial\mathbf{B}}{\partial t} - \nabla\times(\mathbf{v}\times\mathbf{B}) = 0. \tag{2.67}$$

We consider the propagation of a small, low-frequency perturbation. This perturbation triggers first-order changes in the plasma and fields:

$$\begin{aligned}
\mathbf{v}(\mathbf{r},t) &= \delta\mathbf{v}(\mathbf{r},t)\\
n(\mathbf{r},t) &= n_0 + \delta n(\mathbf{r},t)\\
\mathbf{E}(\mathbf{r},t) &= \delta\mathbf{E}(\mathbf{r},t)\\
\mathbf{B}(\mathbf{r},t) &= \mathbf{B_0} + \delta\mathbf{B}(\mathbf{r},t).
\end{aligned} \tag{2.68}$$

The first step towards deriving the dispersion equation consists of linearizing equations (2.60), (2.66) and (2.67) by substituting the tentative solutions (2.68) and suppressing all second-order terms. This leads to the following system of equations:

$$\frac{\partial\delta n}{\partial t} + n_0\nabla\cdot\delta\mathbf{v} = 0. \tag{2.69}$$

$$n_0\frac{\partial\delta\mathbf{v}}{\partial t} + c_s^2\nabla\delta n + \mathbf{B_0}\times\frac{(\nabla\times\delta\mathbf{B})}{m_i\mu_0} = 0. \tag{2.70}$$

$$\frac{\partial\delta\mathbf{B}}{\partial t} - \nabla\times(\delta\mathbf{v}\times\mathbf{B_0}) = 0. \tag{2.71}$$

Next, take the time derivative of (2.70):

$$n_0\frac{\partial^2\delta\mathbf{v}}{\partial t^2} + c_s^2\nabla\frac{\partial\delta n}{\partial t} + \frac{\mathbf{B_0}}{m_i n_0}\times\left(\nabla\times\frac{\partial\delta\mathbf{B}}{\partial t}\right) = 0, \tag{2.72}$$

and substitute $\partial\delta\mathbf{v}/\partial t$ and $\partial\delta\mathbf{B}/\partial t$ from (2.69) and (2.71), respectively. This gives

$$\frac{\partial^2\delta\mathbf{v}}{\partial t^2} - c_s^2\nabla(\nabla\delta\mathbf{v}) + \mathbf{v_A}\times(\nabla\times[\nabla\times(\delta\mathbf{v}\times\mathbf{v_A})]) = 0, \tag{2.73}$$

where we have introduced the Alfvén speed $\mathbf{v_A} = \mathbf{B_0}/\sqrt{m_i n_0\mu_0}$.

Without missing any of the physics, we chose a reference system orientated so that

the wavenumber is given by $\mathbf{k} = k_x\hat{\mathbf{x}} + k_z\hat{\mathbf{z}}$, making an angle θ with the external field. Also, we introduce a test solution in the form of a plane wave $\delta\mathbf{v} = \mathbf{v_0}e^{i(\mathbf{k}\cdot\mathbf{r}-\omega t)}$. Then we obtain [Bittencourt, 2004]

$$-\omega^2\mathbf{v_0} + c_s^2\mathbf{k}\mathbf{k}\cdot\mathbf{v_0} - \mathbf{v_A}\times(\mathbf{k}\times[\mathbf{k}\times(\mathbf{v_0}\times\mathbf{v_A})]) = 0. \tag{2.74}$$

Using the identity $\mathbf{a}\times\mathbf{b}\times\mathbf{c} = \mathbf{b}\mathbf{a}\cdot\mathbf{c} - \mathbf{c}\mathbf{a}\cdot\mathbf{b}$, and after some straightforward algebraic manipulations, the previous relation can be expressed in matrix form as

$$\begin{bmatrix} \omega^2 - (k_z v_A)^2 - k_x^2(c_s^2 + v_A^2) & 0 & -c_s^2 k_x k_z \\ 0 & \omega^2 - (k_z v_A)^2 & 0 \\ -c_s^2 k_x k_z & 0 & \omega^2 - (c_s k_z)^2 \end{bmatrix} \cdot \delta\mathbf{v} = 0. \tag{2.75}$$

The possible modes are given by the determinant:

$$\left[\omega^2 - (k_z v_A)^2\right]\left[\omega^4 - k^2(c_s^2 + v_A^2) + (k_z^2 v_A c_s)^2\right] = 0. \tag{2.76}$$

The Shear Alfvén wave

Notice that equation (2.75) reveals an uncoupled wave mode $\delta\mathbf{v} = \delta v\hat{\mathbf{y}}$ perpendicular to both the background magnetic field and the wave vector, and with phase speed $\omega/k = v_A\cos\theta$. From equation (2.71), it follows that in this case the magnetic perturbation oscillates along the same axis as the velocity pertubation

$$\delta\mathbf{B} = -\frac{B_0}{v_A}\cos\theta\delta\mathbf{v}. \tag{2.77}$$

The electric field is obtained from Ohm's law (2.65)

$$\delta\mathbf{E} = -\delta v B_0\hat{\mathbf{x}}. \tag{2.78}$$

The Poynting flux, $\mathbf{S} = \mathbf{E}\times\mathbf{B}/\mu_0$ indicates that the energy flow is parallel to the background field, independently of the propagation angle θ.

Magnetoacoustic modes

The second factor in the right-hand-side of (2.76) reveals two modes with phase velocities

$$\left(\frac{\omega}{k}\right)^2 = \frac{1}{2}\left[v_A^2 + c_s^2 \pm \sqrt{(v_A^2 + c_s^2)^2 - (2v_A c_s\cos\theta)^2}\right] \tag{2.79}$$

known as *fast*(+) and *slow*(-) magnetoacoustic waves. For these waves, the motion occurs in the plane defined by the wave vector and the magnetic field.

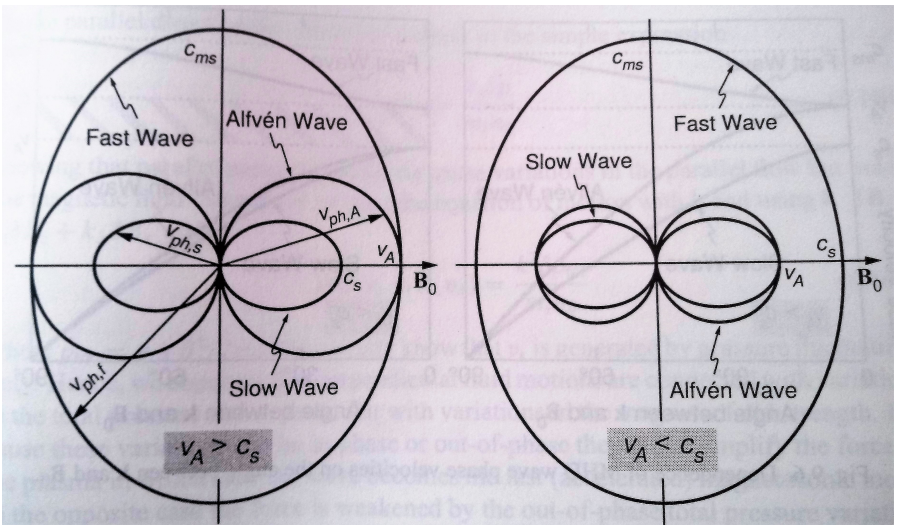

Figure 2.3: Phase diagrams for the MHD Alfvén wave modes. (From [Baumjohann and Treumann, 1997])

Figure 2.3 displays the phase speed of the three MHD modes as a function of θ. In general, the phase speed for the fast mode has a minimum value of $\max(v_A, c_s)$ when propagating parallel to the background magnetic field, and increases with larger θ up to $\sqrt{v_A^2 + c_s^2}$ for $\theta = \pi/2$. The phase speed of the slow mode, on the other hand, decreases from $\min(v_A, c_s)$ when $\theta = 0$, to zero at $\theta = \pi/2$.

2.4.2 Dispersive Alfvén waves

The so-called Dispersive Alfvén Waves (DAWs) are originally shear modes for which ideal MHD conditions break down as the perpendicular scale decreases to the order of the ion acoustic gyroradius or electron skin depth. When that is the case, particles can no more be treated as frozen into the plasma, and consequently, one must account for currents both perpendicular and parallel to the background magnetic field, and parallel electric fields. Perpendicular currents are provided through polarization drift, which is essentially carried by the more massive ions [Stasiewicz et al., 2000]:

$$\mathbf{j}_\perp = \frac{nm_i}{B_0^2}\frac{\partial \mathbf{E}_\perp}{dt}. \tag{2.80}$$

Non-MHD effects are introduced in Ohm's law [Paschmann et al., 2003]

$$\delta\mathbf{E} + \delta\mathbf{v} \times \mathbf{B_0} = \frac{m_e}{n_0 e^2}\frac{\partial \mathbf{j}}{\partial t} - \frac{\nabla p}{n_0 e}, \tag{2.81}$$

from where we can obtain an expression for the parallel electric field

$$\delta E_\parallel = \frac{m_e}{n_0 e^2}\frac{\partial j_\parallel}{\partial t} - \frac{m_i c_s^2}{n_0 e}\frac{\partial \delta n}{\partial z}. \tag{2.82}$$

Notice that equation (2.62) has been invoked to eliminate the pressure. Taking the time derivative of the previous equation, and substituting the term $\partial\delta n/\partial t$ from the continuity equation, yields [Paschmann et al., 2003]

$$\frac{\partial \delta E_\parallel}{\partial t} = \frac{m_e}{n_0 e^2}\frac{\partial^2 j_\parallel}{\partial t^2} - \frac{m_i c_s^2}{n_0 e^2}\frac{\partial^2 j_\parallel}{\partial z^2}. \tag{2.83}$$

Next, let's introduce the time derivative of Faraday's equation:

$$-\frac{\partial^2 \delta\mathbf{B}}{\partial t^2} = \nabla \times \frac{\partial \delta\mathbf{E}}{\partial t} = \nabla \times \left(\frac{\delta \partial E_\parallel}{\partial t}\hat{z} + \frac{\partial \delta \mathbf{E}_\perp}{\partial t}\right). \tag{2.84}$$

Substituting the electric field components from (2.80) and (2.83), we obtain

$$-\frac{\partial^2 \delta\mathbf{B}}{\partial t^2} = \left(\frac{m_e}{n_0 e^2}\frac{\partial^2}{\partial t^2} - \frac{m_i c_s^2}{n_0 e^2}\frac{\partial^2}{\partial z^2}\right)\nabla \times \mathbf{j}_\parallel + \frac{B_0^2}{n_0 m_i}\nabla \times \mathbf{j}_\perp. \tag{2.85}$$

The last equation we need is the curl of Ampere's law, which can be written as

$$-\nabla_\parallel^2 \delta\mathbf{B} - \nabla_\perp^2 \delta\mathbf{B} = \mu_0\left(\nabla_\parallel \times \mathbf{j}_\perp + \nabla_\perp \times \mathbf{j}_\parallel\right). \tag{2.86}$$

Therefore, equation (2.85) becomes

$$\frac{\partial^2 \delta\mathbf{B}}{\partial t^2} = \left(\lambda_e^2\frac{\partial^2}{\partial t^2} - (\rho_s v_A)^2\frac{\partial^2}{\partial z^2}\right)\nabla_\perp^2 \delta\mathbf{B} + v_A^2 \nabla_\parallel^2 \delta\mathbf{B}, \tag{2.87}$$

where $\lambda_e = c/\omega_{pe}$ is the electron inertial length, and $\rho_s = c_s/\omega_{ci}$ is the ion acoustic gyroradius. Fourier analysis of this equation leads to the following dispersion relation:

$$\left(\frac{\omega}{k_\parallel v_A}\right)^2 = \frac{1 + (k_\perp \rho_s)^2}{1 + (k_\perp \lambda_e)^2}. \tag{2.88}$$

The two-fluid effects considered here introduce a nonzero electric field component parallel to the magnetic field. In order to get an approximation of this parallel field, we assume that the electron inertial effect closes the polarization current identically. Then

we have $\nabla \cdot \mathbf{j} = 0$ or

$$\nabla_{\parallel} \cdot \mathbf{j}_{\parallel} = -\nabla_{\perp} \cdot \mathbf{j}_{\perp} = -\frac{1}{\mu_0 v_A^2} \frac{\partial (\nabla_{\perp} \cdot \delta \mathbf{E}_{\perp})}{\partial t}, \tag{2.89}$$

where we have used the definition of the polarization current, equation (2.80). Now we can differentiate (2.83) with respect to the coordinate z to get,

$$\frac{\partial^2 \delta E_{\parallel}}{\partial z \partial t} = \mu_0 \left(\lambda_e^2 \frac{\partial^2}{\partial t^2} - (\rho_s v_A)^2 \frac{\partial^2}{\partial z^2} \right) \frac{\partial j_{\parallel}}{\partial z}. \tag{2.90}$$

Finally, substituting $\partial j_{\parallel}/\partial z$ from equation (2.89), and using Fourier analysis to solve for $\delta \mathbf{E}_{\parallel}$, leads to

$$E_{\parallel} = \left(\frac{\rho_s^2 - \lambda_e^2}{1 + (k_{\perp} \lambda_e)^2} \right) k_{\parallel} k_{\perp} E_{\perp}. \tag{2.91}$$

Equation (2.91) indicates that pressure and inertia effects act oppositely in contributing to the parallel electric field. In the inertial limit ($\lambda_e > \rho_s$), the parallel electric field accelerates the electrons carrying the parallel current, and decelerates them if pressure effects are more important. The criterion to differentiate between the cold and warm regimes is derived from the ratio,

$$\frac{\rho_s}{\lambda_e} = \frac{v_{te}}{v_A}, \tag{2.92}$$

where $v_{te} = \sqrt{T_e/m_e}$. Alfvén waves propagating within regions where $v_{te} > v_A$ are known as *Kinetic Alfvén Waves*. Waves propagating in regions where $v_A > v_{te}$ are called *Inertial Alfvén Waves*.

2.4.3 Kinetic theory of dipersive Alfvén waves

As a final point, we want to find wave solutions using the linear kinetic theory approach, to obtain the wave dispersion relation associated with equations (3.15), (3.22) and (3.25) which are solved in the DK1D code. As stated earlier, a number of simplifications have been made (see section 3.1.1 for a detailed explanation). Among these:

1. the perpendicular current is given by the polarization drift and is carried by the ions, which implies that,

$$\frac{\partial j_{\perp}}{\partial t} = \frac{1}{\mu_0 v_A^2} \frac{\partial^2 E_{\perp}}{\partial t^2}. \tag{2.93}$$

2. the parallel component of the current density is due only to electron motion, and it is calculated through its definition,

$$j_{\parallel} = \int d^3v v_{\parallel} f_e(\mathbf{v}, \mathbf{r}). \tag{2.94}$$

Here f_e is the electron distribution. Notice that in the stationary case, we expect $j_{\parallel} = 0$, which means that the integration will be performed on the perturbation part of the distribution only, which exists due to the presence of the wave.

3. the displacement current term is neglected in Ampere's Law equation. Under this assumption, and substituting the magnetic field from Faraday's law, we have

$$\vec{\nabla}\vec{\nabla} \cdot \vec{E} - \vec{\nabla}^2 \vec{E} = -\mu_0 \frac{\partial \vec{j}}{\partial t}. \tag{2.95}$$

We seek to find wave solutions through linear theory. Following the usual treatment, the distribution is expressed as the superposition of a perturbation (due to the presence of the wave) to the unperturbed velocity and position dependent distribution,

$$f(\mathbf{r}, \mathbf{v}, t) = f_0(\mathbf{r}, \mathbf{v}) + f_1(\mathbf{r}, \mathbf{v}, t). \tag{2.96}$$

The perturbation is assumed to propagate as plane waves, as well as the wave fields:

$$f_1(\mathbf{r}, \mathbf{v}, t) = f_1(\mathbf{v}) e^{i(\mathbf{k}\cdot\mathbf{r} - \omega t)}, \tag{2.97}$$

$$\mathbf{E}(\mathbf{r}, t) = -\nabla\phi_0(z) + \mathbf{E_1}(\mathbf{r}, t) = -\frac{\partial \phi_0(z)}{\partial z}\hat{z} + \mathbf{E_{10}} e^{i(\mathbf{k}\cdot\mathbf{r} - \omega t)}, \tag{2.98}$$

$$\mathbf{B}(\mathbf{r}, t) = \mathbf{B_0}(z) + \mathbf{B_1}(\mathbf{r}, t) = B_0(z)\hat{z} + \mathbf{B_{10}} e^{i(\mathbf{k}\cdot\mathbf{r} - \omega t)}. \tag{2.99}$$

By substituting these expressions in equation (3.20) and expanding, the following is obtained:

$$\frac{\partial f_1}{\partial t} + v_{\parallel}\frac{\partial f_0}{\partial z} + v_{\parallel}\frac{\partial f_1}{\partial z} + \left(-\frac{q}{m}\frac{\partial \phi_0}{\partial z} + \frac{q}{m}\mathbf{E_1}\cdot\hat{z} - \frac{\mu_e}{m}\frac{\partial B_0}{\partial z} - \frac{\mu_e}{m}\frac{\partial \mathbf{B_1}\cdot\hat{z}}{\partial z}\right)\left(\frac{\partial f_0}{\partial v_{\parallel}} + \frac{\partial f_1}{\partial v_{\parallel}}\right) = 0. \tag{2.100}$$

Some simplifications take place at this point. First, compare the previous equation with

its zero-order version,

$$v_\parallel \frac{\partial f_0}{\partial z} + \left(-\frac{q}{m}\frac{\partial \phi_0}{\partial z} - \frac{\mu_e}{m}\frac{\partial B_0}{\partial z} \right) \frac{\partial f_0}{\partial v_\parallel} = 0, \tag{2.101}$$

which simplifies the equation (2.100) into:

$$\frac{\partial f_1}{\partial t} + v_\parallel \frac{\partial f_1}{\partial z} + \left(-\frac{q}{m}\frac{\partial \phi_0}{\partial z} + \frac{q}{m}E_{1\parallel} - \frac{\mu_e}{m}\frac{\partial B_0}{\partial z} - \frac{\mu_e}{m}\frac{\partial B_{1\parallel}}{\partial z} \right) \frac{\partial f_1}{\partial v_\parallel} + \left(\frac{q}{m}E_{1\parallel} - \frac{\mu_e}{m}\frac{\partial B_{1\parallel}}{\partial z} \right) \frac{\partial f_0}{\partial v_\parallel} = 0. \tag{2.102}$$

Next, eliminate all second order terms (recall that $B_{1\parallel} = 0$ since $\mathbf{A} = A_\parallel \hat{z}$) to obtain:

$$\frac{\partial f_1}{\partial t} + v_\parallel \frac{\partial f_1}{\partial z} - \left(\frac{q}{m}\frac{\partial \phi_0}{\partial z} + \frac{\mu_e}{m}\frac{\partial B_0}{\partial z} \right) \frac{\partial f_1}{\partial v_\parallel} = -\frac{q}{m}E_{1\parallel}\frac{\partial f_0}{\partial v_\parallel}. \tag{2.103}$$

For simplicity, let us take the case when spatial variations of the electrostatic potential $\phi_0(z)$ and magnetic field $B_0(z)$ are locally negligible. The perturbation of the distribution takes the form:

$$f_1 = \frac{iq_e}{m_e}\frac{E_\parallel \partial f_0/\partial v_\parallel}{k_\parallel v_\parallel - \omega}. \tag{2.104}$$

Solution of the dispersion equation for Maxwellian plasma

Consider an initially stationary Maxwellian plasma with thermal velocity $u_{te} = \sqrt{2k_B T/m}$,

$$f_0(v) = \frac{n_0}{(\sqrt{\pi}u_{te})^3} e^{-(v/u_{te})^2}, \tag{2.105}$$

from which the parallel current can be calculated as

$$j_\parallel = i\epsilon_0 E_\parallel \omega \left(\frac{\omega_{pe}}{k_\parallel u_{te}} \right)^2 Z'\left(\frac{\omega}{k_\parallel u_{te}} \right), \tag{2.106}$$

where $Z'\left(\frac{\omega}{k_\parallel u_{te}}\right)$ is the derivative of the plasma dispersion function,

$$\begin{aligned} \frac{dZ(\xi)}{d\xi} &= \frac{1}{\sqrt{\pi}}\int_{-\infty}^{\infty} dx \frac{e^{-x^2}}{(x-\xi)^2}, \\ &= -2[1 + \xi Z(\xi)], \end{aligned} \tag{2.107}$$

with

$$\xi = \frac{\omega}{k_{\parallel} u_{te}}. \tag{2.108}$$

Now, we include the two components (2.106) and (2.93) into (2.95) and rearrange them in the following form

$$\begin{pmatrix} k_{\perp}^2 + \left(\frac{\omega}{k_{\parallel}\lambda_e u_{te}}\right)^2 Z'(\xi) & -k_{\parallel}k_{\perp} \\ -k_{\parallel}k_{\perp} & k_{\parallel}^2 - \left(\frac{\omega}{v_A}\right)^2 \end{pmatrix} \cdot \begin{pmatrix} E_{\parallel} \\ E_{\perp} \end{pmatrix} = 0. \tag{2.109}$$

The determinant of last expression gives the dispersion relation, which can be written as

$$\left(\frac{\omega}{k_{\parallel} v_A}\right)^2 = 1 + \frac{(k_{\perp}\rho_s)^2}{1 + \xi Z(\xi)}. \tag{2.110}$$

It is convenient to demonstrate that this relationship is consistent with the two-fluid solution given in (2.88). As indicated by Stasiewicz et al. [2000], the kinetic and inertial limits are mutually exclusive and must be taken one at a time. Let's consider first the kinetic case. In equation (2.88), $\lambda_e \to 0$ and we obtain

$$\left(\frac{\omega}{k_{\parallel} v_A}\right)^2 = 1 + (k_{\perp}\rho_s)^2. \tag{2.111}$$

In equation (2.110), this limit corresponds to the case of hot electrons for which $\xi \to 0$, by taking the limit one trivially recovers the limit case (2.111).

The inertial limit, on the other hand, corresponds to the limit $\rho_s \to 0$, so that (2.88) reduces to

$$\left(\frac{\omega}{k_{\parallel} v_A}\right)^2 = \frac{1}{1 + (k_{\perp}\lambda_e)^2}. \tag{2.112}$$

In the kinetic relationship (2.110) this limit correspond to the case of cold electrons, for which we have $1 + \xi Z(\xi) \simeq -1/(2\xi) = -(k_{\parallel} v_{te}/\omega)^2$ [Lysak and Lotko, 1996] (Here $v_{te} = \sqrt{2} u_{te}$). This can be rearranged into

$$\left(\frac{\omega}{k_{\parallel} v_A}\right)^2 \left(1 + k_{\perp}^2 \left[\frac{\rho_s v_A}{v_{te}}\right]^2\right) = 1. \tag{2.113}$$

The factor inside the squared parenthesis is equal to λ_e (see equation 2.92), and one can see that the resulting relation takes the form of equation (2.112).

Lysak and Lotko [1996] solved the dispersion equation for SAWs in the kinetic and

inertial regimes. The expression for the dispersion relation found by them is (equation 6),

$$\left(\frac{\omega}{k_{\|}v_A}\right)^2 = \frac{\mu_i}{1-\Gamma_0(\mu_i)} + \frac{(k_\perp\rho_s)^2}{\Gamma_0(\mu_e)[1+\xi Z(\xi)]}. \tag{2.114}$$

Here $\mu_i = k_\perp\rho_i$, $\mu_e = k_\perp\rho_e$ ($\rho_x = T_x/m_x\Omega_x^2$ is the gyroradius for species x, Ω_x represents the gyrofrequency of particles of species x), $\rho_s^2 = T_e/m_i\Omega_i^2 = (v_{te}\lambda_e/v_A)^2$ is called the *ion acoustic gyroradius*, $\xi = \omega/k_{\|}u_{te}$, and $\Gamma_0(\mu) = e^{-\mu}I_o(\mu)$ is the modified Bessel function. For a small value of μ, the modified Bessel function is approximated as $\Gamma_0(\mu) \approx 1-\mu+(3/4)\mu^2$. If we consider both small ion ($\Gamma_0(\mu_i) \approx 1-\mu_i$) and electron ($\Gamma_0(\mu_e) \approx 1$) gyroradius, and make the above mentioned substitutions, equation (2.114) turns into (2.110).

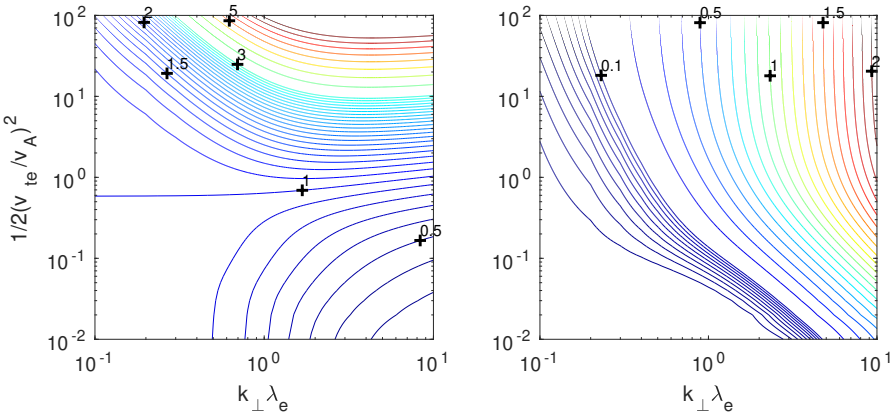

Figure 2.4: Contour solutions of the dispersion equation (2.114) for the case of small ion gyroradius. Left: phase velocity $\omega/(k_{\|}v_A)$. Right: damping rate ω_I/ω_R. Numbers indicate the value pointed at by the adjacent crosses.

Solutions for the case of small ion gyroradius are presented as contour lines of the phase velocity (left) and damping rate (right) in Figure 2.4. The two distinct regions illustrated in the phase velocity diagram correspond to the kinetic and inertial regimes. In the kinetic regime, typical of higher temperatures, the phase velocity is proportional to the quantity $k_\perp\lambda_e$. Cold plasmas, on the other hand, belong to the inertial regime, and here phase velocities decrease with increasing $k_\perp\lambda_e$. Notice that the rather straightforward condition (2.92) is exclusively accurate for the fluid case and does not hold here. The phase velocity graph also indicates that, for a given $k_\perp\lambda_e$, the wave propagates faster at higher temperatures. The damping rate, on the other hand, is everywhere an increasing function of temperature and the $k_\perp\lambda_e$ parameter.

Chapter 3

DK1D numerical code

The Drift Kinetic 1-Dimensional (DK1D) numerical Vlasov solver was developed, maintained and progressively improved from 2002 to 2010 by Dr. Clare Watt at the University of Alberta, in close collaboration with Dr. Robert Rankin and Dr. Richard Marchand, and under the sponsorship of the Canadian Space Agency (DK1D user manual, unpublished).The code simulates the interaction between small-scale shear Alfvén waves and non-relativistic electron plasma distributions along the dimension parallel to the background magnetic field, and accounts for electron inertia and pressure effects, while the influence of ions is included indirectly under the assumptions of quasineutrality and as carriers of the perpendicular current through the polarization current [Stasiewicz et al., 2000] only. A significant improvement of its formulation, relative to other numerical approaches being implemented at the time, is the inclusion of both wave-particle and particle-wave interactions, which derives in the possibility of studying particle acceleration and wave dispersion simultaneously.

In this chapter, the Vlasov-Maxwell coupled system of equations including electron inertial effects is derived and presented, in parallel with a detailed enumeration of the simplifying assumptions of the model. The corresponding discretized model is also described thoroughly, as well as a fair description of the Corner Upwind Transport Method used to solve the Vlasov equation.

The DK1D numerical code has been the cornerstone of several publications. Next, we present a summary of some scientific contributions:

- The first results were introduced in a study on the evolution of the wave fields and electron dynamics under uniform conditions of density, temperature, and magnetic intensity [Watt et al., 2004]. These simulations showed that a fraction of the distribution undergoes a resonant interaction with the wave of the Fermi kind; these

electrons are reflected ahead of the wave forming beam-like structures, time dispersed in nature, such that the energy spectrum of the advected electrons increases with time. The maximum energy of these populations corresponds to velocities on the order of twice the Alfvén speed. On the other hand, significant heating was observed in the bulk plasma at the location of the wave. It was suggested that heating in this region entails an inhomogeneous increase in the phase velocity within the waves spatial domain, causing the original waveform to deform due to different sections of the wave moving at different speeds. Changes of the dispersive nature of the plasma as the wave crosses a given location increase the levels of Landau damping, and from the free energy of this process, electrons that are originally non-resonant can become resonant.

- [Watt et al., 2005] expanded in more detail on the formation of these thermally enhanced features, also called SupraThermal Electron Bursts (STEB), this time focused on the effect of changes in wave amplitude and the perpendicular scale. High wave amplitude and shorter scales are most appropriate for nonlinear beam formation structures. The nonlinear evolution tends to cause wave steepening in the leading section of the wave pulse, which in turn distorts the symmetry of the associated parallel electric field. A careful analysis using particle orbits of energized electrons from before and after the wave reached the observation point suggested that, while resonant electrons endured strong energization enough as to escape the wave, the thermal component of the plasma would sustain a process such that the wave-particle interaction is not strong enough as to prevent the wave to move past them, leaving these particles in a region of smaller magnitude and opposite sign electric field that prevents the formation of beams and thermalize the plasma into the suprathermal signature.

- In Watt et al. [2006], a more realistic dipolar magnetic field variation was introduced which allowed observing the effects of the spatial gradient on the Alfvén speed, and the effect of the mirror force. Variation in the Alfvén speed profile affects the phase velocity of the waves directly, while the mirror force effectively arranges longitudinal-to-transverse kinetic energy transport under the magnetic momentum conservation principle. Under these conditions, beam and plasma heating showed that, as the wave pulse travels into regions of higher magnetic intensity and Alfvén speed, so does increase the minimum energy of the resonant electrons. It was then suggested that the slowest populations of beamed or advected particles could be accelerated at more than one point as the wave catches up with them due to its increasing phase velocity. On the other hand, the simulations showed that the

combined action of electron acceleration and mirror force generate signatures very similar to electron conics.

- Theoretical prediction in the cold plasma limit states that parallel electric field generated by short scale effects maximizes for $k_\perp \delta_e = 1$. [Watt and Rankin, 2007b] studied the nonlinear evolution of parallel electric fields in this context. These simulations showed that both the amplitude of the field and particle energization reach higher levels for $k_\perp \delta_e > 1$, which correspond to slower moving waves. It was suggested that the nonlinear particle-wave interaction might be more efficient for slower moving waves.

- Lorentzian distributions present a Maxwellian-like shape with high-velocity tails. These tails are longer for decreasing values of its κ parameter. Simulations using Lorentzian distributions under homogeneous conditions [Watt and Rankin, 2007a] showed increased levels (relative to the Maxwellian case) of energy flux associated with the beam of resonant electrons. These beam enhancements occur due to the higher number of resonant interactions with the electrons found at the tail of the distribution. Solutions of the linear dispersion equation for this kind of distribution yields higher damping rates for plasmas with lower values of κ, so that wave-particle interactions are stronger for these cases.

- Particle transport from the plasma sheet and their likelihood of causing auroras were investigated in [Watt and Rankin, 2009] for a plasma embedded in a dipolar magnetic field. It was found that under kinetic conditions, a rather efficient wave-plasma energy interchange where the wave traps resonant electrons, preventing the wave from damping. Once the wave moves into more inertial conditions, the parallel electric field decreases and the trapped resonant electrons escape the wave.

- Also within the context of warm plasma transport and auroral displays, [Watt and Rankin, 2010] investigated the conditions under which these energetic particles can trigger auroras. Using numerical simulations of wave propagation originated well into the magnetosphere, they calculated the advection of parallel energy flux at $r \simeq 2.8\ R_E$. These measurements were further scaled to ionospheric altitudes $\simeq 100$ km under the assumptions that particle fluxes are composed of field-aligned electrons only, and that there are no other electron acceleration mechanisms. By comparing these results with real observations, it was concluded that waves with sufficient amplitude generate values of particle energy flux that are comparable to particle fluxes associated with auroral events.

3.1 Mathematical model

3.1.1 Simplifying assumptions

The DK1D code solves numerically a set of equations derived under the following simplifying assumptions:

1. electrons are strongly magnetized, so their gyro-trajectory moves tightly along magnetic field lines. Ions, on the other hand, are not fully magnetized, and their relatively high mass prevents them from moving rapidly by the action of the IAW. In other words, electrons are responsible for parallel currents, while any cross currents are attributed to ions. The continuity equation for each species,

$$\frac{\partial n_s}{\partial t} + \nabla \cdot (n_s \mathbf{v_s}) = 0, \tag{3.1}$$

when used in conjunction with the definition of current density, $\mathbf{j_s} = n_s q_s \mathbf{v_s}$, yields the following equations:

$$\frac{\partial n_i}{\partial t} = -\frac{1}{q_i} \nabla \cdot \mathbf{j}_\perp, \tag{3.2}$$

$$\frac{\partial n_e}{\partial t} = -\frac{1}{q_e} \nabla \cdot \mathbf{j}_\parallel. \tag{3.3}$$

2. electron trajectories are described in terms of gyro-averaged motion. As stated before, the cross field drift of electrons is assumed negligible.

3. wave solutions are given in terms of potentials instead of fields,

$$\mathbf{E} = -\nabla\phi - \frac{\partial \mathbf{A}}{\partial t}, \tag{3.4}$$

$$\mathbf{B} = \nabla \times \mathbf{A}. \tag{3.5}$$

Furthermore, if we recall that we are considering shear mode waves, i.e., the wave magnetic perturbation is perpendicular to the background magnetic field, it can be verified that this is consistent with setting $\mathbf{A} = A_\parallel \hat{z}$; then we can express the field quantities as,

$$\mathbf{B} = \nabla A_\parallel \times \hat{z}, \tag{3.6}$$

$$\mathbf{E}_{\parallel} = -\nabla_{\parallel}\phi - \frac{\partial \mathbf{A}_{\parallel}}{\partial t}, \tag{3.7}$$

$$\mathbf{E}_{\perp} = -\nabla_{\perp}\phi. \tag{3.8}$$

4. all perpendicular variations have the form $e^{ik_{\perp}x}$, where x is the coordinate perpendicular to the geomagnetic field and $k_{\perp}$ is considered a function of z.

5. the displacement current term of the Amperes law is neglected,

$$\nabla \times \mathbf{B} = \mu_0 \mathbf{j}. \tag{3.9}$$

   This particular assumption has to be handled with care; the displacement current term becomes important for low altitude and high Alfvén velocity regions.

6. quasineutrality holds at all times; this constrains the validity of the model to low-frequency modes.

7. the magnetic moment $\mu = K_{\perp}/B$ of the electrons is a constant of motion.

3.1.2 Derivation of the wave equation

With the assumptions we have made, let us first write the parallel component of the current density in terms of the potentials by using (3.6),

$$\nabla \times (\nabla \times \mathbf{A}_{\parallel}) = \mu_0 \mathbf{j}_{\parallel}. \tag{3.10}$$

This equation becomes, under assumption 4,

$$A_{\parallel} = \frac{\mu_0}{k_{\perp}^2} j_{\parallel}. \tag{3.11}$$

As mentioned previously, the parallel current is attributed exclusively to the electrons. The parallel current found in (3.11) can be substituted in (3.3),

$$\frac{\partial n_e}{\partial t} = -\frac{\partial}{\partial z}\left(\frac{k_{\perp}^2 A_{\parallel}}{\mu_0}\right). \tag{3.12}$$

On the other hand, the expression for the polarization current is replaced in (3.2), leading

to,

$$\frac{\partial n_i}{\partial t} = -ik_\perp \left(\frac{\rho_m}{B_0^2}\right) \frac{\partial E_\perp}{\partial t}, \tag{3.13}$$

using assumptions 3 and 4 we obtain,

$$\frac{\partial n_i}{\partial t} = -\left(\frac{k_\perp^2 \rho_m}{B_0^2}\right) \frac{\partial \phi}{\partial t}, \tag{3.14}$$

finally, with the quasineutrality condition (assumption 6) we obtain the wave equation,

$$\frac{\partial \phi}{\partial t} = -\left(\frac{v_A}{k_\perp}\right)^2 \frac{\partial (k_\perp^2 A_\parallel)}{\partial z}. \tag{3.15}$$

3.1.3 The gyro-averaged Vlasov equation

For a plasma embedded in an external magnetic field $\mathbf{B_0} = B_0 \hat{b}$, particles perform gyromotion in a plane perpendicular to the magnetic field. Whenever the time scale of particle gyromotion is small compared to the variation in time of the external fields (as is the case with low-frequency waves), and the cyclotron radius is small relative to the spatial variation of the fields, the important physics can be described by the gyro-averaged motion of electrons. To calculate the gyro-averaged motion, imagine the instantaneous position $\mathbf{r}$ of the particle as a superposition of its gyro-averaged position $\mathbf{R}$ and the actual position of the electron relative to such averaged position,

$$\mathbf{r} = \mathbf{R} + \frac{\mathbf{v} \times \hat{b}}{\Omega_e}, \tag{3.16}$$

where $\Omega_e = q_e B_0 / m_e$ is the gyrofrequency of the electrons. The velocity of the gyro-averaged trajectory is given by,

$$\frac{d\mathbf{R}}{dt} = v_\parallel \hat{b} + \mathbf{v_d}. \tag{3.17}$$

Given the conditions mentioned above, we can express the distribution function through a new system of variables,

$$f(\mathbf{r}, \mathbf{v}, t) \rightarrow f(\mathbf{R}, v_\parallel, \mu, t), \tag{3.18}$$

where $v_\parallel = \mathbf{v} \cdot \hat{b}$ and $\mu = m v_\perp^2 / (2B_0)$. Using these coordinates the Vlasov equation takes

the form,

$$\frac{\partial f}{\partial t} + \frac{d\mathbf{R}}{dt} \cdot \frac{\partial f}{\partial \mathbf{R}} + \frac{dv_\parallel}{dt}\frac{\partial f}{\partial v_\parallel} + \frac{d\mu}{dt}\frac{\partial f}{\partial \mu} = 0, \tag{3.19}$$

which, using assumptions 2 ($\mathbf{v_d} = 0$) and 7 (constant μ), becomes:

$$\frac{\partial f}{\partial t} + v_\parallel \frac{\partial f}{\partial z} + \left(\frac{q_e}{m_e}E_\parallel - \frac{\mu}{m_e}\frac{\partial B_0}{\partial z}\right)\frac{\partial f}{\partial v_\parallel} = 0. \tag{3.20}$$

Notice that the parallel acceleration includes the parallel electric force and the magnetic mirror force.

For numerical convenience [Watt et al., 2004], the DK1D code uses the canonical momentum per unit mass instead of the parallel velocity,

$$p_\parallel = v_\parallel + \frac{q_e}{m_e}A_\parallel. \tag{3.21}$$

Substituting the field quantities in terms of the wave potentials, we finally get,

$$\frac{\partial f}{\partial t} + \left(p_\parallel - \frac{q_e}{m_e}A_\parallel\right)\frac{\partial f}{\partial z} + \left[\frac{q_e}{m_e}\left\{\left(p_\parallel - \frac{q_e}{m_e}A_\parallel\right)\frac{\partial A_\parallel}{\partial z} - \frac{\partial \phi}{\partial z}\right\} - \frac{\mu}{m_e}\frac{\partial B_0}{\partial z}\right]\frac{\partial f}{\partial p_\parallel} = 0. \tag{3.22}$$

3.1.4 Moments of the distribution function, calculation of the vector potential

The response of the wave to the plasma is obtained when the vector potential is known. This is derived from equation (3.11) in the new set of coordinates. By defining $M(n)$ as the n-th moment of the distribution function:

$$M(n) = 2\pi \int d\mu dp_\parallel \frac{B_0}{m_e} p_\parallel^n f(z, p_\parallel, \mu), \tag{3.23}$$

the parallel current is expressed as,

$$j_\parallel = qM(1) + \frac{q^2}{m}A_\parallel M(0), \tag{3.24}$$

which, when substituted in (3.11) leads to:

$$A_\parallel = \frac{\mu_0 q_e M(1)}{k_\perp^2 - \mu_0 \frac{q_e^2}{m_e} M(0)}. \tag{3.25}$$

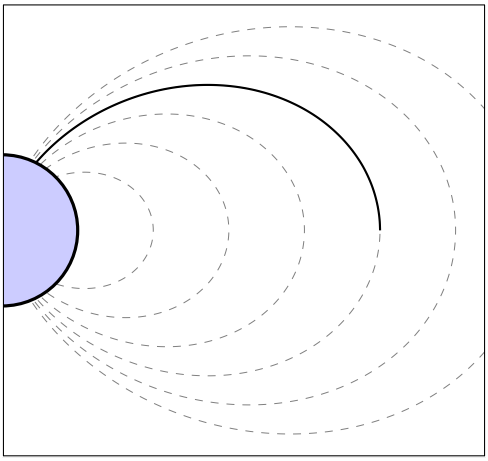

Figure 3.1: Representation of the geomagnetic field as an ideal dipolar field (dashed lines). The spatial simulation domain (bold line) corresponds to a section of one of these dipolar lines

3.2 Background plasma setup

This section describes in detail the spatial profiling of some relevant physical quantities associated with the plasma environment. Background plasma properties and their spatial variation are essential in determining the dispersive properties driving wave propagation. Of these properties, both the magnetic field and the distribution function are especially relevant; the distribution function, in turn, relies on the plasma density and temperature. Other properties can be easily defined from the magnetic field and density models, by specifying additional parameters.The easiest configuration consists of a homogeneous plasma where all these physical properties are constant throughout space. However, for this project, we require an inhomogeneous model that resemble the Alfvénic acceleration region more realistically.

3.2.1 Space configuration and magnetic field

Within the magnetospheric context, the simulation domain runs tangent to a given magnetic field line of the idealized dipolar configuration shown in Figure 3.1. The spatial coordinate z represents the arc-length distance relative to the position of the ionospheric end of the field line. The geomagnetic field model follows the dipolar approximation presented in section 2.2 (see equation 2.39). The magnetic field line itself, represented in spherical coordinates, was also presented (see equation 2.38 on page 26).

We are still to find a relationship between these coordinates and the arc-length distance s measured from the equator. Starting from $(ds)^2 = (dr)^2 + r^2(d\lambda)^2$, and using

equation (2.38), we can express the variation of arc-length as a function of the latitude as:

$$\begin{aligned}\frac{ds}{d\lambda} &= \sqrt{r^2 + \left(\frac{dr}{d\lambda}\right)^2} \\ &= r_{eq}\cos(\lambda)\sqrt{1+3\sin^2(\lambda)}. \end{aligned} \tag{3.26}$$

The form of the anti-derivative of last equation can be written as:

$$s(\lambda) = \frac{1}{2}\left(\sin\lambda\sqrt{1+3\sin^2\lambda} + \frac{\ln(\sqrt{3}\sin\lambda + \sqrt{1+3\sin^2\lambda})}{\sqrt{3}}\right), \tag{3.27}$$

where we have chosen $s(0) = 0$. Thus, $s(\lambda)$ gives the displacement along the field line from the equatorial plane up to any given latitude λ. It is immediate to see that, for any given location on the field line, the combined length of its altitude z and coordinate s give the total distance from the equatorial plane to the surface of the Earth along the geomagnetic field line, $s_E = s(\lambda) + z(\lambda)$. In terms of the latitude, the value for the total length of the field line is found by evaluating equation (3.27) at the latitude λ_E where the field line intersects the Earth surface. Therefore, the z coordinate as a function of latitude follows the relationship,

$$z(\lambda) = s_E - s(\lambda), \tag{3.28}$$

where $s_E = s(\lambda_E)$. Equation (3.28) ultimately allows the magnetospheric environment to be mapped into the computational domain.

3.2.2 Perpendicular scaling

The perpendicular scale length, $\delta_\perp(\lambda)$, is interpreted as the radius of the magnetic flux tube at latitude λ. The code assumes magnetic flux conservation inside the flux tube, which can be expressed as:

$$\pi\delta_{\perp_I}^2 B_I = \pi\delta_\perp^2(\lambda)B(\lambda), \tag{3.29}$$

in terms of typical ionospheric values for perpendicular length and magnetic intensity, $\delta_{\perp_I}$ and B_I. Then the corresponding perpendicular wavenumber, $k_\perp = 2\pi/\delta_\perp$, in terms

of the magnetic intensity, is given by,

$$k_{\perp}(\lambda) = \frac{2\pi}{\delta_{\perp_I}} \sqrt{\frac{B(\lambda)}{B_I}}. \tag{3.30}$$

3.2.3 Plasma model

The mass content within the inertial and kinetic regions is essentially composed of plasmas of magnetospheric and ionospheric origin. At lower altitudes, the ionospheric component presents strong spatial gradients until it is practically depleted at higher altitudes. Since the Alfvén speed has a marked dependence on the ion plasma density, studies of wave propagation at low altitudes require inhomogeneous conditions for plasma density. We define the density as the mixture of a magnetospheric plasma composed of hydrogen ions and electrons, which for practical purposes has constant density along the whole domain, and plasma of ionospheric origin composed of singly-ionized oxygen atoms; this oxygen component decays with altitude depending on a scale factor z_0 as follows:

$$n_e(z) = n_H + n_O \exp\left(-\frac{z}{z_0}\right). \tag{3.31}$$

Based on this expression, we define the ion mass as a weighted average of the relative abundance of each species,

$$m_i(z) = m_P \frac{\left(n_H + A_O n_O e^{-z/z_0}\right)}{n(z)}, \tag{3.32}$$

where m_P represents the proton mass, and A_O is the atomic number for oxygen.

Nonuniform density introduces a spatial dependency on the electron distribution function, such that the time-independent Vlasov equation is identically zero. This is accomplished by defining a space-dependent electrostatic potential across the whole simulation domain [Bittencourt, 2004]. The mathematical construction that consistently couples the distribution function to the density model (5.1) is not part of the original DK1D code, but it has been incorporated as part of this investigation. Details of this implementation are included in the next chapter.

3.3 Code Workflow

This section aims to bring a practical (although not exhaustive) review of the inner workings of the simulation code. A simplified schematic of the main steps of a simulation workflow is presented in Figure 3.2. In DK1D it is possible to run a simulation from the

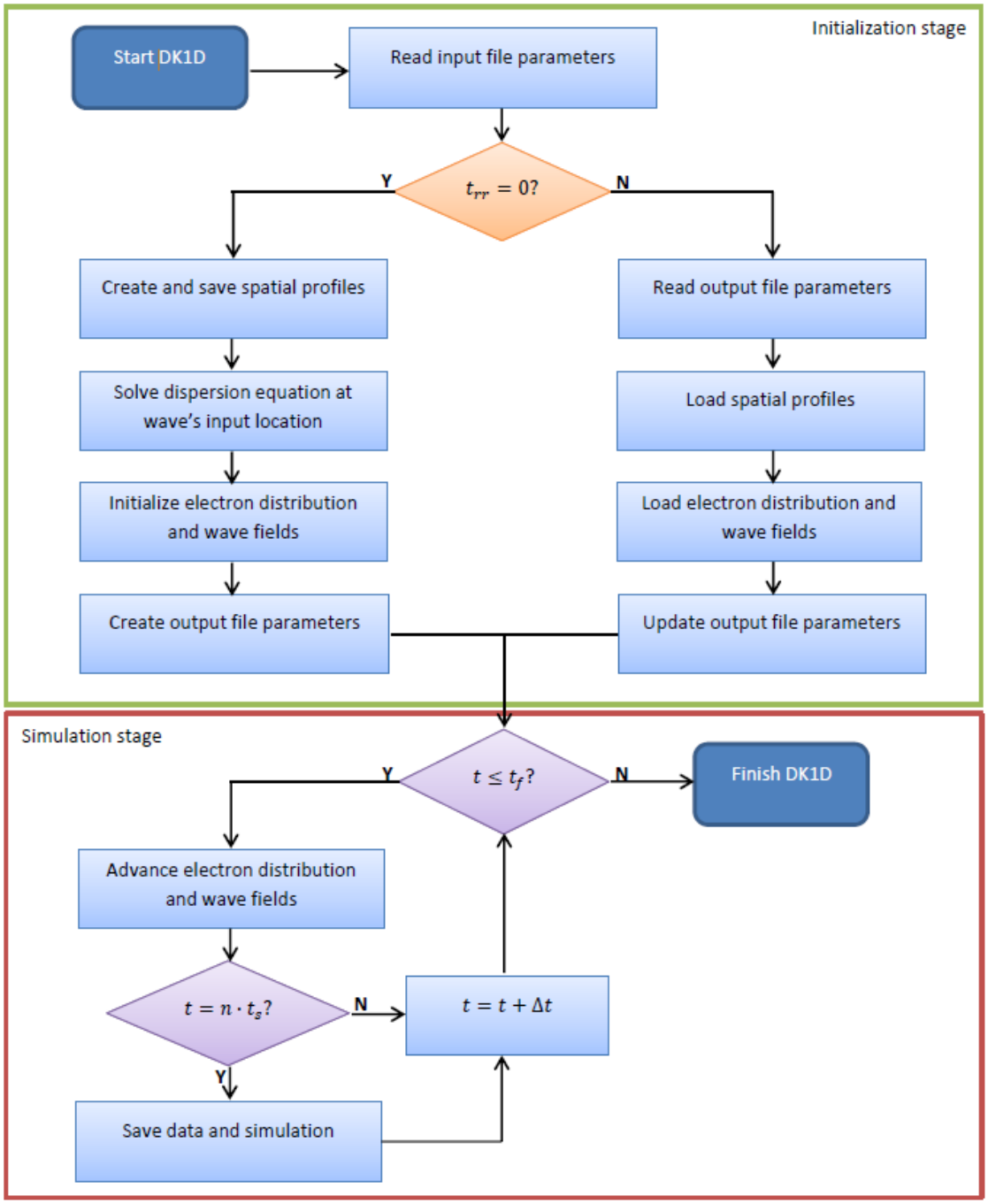

Figure 3.2: Flowchart for DK1D

beginning or to extend a simulation previously run. To run a completely new case, specify $t_{rr} = 0$ into the initial parameters file (see next subsection). To extend a simulation, modify the t_{max} field to a higher value; in this case, the parameter t_{rr} was updated by the program to indicate the number of time steps the simulation reached last. In this documentation, we discuss the steps concerning new simulations only.

3.3.1 Input parameters

The program starts by locating and loading the file 'DK1Dn.in', which includes the essential information necessary to construct the initial profiles and initialize the distribution function. A short description of the initial parameters is provided in table 3.1.

Table 3.1: Initial parameters in DK1Dn

	Parameter	Description
Space domain	Loweralt (m)	lower altitude of simulation domain
	Upperalt (m)	higher altitude of simulation domain
	Δz (m)	distance between grid points
	L-shell (Re)	radial extent of magnetic field line in equatorial plane
	λ_I (m)	perpendicular scale at ionospheric end of magnetic field line
Plasma	κ	κ value for lorentzian distributions
	n_H (m^{-3})	magnetospheric plasma density
	n_O (m^{-3})	ionospheric plasma density
	z_0 (Re)	spatial decay rate of oxygen density
	T_c (eV)	plasma temperature of cold particles
	T_w (eV)	plasma temperature of warm particles
Wave	ϕ_0 (V)	wave amplitude of initial perturbation
	f (Hz)	wave frequency of initial perturbation
Time discretization	t_{rr}	initial iteration number (0 for new simulations)
	t_s (s)	time interval between data saves
	t_{max} (s)	total simulation time
Numerical stability	C_f	Courant Factor. Affects time step value
	mvth	Multiple of thermal velocity. The momentum grid extend up to *mvth* times the thermal speed of the plasma

There are some implicit rules which the program infers depending on the values of some of the parameters. One of them was already mentioned; the value of the t_{rr} parameter defines if the simulation consists of a new case or a continuation of a previous one. Another rule is associated with the initial oxygen density. By setting this value to zero,

the user implicitly indicates that homogeneous conditions of density and temperature are to be implemented. In this case, the program ignores the T_C value and assigns T_W as the temperature all across the domain, and the potential is set to zero. The kappa value sets a rule for the program to choose between Maxwellian or Lorentzian distributions. Since a Lorentzian distribution approximates a Maxwellian as $\kappa \to \infty$, we have set a threshold value. $\kappa \geq 99$ will implement Maxwellian distributions.

3.3.2 Magnetic field and Background plasma setup

Physical properties of the medium are stored on one-dimensional arrays of the size of the spatial discretization array; so that for each physical property, its value and the position where it is defined are associated with the same index. Within the code, the spatial domain is localized within the magnetospheric context by the L-shell value of the magnetic field, and the lower and upper values of the coordinate system whose origin is set at the ionospheric end of the field line arbitrarily set at 110 km above the Earth's surface. The distance between consecutive grid points Δz determines the numerical spatial resolution.

A uniform grid provides simplicity in the numerical scheme. However, the coordinate z to which this uniform grid is associated is not a common choice to define locations on a spherically symmetric system. For this reason, additional arrays store the locations of the discretized points regarding their radial and latitudinal coordinates. The relationships $z(\lambda)$ and $r(\lambda)$ were derived in section 3.2.1. Since we did not find an analytic expression for the relation $\lambda(z)$, in order to obtain the latitude coordinate for a given altitude, a bisection method iterates the right-hand side of the equation

$$z(\lambda) = s_E - \frac{1}{2}\left[\sin\lambda\sqrt{1+3\sin^2\lambda} + \frac{\ln\left(\sqrt{3}\sin\lambda + \sqrt{1+3\sin^2\lambda}\right)}{\sqrt{3}}\right] \tag{3.33}$$

until a numerical value approximates the left-hand side with some desired level of tolerance. The array of latitudes is required in order to obtain the discretized magnetic field values through equation (2.39).

3.3.3 Dispersion equation solution

Once the background plasma properties have been established, it will be necessary to obtain an initial solution for the dispersion equation, to be used later on during the wave input stage. In the cold limit, such solution takes the form given in equation (2.88) on

page 36. The value of this approximation is used as an initial guess into a subroutine that uses Newton's method to find a much better approximation to the solution of the dispersion equation 2.110.

3.3.4 Distribution function setup

At every location along the spatial domain, the particle distribution function defines a two-dimensional phase grid where the parallel and perpendicular components of the distribution are stored. For reasons of practical convenience, phase coordinates are the magnetic moment instead of the perpendicular velocity, and the parallel canonical momentum per unit mass instead of the parallel velocity. Grid spacing in both the magnetic moment and parallel momentum increases geometrically, so that resolution changes monotonically as grid values increase. The base momentum resolution is usually set to a few tenths of the thermal velocity, while both the geometric factors by which the resolution changes and the higher limits of the momentum grid, often require some trial and error strategy based on educated extrapolation and previous experience, as one can not usually predict the final energization levels of the plasma.

Courant condition

A similar approach to determining the top limits of the momentum domain is also followed in order to ensure numerical stability. The Courant condition for the two-dimensional Upwind Method has the form (see B.26),

$$0 < \max\left(\left|\frac{V_{max}\Delta t}{\Delta z}\right|, \left|\frac{P_{max}\Delta t}{\Delta p}\right|\right) \leq 1, \tag{3.34}$$

where V_{max} and P_{max} are (hopefully) good estimates of the maximum parallel momentum that simulation particles can reach, and the maximum force per unit mass these particles will withstand, respectively. This condition is used to obtain a time step unit,

$$dt = \min\left(\left|\frac{C_f\Delta z}{V_{max}}\right|, \left|\frac{C_f\Delta p}{P_{max}}\right|\right), \tag{3.35}$$

3.3.5 Data output

Once all preliminary stages of the simulation are done, and the program is ready to run the time marching loop, a file 'DK1Dn.out' is generated and saved in the physical memory. This file contains necessary information about initial parameters, grid size and resolution of the distribution function, time resolution, and the initial solution of the dispersion equation.

Numerical solution for wave fields and the particle distribution function are stored into physical memory at time intervals given by the t_s parameter, starting at $t = 0$ s. Most quantities are stored in a single file each, which is progressively updated as time evolves. On the other hand, solutions of the particle distribution function at a given time are saved into individual files as the amount of data is often high enough as to cause memory problems during post-processing.

3.4 Numerical Scheme

3.4.1 Space discretization

As indicated in section 3.2.1, the spatial domain consists of a section of a magnetic field line determined by its L-shell value.

The spatial discretization defines two uniform grids with cells of size Δz, one of the grids is shifted in position by a distance $\Delta z/2$ relative to the other to accommodate for the wave potentials to be leap-frogged in space. Space and time *leap-frogging* has become a standard implementation within the framework of electromagnetic codes, ensuring efficient administration of computational resources while keeping second order accuracy on the numerical calculations, at the expense of not having the full knowledge of both potentials at the same locations nor simultaneously [Birdsall and Langdon, 2005]. Figure (3.3) illustrates the arrangement of both the scalar and vector potentials as required by the finite difference version of the wave equation (3.15):

$$\frac{\phi_{i+1/2}^{t+1/2} - \phi_{i+1/2}^{t-1/2}}{\Delta t} \left(\frac{v_{Ai+1/2}}{k_{\perp i+1/2}} \right)^2 \frac{k_{\perp i+1}^2 A_{i+1} - k_{\perp i-1}^2 A_{i-1}}{\Delta z} = 0. \tag{3.36}$$

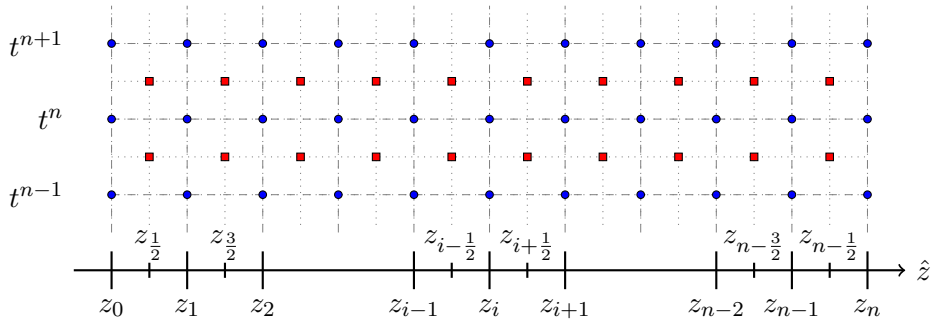

Figure 3.3: Spatial and temporal staggering of wave potentials define the spatial discretization.

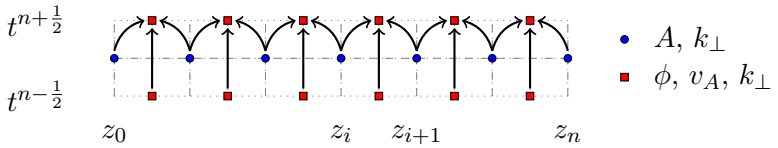

Figure 3.4: Scalar potential update scheme

3.4.2 Wave update 1/2: scalar potential

The wave equation describes the temporal evolution of its electrostatic potential. From its numerical version, equation (3.36), we get:

$$\phi_{i+1/2}^{t+1/2} = \phi_{i+1/2}^{t-1/2} - \frac{\Delta t}{\Delta z} + \left(\frac{v_{Ai+1/2}}{k_{\perp i+1/2}}\right)^2 (k_{\perp i+1} A_{i+1} - k_{\perp i-1} A_{i-1}) \tag{3.37}$$

The diagram in Figure (3.4) illustrates the time advance of the scalar potential at each location, in terms of the surrounding information according to (3.37). Inspection of this equation reveals that the value of the Alfvén speed and the perpendicular wavenumber must be known at the point where the scalar potential is defined since the potential depends directly on these variables. On the other hand, a dependence with the spatial variation means that both the perpendicular scale (again) and the vector potential are to be staggered in adjacent positions. Finally, the time derivative indicates that the updated value of the potential depends on its previous value at the current location.

Boundary conditions

Due to the positioning of the discretized scalar potential inside the simulation domain (see Figure 3.4), this potential is devoid of boundary conditions. However, the gradient of the scalar potential appears explicitly in the Vlasov equation, which requires some assumption about the value of the potential just outside the ends of the spatial domain. For the simulations that take part in this project, the gradient of the scalar potential at the boundaries has been set to zero.

3.4.3 Distribution function update

The Vlasov equation (3.20) has the form of an advection equation in the dimensions z and $p_\parallel$ (see equation (B.23) on page 171):

$$\frac{\partial f_e(z, p_\parallel, \mu, t)}{\partial t} + a \frac{\partial f_e(z, p_\parallel, \mu, t)}{\partial z} + b \frac{\partial f_e(z, p_\parallel, \mu, t)}{\partial p_\parallel} = 0, \tag{3.38}$$

with advection coefficients,

$$a = p_{\parallel} - \frac{q_e}{m_e} A_{\parallel}, \tag{3.39}$$

and,

$$b = \frac{q_e}{m_e}\left[\left(p_{\parallel} - \frac{q_e}{m_e}A_{\parallel}\right)\frac{\partial A_{\parallel}}{\partial z} - \frac{\partial \phi}{\partial z}\right] - \frac{\mu}{m_e}\frac{\partial B}{\partial z}. \tag{3.40}$$

The DK1D program uses the Corner Transport Upwind Method summarized in appendix B to advance the distribution function in time. Its updated form can be written as:

$$\begin{aligned} f_{ijk}^{t+1} := f_{ijk}^{t} &- \frac{\Delta t}{\Delta z}\left(a_{ij}^{+}\nabla_z f_{ijk} + a_{i+1,jk}^{-}\nabla_z f_{i+1,jk}\right) \\ &- \frac{\Delta t}{\Delta p}\left(b_{ijk}^{+}\nabla_p f_{ijk} + b_{i,j+1,k}^{-}\nabla_p f_{i,j+1,k}\right) \\ &- \frac{\Delta t}{\Delta z}\left(F_{i+1,jk} - F_{ijk}\right) - \frac{\Delta t}{\Delta p}\left(G_{i,j+1,k} - G_{ijk}\right). \end{aligned} \tag{3.41}$$

The top line of this equation corresponds to the first order Upwind Method is two dimensions, while the terms on the second line encompass the corrections due to contributions from diagonally located cells and second order limited corrections. These terms are conveniently expressed as correction fluxes:

$$\begin{aligned} F_{ijk} = -\frac{1}{2}\frac{\Delta t}{\Delta p}\Big(&a_{ij}^{-}b_{i,j+1,k}^{-}\nabla_p f_{i,j+1,k} + a_{ij}^{+}b_{i-1,j+1,k}^{-}\nabla_p f_{i-1,j+1,k} + a_{ij}^{-}b_{ijk}^{+}\nabla_p f_{ijk} \\ &+ a_{ij}^{+}b_{i-1,jk}^{+}\nabla_p f_{i-1,jk}\Big) + \frac{|a_{ij}|}{2}\left(1 - \frac{\Delta t}{\Delta z}|a_{ij}|\right)\delta_{zijk}, \end{aligned} \tag{3.42}$$

and,

$$\begin{aligned} G_{ijk} = -\frac{1}{2}\frac{\Delta t}{\Delta z}\Big(&a_{i+1,j}^{-}b_{ijk}^{-}\nabla_z f_{i+1,jk} + a_{i+1,j-1}^{-}b_{ijk}^{+}\nabla_z f_{i+1,j-1,k} + a_{ij}^{+}b_{ijk}^{-}\nabla_z f_{ijk} \\ &+ a_{i,j-1}^{+}b_{ijk}^{+}\nabla_z f_{i,j-1,k}\Big) + \frac{|b_{ijk}|}{2}\left(1 - \frac{\Delta t}{\Delta p}|b_{ijk}|\right)\delta_{pijk}. \end{aligned} \tag{3.43}$$

The gradient limiters δ_z and δ_p, implemented in order to ensure convergence and avoid unwanted harmonic behavior, are known as *monotonized central difference limiters* [van Leer, 1974]. These gradients are given by the expressions:

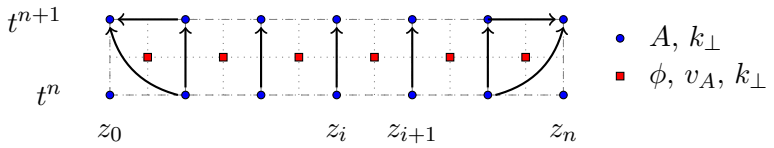

Figure 3.5: Vector potential update scheme

$$\delta_{zijk} = \text{minmod}\left[2\nabla_z f_{i-1,jk}\,,\, 2\nabla_z f_{ijk}\,,\, \nabla_z f_{i-1,jk} + \nabla_z f_{ijk}\right], \tag{3.44}$$

$$\delta_{pijk} = \text{minmod}\left[2\nabla_p f_{i,j-1,k}\,,\, 2\nabla_p f_{ijk}\,,\, \nabla_p f_{i,j-1,k} + \nabla_z f_{ijk}\right]. \tag{3.45}$$

The *minmod* function is defined in equation (B.21).

Boundary conditions

The behavior of the distribution at the boundaries is affected by the field-aligned electric current driven through the boundary in the previous timestep. This current is interpreted as a result of the drift V_D of the core distribution, $j_\parallel = n_e q_e v_D$. Substituting the current with the form of Ampére's law given in equation (3.11), and solving for V_D, leads to,

$$v_D = \frac{k_\perp^2 A_\parallel}{\mu_0 q_e n_e}. \tag{3.46}$$

The distribution function at the boundaries has the same form as the unperturbed case, except for a correction of the velocity due to the passing current:

$$f_e(v, v_D) = f_{e0}(v - v_D). \tag{3.47}$$

3.4.4 Wave update 2/2: vector potential

The self-consistent coupling between the wave and the recently evolved distribution function takes place at the update calculation of the vector potential, which requires the numerical integration of the zeroth and first moments of the distribution at every location, according to equation (3.23). Numerical integration of these moments is performed combining the trapezoidal method and cubic spline integration. The numerical vector potential is calculated as:

$$A_i^{n+1} = \frac{\mu_0 q_e M_i^n(1)}{k_{\perp i}^2 + \mu_0 \frac{q_e^2}{m_e} M_i^n(0)}, \tag{3.48}$$

in accordance with equation (3.25).

Boundary conditions

The value of the vector potential at the boundaries is obtained by assuming that the parallel current changes negligibly across the cells at the edges of the simulation domain. Under such assumption, equation (3.11) leads to:

$$A_0^t = A_1^t \left(\frac{k_{\perp 1}}{k_{\perp 0}}\right)^2, \text{ and } A_N^t = A_{N-1}^t \left(\frac{k_{\perp (N-1)}}{k_{\perp N}}\right)^2. \tag{3.49}$$

3.4.5 Wave input

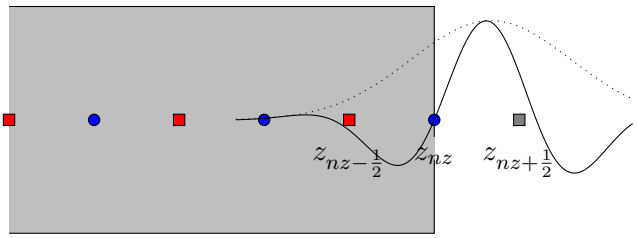

Figure 3.6: A traveling wave pulse moving into the simulation domain.

Waves are introduced into the computational domain through its upper boundary, on an early stage of the simulation that typically lasts a few wave periods. The incoming perturbation is imagined as a traveling wave pulse propagating downwards at some known speed v_w without dispersion up until the point where it is introduced into the simulation domain. This point of entry corresponds to the location closer to the boundary where the scalar potential is defined ($z = z_{nz-\frac{1}{2}}$ according to Figure 3.6). Thus the scalar potential during the wave input stage is set to

$$\phi(z_{nz-\frac{1}{2}}, t) = \phi_0 \exp\left(-\frac{t-t_1}{t_2}\right)^2 \sin(\omega t). \tag{3.50}$$

where t_1 and t_2 determine the shape of the Gaussian envelope. From (3.40), it follows that potential gradients must also be provided at the location z_{nz}, and at time $t := t + \frac{\Delta z}{v_w} + \frac{\Delta t}{2}$ due to spatial and temporal staggering. The scalar potential gradient is obtained as

$$\frac{\partial \phi}{\partial z} = \frac{1}{v_w} \frac{\partial \phi}{\partial t}\bigg|_{t+\frac{\Delta z}{v_w}+\frac{dt}{2}}. \tag{3.51}$$

On the other hand, the vector potential gradient is given in terms of the temporal variation of the scalar potential, according to the wave equation (3.15). In most cases,

one can safely neglect the gradient of the perpendicular scaling at the position where the wave is introduced, and therefore use the simplified form,

$$\frac{\partial A_{\parallel}}{\partial z} = -\frac{1}{v_A^2}\frac{\partial \phi}{\partial t}\bigg|_{t+\frac{\Delta z}{v_w}+\frac{dt}{2}} . \tag{3.52}$$

Chapter 4

Acceleration of suprathermal electrons in the topside ionosphere

Electron time dispersion events appear in energy spectrograms of spacecraft data as high-intensity traces whose average energy decreases monotonically over time [Kletzing and Torbert, 1994]. Typical energies of these events range in the hundreds of eV, but sometimes they can reach several keV, similar to inverted V structures. As opposed to inverted V structures, on the other hand, which present energetic particles at most pitch angles, these dispersive events portray a much stronger parallel component, while their intensity falls off rapidly with increasing pitch angles [McFadden et al., 1987; Kletzing and Torbert, 1994; Andersson et al., 2002; Tanaka et al., 2005].

Initially, these signatures were considered the footprint of field-aligned acceleration over a localized source. Under an impulsive process working over a significant fraction of the local velocity spectrum, the faster electrons of the initial distribution would be accelerated to higher velocities than slower ones, thus generating a time dispersive feature. By measuring the time interval Δt between the arrival of particles at two different given energies, the distance d from the detector to the source of accelerated particles is approximated as

$$d = \frac{\Delta t}{1/v_2 - 1/v_1}, \tag{4.1}$$

where v_1 and v_2 are the velocities associated with the two energies involved. This approach is often known as *time-of-flight* (TOF). TOF assumes a single source location

and time injection for all particles. If this were the case, a simple linear regression model between Δt and $1/v$ would unveil both the source distance and the time of injection from the regression parameters. Uncertainties for these derived quantities are bound to the payloads time sampling rate [Tanaka et al., 2005], so further detail on the origin and evolution of these events had to wait until instrumentation became capable of resolving finer structures.

Eventually, improved capabilities of later spacecraft and instrumentation established the nonlocal nature of many plasma dispersion occurrences. McFadden et al. [1987] studied sounding rockets data in association with flickering aurora. They performed a cross-correlation analysis between different energy channels for some of the dispersed signatures and contrasted their estimations against the relation (4.1). 3 out of 4 events presented strong variability between the source distances as calculated using correlated data from different channels, thus proving that these events correspond to field acceleration over extended sources along field lines. Further research supported this hypothesis. For instance, Clemmons et al. [1994] studied two cases of electron dispersion at altitudes near 1750 km, using data from the Freja spacecraft. Their first measurement used TOF analysis on an event in which particle energies reached a few tenths of keV. Linear regression for this event showed very high correlation, and the source of injection was estimated in the range between 6.2 and 6.8 Re, or at a latitude of -15 ± 10^o. In their second case, data were further reclassified in pitch angle bins. Bins of low pitch angle data ($< 60^o$) consistently indicated the location of the source around 850 km above the spacecraft. However, estimations using bins of broader pitch angle data deviated considerably, thereby suggesting that larger pitch angle electrons originated at higher altitudes along the magnetic field line than particles with lower pitch angles. Tanaka et al. [2005] studied similar time dispersed signatures, using data from a sounding rocket flyby with an altitude of 1102 km in the high latitude cusp region. They reported a chain of events with a periodicity of $0.5 - 1.0$ s, and energies ranging $20 - 250$ eV, both inside and outside inverted V structures. Besides the linear TOF estimation, Δt versus $1/v$ data were fitted with a second-degree polynomial; the changing slope of the quadratic curve is consistent with differentiated injection locations for particles with different energies. Said quadratic fitting achieved higher correlation than linear regression, therefore supporting the idea of particle acceleration occurring over an extended region along the field line. In most cases, the coefficient of the quadratic term was negative, indicating that more energetic electrons were injected at higher altitudes. As a third alternative, pitch angle distribution was also considered; by redefining Δt in equation (4.1) as an integral in space where the particles speed is parametrized regarding its adiabatic motion inside a dipolar magnetic field, to account for the effect of pitch angle dispersion. Estimations

using this approach were not inconsistent with previous findings, but their uncertainty was large as to prevent a conclusive statement.

Kletzing and Torbert [1994] attempted to replicate dispersive signatures as the result of electron acceleration by a quasi-static structure that would cause precipitation along field lines. It was found that agreement with the measured distributions was heavily conditioned to the imposition of an additional plasma component that could not be generated consistently by the model. Later on, Kletzing and Hu [2001] published a simulation where an inertial Alfvén wave accelerates electrons as it travels down the field line. Although their model is not self-consistent in calculating the perturbed plasmas response over the wave, they succeeded to replicate time dispersive bursts with similar characteristics to the ones found in observations. They argued that the variation of the Alfvén speed along the field line is an essential factor in achieving these signatures.

More recently, Cameron [2015] surveyed data from the ePOP satellite and reported the occurrence of time dispersive events reaching energies up to 350 eV, with maximum intensities around $100 - 150$ eV. Pitch angle spectrograms of these events indicate that these populations are mostly field-aligned, which seem inconsistent with large-scale acceleration where the mirror effect would have caused pitch angle scattering and thereby suggesting ionospheric origin. TOF estimations located most of these events sources at altitudes between $2000 - 2500$ km. Although projections based on TOF analysis showed decent agreement with data, the physical mechanism driving these perturbations remains ambiguous; since the source of particle acceleration was not far from the detector, both a localized source, as well as a moving source could show similar dispersion.

In this chapter, we consider field-aligned acceleration by inertial waves which develop and propagate close to the topside ionosphere. At this location, the predominance of oxygen plasma causes the local Alfvén speed to drop considerably, compared to higher altitudes where density decreases and ions become much lighter. These conditions make it plausible for low plasma temperature to interact effectively with the inertial perturbation and cause electron acceleration via Landau or Fermi resonance. One aspect that calls for attention is the fact that energy levels associated with the events reported in Cameron [2015] seem excessively high in comparison to the expectations derived from the basic theory of Fermi interactions. Recall that (see section A) accelerated electrons bounce off the wave potential as long as their initial speed, as measured in the wave frame of reference, falls in the range $[0, v_\phi (= \sqrt{2e\phi/m_e})]$. In the observer's frame, the speed of these particles after the interaction is $2v_w - v_0$. Roughly speaking, we have $v_w \approx v_A$, and we consider that the bulk of interactions occurs for particles with speed $v_0 \approx v_{th}$. Therefore, it seems that these electrons should escape the wave at speeds comparable to the thermal speed of the plasma, and so the dispersive signature should

appear at energies on the thermal level (not higher than a few tenths of eV in this case). Certainly, one can increase the potential of the wave arbitrarily to cause wave-particle interactions with faster particles; however, the amount of additional interacting electrons drops out quickly as v_ϕ moves into the tail of the distribution.

4.1 SEI on e-POP

The *enhanced Polar Outflow Probe* (e-POP) consists of an ensemble of 8 scientific instruments (see table 4.1) designed to obtain high-resolution data relevant for studies of mesoscale and microscale processes associated with plasma outflow in the polar ionosphere, and the influence of auroral currents over these processes [Yau and James, 2015]. E-POP orbits the Earth since late November 2013 on board of the CAScade, Smallsat, and IOnospheric Polar Explorer (CASSIOPE) mission, on an elliptical path with a perigee of 325 km, an apogee of 1500 km, and an inclination of 81^o. To optimize for the different investigations, each of the instruments on e-POP operates with different modes or *atitudes*. Technical aspects like measurement data rate, time resolution, instrument orientation, and the location within the orbit at which these modes are activated depend significantly on the objectives of their respective investigations.

Table 4.1: ePOP instrumentation. (From Yau and James [2015])

	Instrument	Principal investigator	Scientific output
CER	Coherent EM radio tomography	Dr Paul Bernhardt	Electron content
FAI	Fast auroral imager	Dr Leroy Cogger	Infrared and visible images
GAP	GPS attitude and profiling experiment	Dr Richard Langley	Spacecraft position and attitude
IRM	Imaging rapid mass spectrometer	Dr Andrew Yau	Low energy (0.5100 eV) ion detector
MGF	Fluxgate Magnetometer	Dr DonWallis	3D magnetic field and currents
NMS	Neutral mass spectrometer	Dr Hajime Hayakawa	0.12 km/s neutral particles
RRI	Radio receiver instrument	Dr Gordon James	Radio wave propagation
SEI	Suprathermal electron imager	Dr David Knudsen	Low energy electron detection

Relevant to this investigation, the *Suprathermal Electron Imager* (SEI) was included as part of the e-POP instrumentation with the objective of studying relevant aspects

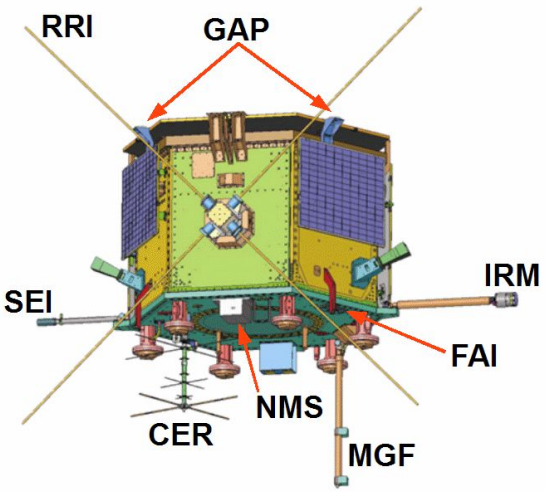

Figure 4.1: ePOP instrumentation on Cassiope. (From `https://epop.phys.ucalgary.ca/payload/`)

of ion flow and wave-particle interactions associated with low energy populations in the high-altitude Ionosphere [Knudsen et al., 2015]. In essence, the SEI consists of a charged-coupled detector (CCD), on top of which a system of hemispherical electrodes are placed to filter and deflect entering particles towards the detector (Figure 4.2). The top hemispheric section presents a circular aperture that allows particles within $\pm 4^o$ the nadir-ram plane inside. The hemispheric pieces are charged to different voltages, so that in the region in between them a radial electric deflects incident particles onto different regions of the detectors surface, according to their incident energy per charge. Through this technique, SEI is capable of measuring pitch angle and energy distributions of suprathermal (< 1 keV) ions and electrons at a very high rate (100 s^{-1}).

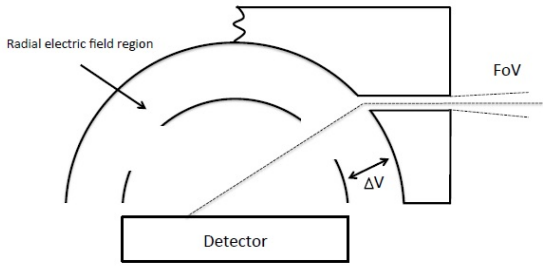

Figure 4.2: Schematic setup of the SEI device. (From Cameron [2015])

4.1.1 Electron dispersion events in the topside Ionosphere

Using recent data from the SEI on ePOP, Cameron [2015] classified a number of low energy dispersive features as *regular* and *inverse*. Inverse dispersion, as opposed to the regular case described at the beginning of this chapter, refers to instances where SEI detects lower energy electrons in advance of the high energy ones. We have borrowed a few representative cases intended to evaluate their compatibility with processes involving electron acceleration due to Alfvénic activity at the topside ionosphere. Unfortunately, hardware malfunction after e-POP was launched prevents the accurate reading of the detector gain (Knudsen, personal communication), so color intensities are expressed in arbitrary units.

Regular dispersion

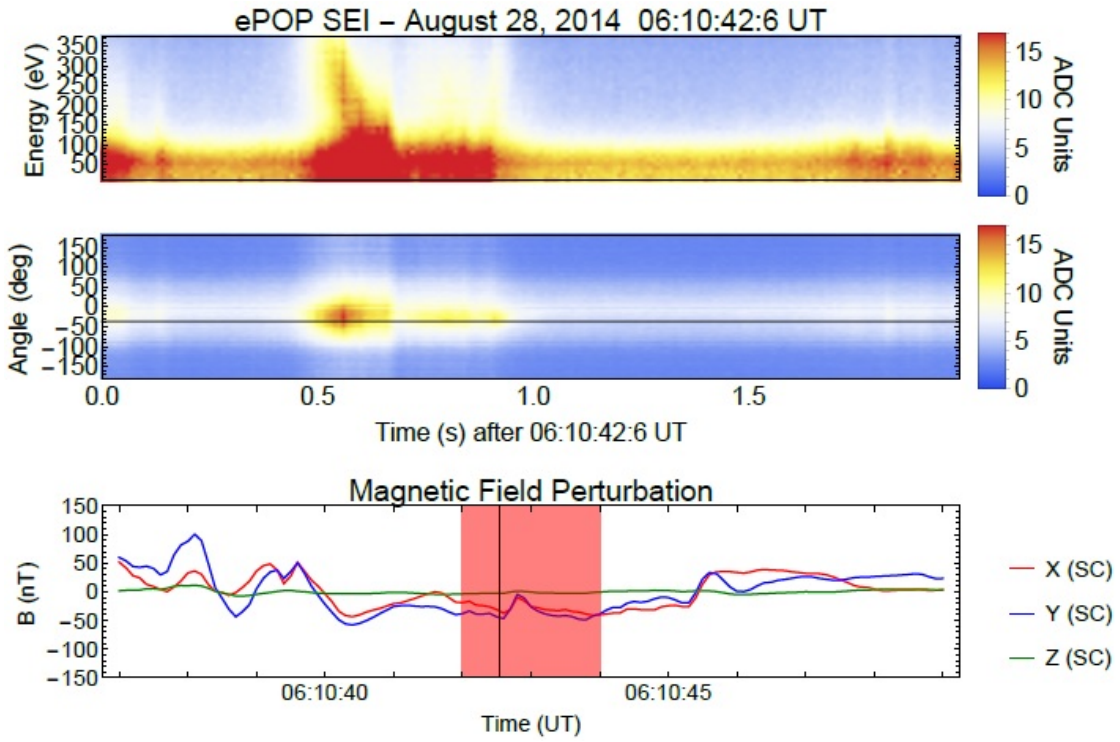

Figure 4.3: Dispersion event detected by the SEI on August 28, 2014. Energy (top) and pitch angle (middle) spectrograms. The shadowed region of the magnetic field perturbation (bottom) corresponds to the time interval from the two top panels. (From Cameron [2015])

Figure 4.3 presents energy (top) and pitch angle (middle) spectrograms of an event that took place on August 28, 2014. The satellite altitude during this event was 1089.5

km, and the source was estimated to be at altitude 2730 km. A distinctive intensity enhancement occurs between 0.5 and 1.0 s, which can be appreciated in both panels. Although there is an increase in the number of counts at practically all energies (including thermal electrons) during this interval, the signature shows higher levels of energetic electrons which decrease over time during the interval between 0.5 to 0.7 s approximately, with what seems to be a time-dependent increase for thermal energies. Pitch angle distribution for the same time interval, shown at the lower panel, remains confined to relatively low angles, which is considered an indication that source electrons are cold [Cameron, 2015], most likely from ionospheric origin. A somewhat resembling signature is presented in Figure 4.4. Based on previous considerations, both the apparent absence of thermal plasma and the narrow pitch angle range of the bursty feature, are consistent with an even colder plasma source than the previous example. This event was recorded at an altitude of 387 km, and the source location was estimated to have an altitude of 840 km.

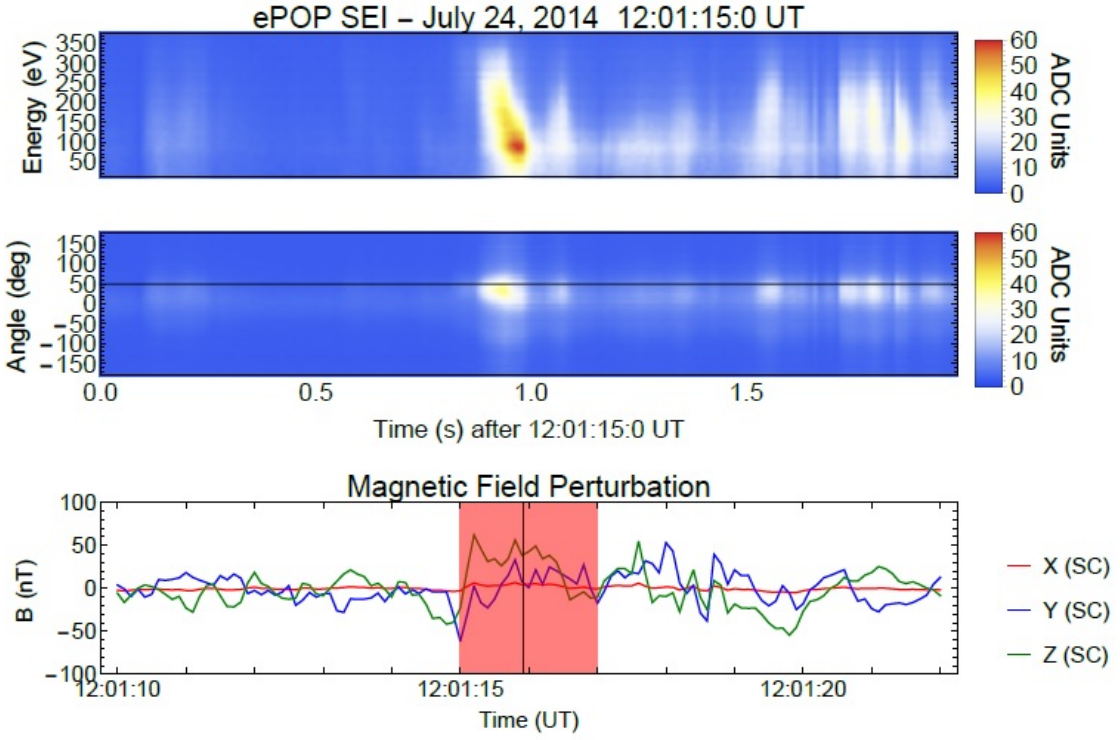

Figure 4.4: Dispersion event detected by the SEI on July 24, 2014. Energy (top) and pitch angle (middle) spectrograms. The shadowed region of the Magnetic field perturbation (bottom) corresponds to the time interval from the two top panels. (From Cameron [2015])

Similar time dispersive features as the ones just presented were reported at early

stages during the wave input phase of numerical simulations with the D1KD code (see Watt et al. [2004]). There are, however, a few inconsistent aspects that suggest important modifications to the physical mechanism based on Fermi interactions put forward by Kletzing [1994], perhaps the most conflictive of them is the relatively high energies of the faster electrons. As pointed out in appendix A, under particle acceleration of the Fermi kind, interacting electrons are expected to reach speeds roughly given by $2v_w - v_0$. Since the bulk of the distribution moves at a rate given by the thermal speed (so that $v_0 \simeq v_t$ for most electrons), the highest intensity of the differential flux should appear at much lower energies than the ones reported on many of e-POP events. Another apparent contradiction against the Fermi acceleration mechanism is the absence of thermalized plasma at dispersive feature's foot in Figure 4.4. According to Watt et al. [2005], as a result of particle-wave interactions, electrons that are initially non-resonant can become resonant if they spend enough time within the spatial domain of the pulse. Since the center of the wave potential constitutes a point of repulsion, as discussed in appendix A, electrons tend to slow down in the frame of reference of the wave while inside said potential. This effect is observed in the absolute frame as an enhancement of thermal plasma traveling with the wave. Such thermal component seem to be present in Figure 4.3, but not in Figure 4.4.

Inverse dispersion

Events categorized as *inverse dispersion* consist of instances where suprathermal electrons with low energy reach the SEI in advance of high energy ones (see top panel in Figure 4.5). The pitch angle distribution shown in the middle panel indicates that this signature consists of downward streaming electrons with little transverse momentum, most likely from an ionospheric source. In fact, Cameron [2015] considered only events with narrow pitch angle distributions as inverse dispersion since, at least in principle, inverted V structures can show a similar energy footprint as the one shown here. As pitch angle distributions for inverted V events typically presents a broad spectrum of transverse energy, inverse dispersion events with narrow pitch angle spectra are easily differentiated from inverted structures.

Inverse dispersion signatures like the one in Figure 4.5 are difficult to explain in the context of inertial Alfvénic acceleration. There is one particular scenario that (in principle) favors it; recall that, for a single wave pulse propagating through the plasma, its magnetic-field-aligned electric field suffers a nonlinear steepening in amplitude [Watt et al., 2005] which causes a gradual increase of the energy of the resonant particles. In this scenario, particle-wave interactions that result in faster electrons take place at

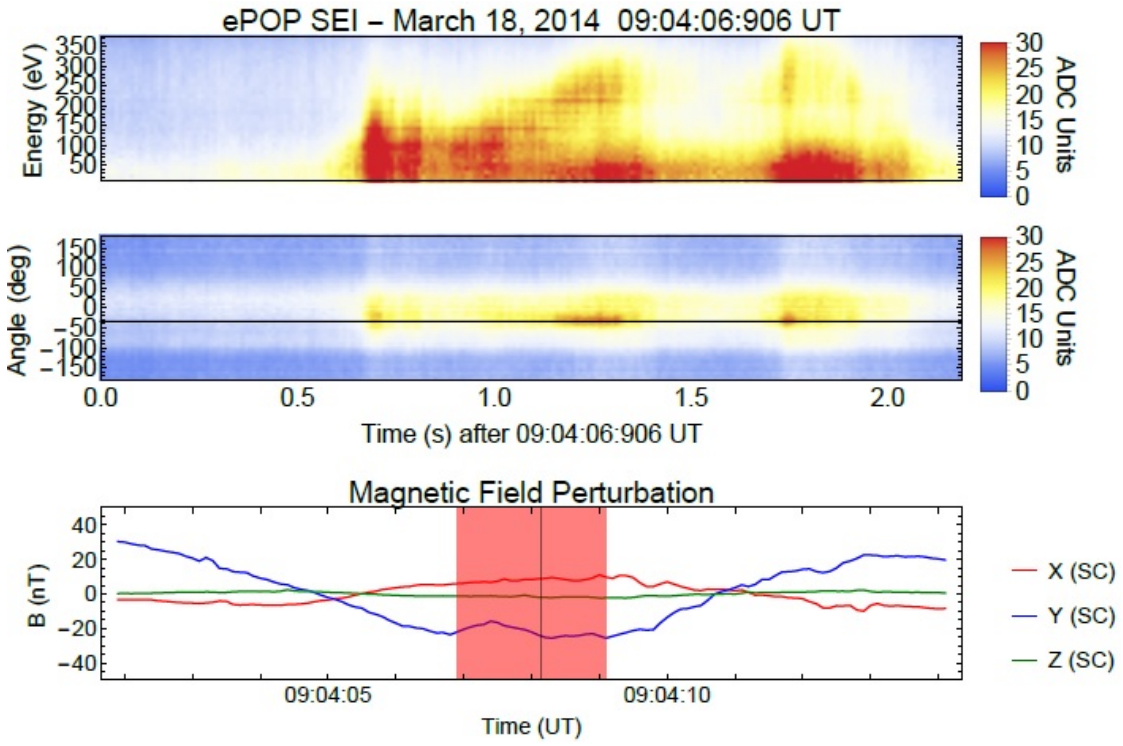

Figure 4.5: Energy (top) and pitch angle (bottom) spectrograms showing an *inverse* time dispersive signature. (From Cameron [2015])

later times; a stationary observer at the right location down the field line could see a beam of electrons where slower particles move ahead of faster ones. We estimate that, for this effect to be perceptible in the simulations, both the wave and its nonlinear evolution would have to occur at an unusually slow pace to keep the faster electrons from catching up with slower ones. We attempted to implement such favorable conditions in a number of simulations. However, slow-moving pulses, as it will be shown below, cause an additional effect that dominates over the Fermi-like interaction.

Alternatively, Cameron and Knudsen [2016] proposed a simple heuristic model with which they were able to obtain some consistent results. Their model consists of an anti-earthward electric field structure contained inside a section of a flux tube with certain extension L_d along the field line, moving transversely across magnetic field lines. As this structure moves into regions of undisturbed plasma at rest, it induces electron precipitation which can be detected by a spacecraft located at a lower altitude. For the case of a constant electric field $E_{\parallel}$ throughout its domain, and provided such domain is wide enough as to allow all electrons to reach its low altitude end, then the amount of energy gained by each particle corresponds to the work of moving it from its initial

position to the bottom of the electric field. The values of such energies depend directly on each particles initial position, the range of energies will be $0 < eE_{\parallel}z/m < eE_{\parallel}L_d/m$. Under these conditions, it was found that both regular and inverse dispersion were possible, depending on the location and velocity of the detector. Later on, we try this approach considering the cross field propagation of Alfvén waves.

4.2 Regular dispersion in the topside ionosphere

In this section, we present results of numerical simulations exploring a scenario where Alfvénic activity drives the generation of regular and inverse dispersion with similar characteristics as some of the events observed by ePOP. Building up from the estimations made in their study, we consider wave pulses generated not farther than 2000 km away from the spacecraft detector. Under such short distances, spatial variations in the plasma properties derived from the inhomogeneous geomagnetic field are expected to have a much lesser impact on the distributions time evolution than the wave-plasma interaction. This assumption allows us to use a simpler version of the Vlasov solver which considers only the parallel distribution, at the cost of losing the physics associated with variations in pitch angle and its effects on the plasma. Since ePOP events reveal very little activity at high pitch angles, we can afford to ignore sources of pitch angle diffusion.

Other than the spatial localization of the spacecraft during events, ePOP data does not report (to my knowledge) any other information regarding the physical state of the background plasma. Moreover, as it was pointed out in the previous section, spectrograms show only relative values of differential flux in arbitrary units. These limitations prevent us from making quantitative estimations of these signatures intensity. Instead, we focus on exploring the formation of dispersive structures under changing conditions of the ionospheric environment; we seek to find the conditions (if any) under which electron energies can reach considerably larger values than the ones expected under Fermi-like interactions. To do so, we have analyzed data from 3 sets of simulations, each of them characterized by an unique value for the Alfvén speed parameter ($v_{A1} = 2 \times 10^3$ km/s, $v_{A2} = 6 \times 10^3$ km/s, $v_{A3} = 10^4$ km/s, respectively). Each set includes a baseline case with the following parameters: perpendicular scale $\lambda_{\perp} = 0.5$ km, plasma density $n_e = 200$ cm^{-3}, temperature $T = 2$ eV; the external magnetic intensity depends on both the plasma density and Alfvén speed. The amplitude and frequency of the wave for these cases are $\phi = 5$ eV, and $f = 1$ Hz, respectively. These simulations are complemented with additional cases that consider the variation of several relevant parameters with respect to their baseline case, one at a time.

Each simulation consists of a magnetic field aligned region $0 \leq z \leq 5000$ km, contain-

ing a Lorentzian ($\kappa = 5$) plasma constituted by single ionized oxygen. At $z = 5000$ km, an Alfvén wave is introduced during the interval $0 < t < 2t_1$ according to the expression

$$\phi(t) = -\phi_0 \exp\left[-\left(\frac{t - t_1}{t_2}\right)^2\right]. \tag{4.2}$$

Here $t_1 = 0.5\tau$, and $t_2 = \tau/\sqrt{4 \ln 100}$ is chosen to ensure the wave enters smoothly into de simulation domain. $\tau = 1/f$ is the *period* of the wave, or in this case the time it takes for the pulse to move across the point of injection.

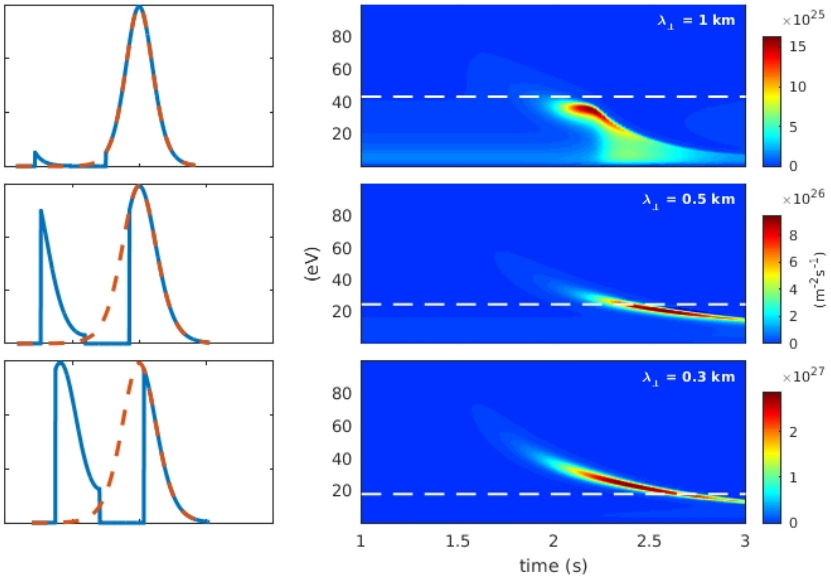

Figure 4.6: Electron dispersion signatures for three cases with $v_A = 6000$ km/s. (left) expected interaction. (right) Dispersive signatures for different values of the perpendicular scale (dashed line marks the expected energy of Fermi-resonant electrons).

Analysis of data from these simulations suggests that a different mechanism, driven by a large inductive response occurring in regions of low Alfvén speed (few $\sim 10^3$ km/s), can cause particle acceleration at much larger energies than the energy of Fermi-resonant electrons. The efficiency of this process also depends on other plasma properties. Figure 4.6 shows three simulation cases featuring different perpendicular scales; the background plasma corresponds to $v_A = 6000$ km/s. Notice that for $\lambda_\perp = 1$ km, the disturbed plasma shows beam formation of resonant electrons at the energy level predicted by the Fermi interaction, indicated by the discontinuous line. At shorter scales, on the other hand, accelerated electrons form up a structure consisting on a stream of particles with rapidly decreasing velocities. Sketches to the left of each spectrogram indicate the expected redistribution of velocities after a Fermi-like interaction. Note that for $\lambda_\perp = 1$ km, the

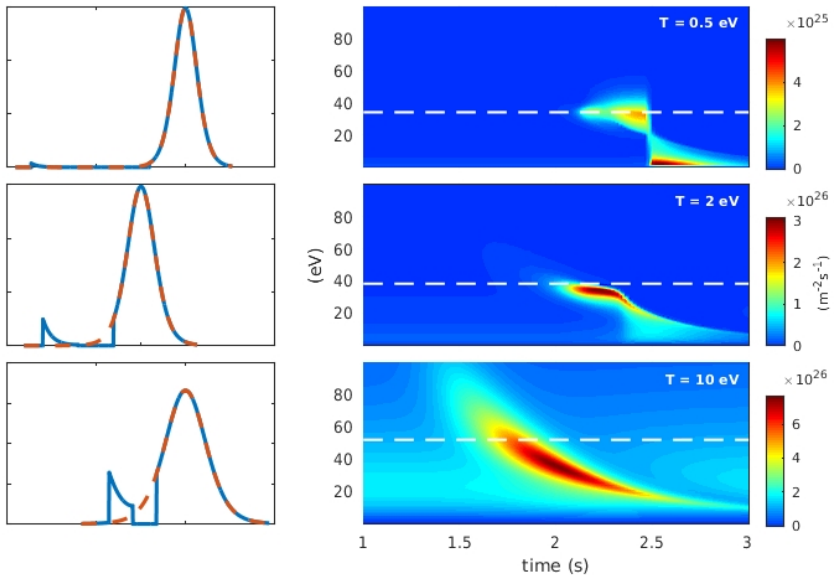

Figure 4.7: Electron dispersion signatures for three cases with $v_A = 10000$ km/s. (left) Expected interaction. (right) Energy-time spectrogram for different values of temperature (dashed line marks the expected energy of Fermi-resonant electrons).

wave merely interacts with electrons at the tail of the distribution, while for cases with lower scales the interaction seems largely nonlinear since it includes large sections of the core plasma.

Similarly, Figure 4.7 compares dispersive forms for cases with different temperatures. Cases with $T_e = 0.5$ and $T_e = 2$ eV evidence Fermi acceleration and beam formation at the expected energies. As for the case with $T_e = 10$ eV, electron acceleration surpasses the Fermi level. Therefore, an increased temperature enhances the inductive response and produces high energy dispersion. As a final example, Figure 4.8 shows that the inductive response is also proportional to the wave amplitude; signatures at higher energies are the result of a larger field-aligned vector potential component.

4.2.1 Fermi-like dispersion vs nonlinear dispersion

Figure 4.9 compares the baseline cases with $v_A = 2 \times 10^3$ km/s (left) and $v_A = 10^4$ km/s (right). Each panel represents electron advection in a way that is analogous to ePOP spectrograms, i.e., as seen by an stationary detector. We will refer to the simulation with $v_A = 2 \times 10^3$ km/s as case 1, and $v_A = 10^4$ km/s as case 2. Top panels show energy-time spectrograms at $z = 3000$ km, or 2000 km away from the source, while bottom panels measure dispersion at $z = 0$ km (5000 km away from the source). White dashed lines

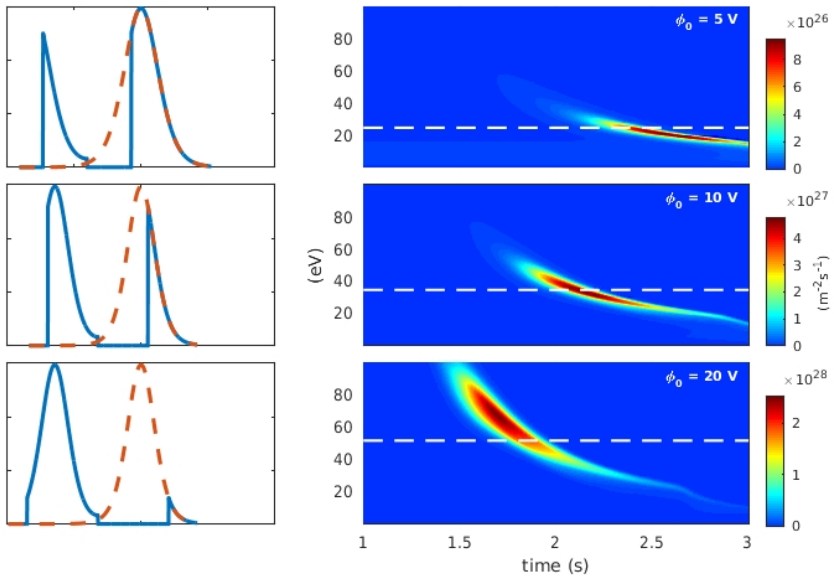

Figure 4.8: Electron dispersion signatures for three cases with $v_A = 6000$ km/s. (left) Expected interaction. (right) Energy-time spectrogram for different values of the wave amplitude (dashed line marks the expected energy of Fermi-resonant electrons).

have been superimposed to indicate the energy of resonant electrons under Fermi-like interactions.

Panels (1a) and (2a) mimic a realistic scenario where the source distance with respect to the satellite is 2000 km. This distance falls within the range of ePOP events. In (1a), there is a significant enhancement of differential flux during the interval $1.0 < t < 1.5$ s approximately; this population of fast electrons has exceeded several times the energy threshold for resonant Fermi-like interactions. As for case 2, electron acceleration in (2a) happens below the dashed line. Notice that, by increasing the Alfvén speed, the pulse now is expected to propagate faster, allowing Fermi-like resonant particles to reach energies of almost 40 eV.

These differences are more pronounced if the source is located further apart. The bottom panels in Figure 4.9 show electron dispersion at distance 5000 km away from the source. Such a large distance might pose a conflict with the assumption of uniform plasma, but we include them with the only purpose of providing additional evidence towards the differentiation between these simulations. Panel (2b) confirms that Fermi-type interactions drive electron acceleration for the case when $v_A = 10^4$ km/s, as it is evident by the characteristic beam of resonant electrons [Kletzing, 1994; Watt et al., 2004, 2005] from $t \sim 2 - 2.4$ s that travels ahead of the wave. In contrast, panel (1b) shows no beam formation by the bulk of accelerated electrons, which continues to stream

at speeds far outside the range expected by Fermi interactions.

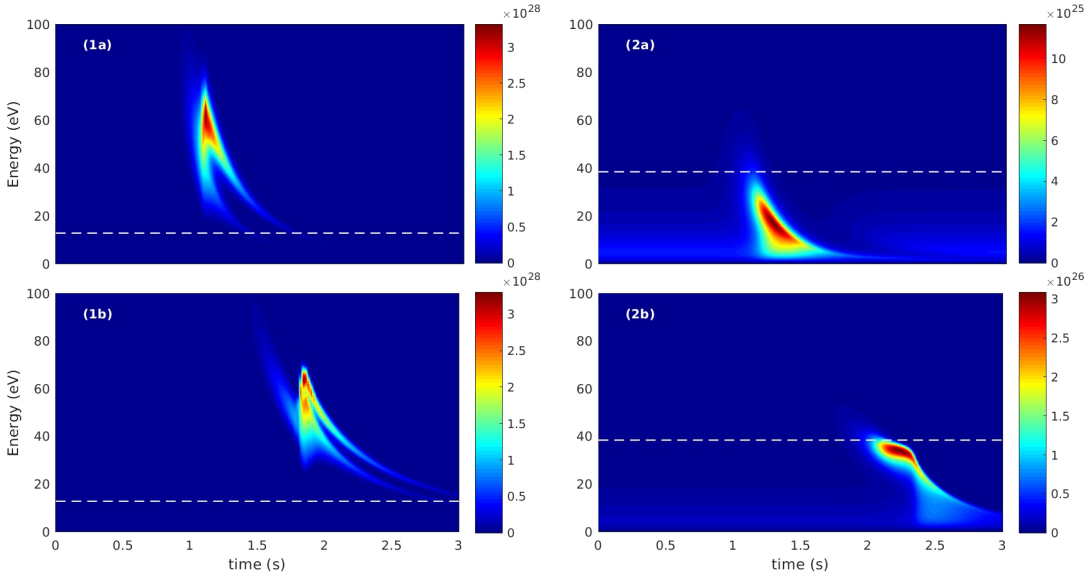

Figure 4.9: Downward electron differential flux for cases with (1) $v_A = 2 \times 10^3$ km/s, and (2) $v_A = 10^4$ km/s. Source distances are (a) 2000 km, and (b) 5000 km from the source.

The behavior obtained for case 1 shows a much different scenario when contrasted with the most common notion of wave-plasma interaction based on Fermi acceleration. Even though these results are consistent with rather high energy populations that are observed within the cold ionospheric environment in some of the ePOP events, this result must be treated with healthy skepticism. Before going further, we decided to put some additional work into strengthening the codes numerical implementation, particularly the conditions ensuring that both the potentials and their derivatives fulfilled the wave equation through the boundaries during the wave input stage. Still, these changes had little effect, and after rerunning these cases, similar results were obtained.

At this point, it is of interest to examine wave dispersion and their effects regarding electron acceleration. For the wave pulse described by equation (4.2), the corresponding $E_\parallel$ consists of a bipolar structure that causes electron deceleration in the wave frame. Figure 4.10 shows the time variation of (a) the perpendicular magnetic perturbation, (b) the perpendicular electric field, (c) the parallel electric field, (d) the parallel current, and (e) the parallel electron energy flux, at $z = 3000$ km. The continuous line refers to case 1 that causes high energy signatures, while the dashed line on each graph corresponds to case 2 driven by Fermi-like interactions. After traveling 2000 km, case 2 presents only mild dispersion and steepening of the leading section of $E_\parallel$ [Watt et al., 2005; Watt and

Rankin, 2007b]. On the other hand, the parallel field for case 1 shows a much different structure, including a 180^o phase change, and a considerable shorter spatial extent. Other field components also differ considerably between these cases. The much larger magnetic perturbation ($B_\perp \sim k_\perp A$) suggests that this pulse has a strong electromagnetic component. Finally, notice that despite a much lower Alfvén speed, the wave in case 1 propagates faster with respect to case 2.

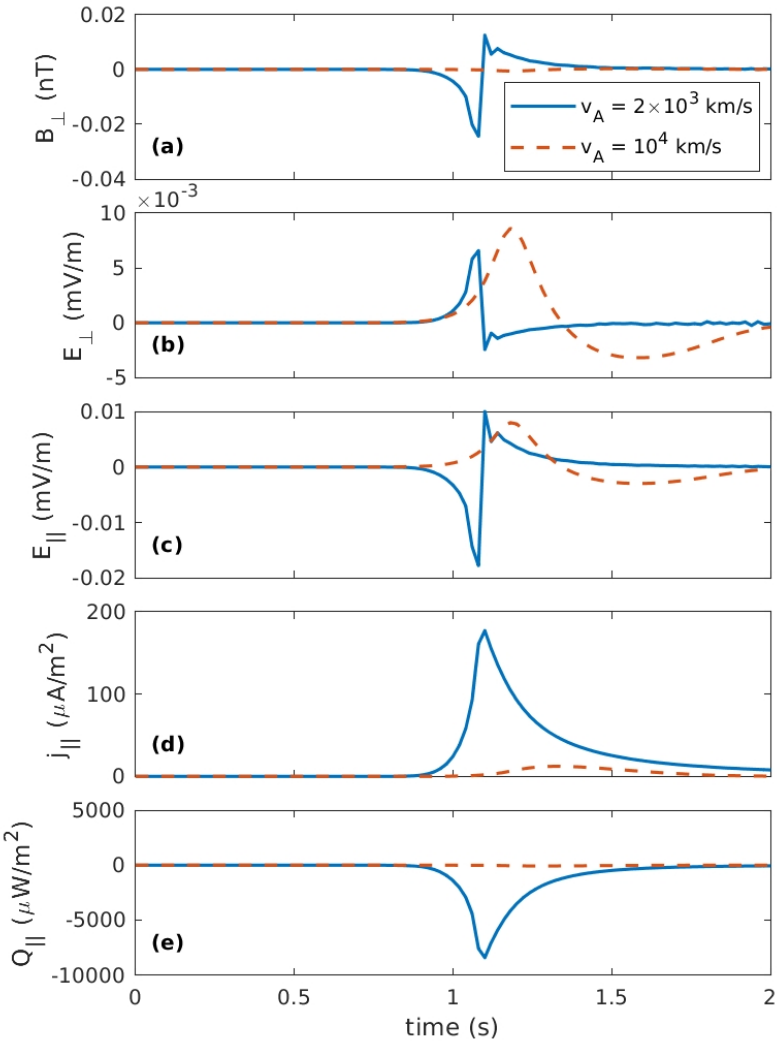

Figure 4.10: (a) perpendicular magnetic intensity, (b) perpendicular electric field, (c) parallel electric field, (d) parallel current, (e) energy flux as a function of time at $z = 3000$ km. The continuous line corresponds to the case $v_A = 2 \times 10^3$ km/s, while for the dashed line $v_A = 10^4$ km/s.

This particular field configuration causes a much different particle-wave interplay. In the wave frame, interacting electrons incoming from either the front or back of the pulse become attracted towards the point where the electric field changes sign, inducing them to quickly stream past the wave, as opposed of being slowed down and eventually reflected, as in case 2. During their passing through the wave, their average energy is higher than their initial energy. Therefore, one expects to see an enhancement in differential flux at energies larger than the thermal level. For this reason, the suprathermal component often observed ahead of the wave [Kletzing, 1994; Watt et al., 2005] is absent in the top-left panel of Figure 4.9.

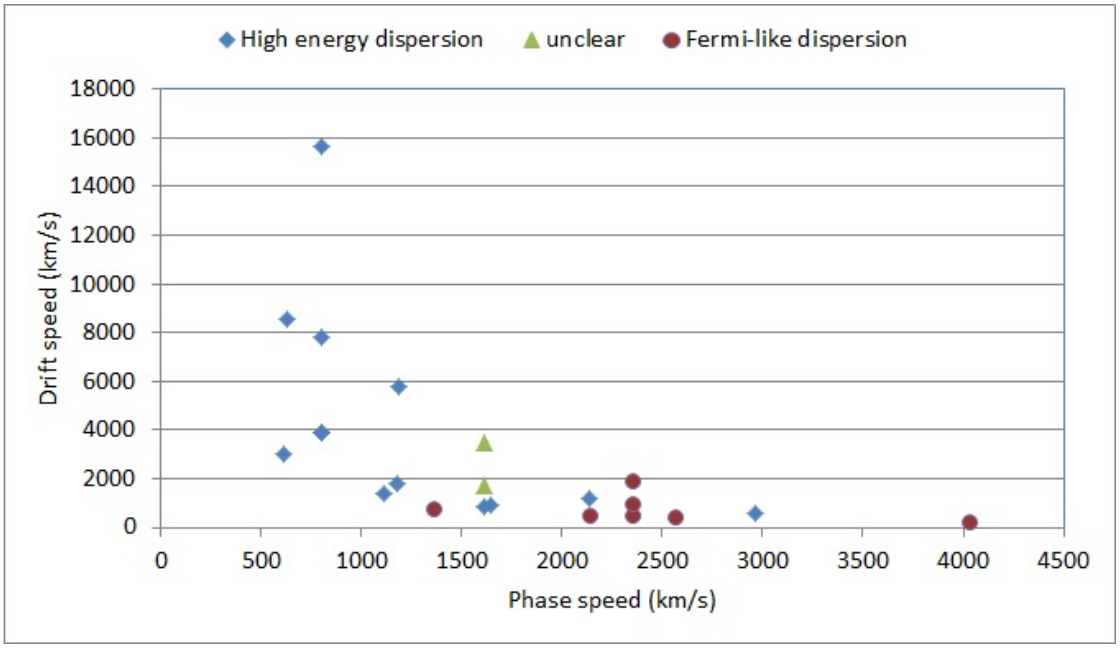

Figure 4.11: Drift speed associated to the inductive response of the plasma to Alfvénic perturbation vs the initial phase speed of the wave.

Animations of the time evolution of the wave indicate that for the case where $v_A = 2 \times 10^3$ km/s, strong damping occurs immediately after the pulse is injected into the simulation domain. At the same time, a large perturbation appears carrying its own fields. From Amperes law, the large $B_\perp$ (see Figure 4.10) induces a strong field-aligned current. Given their inertia and large density in this region, the cold electrons are the most likely candidate to carry the parallel current necessary to support $A_\parallel$. Within the code, boundary conditions provide this current by adding the correct drift velocity term to the electron distribution [Watt et al., 2005]. Therefore, this drift speed can be regarded as a measure of the plasmas inductive response due to the perturbation. Figure 4.11 plots the maximum drift speed of electrons carrying the induced current

during the wave input phase of the simulation, as a function of the initial phase speed of the wave. Through visual analysis of the time evolution of the electron distribution and the electric field, each simulation has been classified according to whether linear or nonlinear interactions are driving electron precipitation. The graph shows that high energy dispersive signatures tend to occur for slower moving waves.

4.2.2 Reproducing ePOP signatures through simulations

It would be useful to find a set of parameters with which to replicate the main physical features of the ePOP events shown in section 4.1.1. We studied the formation and evolution of dispersive forms for all simulations briefly mentioned earlier in this chapter. Based on these cases, one tries to identify patterns in the behavior of the distribution after independent variation of the following parameters: the Alfvén speed, the wave frequency, the wave amplitude, the plasma temperature, and the perpendicular scale. These results should help to find more appropriate initial conditions for the next round of simulations. This strategy is straightforward and can be iterated as needed, yet its execution required much more time than we expected for the following reasons:

- There is empirical evidence (Clare Watt, personal communication) that the numerical solver breaks down in cases of very low plasma temperatures due to the sharp gradients in the velocity distribution. This issue concerns directly the atmospheric region that is a subject of study in the present chapter. Moreover, this is the reason that motivated the use of Lorentzian instead of Maxwellian distributions, since the former have longer tails than the latter. Unfortunately, this effect does not take place at a specific temperature threshold, and often even increasing the momentum resolution to any reasonable level will show little improvement at best. Personal experience indicates that aspects like the numerical resolution in space and time, as well as other properties of the plasma, seem to play a part in this limitation. We have invested a considerable amount of time and computational resources trying to delimitate a technical or empiric criterion that would make it possible to avoid such behavior. However, given the multidimensionality of factors involved, to date, this has not been possible, and simulations with numerical problems are still a common occurrence when one attempts to simulate ionospheric plasma.

- Important initial parameters associated with the background plasma, like temperature and density, not only determine the shape of the distribution; they also affect the dispersive properties of the propagating wave. This two-fold dependence introduces an inherent nonlinearity to the wave-particle interaction, which makes it difficult to induce any desired specific response to the resonant electrons.

Table 4.2: Input parameters and other derived quantities for cases that simulate ePOP events.

		event on Aug. 28	event on Jul. 24
plasma density	n_e (cm^{-3})	2000	200
plasma temperature	T (eV)	20	10
kappa coefficient	κ	7	5
magnetic field	B (μT)	99.0	5.2
perpendicular scale	$\lambda_\perp$ (m)	700	500
Alfvén speed	v_A (km/s)	12000	2000
thermal speed	v_{th} (km/s)	2350	1570
wave phase speed	v_w (km/s)	8700	1200
wave amplitude	ϕ_0 (V)	40	5
wave frequency	f (Hz)	5	
source distance	d (km)	2642.3	858.4

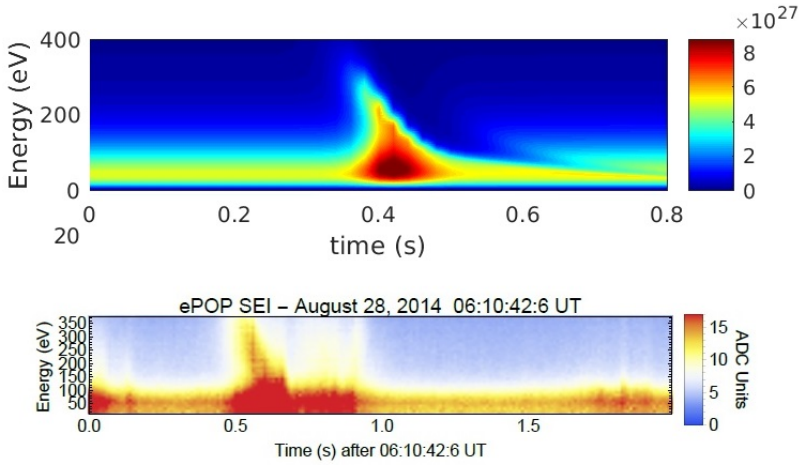

Figure 4.12: (top) Differential flux as a function of energy and time for a simulation showing Fermi-driven dispersion. (bottom) SEI data from Aug. 28, 2014.

Eventually, simulation cases which (to my judgment) present features that approximate the ePOP events were obtained. Table 4.2 summarizes the initial parameters used in these two simulations. Figure 4.12 compares one of such cases (top panel) against the ePOP event reported on Aug 28, 2014 (bottom panel). The time extension of the main dispersive feature is ~ 0.2 s, and the fastest electrons have reached energies higher than 300 eV. The magnetic peak of the pulse (not shown) is ~ 20 nT; this is less than half of the measured magnetic perturbation reported by the fluxgate magnetometer on ePOP at the moment of the event. According to Cameron [2015], these magnetic mea-

surements for most of the ePOP events are not over the level of noise detected by the instrument, so at least we can assert that the magnetic perturbation in the simulation is not inconsistent with the MFG measurement.

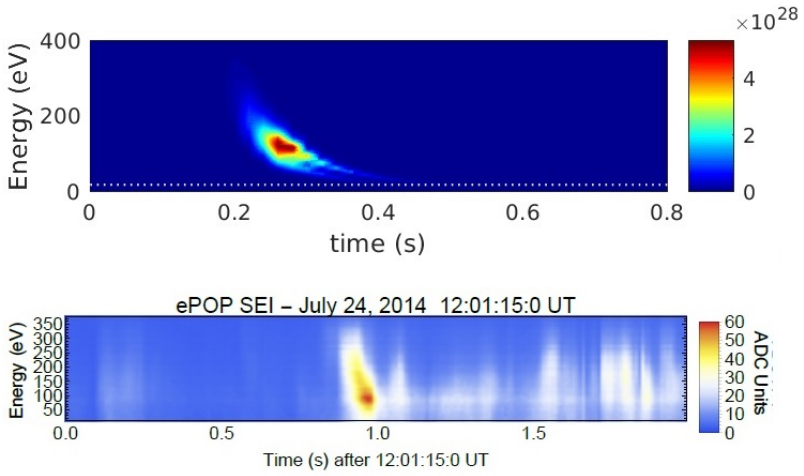

Figure 4.13: (top) Differential flux as a function of energy and time for a simulation showing non-Fermi dispersion. (bottom) SEI data from July 24, 2014.

Analogously, the top panel in Figure 4.13 shows electron acceleration similar to the SEI data from July 24, 2014. In this simulation, the peak magnetic perturbation of the wave is 13 nT (not shown), which again falls below the reading of ePOPs MFG instrument. Electron advection is driven by the sizeable inductive response to the slow wave, so following case 1 discussed previously, no bulk heating occurs due to the change in phase with respect to the input wave. The maximum intensity of differential flux takes place at $\sim$ 100 eV, and although its intensity decays rapidly after 200 eV, the fastest electrons reach energies of $\sim$ 300 eV.

4.3 Inverse dispersion

In this section, we revisit [Cameron and Knudsen, 2016] concept of inverse dispersion as a result of the relative motion of the satellite detector relative to a moving source. We propose a modified mechanism consisting of IAW moving earthward along magnetic field lines as the source of particle acceleration. At the topside ionosphere, electron inertia effects dominate [Hasegawa, 1976] and cause the shear Alfvén mode to become dispersive. Stasiewicz et al. [2000] gives the linear approximation for the dispersion relation of an

IAW:

$$\frac{\omega}{k_{\parallel}} = \frac{v_A}{\sqrt{1+(k_{\perp}\lambda_e)^2}}, \tag{4.3}$$

where v_A is the local Alfvén speed, and $\lambda_e = c/\omega_e$ is the electron skin depth. The group velocity describes how the wave energy is distributed

$$\frac{\partial\omega}{\partial\mathbf{k}} = \frac{v_A}{\sqrt{1+(k_{\perp}\lambda_e)^2}}\hat{\mathbf{b}} - \frac{k_{\perp}\lambda_e^2\omega}{1+(k_{\perp}\lambda_e)^2}\hat{\mathbf{x}}. \tag{4.4}$$

The phase velocity of a traveling localized IAW perpendicular to the ambient field constitutes a source of downward electron precipitation that could potentially have a similar effect as an electrostatic source moving at speeds well above the ExB drift speed.

4.3.1 Dispersion as seen by the observer

To consider perpendicular wave dispersion, we visualize it as an Alfvén wave source moving in the cross plane of the magnetic field line. The premise is simple: a sensor moving in the same direction as the source of accelerated particles, but with some time delay with respect to it, should see first the population of interacting electrons that has accelerated the least, and, as it catches up to the source, it will eventually detect the resonant population. Figure 1 illustrates this scenario: an Alfvén wave source (black circle) moves perpendicular to the ambient field at some arbitrary speed v_S. As it travels, emits a perturbation that propagates downward parallel to the ambient field. Note that the waves emitted at earlier times travel ahead than waves emitted more recently. An observer equipped with an SEI detector follows this source at some vertical distance below with speed v_D. Provided that $v_D > v_S$, the observer should detect later stages of the interaction at first, and then earlier ones corresponding to more recent emissions.

We can construct the energy-time signature of the distribution function as seen by the observer as it moves in the cross-field direction. Consider a situation where the observer shows up delayed by certain time t_0 after the wave has been emitted at the same x-coordinate. Notice that, at the same time, the stage of the emission at a location Δx to the right corresponds to $t_0 - \Delta t_S$, where Δt_S is the time it takes the source to move a distance Δx. To this correction we must also add the time Δt_D it takes for the observer to move the same distance Δx. Therefore, the stage of the simulation seen by the observer is given by $t_0 - \Delta t_S + \Delta t_D$. The relation between time intervals is given by

$$\Delta x = v_S\Delta t_S = v_D\Delta t_D. \tag{4.5}$$

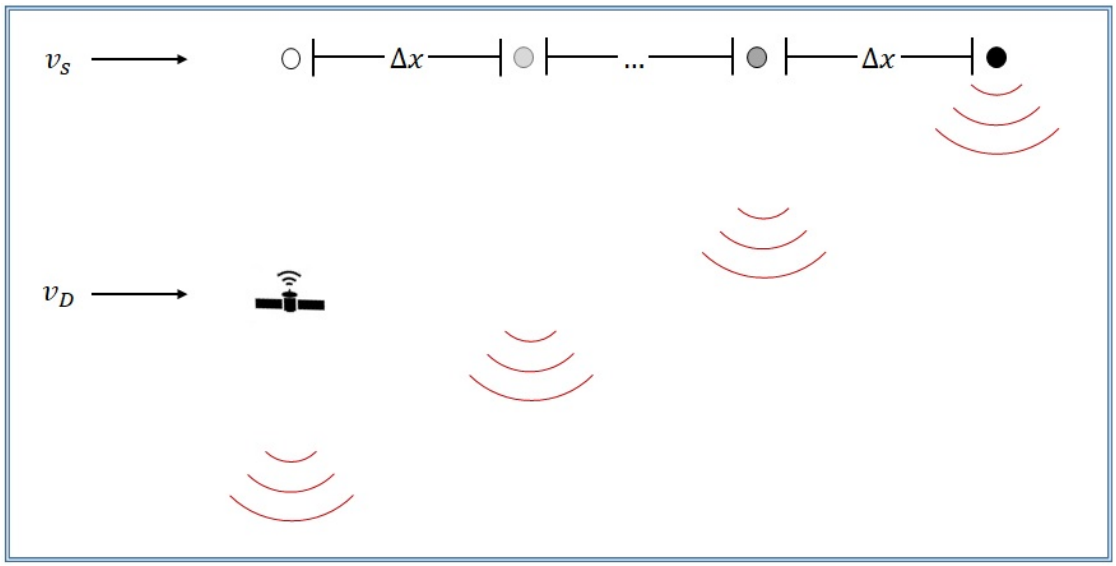

Figure 4.14: Physical scenario: a detector follows a source of Alfvén waves on its trajectory perpendicular to the background magnetic field.

This can be trivially generalized for successive displacements. The electron distribution detected by the observer at a location $n\Delta x$ to the right of its initial position corresponds to the signal as observed by a stationary observer at a time given by

$$t_n = t_0 + n\left(1 - \frac{v_D}{v_S}\right)\Delta t_D. \tag{4.6}$$

Perhaps the most drastic simplification we make is that the moving source produces the same wave at every location $n\Delta x$ on its perpendicular path. This condition is required since the DK1D model does not directly account for plasma evolution perpendicular to the background magnetic field.

4.3.2 Simulation

The numerical algorithm procures the electron distribution function conveniently stored as a three-dimensional array $f(z, p_\parallel, t)$. To obtain an output that is analogous to the energy dispersed spectrograms of *in situ* data, a computer script sorts the distribution local to the detector into energy bins, which in turn is used to calculate the so-called *differential energy flux*:

$$J_E = \frac{2}{m_e^2}E^2 f(E), \tag{4.7}$$

where $f(E)$ represents the distribution function in terms of the energy $E = 1/2 m_e v^2$.

The parameters of this simulation intend to mimic conditions typical of the topside ionosphere, although some of them were stretched out from more typical values to ensure that inertial effects were effective. We consider oxygen plasma which is assumed uniform across the simulation domain with $n_e = 2 \times 10^3$ cm^{-3} and $T_e = 20$ eV. We have implemented a Lorentzian distribution with $\kappa = 7$. The magnetic field is also uniform with value $B_0 = 10^{-4}$ T (Alfvén speed $\sim$ 12000 km/s), and the perpendicular scale is $\lambda_\perp = 0.7$ km. The Alfvénic perturbation consists of a Gaussian pulse with amplitude $\phi_0 = 40$ V and time extent $T = 0.2$ s.

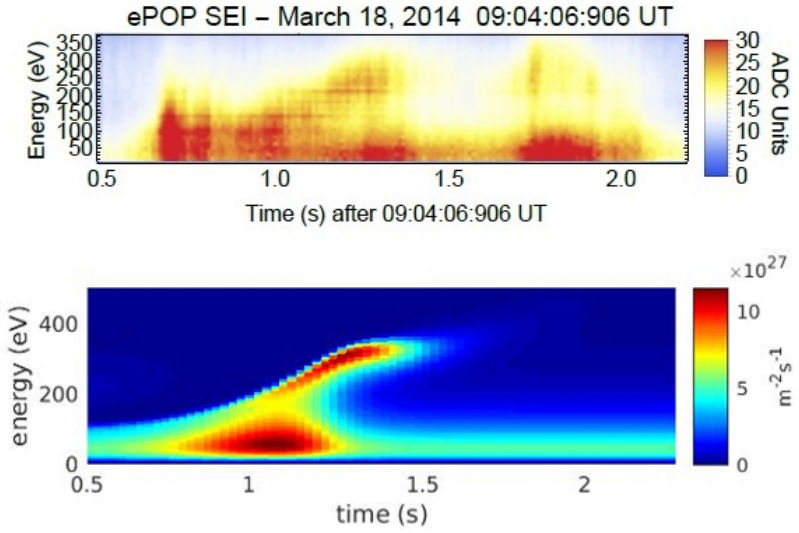

Figure 4.15: (Top) Inverse dispersion event captured by the SEI instrument on March, 2014. (Bottom) Reconstruction of the differential flux reaching a detector that moves at speed $v_D = 1.4 v_S$.

Figure 4.15 contrasts one of the ePOP events against the time-corrected energy spectrogram according to the guidelines described in section 4.3.1. These two cases present close agreement of the time length of the dispersive feature and the spectrum of energies to which interacting electrons are energized. Thus, the simulation and analysis presented here proves that Alfvénic acceleration can be interpreted as inverse dispersion due to the relative motion of the detector with respect to the source. As a consequence, the distortion of dispersive signatures will depend on the relative location and speed of the observer. Figure 4.16 shows that the effect of modifying the relative speed is a stretching or enlarging of the dispersive form; a faster observer will obtain a signature with a lower temporal footprint, while a slower moving one will see enlarged dispersion.

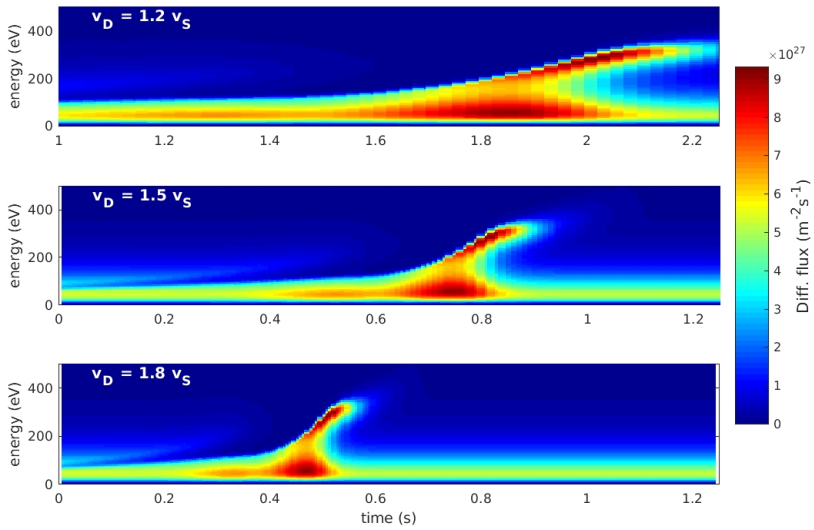

Figure 4.16: Differential flux as seen by the detector moving at different speeds v_D relative to the source.

4.4 Summary

This chapter explored the formation of electron dispersion signatures due to field-aligned acceleration by Inertial Alfvén Waves (IAW) under conditions typical of the topside ionosphere. This was motivated by recent observations using the SEI instrument on ePOP, which reported field-aligned electron acceleration to suprathermal energies ($\sim 10^2$ eV) and source locations between $1000 - 3000$ km altitude in three different categories: regular dispersion with and without heating of the local background plasma, and inverse dispersion.

Numerical simulations using the original DK1D code showed similar dispersive forms for each of these categories under specific conditions. Regular dispersion with background heating was found to be consistent with wave-particle interactions of the Fermi kind under local Alfvén speeds of several 1000 km/s and higher. For conditions such that the local Alfvén speed takes lower values, on the other hand, wave dispersion showed a very strong inductive response including large damping of the original perturbation, and electron acceleration to energies significantly larger than the energy predicted by Fermi interactions. In these cases, the electron dispersion signature presented similar characteristics as the cases of regular electron dispersion without enhanced heating of the thermal component obtained by the SEI instrument. Finally, it was demonstrated that events of inverse dispersion are consistent with field-aligned electron acceleration

as observed by a detector that follows the cross-field path of the source of IAW, if the detector is faster than the source. In this scenario, the temporal extension of the dispersive signature is inversely proportional to the speed of the detector relative to the source, but the energy gain of the accelerated electrons does not depend on it.

The studies presented in this chapter shed further light on the role of Alfvén waves in producing aurora at northern latitudes. They also provide a methodology for interpreting wave particle interaction processes observed by low-orbit satellites in their investigation of the near-Earth space environment.

Chapter 5

Inhomogeneous conditions in DK1D

The original implementation of the DK1D numerical solver considers only uniform density and temperature conditions of the background plasma. This representation is consistent with the kinetic regime of Alfvén wave propagation, where variations in the plasma properties take place over spatial scales of a few Earth radii so that gradients along the magnetic field can reasonably be considered negligible. Moving closer to Earth, on the other hand, the gradual transition towards the ionospheric environment features strong gradients towards higher densities and lower temperatures, drastically changing the Alfvén speed over much shorter spatial scales. Therefore, the study of dispersion effects in the inertial region cannot be correctly modeled by using the assumption of homogeneous plasma conditions.

One of the main contributions of this thesis is the implementation of inhomogeneous conditions of the background plasma density and temperature in the DK1D code, through the inclusion of a time-independent electrostatic potential. Said potential introduces a force term in the Vlasov equation, which is to be used to couple the resulting distribution function to a given density model. Physically speaking, the potential forces electrons to accumulate in what represents the ionospheric end of the simulation domain.

Care must be taken, however, in choosing a density model that ensures the initial distribution function to be consistently defined at the beginning of the simulation. We address the problem of building the electron distribution in such a way that: (i) the distribution is in its stationary state, (ii) integration of the distribution over velocity space yields a given density profile at every position inside the simulation domain, as the formal definition requires, (iii) integration of the second moment of the distribution is

consistent with predetermined boundary temperatures. It has been previously demonstrated [Tikhonchuk and Rankin, 2002; Blanco, 2011] that by including an electrostatic potential $\phi_E(z)$, which is given as a function of position along the geomagnetic field, a simple two-component Maxwellian plasma distribution with constant temperatures is sufficient to account for how the plasma temperature varies from cold to warm as the altitude increases. Note that this is not the only equilibrium state possible; it is the simplest one and contains the realistic assumptions that temperature (density) increases (decreases) with altitude; it also includes a heavy mass component of cold oxygen, which exists due to magnetosphere-ionosphere coupling.

5.1 Plasma density model

A simplified model of the background plasma density within the spatial region establishes the coexistence of two plasma species with different source: a rather energetic solar wind component, composed by hydrogen ions and electrons, which for practical purposes has constant density across the spatial domain; and a singly-ionized component of ionospheric oxygen that decays exponentially with altitude depending on a scale factor z_0, as follows:

$$n_e(z) = n_H + n_O \exp\left(-\frac{z}{z_0}\right). \tag{5.1}$$

5.1.1 Consistency of the distribution function

The spatial dependency on density expressed in (5.1) must be encapsulated on the electron distribution function for consistency, since integration of the distribution in velocity space yields the former identically. Additionally, the distribution must be a solution of the time-independent Vlasov equation,

$$\mathbf{v} \cdot \nabla f(\mathbf{r}, \mathbf{v}, t) + \mathbf{a} \cdot \nabla_{\mathbf{v}} f(\mathbf{r}, \mathbf{v}, t) = 0, \tag{5.2}$$

so that we can assure it corresponds to the plasma's stationary state. For conservative systems, this is accomplished by defining a space dependent electrostatic potential across the whole simulation domain, for which a force term ($m_e\mathbf{a} = -q_e\nabla_{\mathbf{z}}\phi_E(z)$) is associated; this new contribution on the second term of the left hand side in equation (5.2) ultimately cancels the spatial variation that raises from the first term (see Bittencourt [2004] for a detailed demonstration). In practical terms, the distributions dependency on the potential is found by including the potential energy term as part of the total energy dependence on the distribution function. For instance, the potential shows up in

a Maxwellian distribution as:

$$f_0(\mathbf{r},\mathbf{v}) = \frac{n_0}{(\sqrt{\pi}v_{te})^3}\exp\left[-\left(\frac{1/2m_e v^2 - \phi_E(z)}{k_B T}\right)\right], \tag{5.3}$$

where $v_{te} = \sqrt{2k_BT/m_e}$ stands for the electron thermal velocity. For convenience, in this chapter we redefine the temperature and potential to be expressed in energy units by writing $T = k_BT$ and $\phi_E = e\phi_E$.

5.2 Inhomogeneous Maxwellian plasma

A single Maxwellian can reproduce a given density profile, but it predicts uniform temperature conditions. Since clearly we expect to find temperature gradients in the transition region, it is convenient to consider the plasma as the mixture of two noninteracting plasma species, *warm* and *cold*, with different constant temperatures, T_w and T_c, and background densities, n_w and n_c [Tikhonchuk and Rankin, 2002]. The resulting distribution reads:

$$f_e(z,v) = \sum_{s=c,w}\frac{n_s}{(\sqrt{\pi}v_{ts})^3}\exp\left[-\left(\frac{v}{v_{ts}}\right)^2 - \frac{\phi_E(z)}{T_s}\right]. \tag{5.4}$$

Integration of (5.4) in the velocity domain yields a second representation of the plasma density; in this case the spatial dependence is encapsulated into the electrostatic potential

$$n(z) = \sum_{s=c,w} n_s \exp\left(\frac{\phi_E(z)}{T_s}\right). \tag{5.5}$$

Briefly notice that the *cold* and *warm* background densities n_s are not free parameters, but constrained by the fact that equations (5.1) and (5.5) must yield the same values at every location.

The temperature profile is obtained upon calculation of the second moment of the distribution function (5.4), its final expression is:

$$T(z) = \frac{1}{n(z)}\sum_{s=c,w} n_s T_s \exp\left(\frac{\phi_E(z)}{T_s}\right). \tag{5.6}$$

Finally, we need an expression for the electrostatic force due to the potential, $F_E(z) = -\nabla_z\phi_E(z)$. This force is found by calculating the parallel gradient on both sides of

equation (5.10) and solving for $\nabla_z \phi_E(z)$, from which one obtains, in units of eV/m:

$$F_E(z) = \frac{\nabla_z n(z)}{\sum_{s=c,w} \frac{n_s}{T_s} \exp\left(\frac{\phi_E(z)}{T_s}\right)}. \tag{5.7}$$

5.2.1 Determination of the potential

Typically, n_c and n_w are obtained by applying boundary conditions for density at each end of the field line. Notice, however, that doing so would introduce the potentials at the same locations as unknown parameters. By setting the potential to zero at the equator, and by requiring the background cold and warm densities to be positive definite, one finds a closed interval of possible solutions for the potential, which can be shown consists of positive potentials, while negative potentials lead to no possible solutions [Blanco, 2011].

The following workaround provides a simpler path to an acceptable solution of the potential: we can fairly argue that the warm plasma is mainly constituted by magnetospheric electrons, so that,

$$n_w \simeq n_{H_2}. \tag{5.8}$$

Furthermore, by arbitrarily choosing the value of zero potential at the equatorial end of the field line ($\phi_E(z_{eq}) = 0$) and evaluating $n(z_{eq})$, we get

$$n_c = n_O \exp\left(-\frac{z_{eq}}{z_0}\right). \tag{5.9}$$

Now that we have determined the cold and warm densities, we can define the electrostatic potential itself, as the solution to the condition:

$$n_H + n_O \exp\left[-\frac{z}{z_0}\right] = \sum_{s=c,w} n_s \exp\left(\frac{\phi_E(z)}{T_s}\right). \tag{5.10}$$

Even though (5.10) guarantees a unique solution for the potential at every position, the equation cannot be solved analytically unless $T_c = T_w$. For other cases, a numerical solution can be obtained using the Interval Bisection method with the following condition

$$f(\phi_E) := n(z) - \sum_{s=c,w} n_s \exp\left(\frac{\phi_E}{T_s}\right) = 0. \tag{5.11}$$

It is only after these potentials have been found that a discrete array of temperatures can be calculated using equation (5.6).

5.2.2 Maxwellian plasma in equilibrium

At this point, we deviate from the discussion to test the model just described. Here we present a test simulation where no perturbation is excited to corroborate with numerical data that the plasma remains stationary in time.

Table 5.1: Input parameters for a stationary plasma simulation.

altitude domain (km)	$0 \leq z \leq 1.6 \times 10^4$
magnetic field line	$L = 9$
perpendicular scale at the ionosphere (km)	$\lambda_I = 2$
background hydrogen density (cm^{-3})	$n_{H_2} = 17$
background oxygen density (cm^{-3})	$n_{O_2} = 6 \times 10^4$
oxygen decay scale (R_E)	$z_0 = 0.15$
cold plasma temperature (eV)	$T_c = 1$
warm plasma temperature (eV)	$T_w = 5$

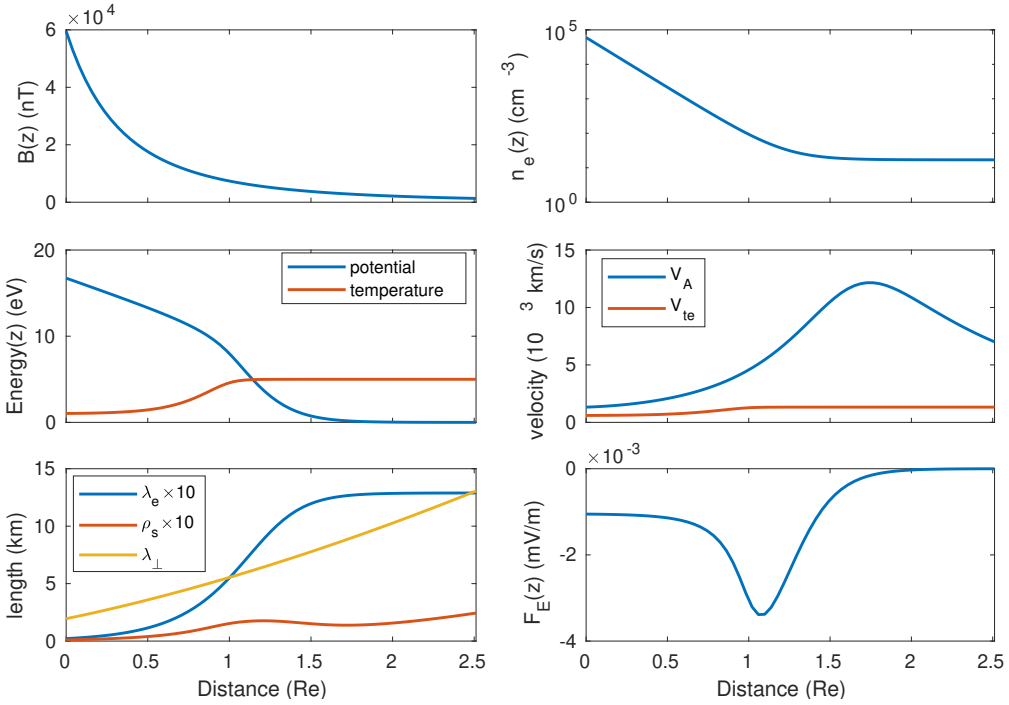

Figure 5.1: (From left to right, top to bottom panels) Spatial dependence of: Magnetic intensity; particle density; plasma temperature and electrostatic potential; Alfvén and thermal speed; electron skin depth, ion acoustic radius, perpendicular scale; and electrostatic force caused by the potential.

Input parameters for this case are listed in table 5.1, these determine the plasma properties and their variation in space, which are displayed in Figure 5.1. The spatial

variation of the magnetic intensity and particle density are explicitly evaluated through the expressions given in (2.39) and (5.1), respectively. The left middle panel shows the Alfvén speed, the thermal speed, and the phase speed of the wave according to the dispersion equation (2.110); the Alfvén velocity is higher than the thermal speed everywhere, indicating the dominance of inertial conditions all across the simulation domain. Large density of ionospheric oxygen produces considerable attenuation of the Alfvén speed at low altitudes. Thus it is clear that implementation of inhomogeneous conditions becomes an important element in determining wave propagation and dispersion, therefore justifying this investigation. The right-middle panel shows the resulting electrostatic potential and plasma temperature. Notice that temperatures at the boundaries are in good agreement with T_c and T_w. The potential generates an electrostatic force on the electrons, which is displayed in the right-bottom panel.

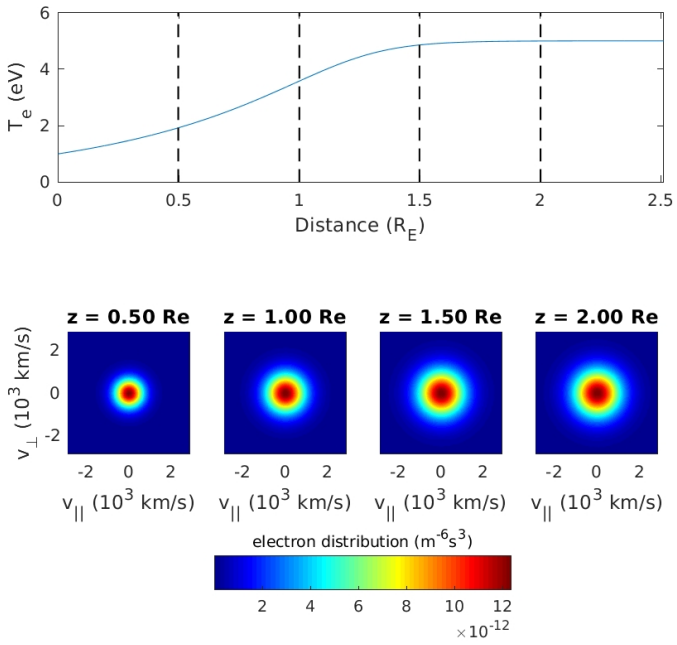

Figure 5.2: (top) Plasma temperature as a function of position. (bottom) Electron distribution at several locations.

Figure 5.2 shows in its top panel the electron temperature variation across the simulation domain; in the lower portion of the figure we have displayed, from left to right, the local electron distribution at locations $z = 0.5$, 1.0, 1.5 and 2.0 R_E, respectively. There is a clear correspondence between the temperature trend and the spread in velocity of the local distribution of electrons; while at $z = 0.5$ R_E most of the particles present low velocities, as it is expected for a low-temperature plasma, the local velocity distribution

at $z = 1.0\ R_E$ and $z = 1.5\ R_E$ spread out as there is an increase of temperature; There is no further visible change in the electron distribution at $z = 2.0\ R_E$, since there is no noticeable temperature variation for distances $z \geq 1.25\ R_E$.

Animations of the time evolution for density and the distribution function (not shown here) confirmed that the electron configuration remains stationary in the absence of Alfvénic perturbations. The electrostatic potential causes the plasma to remain in its stationary state.

5.3 Inhomogeneous Lorentzian plasma

Maxwellian statistics are widely used because they approximate well collisionless plasmas while allowing a rather straightforward mathematical treatment in MHD and kinetic theory. More realistic astrophysical plasmas, however, are more Maxwellian-like distributions with high-energy tails [Summers and Thorne, 1991; Pierrard and Lemaire, 1996] (and references therein). Lorentzian distributions are often useful to model such plasmas. Initially, this project was intended to be carried out using Maxwellian plasmas only. Unfortunately, implementation of these distributions often leads to numerical instability. There are reasons to believe that the sharp velocity gradient might partially cause such behavior in the distribution grid at low temperatures. Eventually, these numerical issues forced us to also implement Lorentzian distributions in this code, since they have been proven to be more numerically stable than Maxwellian distributions [Watt and Rankin, 2007a, 2010].

5.3.1 Basic properties of the Lorentzian distribution

Lorentzian distributions have the form:

$$f_\kappa(v) = A_\kappa \left(1 + \frac{v^2}{\kappa v_\kappa^2}\right)^{-(\kappa+1)} . \tag{5.12}$$

The normalization constant A_κ is found through integration of the lowest moment that leads to the density

$$n_\kappa = 4\pi A_\kappa \int_0^\infty dv\, v^2 \left(1 + \frac{v^2}{\kappa v_\kappa^2}\right)^{-(\kappa+1)} . \tag{5.13}$$

Notice that integration is performed in spherical coordinates, and that the distribution

is assumed isotropic. It is convenient to introduce a new variable,

$$x = \left(1 + \frac{v^2}{\kappa v_\kappa^2}\right)^{-1}, \qquad dx = -\frac{2vdv}{\kappa v_\kappa^2}\left(1 + \frac{v^2}{\kappa v_\kappa^2}\right)^{-2}, \tag{5.14}$$

in terms of which, equation (5.13) turns into

$$n_\kappa = 2\pi A_\kappa (\kappa v_\kappa^2)^{3/2} \int_0^1 dx\, \sqrt{x-1} x^{\kappa - 3/2}. \tag{5.15}$$

The resulting integral has the form of a β function:

$$\beta(p+1, q+1) = \int_0^1 dx\, x^p (1-x)^q, \tag{5.16}$$

with solution given by

$$\beta(a,b) = \frac{\Gamma(a)\Gamma(b)}{\Gamma(a+b)}, \tag{5.17}$$

where $\Gamma(x)$ is the Gamma function. The density integral turns into:

$$n_\kappa = 2\pi A_\kappa (\kappa v_\kappa^2)^{3/2} \frac{\Gamma(\kappa - 1/2)\Gamma(3/2)}{\Gamma(\kappa+1)}. \tag{5.18}$$

Substituting $\Gamma(3/2) = \sqrt{\pi}/2$, and solving for A_κ we find

$$A_\kappa = \frac{n_\kappa}{(\pi\kappa v_\kappa^2)^{3/2}} \frac{\Gamma(\kappa+1)}{\Gamma(\kappa - 1/2)}, \tag{5.19}$$

so the explicit form of the Lorentzian distribution is:

$$f_\kappa(v) = \frac{n_\kappa}{(\pi\kappa v_\kappa^2)^{3/2}} \frac{\Gamma(\kappa+1)}{\Gamma(\kappa - 1/2)} \left(1 + \frac{v^2}{\kappa v_\kappa^2}\right)^{-(\kappa+1)}. \tag{5.20}$$

Next, let's calculate the kinetic pressure. Since we assume the plasma to be isotropic, there is no need to calculate the pressure tensor. Instead, notice that

$$\begin{aligned} p &= \frac{1}{3}\int d^3v\, m v^2 f_\kappa(v) \\ &= \frac{4\pi m}{3} A_\kappa \int_0^\infty dv\, v^4 \left(1 + \frac{v^2}{\kappa v_\kappa^2}\right)^{-(\kappa+1)}. \end{aligned} \tag{5.21}$$

This integral can be solved following a similar treatment as the integration for the density.

Performing the change of variable (5.14), one eventually reaches the expression,

$$p = \frac{2\pi m}{3} A_\kappa (\kappa v_\kappa^2)^{5/2} \frac{\Gamma(\kappa - 3/2)\Gamma(5/2)}{\Gamma(\kappa + 1)}. \tag{5.22}$$

By substitution of A_κ from (5.19), and by using the property $\Gamma(x) = (x-1)\Gamma(x-1)$, one obtains

$$p = \frac{n_\kappa m \kappa v_\kappa^2}{2\kappa - 3}. \tag{5.23}$$

If we assume that the equation of state of the plasma follows the ideal gas approximation, $p = nT$, then the *thermal velocity* of the Lorentzian plasma is found to be

$$v_\kappa = \sqrt{\frac{2T}{m} \frac{\kappa - 3/2}{\kappa}}. \tag{5.24}$$

At this point, it is worth noticing that the velocity distribution (5.20) as a probability function is required to remain finite (as well as positive and real), this condition restricts the range of meaningful kappa values to $\kappa > 1/2$. Moreover, defining a real *thermal speed* that characterizes the average energy requires $\kappa > 3/2$. Higher moments of the distribution will impose more restrictive conditions [Treumann, 1999]. For a given temperature, the Lorentzian thermal velocity, and therefore its mean energy, is lower than the Maxwellian counterpart at the same temperature. As $\kappa \to \infty$, $v_\kappa \to \sqrt{2T/m}$.

5.3.2 Lorentzian plasma in the presence of an external potential

The stationary state under the influence of an external potential $\phi_e(r)$ is obtained by introducing the potential energy term in the energy distribution; this leads to the form:

$$f_\kappa(r, v) = A_\kappa \left(1 + \frac{1/2mv^2 - \phi_e(r)}{\kappa T_\kappa}\right)^{-(\kappa+1)}, \tag{5.25}$$

where $T_\kappa = (\kappa - 3/2)T/\kappa = 1/2mv_\kappa^2$. The expressions for density and kinetic pressure can be obtained using the same procedure discussed in the previous section. First of all, define the following quantity:

$$x(r) = 1 - \frac{\phi_e(r)}{\kappa T_\kappa}, \tag{5.26}$$

so we can write (5.25) in a form that resembles (5.12):

$$f_\kappa(v, r) = \frac{A_\kappa}{x(r)^{\kappa+1}} \left(1 + \frac{v^2}{\kappa v_\kappa^2 x(r)}\right)^{-(\kappa+1)}. \tag{5.27}$$

The previous expression is integrable as long as $x(r) > 0$, and integration is carried on using the same approach used for the case of no potential. Following that procedure, one obtains for the density

$$n(r) = n_0 \left(1 - \frac{\phi_e(r)}{\kappa T_\kappa}\right)^{1/2-\kappa}, \tag{5.28}$$

while the kinetic pressure yields

$$p(r) = \frac{n_0 m \kappa v_\kappa^2}{2\kappa - 3} \left(1 - \frac{\phi_e(r)}{\kappa T_\kappa}\right)^{3/2-\kappa}. \tag{5.29}$$

Again, assuming the plasma behaves like an ideal gas, so that $p(r) = n(r)T(r)$, one obtains for the temperature

$$T(r) = T_0 \left(1 - \frac{\phi_e(r)}{\kappa T_\kappa}\right), \tag{5.30}$$

where n_0 and T_0 represent the density and temperature at the point of zero potential; typically and just out of convenience, we arbitrarily choose it to be the upper boundary of the simulation. One should notice that, as opposed to the Maxwellian case, the Lorentzian formulation establishes the temperature to be explicitly dependent on the potential.

5.3.3 Solution to the dispersion equation for Lorentzian plasma

If one intends to use Lorentzian distributions, it must be able to obtain wave solutions for the corresponding dispersion equation. As we did previously for the Maxwellian case, we want to derive the dispersion equation that is consistent with the physics on which the numerical algorithm is grounded. First, we find the parallel current by integrating the perturbation (2.104) into (2.94). In order to save a few steps in this derivation, we use the one-dimensional form of the distribution

$$f_{\kappa 0}(v) = \frac{n}{\sqrt{\pi} v_\kappa} \frac{\Gamma(\kappa+1)}{\kappa^{3/2}\Gamma(\kappa-1/2)} \left(1 + \frac{v^2}{\kappa v_\kappa^2}\right)^{-\kappa}. \tag{5.31}$$

The perturbation $f_{\kappa 1}$ due to the wave is given by (2.104), which once obtained is to be integrated as indicated. For simplicity, from here onwards we write v instead of $v_\parallel$. Then we have

$$j_\parallel = -\frac{2iE_\parallel}{\mu_0 \sqrt{\pi} k_\parallel v_\kappa^2 \lambda_e^2} \frac{\Gamma(\kappa+1)}{\kappa^{3/2}\Gamma(\kappa-1/2)} \int_{-\infty}^{\infty} dv \, \frac{v^2}{v - \omega/k_\parallel} \left(1 + \frac{v^2}{\kappa v_\kappa^2}\right)^{-(\kappa+1)}. \tag{5.32}$$

Note that we can write $v^2/(v-a) = v + a + a^2/(v-a)$. This substitution results in thee integrals, the first of which is zero since it is an odd integral. At this point is convenient to introduce a change of variable $s = v/v_\kappa$, and define $\xi = \omega/(k_\parallel v_\kappa)$. We get the expression

$$j_\parallel = -\frac{2iE_\parallel}{\mu_0\sqrt{\pi}k_\parallel v_\kappa \lambda_e^2}\frac{\Gamma(\kappa+1)}{\kappa^{3/2}\Gamma(\kappa-1/2)} \left[\xi\int_{-\infty}^{\infty}\frac{ds}{(1+s^2/\kappa)^{(\kappa+1)}} + \xi^2\int_{-\infty}^{\infty}\frac{ds}{(s-\xi)(1+s^2/\kappa)^{(\kappa+1)}}\right]. \quad (5.33)$$

The first integral can be expressed in term of hypergeometric functions [Mace and Hellberg, 1995]. In the simulations presented here, however, we stick to integer values of kappa, for which we can use the following relation [Gradshteyn and Ryzhic, 2000]

$$\int_{-\infty}^{\infty}\frac{dx}{(ax^2+bx+c)^n} = \frac{(2n-3)!!\pi a^{n-1}}{(2n-2)!!(ac-b)^{n-1/2}}, \quad (5.34)$$

with $a = 1/\kappa$, $b = 0$, $c = 1$, $n = \kappa + 1$. This lead us to

$$\int_{-\infty}^{\infty}\frac{ds}{(1+s^2/\kappa)^{(\kappa+1)}} = \frac{(2\kappa-1)!!\pi\sqrt{\kappa}}{(2\kappa)!!} \quad (5.35)$$

The double factorial in the numerator is equal to $2^\kappa\Gamma(\kappa+1/2)/\sqrt{\pi}$. On the other hand, it is not difficult to see that $(2\kappa)!! = 2^\kappa\kappa! = 2^\kappa\Gamma(\kappa+1)$. The second integration in (5.33) has the form of the so called *modified plasma dispersion function* [Summers and Thorne, 1991]:

$$Z_\kappa(\xi) = \frac{1}{\sqrt{\pi}}\frac{\Gamma(\kappa+1)}{\kappa^{3/2}\Gamma(\kappa-1/2)}\int_{-\infty}^{\infty}\frac{ds}{(s-\xi)(1+s^2/\kappa)^{(\kappa+1)}}, \qquad \mathrm{Im}(\xi) > 1. \quad (5.36)$$

Making the necessary substitutions, and after a good deal of algebra, one finally gets

$$j_\parallel = -\frac{2iE_\parallel}{\mu_0\lambda_e^2 k_\parallel v_\kappa}\left[\xi\left(1-\frac{1}{2\kappa}\right) + \xi^2 Z_\kappa(\xi)\right]. \quad (5.37)$$

The rest of the derivation is very much like the Maxwellian case, and the reader can retrace the steps followed in section 2.4.3; it consists of substituting the current components (5.37) and (2.93) into (2.95), and expressing the result as the multiplication

of a matrix times the electric field vector. Eventually, one obtains

$$\begin{pmatrix} k_\perp^2 - 2\left(\frac{\xi}{\lambda_e}\right)^2\left[\left(1-\frac{1}{2\kappa}\right)+\xi Z_\kappa(\xi)\right] & -k_\parallel k_\perp \\ -k_\parallel k_\perp & k_\parallel^2 - \left(\frac{\omega}{v_A}\right)^2 \end{pmatrix} \cdot \begin{pmatrix} E_\parallel \\ E_\perp \end{pmatrix} = 0. \tag{5.38}$$

The determinant of the previous matrix equalized to zero gives the dispersion equation:

$$\left(\frac{\omega}{k_\parallel v_A}\right)^2 + 2\left(\frac{\xi}{k_\perp \lambda_e}\right)^2\left[1-\left(\frac{\omega}{k_\parallel v_A}\right)^2\right]\left[\left(1-\frac{1}{2\kappa}\right)+\xi Z_\kappa(\xi)\right] = 0. \tag{5.39}$$

Finally, notice that $\xi = [\omega/(k_\parallel v_A)]v_A/v_\kappa$. Making this substitution, and solving for $\omega/(k_\parallel v_A)$, we obtain the form

$$\left(\frac{\omega}{k_\parallel v_A}\right)^2 = 2 + \left(\frac{k_\perp \lambda_e v_\kappa}{v_A}\right)^2\left[\left(1-\frac{1}{2\kappa}\right)+\xi Z_\kappa(\xi)\right]^{-1}. \tag{5.40}$$

5.3.4 Electrostatic potential for an oxygen decaying Lorentzian atmosphere

We seek to set up a stationary Lorentzian in equilibrium, such that it self-consistently fits the plasma model, (equation 5.1). One can, as in section 5.2.1, consider a mixture of *cold* and *warm* plasma species, which are to reproduce the density model (5.1), while consistently yielding the predefined boundary temperatures T_w and T_c. By following this approach, however, one eventually realizes that the natural dependency of temperature with the potential prevents finding a consistent solution for the potential.

One can always simply find the potential that follows the explicit density and temperature variations given in equations (5.28) and (5.30). We need an expression for the electrostatic force due to the potential, $F_e(z) = -\nabla_z \phi_e(z)$. This force is found by calculating the parallel gradient on both sides of equation (5.28) and solving for $\nabla_z \phi_e(z)$, from which one obtains, in units of eV/m:

$$F_e(z) = \kappa T_\kappa \frac{\nabla_z n(z)}{n(z)}\left(1-\frac{\phi_e(z)}{\kappa T_\kappa}\right). \tag{5.41}$$

This formulation defines the temperature in terms of a unique parameter T_0; this might be less convenient than the Maxwellian formulation, which allowed us to set the boundary temperatures arbitrarily. Alternatively, one could enforce arbitrary values for the temperature at the boundaries by freeing the kappa parameter.

5.4 Electron acceleration by Inertial Alfvén Waves under inhomogeneous conditions

Next, we test the modifications introduced in the previous sections, by observing a case of wave propagation through the Ionospheric Alfvén Resonator (IAR). The IAR extends along magnetic field lines, from the topside ionosphere to the location where the Alfvén speed becomes maximum. In between these two points, the ionospheric oxygen decays sharply with altitude on scales that can be compared to the wavelength of incoming perturbations and, as a consequence, nonlinear effects become relevant. Particularly, the plasma conductivity $\Sigma_A = (\mu_0 v_A)^{-1}$ modifies the reflection coefficient so that incoming waves suffer partial trapping and reflection; natural modes of the IAR range from $0.1-1.0$ Hz [Lysak, 1991].

There have been previous attempts to describe electron acceleration under inhomogeneous conditions. In some models, inhomogeneity araises self-consistently from the adiabatic motion of particles inside a magnetic mirror configuration, subject to additional constraints, like quasineutrality [Chiu and Schulz, 1978] or charge separation according to Poisson equation [Pierrard and Lemaire, 1996]. In these cases, the resulting distribution imposes an electrostatic potential in space. These models have been useful to describe the main characteristics of inverted V structures. However, they cannot describe the existence and time evolution of transient fields often found in the auroral acceleration region [Louarn et al., 1994; Chaston et al., 2000; Stasiewicz et al., 2000; Andersson et al., 2002; Chaston et al., 2002a; Ergun et al., 2005], sometimes even in the presence of inverted V potentials [McFadden et al., 1987; Chaston et al., 2002b; Chen et al., 2005; Tanaka et al., 2005]. These features are better explained in terms of Alfvénic activity instead. Models grounded on Alfvén wave propagation rely mostly on dispersive effects due to short perpendicular scales to justify the existence of field-aligned electric fields in an otherwise highly conductive media [Hasegawa, 1976; Goertz and Boswell, 1979]. Since the dispersive properties depend on the background plasma, one can describe the time evolution of fields and currents once the spatial gradients in the plasma are provided; however, these models do not describe the self-consistent evolution of these due to particle acceleration. Nonetheless, their use in conjunction with test particles has reproduced many dispersive features frequently observed. Thompson and Lysak [1996] used a test particle approach based on this idea, but also including a procedure to enforce energy conservation. This study suggested Landau resonance, and the presence of an anti-earthward electrostatic field, as primordial mechanisms for particle acceleration. Regarding wave propagation, it showed that resonant harmonics are favored within the

IAR, and that partial reflection takes place off the density gradient. The model also reproduced electron conics, but only with the addition of a large electrostatic field across the simulation domain.

Su et al. [2004] implemented a linear gyrofluid solver to evaluate wave propagation under conditions typical of the dayside auroral region. Their model considered the motion of oxygen and hydrogen ions and electrons in a dipolar geomagnetic field, and subject to given initial spatial profiles describing the plasmas composition and temperature. According to their model, the formation of structures associated with electron resonance was subjected to a rather large ionospheric oxygen component extending over $\sim 3\,R_E$ altitude. The high density in oxygen effectively decreases the phase speed of the wave to closer values relative to the thermal speed of the cold plasma, thereby allowing for higher levels of Landau and Fermi resonances. This condition is, however, in disagreement with the general notion of plasma composition in the topside ionosphere, which estimates the scale of oxygen decay rate well below $1\,R_E$. Even though the study demonstrated the effect of increased oxygen levels in the dayside region, their assumption draws important implications regarding other properties of the plasma that also affect wave propagation, and should have been further justified. Incidentally, Chaston et al. [2000] were able to reproduce Suprathermal Electron Bursts (STEB) using the same scheme as in Thompson and Lysak [1996], using parameters retrieved from the FAST spacecraft while over the dayside oval; in this case, the oxygen density decayed over a distance $\sim 1/3\,R_E$.

Using a somewhat different approximation based on charge and current neutrality valid for the inertial regime exclusively, Kletzing and Hu [2001] identified dispersed electron signatures similar to rocket measurements as a result of wave propagation under nonuniform conditions. Instead of using test particles, in this case, the distribution function for a given observation time is constructed by backtracking the phase space in time, one velocity at a time, using the time evolution of the electric field. Assuming a given solution of the equilibrium distribution, it is possible to map its time evolution following Liouville's theorem. More recently, Shi et al. [2013] introduced a partially kinetic formulation based on the DK1D to simulate the movement of hot electrons, complemented with a linear fluid approximation in charge of cold particles. This model revealed various aspects of wave propagation under inhomogeneous conditions. The numerical algorithm used here is different from the one presented by Shi et al. [2013] in that the whole plasma is treated kinetically.

5.4.1 Test simulation: Wave-plasma interaction in the Ionospheric Alfvén resonator

Simulation parameters for this case were set to similar values as in Shi et al. [2013], for comparison purposes. These are summarized in table 5.2. The wave consists of a Gaussian pulse with amplitude $\phi_0 = 100$ V and $f = 5$ Hz.

Table 5.2: Input parameters for simulation of plasma under inhomogeneous conditions.

altitude domain (km)	$0 \leq z \leq 2 \times 10^4$
magnetic field line	$L = 9$
perpendicular scale at the ionosphere (km)	$\lambda_I = 1.57$
background hydrogen density (cm^{-3})	$n_{H_2} = 8$
background oxygen density (cm^{-3})	$n_{O_2} = 2.5 \times 10^5$
oxygen decay scale (R_E)	$z_0 = 0.07$
warm plasma temperature (eV)	$T_w = 50$

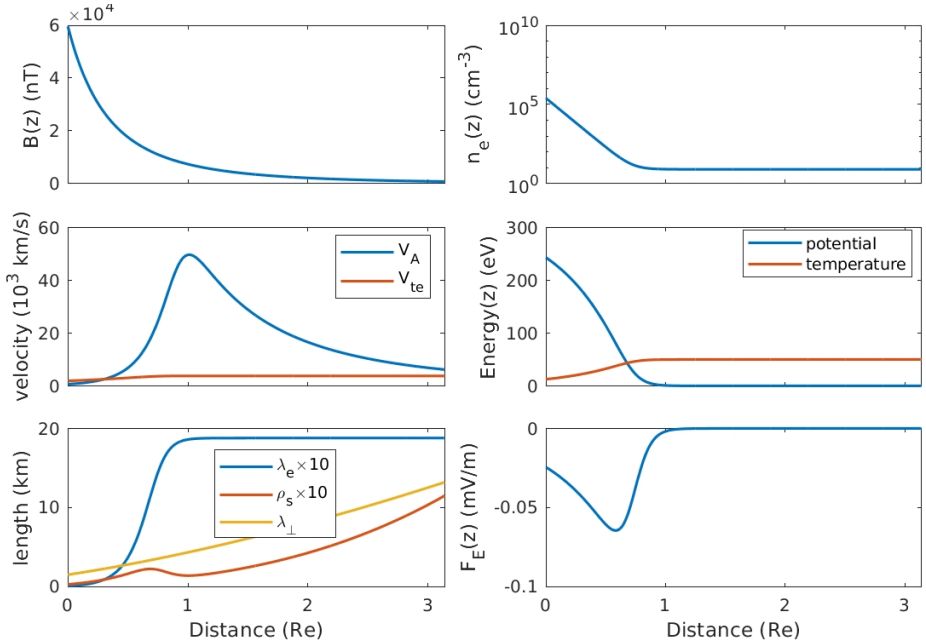

Figure 5.3: Spatial variation of macroscopic parameters: magnetic field (top left); electron density (top right); Alfvén and thermal speed (middle left); average kinetic energy/temperature and potential energy due to the electrostatic potential (middle right); the perpendicular scale, the ion gyroradius, and the skin depth (bottom left); the force due to the electrostatic potential (bottom right).

Figure 5.3 presents the spatial variation for the resulting macroscopic properties. Profiles for the magnetic intensity and plasma density correspond to equations (2.39)

and (5.1), respectively. Other profiles depend on the stationary electrostatic potential, which has been plotted in the middle right, together with the temperature profile. This potential is naturally constant in the region of constant density; its variation at low altitudes provides an electrostatic force (bottom-right) whose effect is to balance the magnetic gradient and the pressure gradient. Spatial variation of the Alfvén speed (left-middle panel) presents a sharp increase due to the exponential drop of ionospheric oxygen until it reaches its maximum at $\sim 1\,R_E$; for higher altitudes, it decreases gradually due to the variation in magnetic intensity. Notice that $v_{th} < v_A$ across the simulation domain, so inertial conditions dominate everywhere.

Figure 5.4 shows the wave field intensities (top 3 panels), plus the parallel current and energy flux (bottom two panels). The fourth panel shows the Alfvén speed profile, and the corresponding Alfvénic conductivity $\Sigma_A = (\mu_0 V_A)^{-1}$. The wave advances from the lower-right corner, moving towards lower altitudes as time increases. The speed of the wave is inferred as inversely proportional to each of the fields trace inclination. It can be seen that the pulse travels faster in the region $0.7 \leq z \leq 2.0$ Re and moves slower at low altitudes where v_A drops due to the drastic increase of oxygen. A bifurcation can be appreciated in all the fields at $z \simeq 1.25\,R_E$ and $t \simeq 1.75$ s, indicating the partial reflection of the wave off of the sharp gradient in density at that location. The reflected wave is such that its perpendicular electric (magnetic) field has opposite (the same) polarization as the incident wave. The reflected component of the electric field is positive; therefore, it produces upward electron acceleration.

The parallel electric field starts as a bipolar structure, its leading section is positive and produces downward electron acceleration. In the $E_\parallel$ graph there is a signature that remains close to the upward boundary during practically the whole simulation; this is considered a numerical artifact maybe as a result of imperfect coupling between wave and plasma due to the boundary conditions. As per the actual electric field, it undergoes considerable damping during the first 0.5 s into the simulation; its amplitude increases again shortly after due to nonlinear steepening of the leading section of the wave as described in Watt et al. [2005]. The thickness of the red trace becomes much narrower than the blue trace, an indication of steepening occurring in the positive section. Once it enters the IAR region ($z < 1\,R_E$), the electric field decreases rapidly. It can be argued, that due to the increased availability of cold electrons originated from the ionization of ionospheric oxygen in this region, the parallel electric field is effectively short-circuited, and these cold electrons become carriers of the current that supports the wave. Notice that at low altitudes the current seems to adopt a dipolar configuration. According to Shi et al. [2013], the displacement caused by currents carrying the wave induces a current in the opposite sense to restore charge balance. Although in their publication the total

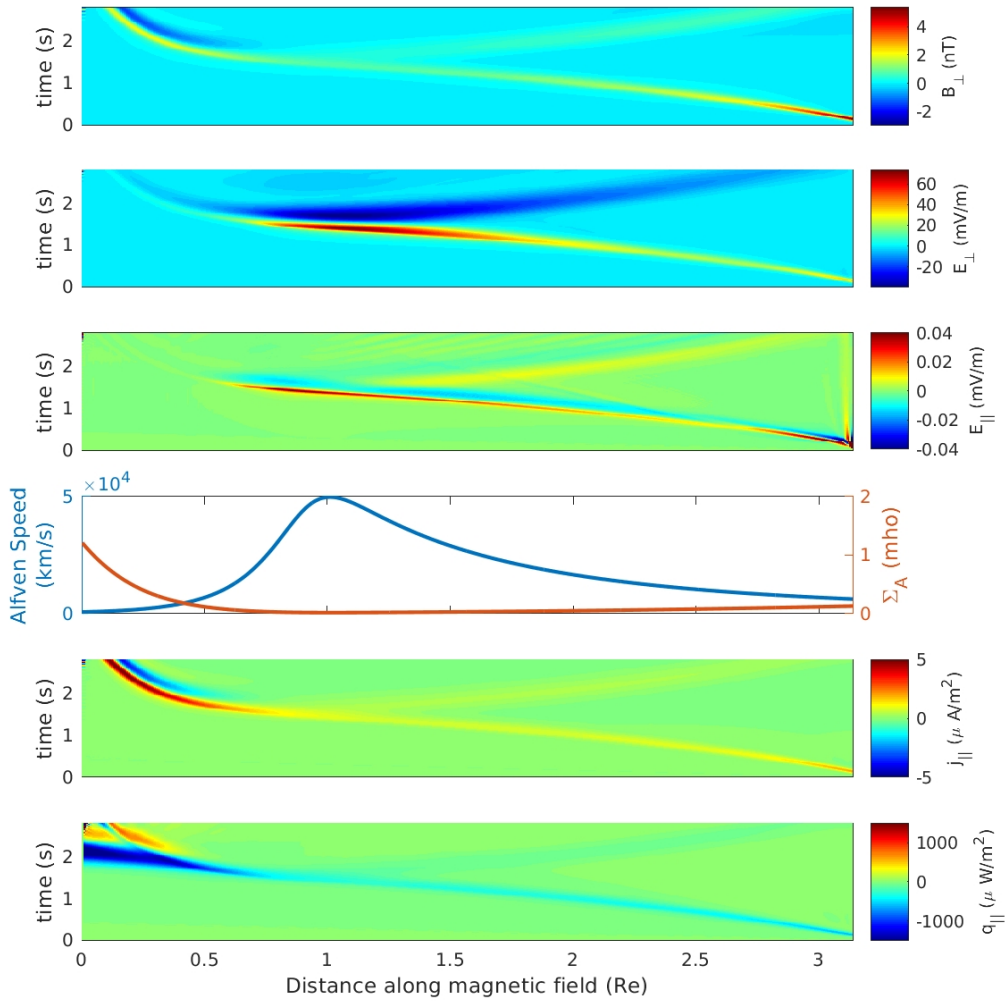

Figure 5.4: Wave propagation as a function of time and altitude. From top to bottom panels: $B_\perp$, $E_\perp$, $E_\parallel$, the Alfvén speed profile, parallel current and parallel energy flux.

current was zero because both currents seemed to cancel each other, the dipolar nature of the current at low altitudes is consistent with this interpretation.

Figure 5.5 shows a time sequence of the total differential flux as a function of position and parallel speed. Downward (upward) flux corresponds to negative (positive) velocities. We have normalized this quantity to the initial density at every location in order to decrease the intensity at low altitudes, so that the color scale in the figure can capture better flux variation. The corresponding profiles of $E_\parallel(z)$ and $j_\parallel(z)$ are shown at the

bottom. Differential flux snapshots show locally increased (decreased) levels of downward (upward) flux at all times. The direction of wave propagation determines this asymmetry. The electron's bahavior due to the interaction is described in appendix A; basically, the electric field induces downward motion on its leading section and upward motion on its trailing side. In the wave frame of reference, counterstreaming electrons are decelerated which causes particles to remain under the wave for a longer time span than they would have in the case of no wave, therefore causing the accumulation of particles *traveling with the wave*. A fraction of these trapped electrons were initially moving upward in the absolute frame of reference, which explains the local decrease in upward flux at $t = 1.2$ s, $z = 1.5\,R_E$.

Downward acceleration comes in two flavors: resonant and nonresonant. The former refers to electrons that, in the wave frame of reference, have initial kinetic energy just under the amount needed to overcome the potential. Resonant particles appear as the sharp trace at larger (negative) speeds. The nonresonant population is manifested as an enhancement of downward ($v < 0$) differential flux (see equation 4.7 on page 82) covering a broader spectrum of lower energies. On the trailing side of the pulse, downward moving electrons that catch up with the wave, but cannot overcome the potential, are also reflected and can potentially form upward beams if the conditions are appropriate. However, due to the relative speed of the wave, in the absolute frame of reference these beams fall in the thermal level, effectively contributing to plasma heating behind the wave.

Once the pulse advances from the Alfvén speed peak, its speed decreases drastically, causing many nonresonant electrons to become resonant and form low energy beams. A secondary beam can be seen at $z \sim 0.6$ Re and after $t = 1.7$ s. Large energy transfer is also expected in this region due to increased levels of Landau resonance [Shi et al., 2013]. In the same region, and from 1.7 s onwards, an important increase of upward flux takes place and extends towards higher altitudes. Note that these particles move behind the reflected wave, so they cannot be accelerated by it. Instead, the rapid decrease of v_A suppresses the source of downward impulse, and most of them are reflected by the mirror force.

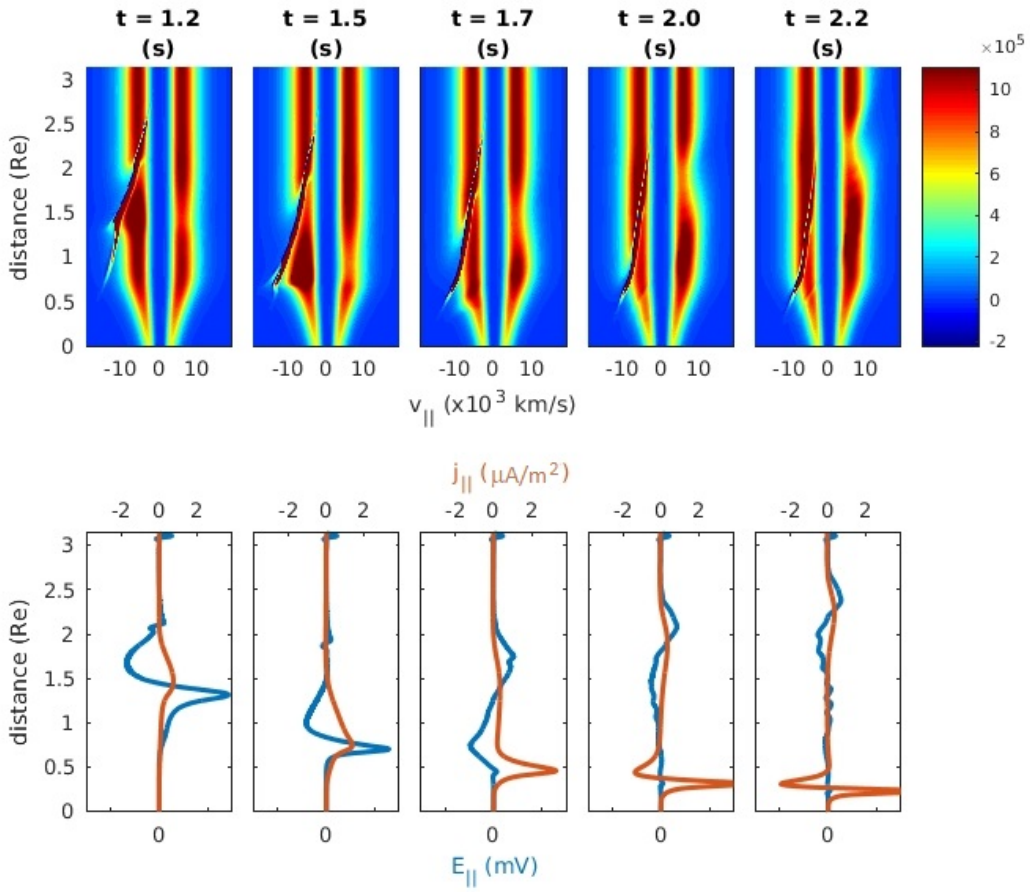

Figure 5.5: Time evolution of differential flux (top), and $E_{||}(z)$ and $j_{||}(z)$ (bottom) as a function of velocity and position.

5.5 Summary

In this chapter, the formulation of an extended version of the DK1D code [Watt et al., 2004] is introduced. This modified algorithm incorporates an spatially inhomogeneous plasma density model constituted by a mixture of magnetospheric hydrogen and ionospheric single-ionized oxygen, the last of which decreases exponentially with altitude. The distribution function in its stationary state is made consistent with the plasma density by defining a time-independent electrostatic potential across the spatial domain [Tikhonchuk and Rankin, 2002]. The altitude dependence of the magnetic field and the plasma density results in a sharp increase of the Alfvén speed followed by a gradual decline at higher altitudes. The code supports both Maxwellian and Lorentzian distributions.

A simulation intended to observe the time evolution of wave-plasma interaction in the magnetosphere-ionosphere transition region was also presented. It was found that the wave suffered partial reflection around the location where the Alfvén speed takes its maximum value. Both incident and reflected waves induce electron acceleration in their respective directions of propagation as a result of wave-particle Fermi interactions. Similar behavior has been previously reported in Chaston et al. [2002a]; Shi et al. [2013]. On the other hand, a fraction of the original pulse is transmitted into the topside ionosphere, where its phase speed decreases considerably due to the large density of ionospheric electrons. Furthermore, these cold electrons become carriers of the current required to support the wave, effectively suppressing the field-aligned component of the wave electric field. With the strong attenuation of $E_{\parallel}$ at altitudes just below the point of maximum v_A, previously accelerated electrons traveling with the wave suddenly lose their source of downward impulse, and are shortly after reflected by the magnetic mirror force. The lack of these electrons within the IAR should lead to weak intensity horseshoe distributions that are the subject of chapter 7.

Chapter 6

Electron trapping by Kinetic Alfvén Waves in the inner magnetosphere

Up until now, we have addressed processes for which the underlying physical mechanism involves Fermi-like interactions between Inertial (IAW) or Kinetic Alfvén Waves (KAW) and magnetospheric electrons. Basically, the perturbation is considered as a moving potential wall against which low energy electrons (in the reference frame of the wave) bounce off elastically. This effect requires the potential to be negative relative to the background plasma. A positive potential, on the other hand, constitutes a potential well, where low energy electrons can become trapped and unable to escape until they can overcome the wave potential, whether through some form of energy gain or if the wave undergoes damping.

The dynamics of trapped particles is inherently nonlinear. In fact, the linear stage of the interaction derives into the well-documented picture of Landau damping. It is mostly the trapped electrons who modify the distribution and ultimately cause wave damping or growth, depending on the sign of $\partial f_0(v)/\partial v$ at $v \simeq \omega/k$. During this stage, the induced density perturbation grows linearly in time, eventually breaking down the linear approximation. By the time this happens, slightly slower and faster electrons have been speeded up and slowed down, respectively. Altogether, the distribution of resonant electrons has formed a plateau within some range of velocities $\omega/k \pm v_{tr}$, effectively halting further damping since under the new configuration $\partial f/\partial v \simeq 0$ in the neighborhood of the wave phase velocity.

Nonlinear trapping has been found to occur in the parallel potential of inertial and

kinetic scale Alfvén waves. Using a self-consistent numerical code, Rankin et al. [2007] explained how Landau damping of standing Alfvén waves is suppressed by warm plasma effects at altitudes within the kinetic regime. Wave dispersion of these standing modes can induce parallel electric fields, where trapping can develop if Landau damping is low. It was demonstrated that a decrease of the perpendicular scale favors electron trapping by increasing v_{tr}, even in cold plasma where the little number of resonant electrons limits the trapping process. In the kinetic regime, higher temperatures enhance trapping due to the increase in $E_\parallel$. Electron trapping on standing waves effectively dissipates wave energy through damping. On traveling shear Alfvén pulses, on the other hand, trapping has been shown to suppress Landau damping [Watt and Rankin, 2009], enabling these waves to survive longer during their propagation from high to low altitudes. At lower altitudes where inertial conditions become dominant, these waves are heavily damped, and electrons escape forming beams of energy up to a keV or so.

Recently, Artemyev et al. [2015b] investigated trapping by KAW of electrons with energies up to $\sim$ 100 eV at equatorial latitudes, using a theoretical model of trapping into an effective potential generated by the scalar and vector potentials parallel to geomagnetic field lines. This model described wave dispersion in the kinetic limit ($\omega = k_\parallel v_A \sqrt{1 + (k_\perp \rho_s)^2 (1 + T_i/T_e)}$), although nonlinear effects were ignored. Particle motion is driven by the effective potential and the mirror force of an external geomagnetic field. Simulation of particle trajectories showed that trapped electrons undergo many bounces in the effective potential of the wave; at each bounce, the trapped particle must gain enough parallel momentum to keep up with the increasing speed of the wave, while the mirror force transfers some of that gain into faster gyromotion. The electric field decreases as the wave moves to regions of cold plasma. By the time the mirror force becomes stronger than the wave electric field force, the electron has increased its energy in several 100 eV, and undergo a considerable decrease in its equatorial pitch angle.

The content of this chapter is arranged as follows: section 6.1 is devoted to providing a basic notion on the nonlinear dynamics of trapped particles for the case of an electrostatic wave in a uniform plasma. Section 6.2 reviews the theory for propagation of KAW into a locally dispersive medium; this formulation goes beyond O'Neil theory in that it accounts for inductive effects. Then, in section 6.3, we present results of Vlasov simulations of kinetic scale Alfvén waves that show evidence of nonlinear trapping, discuss conditions under which trapping is important, and compare these results against the predictions made by the model presented in section 6.2.

6.1 The dynamics of trapped distributions

As a starting point, let us consider an electrostatic wave:

$$\phi(x,t) = \phi_0 \cos(kx - \omega t) \tag{6.1}$$

$$E(x,t) = -\nabla\phi(x,t) = E_0 \sin(kx - \omega t), \qquad E_0 = k_\perp \phi_0 \tag{6.2}$$

propagating in the $\hat{x}$ direction within a uniform, demagnetized (or magnetized parallel to the wave vector), and initially undisturbed plasma. In the frame of reference moving with the wave, $x \to x - \omega/kt$, the motion equation for the particles is

$$m_e \frac{d^2x}{dt^2} = eE_0 \sin(kx). \tag{6.3}$$

Notice that, for small amplitude oscillations, $\sin(kx) \sim kx$, and equation (6.3) predicts harmonic motion with frequency

$$\omega_b = \sqrt{\frac{ekE_0}{m_e}}. \tag{6.4}$$

Solutions for larger amplitude orbits are not so trivial [O'Neil, 1965]. Time integration of (6.3) leads to

$$W_e = \frac{1}{2} m_e v^2 - e\phi_0 \cos(kx), \tag{6.5}$$

where W_e is a constant representing the electron energy in the wave frame of reference.

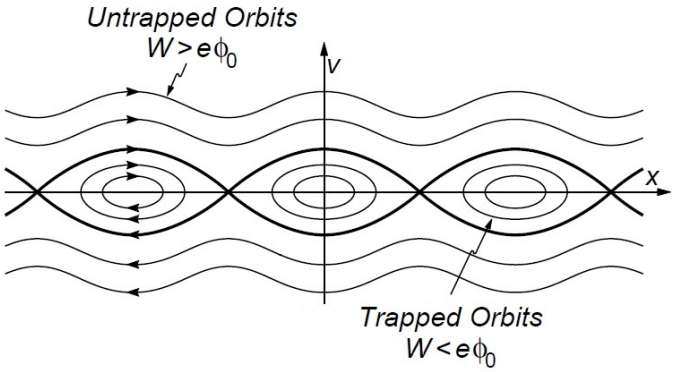

Figure 6.1: Phase space trajectories of particles as seen in the wave frame. (From Treumann and Baumjohann [1997])

The contour lines shown in Figure 6.1 describe the phase space trajectories associated

with the motion (6.3). Each line corresponds to a different value of W_e in equation (6.5). Particles whose kinetic energy is larger than the wave potential will *surf* over the crests, periodically increasing their speed momentarily, while particles for which the potential term dominates become trapped and forced into closed trajectories. An electron represented by the separatrix between trapped and untrapped electrons has total energy $W_e = 0$, and its top speed defines the interval of velocity v_{tr} over which particles are trapped:

$$v_{tr} = 2\sqrt{\frac{e\phi_0}{m_e}}. \tag{6.6}$$

Dawson [1961] investigated the Landau damping evolution during its linear stage, based on a physical model in which the main part of the plasma is considered separately from the resonant contribution. Their linearized system included the continuity and momentum equations, coupled with the Poisson equation with a source field of the form (6.2), and initial conditions $n_1(t = 0) = 0$ and $v_1(t = 0) = 0$. The kinetic energy of the particles was considered up to second order. It was determined that the density perturbation grows linearly with time; except close to the resonance, where this perturbation grows like t^2; this defines a time frame that takes for the perturbation to become the same order as the background density,

$$t_l = \sqrt{\frac{m_e}{eE_0k}}, \tag{6.7}$$

after which the linear approximation breaks down. The first order solutions were used to estimate the energy of resonant electrons and demonstrated that, as time progresses, most of the absorption is concentrated in the resonant electrons. If the wave has not damped away by the time when only the trapped particles interchange energy with the wave, then trapping becomes dominant, the trapped electrons cannot absorb any more energy, and Landau damping gives way to an asymptotic equilibrium.

The exact behavior of the distribution under nonlinear conditions was later derived in O'Neil [1965]. Analogous to Dawson [1961], the resonant and nonresonant components of the distribution were treated separately. He obtained exact solutions of the Vlasov equation for the resonant electrons in terms of elliptic functions. He also calculated the generalized damping rate and demonstrated that it reduces to the Landau result for $t/t_l \ll 1$. For cases where $t/t_l \simeq 1$, the damping coefficient becomes oscillatory; it was argued that this behavior is caused by the trapped electrons at the bottom of the potential well, which carry their density coherently with them as they oscillate. Trapped electrons doing larger amplitude oscillations, on the other hand, tend to thermalize as

a consequence of phase mixing. As $t/t_l \to \infty$, even the most resonant electrons lose coherence, and the damping coefficient eventually becomes zero.

Putting aside the complex inner physics of Landau damping and particle trapping, it should be clear that both processes compete to drive the motion of resonant particles. Nonlinear trapping can be neglected only under the condition [Treumann and Baumjohann, 1997]

$$\omega_b \ll \gamma_L, \tag{6.8}$$

where γ_L is the Landau damping coefficient.

The concepts exposed so far are strictly valid for monochromatic or nearly monochromatic waves. If the wave packet is constituted by several wave modes, each component will attempt to induce their own trapping domain. The nonlinear overlap between different resonances prevents the formation of trapping islands, and favors stochastic motion instead. In this scenario, Landau damping can continue indefinitely. Furthermore, stochastic motion leads to plasma heating [Karney, 1978].

6.2 A model for electron trapping by KAW based on linear dispersion

The occurrence of particle trapping within the kinetic regime makes a compelling case: due to the condition $v_{th} > v_A \sim \omega/k$, one can infer that the resonant electrons could potentially fall in the subthermal section of the distribution where Landau damping is not optimal. In this scenario, nonlinear trapping could take place, provided that most of the spectral power of the wave belongs to a single frequency.

There is available literature on the dynamics of trapped particles in electromagnetic waves, the bulk of which takes advantage of the Hamiltonian formulation (I found the presentation in Shklyar and Matsumoto [2009] particularly enlightening). In this section we deviate from this formalism in favor of a simpler model [Artemyev et al., 2015b] (see appendix C) of magnetospheric plasma embedded in a dipolar magnetic field $B(z, L)$ (2.39) that considers linear dispersion. This analysis disregards the effect of the electric field transverse component, as well as the drifting of particles due to the magnetic field curvature; and considers strongly magnetized electrons, such that their magnetic moment μ is a constant of motion. The wave equation (3.15), for the case of high-frequency waves, reads

$$\frac{\partial \phi}{\partial t} + v_A^2 \frac{\partial A}{\partial z} = 0. \tag{6.9}$$

We consider a wave input $\phi = \phi_0 \cos(\psi)$, with phase $\psi = \int dz'\, k_\parallel(z') - \omega t$. A solution for the wave vector potential that satisfies equation (6.9) is $A = (\omega/k_\parallel)\phi/v_A^2$. Dispersion of the original wave pulse generates the parallel electric field

$$\begin{aligned} E_\parallel &= -\frac{\partial \phi}{\partial z} - \frac{\partial A}{\partial t} \\ &= -k_\parallel \left[1 - \left(\frac{\omega}{k_\parallel v_A} \right)^2 \right] \phi \\ &= k_\parallel (k_\perp \rho_s)^2 \phi, \end{aligned} \tag{6.10}$$

where we have substituted in the kinetic limit of the dispersion equation (2.111). Notice that, to first order, $E_\parallel = -\nabla\Phi$, where $\Phi = [1 - (v_w/v_A)^2]\phi$ is an effective potential. The forces that determine the particle trajectory are the mirror force (see equation 2.28 on page 24) and the electric force due to the wave:

$$m\frac{dv}{dt} = -\mu \nabla_z B(z) - eE_\parallel(z,t). \tag{6.11}$$

In the absence of waves, electrons bounce between mirror points, and their gyroaveraged trajectories can be uniquely parameterized by their total energy h and equatorial pitch angle $\alpha_{eq,0}$. On the other hand, a KAW will gradually increase its speed as it travels down the field line. Trapping occurs at a certain location z_r where the wave catches up with an electron that has resonant speed $v_r = v_w(z_r) = \omega/k_\parallel(z_r)$. The likelihood of trapping decreases with latitude since (i) the wave phase speed moves gradually towards the tail of the distribution where there are fewer electrons available for resonance, and (ii) the parallel electric field decreases in amplitude as it moves into colder plasma. The resonant position $z_r(h, \alpha_{eq,0})$ at which a given electron could get trapped is obtained through the condition

$$h = \frac{1}{2} m v_r^2 + h \sin^2(\alpha_{eq,0}) B(z_r). \tag{6.12}$$

Once the particle is under the domain of the wave, its energy will depend on the effective potential. The particle motion consists of a superposition of transport at speed $v_w(z)$, plus fast longitudinal oscillations inside the effective potential. Trapped electrons must increase their parallel momentum in order to keep up with the wave, while simultaneously the mirror force transfers some of this gain into their perpendicular gyromotion. As the wave moves deeper into the geomagnetic field, the magnetic force becomes stronger. At some point z_e, the mirror force overcomes the parallel electric field, and the particle is forced out of the potential. Thus, the escape point is obtained

through the following condition

$$h \sin^2 \alpha_{eq,0} \nabla_z B(z_e) = e \max(E_{\parallel}(z_e)). \tag{6.13}$$

Once an electron escapes, its subsequent motion consists of periodic bouncing between new mirror points, now located at higher latitudes as a consequence of their increased energy. The following relation gives the location of the mirror point z_m:

$$\frac{1}{2} m_e v_w(z_e)^2 + h \sin^2 \alpha_{eq,0} B(z_e) = h \sin^2 \alpha_{eq,0} B(z_m) = H, \tag{6.14}$$

where H is the particle's total energy after escaping the wave. The equatorial pitch angle for the new trajectory is given by the invariance of the magnetic moment, leading to

$$\sin \alpha_{eq} = \sqrt{\frac{B_{eq}}{B(z_m)}}. \tag{6.15}$$

Artemyev et al. [2015b] set up and solved 10^4 trajectories of particles initially distributed uniformly in space and pitch angle, upon interaction with a wave of given amplitude. Once the wave reached latitude $\lambda = 45^o$, the trapping probability was estimated as the ratio of particles for which $H > 1.5h$, to the total number of particles (see Figure C.5 in the appendix C). The dependence in ϕ_0 is expected since $v_{tr} \propto \sqrt{\phi_0}$ provides a larger fraction of the distribution interacting with the wave. For $\lambda_\perp = 650$ km, the probability of trapping maximizes for particles with initial energies $\sim 200 - 300$ eV, and drops for particles with higher energies since, as the total energy of an electron increases, a large pitch angle is required so that their parallel speed is low enough to fall in the interval of resonance. At lower transverse wavelengths, on the other hand, the wave phase speed increases, and electrons with most pitch angles can become resonant.

6.3 Simulation results

In this section, we present results of simulations that explore the formation of trapping islands after interaction of the plasma with a kinetic wave pulse, each simulation providing different conditions of temperature and perpendicular wavelength. All background plasma properties and their variation along the spatial domain were implemented following the guidelines discussed in chapter 4 for inhomogeneous plasma. Table 6.1 summarizes the parameters that are common to all cases; the spatial domain extends $\sim 6.3\, R_E$ along the magnetic field line that is $9\, R_E$ away from the Earth in its equatorial end.

Table 6.1: Initial parameters common to all simulations

Magnetic field line	$L = 9$
Altitude domain (km)	$10^4 \leq z \leq 5 \times 10^4$
Background hydrogen density (m^{-3})	$n_{H_2} = 10^6$
Background oxygen density (m^{-3})	$n_{O_2} = 10^{10}$
Scale factor of oxygen decrease (Re)	$z_0 = 0.2$
Wave frequency (s^{-1})	$f = 2$
Kappa	$\kappa = 8$

In the initial stage of every simulation an electromagnetic wave with scalar potential

$$\phi(t) = \phi_0 \sin(\omega t) \exp\left[-\left(\frac{t-3\tau}{2\tau}\right)^2\right] \tag{6.16}$$

is introduced at the equatorial end of the simulation domain and propagates to lower altitudes. In order to incorporate waves with identical energy input in all cases, we use the fact that $\mathbf{E}_\perp = -\nabla_\perp \phi$; by fixing $E_\perp$ to some arbitrary value, the initial scalar potential amplitudes will be constrained by a relation of the form $\phi_0/\lambda_{\perp I} = const.$

Table 6.2: Temperature, ionospheric perpendicular wavelength and initial wave amplitude for each case study. Estimation of the phase speed, trapping speed, Landau damping coefficient, and bounce frequency of trapped electrons at the wave input location.

Simulation	T_w (eV)	$\lambda_{\perp I}$ (km)	ϕ_0 (V)	v_w (km/s)	v_{tr} (km/s)	γ_L (s^{-1})	ω_b (s^{-1})
1	200	1	225	4380	12581	8.26	18.03
2	200	2	450	3260	17793	4.18	34.26
3	200	4	900	2330	25163	1.70	67.90
4	500	1	225	6740	12581	8.52	11.73
5	500	2	450	4790	17793	4.52	23.36
6	500	4	900	3050	25163	2.07	51.86

We include six simulations cases combining two different temperatures and three values for the ionospheric perpendicular wavelength (see Table 6.2). The spatial variation of several plasma properties as functions of altitude is shown in panels (a)-(f) of Figure 6.2. It is expected that, on its way into the inertial regime some degree of electron trapping occurs, and that the trapped electrons will escape the wave close to the point of separation between the kinetic and inertial regions [Watt and Rankin, 2009], where Landau damping is most effective. The intersection between Alfvén and thermal speed profiles indicates the separation of the inertial and kinetic regions. At low altitudes, the rapid decrease in electron density shown in panel (a) represents the depletion of cold

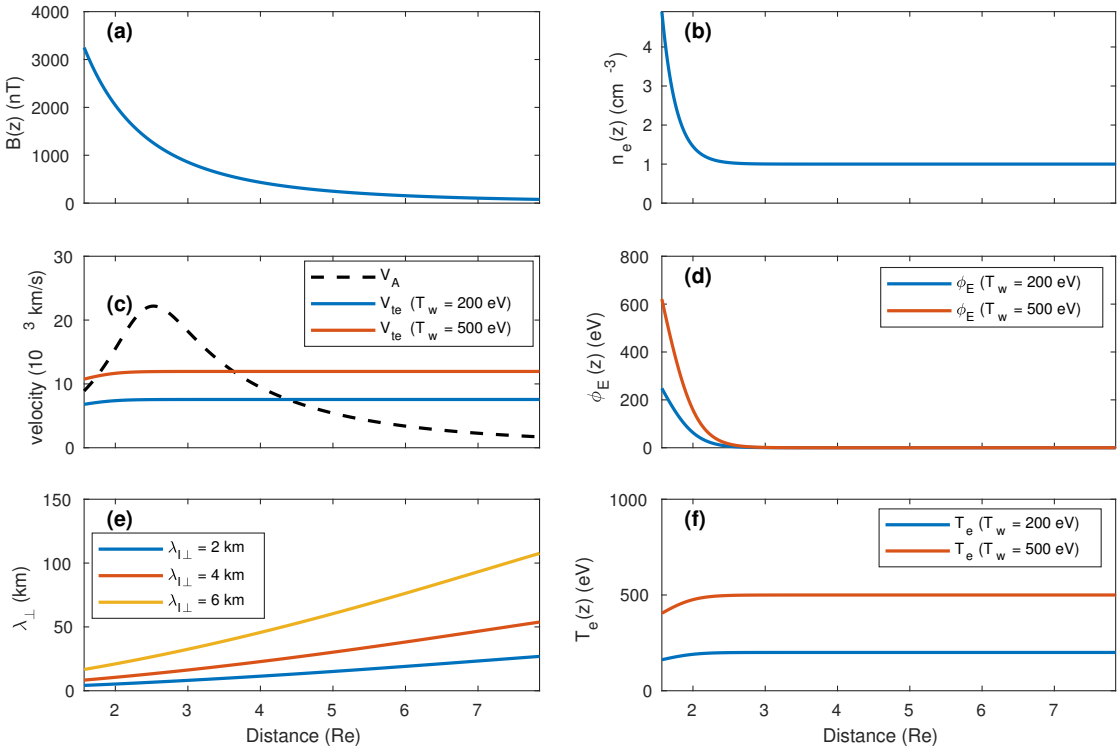

Figure 6.2: Background plasma properties for cases 1-6 specified in table 6.2, as a function of the coordinate z. (a) Magnetic intensity. (b) Electron density. (c) Alfvén and thermal velocities. (d) Electrostatic potential for inhomogeneous equilibrium. (e) Perpendicular wavelength. (f) Temperature. In panel (c), the kinetic regime for cases 1-3 extends along the region $z > 4.44\,R_E$, and $z > 3.7\,R_E$ for cases 4-6.

ionospheric plasma. The oxygen decrease rate is determined by the scale factor z_0 in equation (5.1), and it is indirectly responsible for the non-uniformity of the temperature and electrostatic potential profiles.

We also obtained numerical solutions to the dispersion relation (equation 5.40 on page 97), in terms of the secondary parameters v_{te}/V_A and $k_\perp \lambda_e$ at every point within the spatial domain. Although these solutions are only approximate, they should give a first glance of what to expect in the simulations regarding wave propagation at high altitudes (where the wave is introduced in the simulation). Phase speeds and growth rates for all simulations are plotted in Figure 6.3. These preliminary solutions indicate that, for the incoming wave pulse, phase velocities and damping rates are both proportional to temperature and the $k_\perp$ parameter (this temperature trend reverses in the inertial region). Overall, larger phase speed cases are also associated with stronger Landau damping. Table 6.2 includes specific values of the wave solution corresponding to the upper boundary location. These are to be compared against the expected trapping speed

(6.6) and the bounce frequency (6.4).

The wave input associated with these simulations correspond to $E_\perp \simeq 53$ mV/m. Wave potential amplitudes used in these simulations are in the same order as other studies regarding Alfvén waves in the magnetosphere [Watt and Rankin, 2010; Artemyev et al., 2015b]. The energy required to escape said potentials is comparable or even higher than the temperature for some of the cases, implying that large sections of the bulk distribution take part of the interaction. If these wave amplitudes are typical for the kinetic region, then it is reasonable to think that electron trapping frequently occurs in the magnetosphere. The estimated Landau coefficients and frequencies of trapping, when evaluated in the condition (6.8), support that idea.

6.3.1 Plasma behavior under the influence of a SAW

Wave dispersion of the shear Alfvén pulse at high altitudes produces a parallel electric field $E_\parallel/E_\perp \sim k_\parallel k_\perp(\lambda_e v_{th}/v_A)^2 \propto T/\lambda_\perp$, where $k_\parallel$ is the parallel wavenumber and λ_e is the electron skin depth. This field should have a considerable amplitude at the top of the simulation domain when the local plasma is warm enough. As one moves into lower altitude, however, the field amplitude decreases due to rising of the Alfvén speed. On the other hand, $v_w \propto v_A$ (see top graph in Figure 6.3) and the wave increases speed while moving into an increasing magnetic intensity region, keeping up with some of the fast electrons and even catching up with some energetic ones that might have escaped the wave. The leading crest of the wave should generate a beam of electrons with increasing parallel velocities. Inside the wave packet, though, accelerated electrons that overcome the wave speed move into a region where the electric field changes sign, so these particles start losing energy to the wave again; it is here where electron trapping takes place.

Figure 6.4 represents the time history of simulation 5 through snapshots of both field-aligned electric field component and distribution function. Other cases present similar behavior, with differences which will be discussed below. Downward electron acceleration takes place at the crests ($E_\parallel > 0$), while valleys ($E_\parallel < 0$) induce upward acceleration. The self-consistent response of the plasma quickly distorts the sinusoidal pulse, attempting to steepen the crests, as described in Watt et al. [2005]. Trapping regions form consistently at the crests of the wave, such that the maximum (negative) speed of the trapped electrons is proportional to the local electric field magnitude. If there is a difference in the field magnitude between a crest and the valley immediately ahead of it, the fastest electrons within the trapping island will have enough energy to move past the valley and form downgoing beams, thereby sinking a fraction of the wave energy through Fermi acceleration. A clear example of this can be seen at $t = 2$ s, and

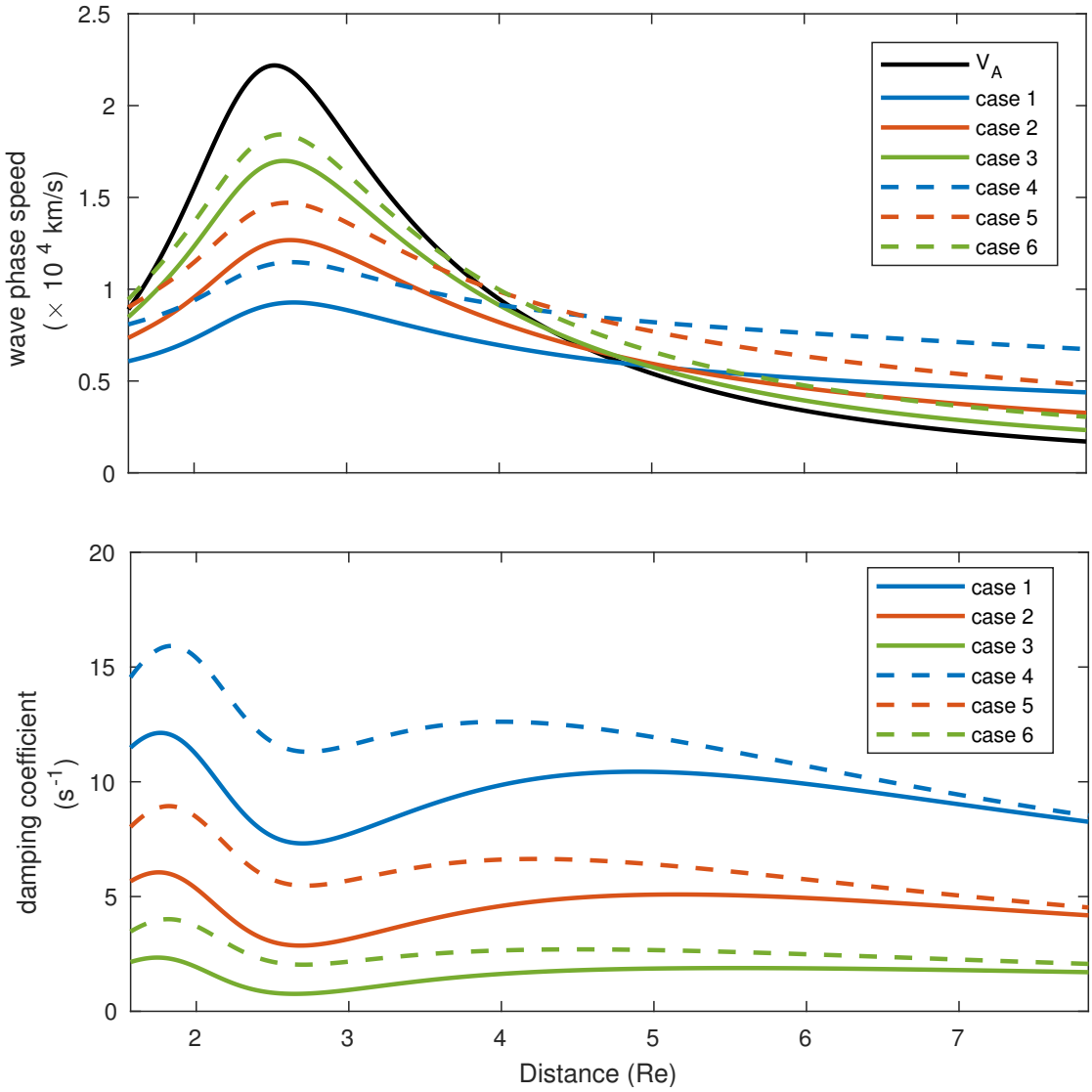

Figure 6.3: Solution to the dispersion equation as a function of position. Wave phase speed v_w (top), and damping coefficients (bottom) for all the simulation cases.

in a lesser degree at $t = 1$ s. The wave pulse takes $t = 3$ s to be injected into the spatial domain. After this time and in the absence of a source, the wave seems to damp away at a faster rate than before. By the time $t = 5$ s the pulse is practically gone, the last of previously trapped electrons are now free and form velocity dispersed signatures, and the distribution at high altitudes remains significantly disturbed due to the slow advection of low energy electrons from the upper boundary.

Figure 6.5 compares the field-aligned distribution function and the corresponding parallel electric field at $t = 3$ s, as a function of altitude for the whole set of simulations.

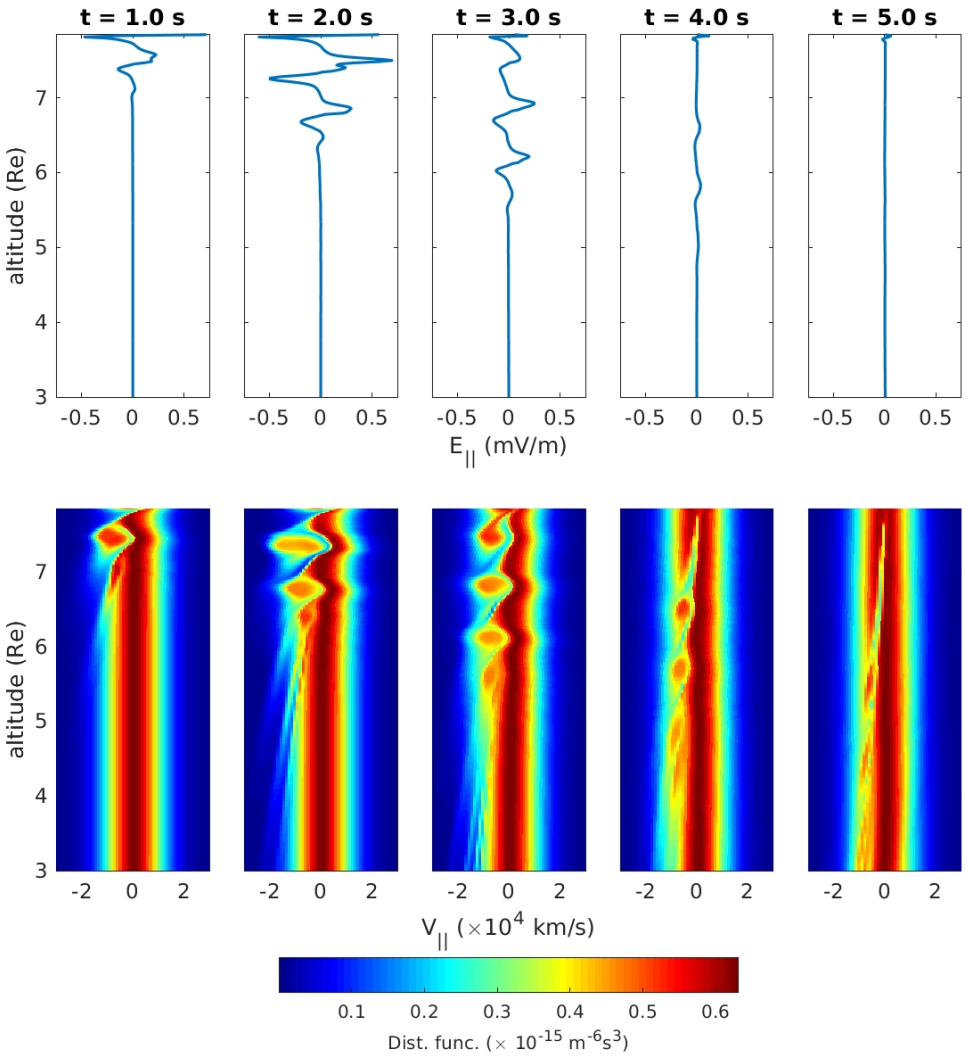

Figure 6.4: Time evolution of $E_{\parallel}(z)$ (top) and $f_e(z, v_{\parallel}, \mu = 0)$ (bottom) for simulation case 4 ($T = 500$ eV, $\lambda_{\perp I} = 2$ km).

We refer to the first three cases as the *low-temperature limit*, while cases 4 to 6 constitute the *high-temperature limit*. There are differences in the color scale between simulations with different temperatures; the most intense corresponds to the lower temperature cases. As previously speculated, most cases show trapping to some extent. In general, trapped electrons stick to regions where the electric field peaks, the range of parallel velocities over which they concentrate is proportional to the perpendicular length.

In both the low and high-temperature limits, the electric field plots show much stronger wave damping at lower values of the perpendicular wavelength. The wave

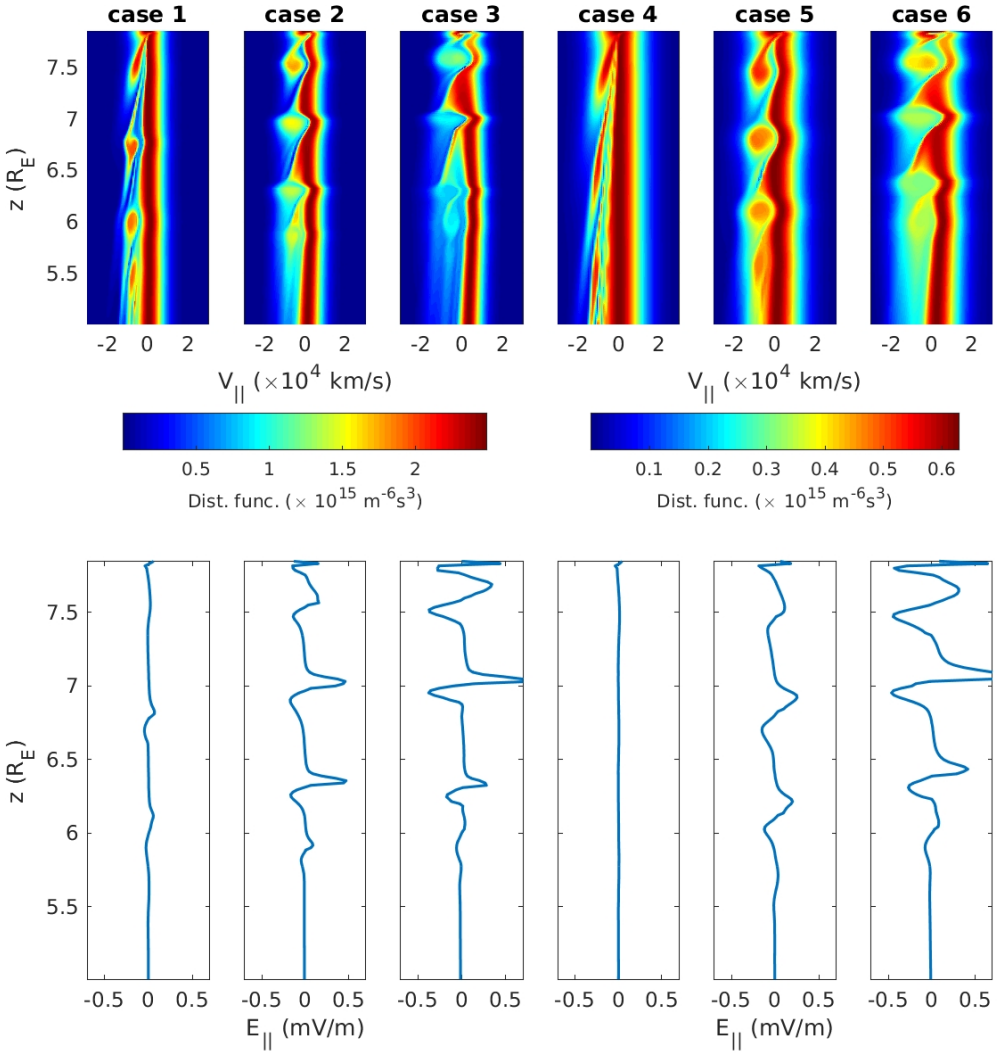

Figure 6.5: Field-aligned distribution (top) and parallel electric field (bottom) as a function of altitude at $t = 3$ s for all simulation cases.

phase speed is also higher at lower scales; this might not seem too evident from the electric field graphs, but should become clear by the relative position of corresponding trapping islands between simulations. The behavior of the wave in terms of these two aspects (damping and phase speed) correlates well with the solutions provided in Figure 6.3, which indicated a marked increase of the damping coefficient al lower perpendicular lengths. On the other hand, for otherwise identical conditions, cases with increased temperature show a mild decrease in the $E_{||}$ amplitude. This seems also consistent with Figure 6.3 (bottom panel), which shows that the damping coefficient presents modest

growth for cases with increased temperature in the region $z > 6\ R_E$. However, recall that according to the fluid approximation, the ratio of $E_\parallel$ amplitudes between cases with different temperatures is expected to be roughly similar as the ratio of temperatures, that is, wave amplitudes in the high-temperature limit would in principle be 2.5 times the amplitude at a lower temperature. For the cases shown here, it seems that the damping nearly counteracts the temperature variation of the electric field. A similar effect seems to occur for variations in the perpendicular scale, where larger wave amplitudes are expected at shorter scales ($E_\parallel \propto \lambda_\perp^{-1}$); since higher damping rates occur at lower scales, once again the inherent dependence of the electric field is counteracted by the increased damping rates. This might be a factor for which, Based on the cases shown here, the trapping process seems more efficient at intermediate scales, as it follows from the more consistent shape among the islands of trapped electrons (cases 2 and 5), and from the fact that $E_\parallel$ maintains a constant amplitude over larger distances. It is not clear if the wave damping at altitudes just below $6.5\,R_E$ in cases 3 and 6 is caused by the partial destruction of the trapping islands, or vice-versa. It looks plausible that, as a consequence of damping on the leading crest, beam formation would take place due to the difference of amplitude between subsequent crests, effectively removing the most energetic electrons of the trapped population.

O'Neil [1965]'s theory identifies Landau damping and particle trapping as mutually exclusive stages of the wave-particle interaction, yet in these cases, it seems evident that both processes are at work simultaneously. We are not in a position to describe the microphysics of this system due to its strong nonlinearity and inhomogeneity. We can say, however, that the extent to which the underlying assumptions that support O'Neil theory are fulfilled (uniform plasma, electrostatic wave, invariance of the wave amplitude in the average sense) is challenged here. Even though we have implemented a simple model that brings uniform conditions of density and temperature in the region where the wave is most influential, the dipolar field introduces wave dispersion through modification of $k_\perp$, v_A, and $E_\parallel$. Watt and Rankin [2009] reported that, on simulations using homogeneous conditions, trapping persists throughout the spatial domain. Local wave dispersion induced by inhomogeneous conditions, and nonlocal dispersion due to the nonlinear wave-particle interactions, might cause redistribution of the spectral energy into additional waves modes, which would undermine the efficiency with which closed orbits halt Landau damping.

Data from these simulations confirm that the electric field often presents a nonzero electromagnetic contribution, sometimes of even larger amplitude than the electrostatic component. The need to include electromagnetic effects into the formulation has motivated the use of Hamiltonian models [Shklyar and Matsumoto, 2009; Artemyev et al.,

2013, 2014, 2015b] and references within. So far these models are based on linear perturbation theory, so important effects like nonlocal dispersion are ignored. At this point, we would like to evaluate the conclusions on Artemyev et al. [2015b] study (see appendix C) against the findings presented here. Their low transverse wavelength case ($\lambda_{\perp eq} = 150$ km) compares with simulation cases 3 and 6, for which $\lambda_{\perp eq} \simeq 107$ km. Conveniently, these cases present the lowest levels of Landau damping. On the downside and despite these coincidences, there is very little common ground for comparison, as their data measuring techniques are incompatible with the use of distributions. For instance, their conclusions on particle energization and the probability of trapping are based on particles regardless of their final position; this is something we cannot quantify using distributions, due to the impossibility of fully identify accelerated electrons from undisturbed ones.

In general, the estimations given in Artemyev et al. [2015b] rely heavily on the wave being able to survive until reaching high latitudes. The energy of trapped electrons comes from the wave itself, and the large gain on some of the electrons requires a strong magnetic gradient efficiently transferring longitudinal momentum into transverse momentum so that under the subsequent deceleration, the wave is forced to accelerate the trapped particle further. According to the simulations presented here, even in cases with lower rates of damping, the wave cannot survive distances over 3 Re before damping completely. By comparison, in Artemyev et al. [2015b] the wave is let travel from the equator up to $\lambda = 45^o$, which means the wave travels more than $7\,R_E$ in $L = 9$. Moreover, according to the simulations, as the wave goes into intermediate states of damping, it continually loses its fastest electrons. Even though it could be the case that the parallel electric field becomes negligible over a significant fraction of its trajectory due to its dependence on temperature, there is a good chance that the energy gain of the trapped electrons, and consequent decrease in pitch angle, are significantly overestimated.

6.4 Summary

At altitudes where kinetic effects dominate wave dispersion, the condition $v_{te} \gg v_A$ suggests low levels of Landau resonance, while favoring the trapping of electrons in the wave potential. In this chapter, numerical simulations of nonlinear wave-particle interactions reveal that, at equatorial latitudes, the occurrence of particle trapping in the wave potential of dispersive Alfvén waves is influenced by Landau damping. Growth rate estimations based on linear kinetic theory describe damping of these waves fairly well: wave damping is found to increase significantly with decreasing perpendicular wavelengths, and shows a moderate increase for increasing temperatures. On the other

hand, electric field amplitudes and Landau damping increase under the same conditions, implying that nonlinear dynamics is sensitive to parameters. Electron trapping is found to be more efficient at intermediate values of the perpendicular wavelength. Although this condition is consistent with the intrinsic variation of $E_{\parallel}$ and the damping coefficient, other factors play an important role. Wave dispersion and wave-particle interactions eventually lead to the destruction of the trapping islands at some altitude along the geomagnetic field.

The significant differences between results of Vlasov simulations and simple analytic models [Artemyev et al., 2015b] of particle trapping reveals the highly nonlinear nature of the process and need for better models with increased spatial and temporal resolution.

Chapter 7

Inertial Alfvén Waves as a possible driver for AKR

In this chapter, we test the efficiency of AKR formation as a result of electron acceleration into a converging magnetic field by IAW propagation. As accelerated particles move into regions of increased magnetic intensity, they increase their pitch angle as per conservation of their magnetic moment, resulting in the formation of shell or *horseshoe* distributions in velocity space. Numerical distributions obtained from simulations are parametrized so that an analytic representation of them is constructed. This functional form of the distribution is used to obtain an estimation of the waves growth rate associated with electron cyclotron resonance, according to Bingham and Cairns [2000].

Given that AKR emissions occur at or near to the local electron cyclotron frequency, their source can be determined through spatial mapping of its corresponding magnetic field. This has helped researchers to use remote sensing to understand the vertical structure of the acceleration region better. Several studies [Hanasz et al., 2001; Olsson et al., 2004; Su et al., 2007; Morioka et al., 2007, 2008] have reported events at various altitudes up to ~ 4.5 Re radial distance. Some of these publications provide evidence that the vertical distribution of events is particularly sensitive to the plasma density, such that events occur more frequently around density cavities, during winter months, and all year round in the evening and midnight sectors, possibly due to lower ionization rates than their counterparts [Olsson et al., 2004; Su et al., 2008].

Many of these events are correlated with auroral substorms. For example, wideband bursts (WBB-AKR) [Hanasz et al., 2001] experiment an explosive (< 1 min) intensification over a wide range of frequencies ($30 - 900$ kHz) triggered at the substorm expansion phase, followed by a slower decay (~ 10 min). The higher frequency part of these emis-

sions was found to rise and decay at time scales of the same order as the expected saturation time of the ECI, suggesting generation by a saturated ECI. It was pointed out that the expansion drift speed would depend on the initial altitude of the source; sources located at lower altitude would present low drift expansion ($\sim 10^0$ km/s), while higher altitude sources would drift at speeds comparable to the local Alfvén speed ($\sim 10^3$ km/s).

More evidence on the differentiated behavior of AKR sources with altitude was eventually unveiled. The term *low-frequency AKR* (LFAKR) was used by Olsson et al. [2004] to denote events in the < 100 kHz range (altitudes ≥ 3 Re), which coincide with the statistical peak of density cavity formation [Janhunen et al., 2004]. LFAKR occurs almost exclusively during high substorm activity, primarily in the midnight sector, and with higher frequency during winter months. Sometimes, strong AKR appears at ~ 50 kHz; these correspond to a subclass of LFAKR denominated *Dot-AKR*. Alfvén wave activity at the source has been reported simultaneously with LFAKR in some of the events, but it was pointed out that the lack of it does not necessarily imply the absence of waves. The mechanism suggested was IAW propagation into pre-existing density cavities. It was argued that, in the limit of large perpendicular wavelengths, the parallel component of the electric field should increase with decreasing density. This enhanced component can accelerate electrons to form horseshoe distributions and produce AKR radiation.

Morioka et al. [2007] identified 2 AKR source regions at different altitudes, which become active during substorms, and studied their spatial development and evolution. The lower altitude source is located at 4000-5000 km; in this region, AKR appears both before and after the substorm onset, showing considerable intensification a few minutes prior the substorm onset. At higher altitudes (6000-12000 km), a second source develops abruptly at substorm onset, increasing its intensity by several orders of magnitude over ~ 30 s interval. Careful observation of the second source during the development phase evidences seemingly randomly distributed small AKR structures which intensify simultaneously, instead of a systematic drift of a single source.

Some observations [Hanasz et al., 2006] have shown simultaneous occurrence, and similar modulation at Pc5 frequencies, of AKR signals and FLRs, which suggests that AKR can be produced within the FLR structures. Location of the footprint of the AKR source is well correlated with discrete auroral arcs that are associated with the FLRs. Nonlinear effects associated with the coupling of standing SAW with compressional modes can diminish the initially large perpendicular scaling down to values where inertial effects become important and parallel electric fields can be generated. It was also argued that the concentration of wave energy in the resonance region would eventually lead to nonuniform pressure distribution, possibly driven by plasma fluctuations, leading

to cavity formation. Favorable conditions for AKR are thought to occur only during half cycle of the FLR period.

7.1 Estimation of growth rates

In this section, we follow the steps of Bingham and Cairns [2000] to evaluate the effect of a horseshoe distribution on the stability of the *transverse magnetic* (TM) mode under which the electron cyclotron resonance is expected to occur. The TM mode describes emission perpendicular ($k_{\|} = 0$) to the background magnetic field in hot plasmas [Bittencourt, 2004]. This mode reduces to the extraordinary mode in cold plasma. The following analysis is valid assuming that the Larmor radius of the electrons is much smaller than the perpendicular scale, and that the relativistic mass correction at the cyclotron frequency,

$$\omega_{ce} = \frac{q_e B}{\gamma m_e} \simeq \Omega_{e0} \left[1 - \frac{1}{2} \left(\frac{p}{mc} \right)^2 \right], \tag{7.1}$$

is relevant when evaluating the growth rate exclusively.

7.1.1 Derivation of the dielectric coefficients

We consider emission strictly perpendicular to the background magnetic field. The dielectric tensor components (see [Gurnett and Bhattacharjee, 2005] pag. 370) evaluated for a single electron species take the form:

$$K_{xx} = 1 - \frac{\omega_{pe}^2}{\omega} \sum_{n=-\infty}^{\infty} 2\pi \int_{-\infty}^{\infty} dp_{\|} \int_0^{\infty} dp_{\perp}\, p_{\perp}^2 \frac{\partial F_{e0}}{\partial p_{\perp}} \frac{n^2 J_n^2(\beta_e)}{\beta_e^2 (n\omega_{ce} - \omega)}, \tag{7.2}$$

$$K_{yy} = 1 - \frac{\omega_{pe}^2}{\omega} \sum_{n=-\infty}^{\infty} 2\pi \int_{-\infty}^{\infty} dp_{\|} \int_0^{\infty} dp_{\perp}\, p_{\perp}^2 \frac{\partial F_{e0}}{\partial p_{\perp}} \frac{(n J_n'(\beta_e))^2}{(n\omega_{ce} - \omega)}, \tag{7.3}$$

$$K_{xy} = -K_{yx} = i \frac{\omega_{pe}^2}{\omega} \sum_{n=-\infty}^{\infty} 2\pi \int_{-\infty}^{\infty} dp_{\|} \int_0^{\infty} dp_{\perp}\, p_{\perp}^2 \frac{\partial F_{e0}}{\partial p_{\perp}} \frac{n J_n(\beta_e) J_n'(\beta_e)}{\beta_e (n\omega_{ce} - \omega)}. \tag{7.4}$$

Here F_{e0} represents the distribution function normalized to unity, and $\beta_e = k_{\perp} v_{\perp}/(q_e B)$. The other components (except K_{zz}) involve integration of odd functions in $p_{\|}$, from $-\infty$ to ∞. Then we have

$$K_{xz} = K_{zx} = K_{yz} = K_{zy} = 0, \tag{7.5}$$

provided that $F_{e0} = F_{e0}(p_\parallel^2)$, which is the case for both Maxwellian and Lorentzian distributions.

Under the assumption $r_e \ll \lambda_\perp$, $\beta_e \simeq 0$. The Bessel functions take the approximate values:

$$\begin{aligned} J_0(\beta_e) &\simeq 1 \\ J_{\pm 1}(\beta_e) &\simeq \pm\frac{\beta_e}{2} \\ J_{\pm(n>1)}(\beta_e) &\simeq 0. \end{aligned} \tag{7.6}$$

Evaluation of the small limit argument leads to

$$\varepsilon_\perp = 1 + \frac{\omega_{pe}^2}{4\omega} 2\pi \int_{-\infty}^{\infty} dp_\parallel \int_0^\infty dp_\perp \, p_\perp^2 \frac{\partial F_{e0}}{\partial p_\perp} \left(\frac{1}{\omega + \omega_{ce}} + \frac{1}{\omega - \omega_{ce}} \right), \tag{7.7}$$

$$\varepsilon_{xy} = -\frac{\omega_{pe}^2}{4\omega} 2\pi \int_{-\infty}^{\infty} dp_\parallel \int_0^\infty dp_\perp \, p_\perp^2 \frac{\partial F_{e0}}{\partial p_\perp} \left(\frac{1}{\omega + \omega_{ce}} - \frac{1}{\omega - \omega_{ce}} \right), \tag{7.8}$$

where we have replaced $\varepsilon_\perp = K_{xx} = K_{yy}$ and $\varepsilon_{xy} = iK_{xy} = -iK_{yx}$. Both expressions include the term $\int d^3p \, p_\perp \, \partial F_{e0}/\partial p_\perp$. Using integration by parts it is trivial to prove that

$$2\pi \int_{-\infty}^{\infty} dp_\parallel \int_0^\infty dp_\perp \, p_\perp^2 \frac{\partial F_{e0}}{\partial p_\perp} = -2. \tag{7.9}$$

On both equations (7.7) and (7.8), the second integration contains a simple pole that lies over the real axis. Poles of this type have solutions given by the principal value integral, plus half the residue

$$\lim_{\zeta \to 0} \frac{1}{x - a \pm i\zeta} = PV \left[\frac{1}{x-a} \right] \mp i\pi\delta(x-a). \tag{7.10}$$

Furthermore, Bingham and Cairns [2000] assume that the relativistic correction is essential only for the growth rate, while everywhere else $\omega_{ce} \simeq \Omega_{e0}$ is taken. This yields

$$\varepsilon_\perp = \frac{\omega^2 - \omega_{uh}^2}{\omega^2 - \Omega_{e0}^2} - i\alpha, \tag{7.11}$$

$$\varepsilon_{xy} = -\frac{\omega_{pe}^2 \Omega_{e0}}{\omega(\omega^2 - \Omega_{e0}^2)} - i\alpha, \tag{7.12}$$

with $\omega_{uh}^2 = \omega_{pe}^2 + \Omega_{e0}^2$ the *upper hybrid* frequency, and α given by

$$\alpha = -\frac{\pi}{4}\frac{\omega_{pe}^2}{\Omega_{e0}} 2\pi \int_{-\infty}^{\infty} dp_{\parallel} \int_0^{\infty} dp_{\perp}\, p_{\perp}^2 \frac{\partial F_{e0}}{\partial p_{\perp}} \delta \left[\omega - \Omega_{e0} + \frac{\Omega_{e0}}{2}\left(\frac{p}{mc}\right)^2\right] \tag{7.13}$$

The dispersion equation

The dispersion relation is obtained by equalizing the determinant of equation (2.59) to zero, which yields

$$\left[K_{xx}\left(K_{yy} - \eta^2\right) - K_{xy}K_{yx}\right]\left(K_{zz} - \eta^2\right) = 0, \tag{7.14}$$

where η is the refractive index. The TM mode mentioned above corresponds to the expression enclosed in squared parenthesis. The refraction index for this mode can be written as

$$\eta^2 = \varepsilon_{\perp} - \frac{\varepsilon_{xy}^2}{\varepsilon_{\perp}}. \tag{7.15}$$

We want to obtain an expression for the imaginary part of the refraction index, which implies expanding equation (7.15) in its real and imaginary parts η_R and η_I. If we define $r_{\perp} = \Re\{\varepsilon_{\perp}\}$ and $r_{xy} = \Re\{\varepsilon_{xy}\}$, then we can write (7.15) as

$$\eta^2 = \eta_R^2 - \eta_I^2 + 2i\eta_R\eta_I = \frac{(r_{\perp} - i\alpha)^2 - (r_{xy} - i\alpha)^2}{r_{\perp} - i\alpha} \tag{7.16}$$

$$= \frac{r_{\perp}\left(r_{\perp}^2 - r_{xy}^2\right) + 2\alpha^2\left(r_{\perp} - r_{xy}\right) - i\alpha\left(r_{\perp} - r_{xy}\right)^2}{r_{\perp}^2 + \alpha^2}. \tag{7.17}$$

If we assume that both η_I and α are first-order quantities, then

$$\eta_R^2 \simeq \frac{\left(r_{\perp}^2 - r_{xy}^2\right)}{r_{\perp}} \tag{7.18}$$

$$= \frac{\omega^2(\omega^2 - \omega_{uh}^2)^2 - (\omega_{pe}^2\Omega_{e0})^2}{\omega^2(\omega^2 - \Omega_{e0}^2)(\omega^2 - \omega_{uh}^2)}. \tag{7.19}$$

$$\eta_I \simeq -\frac{\alpha}{2\eta_R}\frac{(r_\perp - r_{xy})^2}{r_\perp^2} \tag{7.20}$$

$$= -\frac{\alpha\,(\omega-\Omega_{e0})^2}{2\eta_R}\frac{\left[\omega^2+\omega\Omega_{e0}-\omega_{pe}^2\right]}{\left[\omega\left(\omega^2-\omega_{uh}^2\right)\right]^2}. \tag{7.21}$$

Calculation of the α parameter

To evaluate (7.13), it is convenient to switch to spherical coordinates; $p=\sqrt{p_\parallel^2+p_\perp^2}$, $\mu=\cos\theta$, ϕ. The volume integral changes into

$$2\pi\int_{-\infty}^{\infty}dp_\parallel\int_0^\infty dp_\perp\,p_\perp \to 2\pi\int_{-1}^{1}d\mu\int_0^\infty dp\,p^2. \tag{7.22}$$

Also,

$$p_\perp\frac{\partial F_{e0}}{\partial p_\perp} = p(1-\mu^2)\left(\frac{\partial}{\partial p}-\frac{\mu}{p}\frac{\partial}{\partial\mu}\right)F_{e0}. \tag{7.23}$$

Finally, one uses the composition property, $\delta(h(x))=\sum_n\delta(x-x_n)/|h'(x_n)|$ to express the dirac delta term in terms of momentum instead of frequency. Then (7.13) turns into

$$\alpha = -\frac{(\omega_{pe}\pi m_e c)^2}{2\Omega_{e0}^2}\int_{-1}^{1}d\mu\,(1-\mu^2)\int_0^\infty dp\,p^2\left(\frac{\partial}{\partial p}-\frac{\mu}{p}\frac{\partial}{\partial\mu}\right)F_{e0}\delta\left(p-p_R\right). \tag{7.24}$$

where the resonant momentum, p_R, is equal to

$$p_R = mc\sqrt{2\frac{(\Omega_{e0}-\omega)}{\Omega_{e0}}}. \tag{7.25}$$

The next step is to include the explicit form of the unperturbed distribution; this is written in the form

$$F_{e0}(p) = f_m(p) + f_h(p)g(\mu). \tag{7.26}$$

The first term in (7.26) consists of a Maxwellian contribution

$$f_m(p) = k_m\exp\left[-\left(\frac{p}{p_{tm}}\right)^2\right], \tag{7.27}$$

while the second term represents the Horseshoe itself, which consists of a shell that takes

its maximum value at some prescribed momentum p_b,

$$f_h(p) = k_h \exp\left[-\left(\frac{p-p_b}{p_{th}}\right)^2\right], \tag{7.28}$$

modulated by a factor that causes the shell to fade away as $\mu \to -1$. Bingham and Cairns [2000] choice for $g(\mu)$, written in terms of the Heaviside function $\theta(\mu)$, has the following form

$$g(\mu) = \theta(\mu-\mu_0)\sqrt{\frac{\mu-\mu_0}{1-\mu_0}}, \qquad -1 < \mu_0 < 1. \tag{7.29}$$

The constants k_m and k_h in (7.27) and (7.28) determine the ratio of densities between the Maxwellian and shell distributions, and must be such that F_{e0} is normalized to unity. After substitution and evaluation of (7.27), (7.28) and (7.29) into (7.24), one eventually reaches the expression

$$\begin{aligned}\alpha =& \frac{(\pi\omega_{pe}m_e c)^2}{2\Omega_{e0}^2} \\ & \left(\frac{8/3}{p_{tm}^2}[p^3 f_m(p)]\Big|_{p=p_R} + \frac{2}{p_{ht}^2}P(\mu_0)[p^2(p-p_b)f_h(p)]\Big|_{p=p_R} - Q(\mu_0)[pf_h(p)]\Big|_{p=p_R}\right),\end{aligned} \tag{7.30}$$

where

$$P(\mu_0) = \int_{\mu_0}^{1} d\mu\,(1-\mu^2)g(\mu) = \frac{8}{105}(2\mu_0+5)(1-\mu_0)^2, \tag{7.31}$$

and

$$Q(\mu_0) = \int_{\mu_0}^{1} d\mu\,(1-3\mu^2)g(\mu) = -\frac{4}{105}(1-\mu_0)(12\mu_0^2+18\mu_0+5). \tag{7.32}$$

The first term in equation (7.30) represents the effect of the unperturbed distribution; this term is positive, so it induces wave damping. The second term becomes unstable if the resonant momentum falls in a region where the gradient is positive, in accordance with the ECI theory. Finally, the last term induces wave damping for a horseshoe with a low angular opening, but it becomes unstable at large values of μ_0.

Bingham and Cairns [2000] illustrated this method by considering a Maxwellian plasma with temperature 312 eV, and a horseshoe distribution with $p_b = 0.1 m_e c$, $p_{th} = 0.02 m_e c$, and an opening angle 60^o ($\mu_0 = 0.5$). $n_h = 2n_m$ and $\omega_{pe}/\Omega_{e0} = 1/40$. The

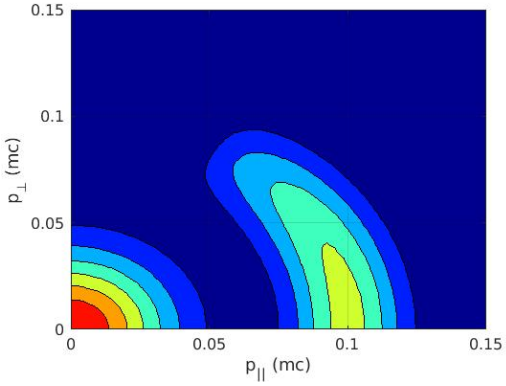

(a) Electron distribution

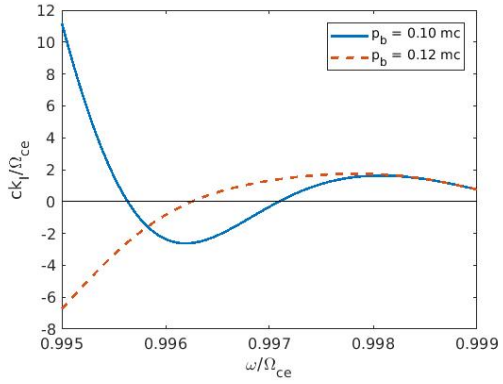

(b) Beam momentum variation

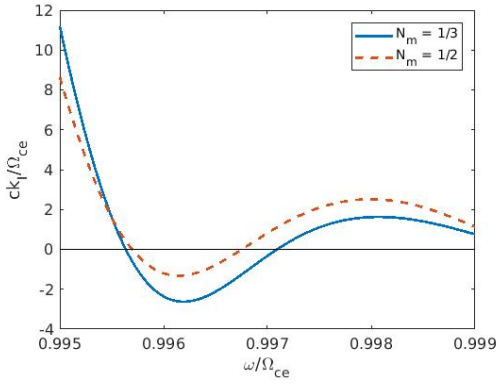

(c) Density variation of the Maxwellian component

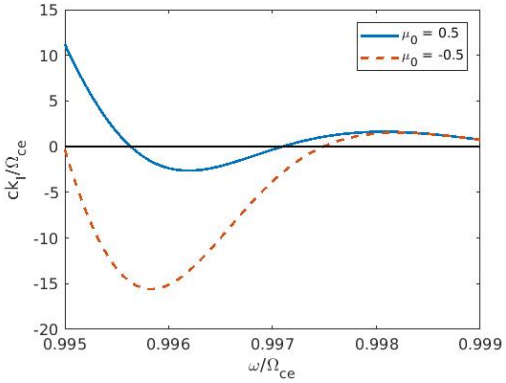

(d) Angular opening variation

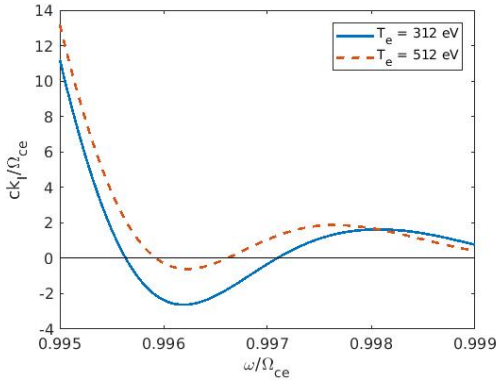

(e) Temperature variation

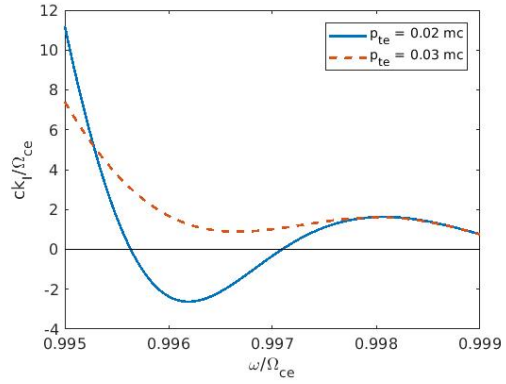

(f) Thermal width variation

Figure 7.1: The top-left panel shows the distribution that results from Bingham and Cairns [2000]. Subsequent panels compare the original solution, against variation of different parameters.

distribution is shown in the top-left panel on Figure 7.1. The rest of panels compare growth rates for the baseline case (dark line), against small variations of the parameters that determine the distribution. It is instructive to observe the effect that variations of these parameters have over the growth rate. The top-right panel in Figure 7.1 shows the effect of increasing the radius (in momentum space) of the shell distribution. For a beam of electrons traveling earthward, this radius will in principle increase proportionally to the magnetic intensity due to conservation of the first adiabatic invariant. Accelerated electrons, however, can only reach into the converging magnetic field as much as their energy gain from the interaction allows them. The bottom line is, a horseshoe with longer radius results from electrons with higher energy gain, and therefore, has more energy available for wave amplification; this seems reflected in the figure, which indicates higher growth rates for a horseshoe with a longer radius. The graph also shows a significant shift in the band of frequencies at which the instability can take place; an increase in p_b will cause emission to occur at lower frequencies. This aspect probably has to do with the relativistic nature of the process. A somewhat similar effect seems to occur in the middle-right graph that illustrates the effect of increasing the horseshoes angular range. The middle-left and lower-left graphs illustrate the change of growth rate due to the variation of the unperturbed component. Note that an increase on whether the temperature or density should naturally damp the wave due to interaction with a higher number of thermal particles. No shift in the spectrum of frequencies seems evident in these cases. Finally, the lower-right panel shows the effect upon changes in the horseshoe width. Favorable conditions for wave growth include a narrower horseshoe. The theory of ECI supports this since, for a distribution with a given density, a smaller width is consistent with a larger positive momentum gradient.

7.2 Generation of horseshoe distributions by an Inertial Alfvén Wave

The literature cited in the introductory paragraphs of this chapter gives the notion that AKR amplification occurs within density cavities of $\sim 10^4 - 10^5$ m^{-3}. Next, we consider the formation of unstable horseshoe distributions under conditions which should be favorable for AKR emission. Unfortunately, the algorithm used here often runs into numerical issues at low densities, and despite multiple efforts, we were not able to obtain a higher number of working cases spanning a wider variation of the initial parameters. Still, the cases presented here provide necessary evidence that Alfvénic acceleration can, in fact, ultimately drive AKR emission. Consider the following scenario for horseshoe

formation: an initially unperturbed plasma interacts with a kinetic or inertial Alfvén wave causes electron acceleration parallel to the external magnetic field. After interaction, Fermi-resonant electrons stream down the field line with speeds roughly twice the Alfvén speed according to Kletzing and Torbert [1994]. Conservation of the magnetic moment causes pitch angle dispersion as these particles move into regions of more intense geomagnetic field. This effect gives rise to a partial ring or horseshoe when one observes the local distribution in a phase diagram; the ring formation appears incomplete due to the absence of the most field-aligned electrons located inside the loss cone. Since we cannot use an arbitrary low density due to the occurrence of numerical instability, a relatively high Alfvén speed is maintained by using a lower L-shell value ($L = 5$) that does not correspond to auroral latitudes.

The baseline simulation features a Gaussian pulse with amplitude $\phi_0 = 300$ V and frequency $f = 4$ s^{-1}, propagating down the field line from an initial altitude $z = 3 \times 10^4$ km. All background plasma properties and their variation along the spatial domain were implemented following the guidelines discussed in chapter 4 for inhomogeneous plasma. Background densities for hydrogen and oxygen are $n_H = 10^5$ and $n_O = 10^9$ m^{-3} respectively, the oxygen component decays exponentially by a factor $z_0 = 0.2$ Re; the unperturbed plasma is Lorentzian with $\kappa = 10$; the initial temperature is 200 eV at the upper boundary and decreases at lower altitudes. The perpendicular scale at the ionosphere is 2 km.

Graphical fitting and growth rate estimation

The procedure used to parametrize the numerical distribution at a given location and time is, in principle, quite straightforward. A first step consists on obtaining an analytical representation of the thermal component of the plasma. Figure 7.2 (a) shows the phase diagram of the local distribution at $z = 2$ Re ($\sim$ 13000 km) and $t = 1.16$ s; the graphs in (b) and (c) plot its projection along the parallel and perpendicular axes (blue line), respectively. Recall that, in the context of section 7.1, $k_m \equiv f_m(p = 0)$, and $p_{mt} \equiv k_m \exp(-1)$. The corresponding analytic representation is plotted in red on panels (b) and (c). Once the thermal component is parameterized, it is subtracted from the original distribution to obtain the perturbation (see Figure 7.2(d)). One can readily see that the resulting horseshoe is not entirely centered at the origin. Physical implications arising from this fact will be discussed below. At this point, a computational script sweeps through the matrix containing data from the perturbed distribution, identifying the intensity and coordinates of the horseshoe. This procedure is complicated by the fact that, especially at large $p_\perp$, both thermal and perturbed contributions overlap close to

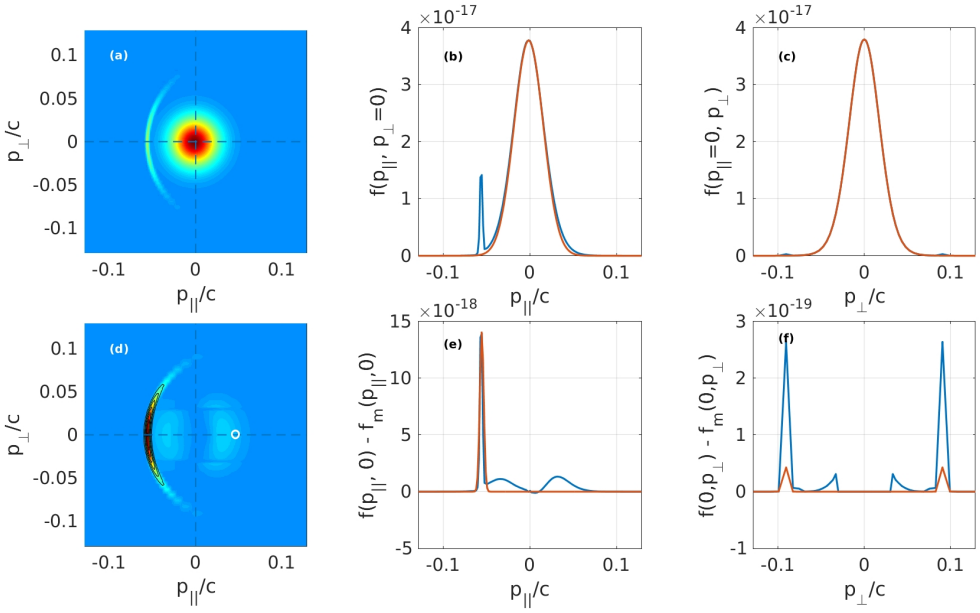

Figure 7.2: Local distribution function at $z = 2$ Re and $t = 1.16$ s. (a) Velocity distribution. (b) Parallel projection of the numerical distribution (blue), and graphical fit of the unperturbed component (red); (c) Perpendicular projection (blue), and its graphical fit (red). (d) Velocity distribution of the perturbed component. Contours represent the obtained parametrization of the horseshoe. (e) Parallel projection (blue) of the numerical perturbation, and graphical fit of the unperturbed component (red); (f) Perpendicular projection (blue), and its graphical fit (red).

$p_\parallel = 0$, which makes it difficult to tell them apart; at this point, we resort to assuming that the background distribution remains constant. This assumption is likely less accurate at times when the wave is present and moving across their location; this passing of the wave causes noticeable drifting and distortion of the background distribution, which further complicates distinction of the perturbation. This script outputs the necessary data to find the central location, the radius p_b, and the function $g(\mu)$ of the horseshoe, while its thermal width is chosen so that it fits the main peak along the $p_\parallel$ axis (see panel (e)).

The normalized variation of intensity along the resonant surface is shown in Figure 7.3(a). Also two different forms of the function $g(\mu)$ are shown that fit said variation such that each function minimizes the total sum of squared differences relative to the data points. The exponential fit follows the data much closer than the Bingham function. The analytic construction of the horseshoe using an exponential fit has been superimposed as contours on top of the phase diagram in Figure 7.2(d). As pointed out before, this

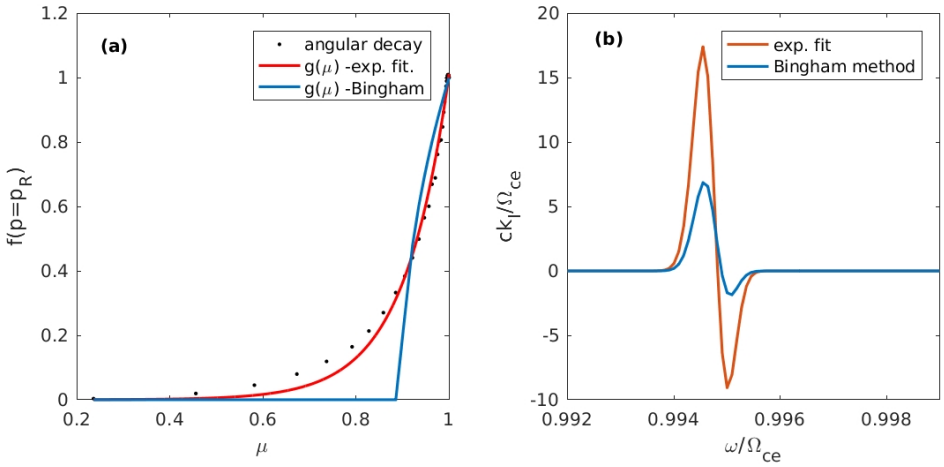

Figure 7.3: (a) Angular variation of the horseshoe distribution intensity (normalized). (b) Frequency variation of the growth rates associated to each function $g(\mu)$.

representation is not symmetrically centered with respect to the thermal component, as required by the condition (7.5). Nonetheless, since the growth rate calculation requires evaluation exclusively at the resonant momentum, the error introduced should be small as long as the thermal particles stay clear from the resonant surface; that is, if the first term on the right-hand side of equation (7.30) is zero. The imaginary wavenumber as a function of frequency for the TM mode, in this case, is shown in Figure 7.3(b), there is a very narrow band, centered at $\omega = 0.995\Omega_{e0}$, under which the instability takes place. The local minimum indicates the shortest convective distance $L_c = 2\pi/k_I$, which in this case is equal to 585 m for the exponential fit case (vs. 2800 m using Bingham approach). Shorter distances indicate higher efficiency in wave amplification since they allow more foldings within a given region. The estimated latitudinal width of the auroral density cavity is 100 km, so wave amplification can be expected in this case.

7.3 Optimal conditions for wave amplification

We have established a procedure to estimate convective lengths out of simulation data, based on the theoretical framework given by Bingham and Cairns [2000]. In this section, we use this framework to determine conditions under which wave amplification is favorable.

7.3.1 Altitude dependence

Let us start by comparing emission rates at different altitudes along the field line. Recall that the efficiency of the ECI depends on the condition Treumann [2006]

$$\left(\frac{\omega_{pe}}{\omega_{ce}}\right)^2 \ll 1. \tag{7.33}$$

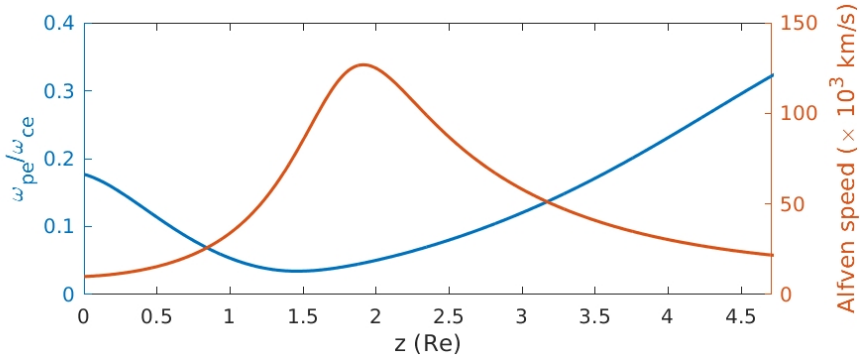

Figure 7.4: Spatial variation of ω_{pe}/ω_{ce}.

Figure 7.4 shows the spatial dependence of this ratio during unperturbed conditions; the Alfvén speed profile is also overlayed for reference. The highest efficiency of ECI is expected at $z \simeq 1.5\,R_E$, where the Alfvén speed seems to increase faster with altitude. We have measured the convective length at several locations within this neighborhood in the following way: at each location, the time intervals when horseshoe distributions occur are determined through visual inspection of the local differential flux; next, their minimum convective lengths and their corresponding frequencies are calculated using the procedure outlined in the previous section. These results are summarized in Figure 7.5. Convective lengths are plotted against their normalized resonant frequency, but the time variation can be appreciated in that consecutive points joined by each line correspond to sequential measurements with a sampling time of 0.2 s. For all cases, earlier estimations present larger convective scales (and lower frequencies relative to Ω_e); at later times, as the horseshoe becomes more dense, especially at larger pitch angles, convective scales decrease considerably, often dropping by a few orders of magnitude in less than a second. Notice that, even though in all cases L_c showcases a decreasing trend, there are important levels of variability from one point to the next, which suggests that these growth rate estimations should better be trusted in the average sense.

Variability of the convective scale is exceptionally high during later times at altitudes $z = 2$ and $z = 2.5\,R_E$; this might be at least partially attributable to the presence of

reflected waves originated at the region of steep Alfvén speed gradient, as discussed in chapter 4.

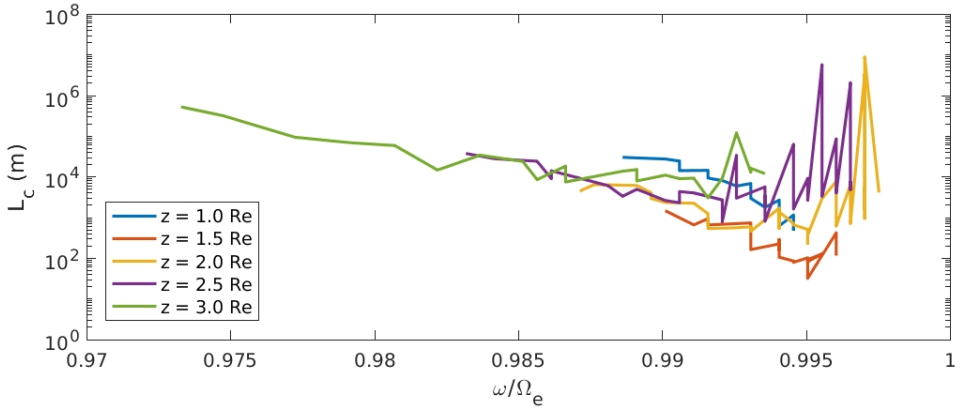

Figure 7.5: Maximum convective length at different locations. Earlier estimations correspond to the largest values.

Comparison between different altitudes demonstrates how convective lengths decrease proportionally to the distance relative to $1.5\,R_E$, where ω_{pe}/ω_{ce} is minimum. Notice however, that the average values for altitudes $z = 1$ and $z = 2\,R_E$ differ by more than an order of magnitude, despite that the ratio ω_{pe}/ω_{ce} is very similar at these locations. The difference lies in the number of particles that make the unstable populations between these two locations. At $z = 2\,R_E$, the wave speed is growing and produces accelerated electrons continuously. Conversely, at $z = 1\,R_E$ both the wave amplitude and speed have decreased significantly due to the drastic increase in ionospheric density, and the mirror force has reflected most of the energetic electrons (see discussion in section 5.4.1).

7.3.2 Variation of other parameters

Table 7.1: Modified input parameters

	ionospheric $\lambda_\perp$ (km)	T_e (eV)	n_H m^{-3}
case 1 (baseline)	2	200	10^5
case 2	4	200	10^5
case 3	2	500	10^5
case 4	2	200	10^6

As a final point of this section, we briefly address AKR efficiency after modification of some initial parameters. We have complemented the baseline case with three simulations cases featuring changes of (i) the perpendicular scale at the ionosphere, (ii) the initial

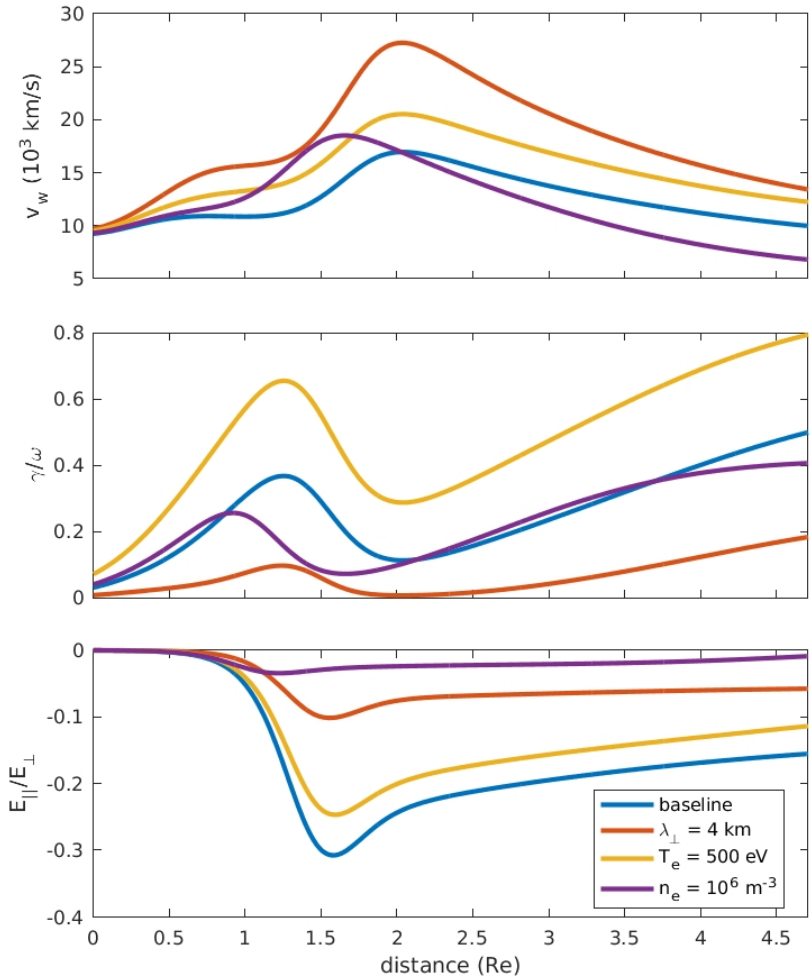

Figure 7.6: Phase speed (top), growth rate (middle), and parallel electric field (bottom) along the spatial domain.

temperature, and (iii) the hydrogen density, respectively and one at a time. Specific values are summarized in table 7.1. Figure 7.6 includes preliminary solutions of the dispersion relation (equation 6 on Lysak and Lotko [1996], or 2.114 on page 41) and the 2-fluid approximation of the electric field (see equation 2.91 on page 37) for all cases.

Inertial conditions dominate in all these cases. Naturally, larger electric field amplitudes are expected at lower values of the transverse scale, which in principle implies more energy for particle acceleration. On the other hand, increasing the perpendicular scale has the effect of reducing wave damping and increasing the wave phase speed; a consequence of faster wave propagation is that resonant electrons would escape the wave

with larger velocities. An increase of the temperature relative to the baseline case suggests higher wave damping rates, and also a weaker parallel electric field. On the other hand, it should induce faster wave propagation, which again it means a higher speed of the resonant particles. Finally, notice that an increase in density radically reduces the chance of energetic particles altogether. We are not that interested in testing the effect of increasing the density, but instead want to obtain an estimation of the convective length, to see if it AKR amplification seems possible in regions outside density cavities.

The convective distances for these cases were estimated at the altitude where condition (7.33) predicts an optimal efficiency of the ECI, in the same fashion as in the last subsection. Comparisons of the baseline case with the other simulations are plotted in Figure 7.7. According to graphs 7.7(a) and (b), an increase of either the perpendicular scale or background temperature results in lower convective scales, and therefore more favorable conditions for wave amplification. Case 2 presents enormous variability during the latter stage of the horseshoe development, at times where large amplitude reflected waves crossed the point of observation. Note that no such variations are present in Figure 7.7(b), where no wave reflection takes place due to large wave damping. From the considerations arising from Figure 7.6, one can infer that more efficient emission of AKR seems to occur under conditions associated with faster wave propagation, even though (as in case 2) wave damping is higher. Although lower damping rates should help in continually feeding the horseshoe with resonant electrons, it did not result in favorable conditions for AKR.

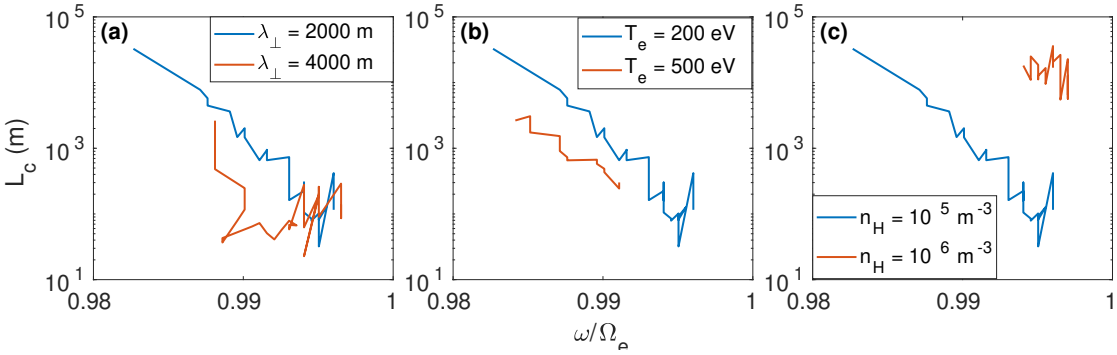

Figure 7.7: Comparison of convective scales at $z = 1.5\,R_E$ between the baseline simulation against increased (a) perpendicular scale, (b) temperature, (c) density.

7.4 Summary

In this chapter, the formation and time evolution of unstable horseshoe distributions as a result of electron acceleration by an IAW along geomagnetic field lines has been simulated in the context of an inhomogeneous plasma as described in chapter 5. Numerical data corresponding to these distributions were subsequently parametrized into an analytic representation, which was used to evaluate the convective growth length associated with the efficiency of AKR amplification through the ECI; following Bingham and Cairns [2000]. Smaller values of the convective length indicate increased wave amplification. The convective length at altitudes above the IAR decreases by a few to several orders of magnitude over a few seconds to values well below the size of the auroral cavity, which is strong evidence that dispersive Alfvén waves can generate AKR.

An estimation of the convective growth length at different locations along the magnetic field indicates that optimum conditions for AKR emission occur where the ratio of the electron plasma frequency to the cyclotron frequency is minimum, roughly at the same location where the gradient of the Alfvén speed profile is a maximum. At lower and higher altitudes the convective length increases, indicating lower efficiency of wave amplification. Within the IAR, AKR emission is very limited because a large fraction of accelerated electrons is reflected at the higher altitude end of the IAR.

Background plasma properties also affect the efficiency of AKR generation. By running additional simulations, it was found that lower convective scales are achieved by increasing the plasma temperature and the perpendicular wavelength. An increase in the plasma electron density, on the other hand, has the opposite effect of reducing the efficiency of wave amplification. In all cases, lower convective lengths coincide with an increased wave phase speed, regardless of the magnitude of wave damping.

Chapter 8

Conclusion

In this thesis, numerical simulations were used to investigate plasma dynamics upon interaction with dispersive Alfvén wave signals in various interesting contexts. Specifically, regular and inverted time dispersive signatures of suprathermal electrons in the topside ionosphere (chapter 4), wave propagation in the Ionospheric Alfvén Resonator (chapter 5), nonlinear electron trapping and transport in the kinetic regime (chapter 6), and generation of Auroral Kilometric Radiation in the Alfvénic density cavity (chapter 7). To this end, the original version of the drift kinetic (DK1D) Vlasov solver [Watt et al., 2004] was improved by expanding its range to include spatially inhomogeneous plasmas, while maintaining self-consistency between plasma and wave interactions. This was achieved by setting a time-invariant electrostatic potential across the simulation domain, uniquely defined by a given density model through the Vlasov condition for stationarity in the absence of wave fields. Spatial variation of the plasma temperature is also indirectly determined by this potential. Although these modifications were originally considered for Maxwellian distributions, frequent numerical issues eventually forced us into adapting the code to work with Lorentzian distributions, which are more numerically stable. A detailed description of the extended DK1D version is included in chapter 5. As a final point of this chapter, and as a testing exercise of code performance, wave propagation across the Ionospheric Alfvén Resonator was presented. Obtained results reproduce a number of known features commonly reported in observations: wave acceleration and deceleration modulated by the local Alfvén speed; wave reflection at the sharp density gradient near the peak of the Alfvén speed profile; electron beams produced by resonant acceleration, local thermalization by nonresonant interactions with the wave; strong damping of the parallel electric field in the cold plasma region; upward electron fluxes due to wave reflection; and upward fluxes due to magnetic convergence.

In chapter 4, the possible link between Alfvén wave propagation at the topside ionosphere and the occurrence of suprathermal dispersion, as recorded by the SEI instrument on board of ePOP and documented by Cameron [2015], was investigated. Observed events showed little pitch angle dispersion, and source locations ranged $2000 - 5000$ km. Given that the mirror effect was negligible along such short distances, a simplified version of the code, valid for a uniform magnetic field, was used in these cases. The simulations presented suggest that the plasma response to the wave becomes increasingly inductive as the local Alfvén speed is reduced. For cases where v_A takes typical values of the lower ionosphere (a few 1000 km/s), time sequences of the wave show strong damping of the original pulse, while a secondary structure faster than the original develops bearing its own fields and currents. In this scenario, dispersive signatures show energy decreasing electrons at energies well over expectation and with little to no evidence of thermalization due to nonresonant interaction. This response was also found to be sensitive to the perpendicular scale of the wave: with smaller scales enhancing the inductive effect. It is observed that typically, particle-wave interactions affect large sections of the unperturbed distribution to the extent that nonlinear effects are expected. Although a detailed physical mechanism explaining this behavior is not provided, sets of parameters which reproduce time dispersive signals with qualitative features and in a similar energy range to events observed by the SEI instrument are reported. Inverse dispersion was also attributed to the relative motion between source and detector: a spacecraft that follows the cross-field path of an Alfvén wave source, at a certain altitude lower than the source, will detect slow energy electrons ahead of higher energy ones, provided that the detector speed is faster than the wave source itself. The temporal extent of the energy inversion is inversely proportional to the vertical distance between the source and detector, but is also affected by the relative speed of the detector.

Chapter 6 discusses trapping of electrons by Kinetic Alfvén Waves originated near the equatorial region. Simulations indicate that Landau damping remains an active and influential factor in wave-particle dynamics for low latitude magnetospheric plasmas, despite that conditions are more favorable for particle trapping instead. This is an indication that the nonlinear theory of resonant interactions by O'Neil [1965] is unsuitable for the system at hand. A parametric study shows that damping rates increase rather sensitively with decreasing perpendicular scales, and to a lesser degree with increasing temperatures. Fluid theory predicts a similar dependence of the electric field magnitude under the same parameters. Thus, Landau damping effects are enhanced when there is an increase of the electric field. This is related to the fact that trapping of electrons is more efficient at intermediate values of the wave perpendicular scale. Regardless of the efficiency of trapping, the simulations reveal that waves are unable to survive for

distances longer than 3 Re. This emphasizes the importance of studying electron trapping in the magnetosphere using a formulation that incorporates nonlocal dispersive effects. Disregarding the effects of Landau damping will also likely lead to a large over- or under-estimation of the energy gain of interacting electrons.

Chapter 7 focused on the formation of unstable horseshoe distributions as a combined result of electron acceleration by inertial Alfvén waves and subsequent pitch angle dispersion due to magnetic convergence. The time evolution of the local distribution at selected points along the simulation domain was followed, and clearly identified horseshoe distributions that did not overlap with the bulk plasma were analyzed including the formation of horseshoe distribution before the appearance of electron conics. A computational procedure applied to the numerical distributions is used to identify the unstable component and fit it to an analytic expression. These functional representations were used to evaluate the convective growth length of the transverse magnetic mode following Bingham and Cairns [2000]. The convective growth length is inversely proportional to the wave growth rate and so small values are an indication of large emission. In general, the time evolution at a given location indicates that convective lengths decrease with time in an average sense, while exhibiting considerable time variability. As a function of time, the frequency of emission shifts towards the local electron cyclotron frequency. In some cases, the convective length shows drastic variations, typically by several orders of magnitude over very short time intervals. These abrupt changes take place where waves that have been reflected within the IAR reach the simulated point of observation. Comparison between results at different locations confirms that the maximum efficiency of the ECI occurs at the location where ω_{pe}/ω_{ce} takes its minimum value.

The efficiency of AKR generation due to variations of the plasma temperature and perpendicular scale was investigated. Comparison cases against the baseline case discussed in chapter 7 suggests that larger growth rates are associated with waves with larger phase velocities, regardless of wave damping. Unfortunately, the efficiency of AKR generation at low values of magnetospheric density could not be investigated as it was out of the dynamic range of DK1D. However, the density variation of magnetospheric electrons was investigated. It was found that for densities one order of magnitude larger than the ranges reported by *in situ* or remote observations, in cavities where AKR has been measured, the estimated convective lengths obtained are of the same order of size as the auroral density cavity, where no significant emission is expected.

The findings reported in this thesis substantiate the importance of dispersive Alfvén waves in Earth's magnetosphere, and identify the need for improved nonlinear and higher-dimensional simulation codes that have the improved spatial and temporal resolution needed to address trapping and generation of AKR.

Bibliography

Oleksiy Agapitov, Anton Artemyev, Vladimir Krasnoselskikh, Yuri V. Khotyaintsev, Didier Mourenas, Hugo Breuillard, Michael Balikhin, and Guy Rolland. Statistics of whistler mode waves in the outer radiation belt: Cluster staff-sa measurements. *Journal of Geophysical Research: Space Physics*, 118(6):3407–3420, 1974. doi: 10.1002/jgra.50312. URL https://agupubs.onlinelibrary.wiley.com/doi/abs/10.1002/jgra.50312.

S. I. Akasofu. A study of auroral displays photographed from the dmsp-2 satellite and from the alaska meridian chain of stations. *Space Science Reviews*, 16(5):617–725, Nov 1974. ISSN 1572-9672. doi: 10.1007/BF00182598. URL https://doi.org/10.1007/BF00182598.

L. Andersson, N. Ivchenko, J. Clemmons, A. A. Namgaladze, B. Gustavsson, J.-E. Wahlund, L. Eliasson, and R. Yu. Yurik. Electron signatures and Alfvén waves. *Journal of Geophysical Research: Space Physics*, 107(A9):SMP 15–1–SMP 15–14, 2002. ISSN 2156-2202. doi: 10.1029/2001JA900096. URL http://dx.doi.org/10.1029/2001JA900096. 1244.

V. Angelopoulos, J. A. Chapman, F. S. Mozer, J. D. Scudder, C. T. Russell, K. Tsuruda, T. Mukai, T. J. Hughes, and K. Yumoto. Plasma sheet electromagnetic power generation and its dissipation along auroral field lines. *Journal of Geophysical Research: Space Physics*, 107(A8):SMP 14–1–SMP 14–20, 2002. doi: 10.1029/2001JA900136. URL https://agupubs.onlinelibrary.wiley.com/doi/abs/10.1029/2001JA900136.

V. V. Kozlov Arnold V. I. and A. I. Neishtadt. *Mathematical Aspects of Classical and Celestial Mechanics*. Springer-Verlag Berlin Heidelberg, 2006.

R. L. Arnoldy. Auroral particle precipitation and birkeland currents. *Reviews of Geophysics*, 12(2):217–231, 1974. doi: 10.1029/RG012i002p00217. URL https://agupubs.onlinelibrary.wiley.com/doi/abs/10.1029/RG012i002p00217.

A. V. Artemyev, A. I. Neishtadt, L. M. Zelenyi, and D. L. Vainchtein. Adiabatic description of capture into resonance and surfatron acceleration of charged particles by electromagnetic waves. *Chaos: An Interdisciplinary Journal of Nonlinear Science*, 20(4): 043128, 2010. doi: 10.1063/1.3518360. URL `https://doi.org/10.1063/1.3518360`.

A. V. Artemyev, V. V. Krasnoselskikh, O. V. Agapitov, D. Mourenas, and G. Rolland. Non-diffusive resonant acceleration of electrons in the radiation belts. *Physics of Plasmas*, 19(12):122901, 2012. doi: 10.1063/1.4769726. URL `https://doi.org/10.1063/1.4769726`.

A. V. Artemyev, A. A. Vasiliev, D. Mourenas, O. V. Agapitov, and V. V. Krasnoselskikh. Nonlinear electron acceleration by oblique whistler waves: Landau resonance vs. cyclotron resonance. *Physics of Plasmas*, 20(12):122901, 2013. doi: 10.1063/1.4836595. URL `https://doi.org/10.1063/1.4836595`.

A. V. Artemyev, O. V. Agapitov, F. Mozer, and V. Krasnoselskikh. Thermal electron acceleration by localized bursts of electric field in the radiation belts. *Geophysical Research Letters*, 41(16):5734–5739, 2014. doi: 10.1002/2014GL061248. URL `https://agupubs.onlinelibrary.wiley.com/doi/abs/10.1002/2014GL061248`.

A. V. Artemyev, O A Agapitov, D. Mourenas, V. V. Krasnoselskikh, and F. S Mozer. Wave energy budget analysis in the earth's radiation belts uncovers a missing energy. In *Nature communications*, 2015a.

A. V. Artemyev, R. Rankin, and M. Blanco. Electron trapping and acceleration by kinetic Alfvén waves in the inner magnetosphere. *Journal of Geophysical Research: Space Physics*, 120(12):10,305–10,316, 2015b. doi: 10.1002/2015JA021781. URL `https://agupubs.onlinelibrary.wiley.com/doi/abs/10.1002/2015JA021781`.

M. Balikhin, M. Gedalin, and A. Petrukovich. New mechanism for electron heating in shocks. *Phys. Rev. Lett.*, 70:1259–1262, Mar 1993. doi: 10.1103/PhysRevLett.70.1259. URL `https://link.aps.org/doi/10.1103/PhysRevLett.70.1259`.

W. Baumjohann and R. Treumann. *Basic Space Plasma Physics*. Imperial College Press, 1997.

T. F. Bell. The nonlinear gyroresonance interaction between energetic electrons and coherent vlf waves propagating at an arbitrary angle with respect to the earth's magnetic field. *Journal of Geophysical Research: Space Physics*, 89(A2):905–918, 1984. doi: 10.1029/JA089iA02p00905. URL `https://agupubs.onlinelibrary.wiley.com/doi/abs/10.1029/JA089iA02p00905`.

R. Bingham and R. A. Cairns. Generation of auroral kilometric radiation by electron horseshoe distributions. *Physics of Plasmas*, 7(7):3089–3092, 2000. doi: 10.1063/1.874163. URL `https://doi.org/10.1063/1.874163`.

Charles K. Birdsall and A. Bruce Langdon. *Plasma physics via computer simulation*. Series in plasma physics. Taylor & Francis, New York, 2005. ISBN 0-7503-1025-1.

J. A. Bittencourt. *Fundamentals of Plasma Physics*. Springer, 2004.

J. M. Blanco. Electron acceleration by Inertial Alfvén Waves. Master's thesis, University of Alberta, Canada, 2011.

D. A. Bryant, A. C. Cook, Z.-S. Wang, U. Angelis, and C. H. Perry. Turbulent acceleration of auroral electrons. *Journal of Geophysical Research: Space Physics*, 96(A8): 13829–13839, 1991. doi: 10.1029/91JA01105. URL `https://agupubs.onlinelibrary.wiley.com/doi/abs/10.1029/91JA01105`.

Taylor Cameron. Acceleration of auroral electrons. Master's thesis, University of Calgary, Canada, 2015.

Taylor Cameron and David Knudsen. Inverse electron energy dispersion from moving auroral forms. *Journal of Geophysical Research: Space Physics*, 121(12):11,896–11,911, 2016. doi: 10.1002/2016JA023045.

C. C. Chaston, C. W. Carlson, W. J. Peria, R. E. Ergun, and J. P. McFadden. FAST observations of inertial Alfvén waves in the dayside aurora. *Geophysical Research Letters*, 26(6):647–650, Mar 15 1999.

C. C. Chaston, Carlson C. W., Ergun R. E., and McFadden J. P. Alfvén Waves, Density Cavities and Electron Acceleration Observed from the FAST Spacecraft. *Physica Scripta*, 2000(T84):64, 2000. URL `http://stacks.iop.org/1402-4896/2000/i=T84/a=014`.

C. C. Chaston, J. W. Bonnell, C. W. Carlson, M. Berthomier, L. M. Peticolas, I. Roth, J. P. McFadden, R. E. Ergun, and R. J. Strangeway. Electron acceleration in the ionospheric Alfvén resonator. *Journal of Geophysical Research: Space Physics*, 107 (A11):SMP 41–1–SMP 41–16, 2002a. ISSN 2156-2202. doi: 10.1029/2002JA009272. URL `http://dx.doi.org/10.1029/2002JA009272`. 1413.

C. C. Chaston, J. W. Bonnell, L. M. Peticolas, C. W. Carlson, J. P. McFadden, and R. E. Ergun. Driven Alfvén waves and electron acceleration: A FAST case study.

Geophysical Research Letters, 29(11):30–1–30–4, 2002b. ISSN 1944-8007. doi: 10.1029/2001GL013842. URL http://dx.doi.org/10.1029/2001GL013842.

C. C. Chaston, C. Salem, J. W. Bonnell, C. W. Carlson, R. E. Ergun, R. J. Strangeway, and J. P. McFadden. The Turbulent Alfvénic Aurora. *Physical Review Letters*, 100(17): 175003, May 2008. doi: 10.1103/PhysRevLett.100.175003.

C. C. Chaston, J. W. Bonnell, L. Clausen, and V. Angelopoulos. Energy transport by kinetic-scale electromagnetic waves in fast plasma sheet flows. *Journal of Geophysical Research: Space Physics*, 117(A9), 2012. doi: 10.1029/2012JA017863. URL https://agupubs.onlinelibrary.wiley.com/doi/abs/10.1029/2012JA017863.

C. C. Chaston, J. W. Bonnell, and C. Salem. Heating of the plasma sheet by broadband electromagnetic waves. *Geophysical Research Letters*, 41(23):8185–8192, 2014. doi: 10.1002/2014GL062116. URL https://agupubs.onlinelibrary.wiley.com/doi/abs/10.1002/2014GL062116.

Li-Jen Chen, Craig A. Kletzing, Shuanghui Hu, and Scott R. Bounds. Auroral electron dispersion below inverted-V energies: Resonant deceleration and acceleration by Alfvén waves. *Journal of Geophysical Research: Space Physics*, 110(A10):n/a–n/a, 2005. ISSN 2156-2202. doi: 10.1029/2005JA011168. URL http://dx.doi.org/10.1029/2005JA011168. A10S13.

Y. T. Chiu and Michael Schulz. Self-consistent particle and parallel electrostatic field distributions in the magnetospheric-ionospheric auroral region. *Journal of Geophysical Research: Space Physics*, 83(A2):629–642, 1978. doi: 10.1029/JA083iA02p00629.

K. R. Chu. The electron cyclotron maser. *Reviews of Modern Physics*, 76(2):489–540, Apr 2004.

J. H. Clemmons, M. H. Boehm, G. E. Paschmann, and G. Haerendel. Signatures of energy-time dispersed electron fluxes measured by Freja. *Geophysical Research Letters*, 21(17):1899–1902, 1994. ISSN 1944-8007. doi: 10.1029/94GL00885. URL http://dx.doi.org/10.1029/94GL00885.

P. A. Damiano and A. N. Wright. Two-dimensional hybrid MHD-kinetic electron simulations of an Alfvén wave pulse. *Journal of Geophysical Research: Space Physics*, 110(A1), 2005. doi: 10.1029/2004JA010603. URL https://agupubs.onlinelibrary.wiley.com/doi/abs/10.1029/2004JA010603.

John Dawson. On Landau damping. *The Physics of Fluids*, 4(7):869–874, 1961. doi: 10.1063/1.1706419. URL https://aip.scitation.org/doi/abs/10.1063/1.1706419.

A. G. Demekhov. Generation of vlf emissions with the increasing and decreasing frequency in the magnetosperic cyclotron maser in the backward wave oscillator regime. *Radiophysics and Quantum Electronics*, 53(11):609–622, Apr 2011. ISSN 1573-9120. doi: 10.1007/s11141-011-9256-x. URL https://doi.org/10.1007/s11141-011-9256-x.

M. H. Denton, M. F. Thomsen, H. Korth, S. Lynch, J. C. Zhang, and M. W. Liemohn. Bulk plasma properties at geosynchronous orbit. *Journal of Geophysical Research: Space Physics*, 110(A7), 2005. doi: 10.1029/2004JA010861. URL https://agupubs.onlinelibrary.wiley.com/doi/abs/10.1029/2004JA010861.

R. E. Denton, K. Takahashi, I. A. Galkin, P. A. Nsumei, X. Huang, B. W. Reinisch, R. R. Anderson, M. K. Sleeper, and W. J. Hughes. Distribution of density along magnetospheric field lines. *Journal of Geophysical Research: Space Physics*, 111(A4), 2006. doi: 10.1029/2005JA011414. URL https://agupubs.onlinelibrary.wiley.com/doi/abs/10.1029/2005JA011414.

R. E. Ergun, C. W. Carlson, J. P. McFadden, F. S. Mozer, G. T. Delory, W. Peria, C. C. Chaston, M. Temerin, R. Elphic, R. Strangeway, R. Pfaff, C. A. Cattell, D. Klumpar, E. Shelley, W. Peterson, E. Moebius, and L. Kistler. Fast satellite wave observations in the AKR source region. *Geophysical Research Letters*, 25(12):2061–2064, 1998. ISSN 1944-8007. doi: 10.1029/98GL00570. URL http://dx.doi.org/10.1029/98GL00570.

R. E. Ergun, C. W. Carlson, J. P. McFadden, G. T. Delory, R. J. Strangeway, and P. L. Pritchett. Electron-cyclotron maser driven by charged-particle acceleration from magnetic field-aligned electric fields. *Astrophysical Journal*, 538(1, 1):456–466, Jul 20 2000. doi: 10.1086/309094.

R. E. Ergun, L. Andersson, Y. J. Su, D. L. Newman, M. V. Goldman, W. Lotko, C. C. Chaston, and C. W. Carlson. Localized parallel electric fields associated with inertial Alfvén waves. *Physics of Plasmas*, 12(7), Jul 2005.

R. E. Ergun, K. A. Goodrich, J. E. Stawarz, L. Andersson, and V. Angelopoulos. Large-amplitude electric fields associated with bursty bulk flow braking in the earth's plasma sheet. *Journal of Geophysical Research: Space Physics*, 120(3):1832–1844, 2015. doi: 10.1002/2014JA020165. URL https://agupubs.onlinelibrary.wiley.com/doi/abs/10.1002/2014JA020165.

Xiangrong Fu, Misa M. Cowee, Reinhard H. Friedel, Herbert O. Funsten, S. Peter Gary, George B. Hospodarsky, Craig Kletzing, William Kurth, Brian A. Larsen, Kaijun Liu, Elizabeth A. MacDonald, Kyungguk Min, Geoffrey D. Reeves, Ruth M. Skoug,

and Dan Winske. Whistler anisotropy instabilities as the source of banded chorus: Van allen probes observations and particle-in-cell simulations. *Journal of Geophysical Research: Space Physics*, 119(10):8288–8298, 2014. doi: 10.1002/2014JA020364. URL `https://agupubs.onlinelibrary.wiley.com/doi/abs/10.1002/2014JA020364`.

C. Gabrielse, V. Angelopoulos, A. Runov, and D. L. Turner. The effects of transient, localized electric fields on equatorial electron acceleration and transport toward the inner magnetosphere. *Journal of Geophysical Research: Space Physics*, 117(A10), 2012. doi: 10.1029/2012JA017873. URL `https://agupubs.onlinelibrary.wiley.com/doi/abs/10.1029/2012JA017873`.

N. Y. Ganushkina, O. A. Amariutei, Y. Y. Shprits, and M. W. Liemohn. Transport of the plasma sheet electrons to the geostationary distances. *Journal of Geophysical Research: Space Physics*, 118(1):82–98, 2013. doi: 10.1029/2012JA017923. URL `https://agupubs.onlinelibrary.wiley.com/doi/abs/10.1029/2012JA017923`.

C. K. Goertz and R. W Boswell. Magnetosphere-ionosphere coupling. *Journal of Geophysical Research: Space Physics*, 84(A12):7239–7246, 1979. ISSN 2156-2202. doi: 10.1029/JA084iA12p07239.

I. Gradshteyn and I. Ryzhic. *Table of Integrals, Series and Products*. Elsevier, New York, 6th edition, 2000. p. 322.

Donald A. Gurnett and Amitava Bhattacharjee. *Introduction to Plasma Physics with space and laboratory applications*. Cambridge University Press, 2005.

Vincent Gnot, P Louarn, and F Mottez. Alfvn wave interaction with inhomogeneous plasmas: Acceleration and energy cascade towards small-scales. *Ann Geophys*, 22, 06 2004. doi: 10.5194/angeo-22-2081-2004.

J. Hanasz, H. Feraudy, R. Schreiber, G. Parks, M. Brittnacher, M. M. Mogilevsky, and T. V. Romantsova. Wideband bursts of auroral kilometric radiation and their association with UV auroral bulges. *Journal of Geophysical Research: Space Physics*, 106(A3):3859–3871, 2001. doi: 10.1029/2000JA900098. URL `https://agupubs.onlinelibrary.wiley.com/doi/abs/10.1029/2000JA900098`.

J. Hanasz, H. de Feraudy, R. Schreiber, and M. Panchenko. Pulsations of the auroral kilometric radiation. *Journal of Geophysical Research: Space Physics*, 111(A3), 2006. doi: 10.1029/2005JA011302. URL `https://agupubs.onlinelibrary.wiley.com/doi/abs/10.1029/2005JA011302`.

Jan Hanasz, Roman Schreiber, Jolene Pickett, and Herv de Feraudy. Pulsations of auroral kilometric radiation at PC1 frequencies. *Geophysical Research Letters*, 35(15): n/a–n/a, 2008. doi: 10.1029/2008GL034609.

Akira Hasegawa. Particle acceleration by MHD surface wave and formation of aurora. *Journal of Geophysical Research*, 81(28):5083–5090, 1976. doi: 10.1029/JA081i028p05083.

Akira Hasegawa and Kunioki Mima. Exact solitary alfvén wave. *Phys. Rev. Lett.*, 37: 690–693, Sep 1976. doi: 10.1103/PhysRevLett.37.690. URL `https://link.aps.org/doi/10.1103/PhysRevLett.37.690`.

Akira Hasegawa and Kunioki Mima. Anomalous transport produced by kinetic alfvn wave turbulence. *Journal of Geophysical Research: Space Physics*, 83(A3):1117–1123, 1978. doi: 10.1029/JA083iA03p01117. URL `https://agupubs.onlinelibrary.wiley.com/doi/abs/10.1029/JA083iA03p01117`.

Richard B. Horne, Gavin V. Wheeler, and Hugo St. C. K. Alleyne. Proton and electron heating by radially propagating fast magnetosonic waves. *Journal of Geophysical Research: Space Physics*, 105(A12):27597–27610, 2000. doi: 10.1029/2000JA000018. URL `https://agupubs.onlinelibrary.wiley.com/doi/abs/10.1029/2000JA000018`.

P. Janhunen, A. Olsson, J. Hanasz, C. Russell, H. Laakso, and J. Samson. Different Alfvén wave acceleration processes of electrons in substorms at 4-5 RE and 2-3 RE radial distance. *Annales Geophysicae*, 22:2213–2227, June 2004. doi: 10.5194/angeo-22-2213-2004.

C. F. F. Karney. Stochastic ion heating by a lower hybrid wave. *The Physics of Fluids*, 21(9):1584–1599, 1978. doi: 10.1063/1.862406. URL `https://aip.scitation.org/doi/abs/10.1063/1.862406`.

I. V. Karpman and David Shklyar. Nonlinear damping of potential monochromatic waves in an inhomogeneous plasma. *Journal of Experimental and Theoretical Physics - J EXP THEOR PHYS*, 35, 01 1972.

V I Karpman, Ja N Istomin, and D R Shklyar. Nonlinear theory of a quasi-monochromatic whistler mode packet in inhomogeneous plasma. *Plasma Physics*, 16 (8):685, 1974. URL `http://stacks.iop.org/0032-1028/16/i=8/a=001`.

C. F. Kennel and H. E. Petschek. Limit on stably trapped particle fluxes. *Journal of Geophysical Research*, 71(1):1–28, 1966. doi: 10.1029/JZ071i001p00001. URL `https://agupubs.onlinelibrary.wiley.com/doi/abs/10.1029/JZ071i001p00001`.

M. Kivelson and C. Russel. *Introduction to Space Physics*. Cambridge University Press, 1995.

C. A. Kletzing. Electron acceleration by kinetic Alfvén waves. *Journal of Geophysical Research: Space Physics*, 99(A6):11095–11103, 1994. ISSN 2156-2202. doi: 10.1029/94JA00345. URL http://dx.doi.org/10.1029/94JA00345.

C. A. Kletzing and S. Hu. Alfvén wave generated electron time dispersion. *Geophysical Research Letters*, 28(4):693–696, 2001. ISSN 1944-8007. doi: 10.1029/2000GL012179. URL http://dx.doi.org/10.1029/2000GL012179.

C. A. Kletzing and R. B. Torbert. Electron time dispersion. *Journal of Geophysical Research: Space Physics*, 99(A2):2159–2172, 1994. ISSN 2156-2202. doi: 10.1029/93JA01745. URL http://dx.doi.org/10.1029/93JA01745.

C. A. Kletzing, J. D. Scudder, E. E. Dors, and C. Curto. Auroral source region: Plasma properties of the high-latitude plasma sheet. *Journal of Geophysical Research: Space Physics*, 108(A10), 2003. doi: 10.1029/2002JA009678. URL https://agupubs.onlinelibrary.wiley.com/doi/abs/10.1029/2002JA009678.

D. J. Knudsen, J. K. Burchill, T. G. Cameron, G. A. Enno, A. Howarth, and A. W. Yau. The CASSIOPE/e-POP suprathermal electron imager (sei). *Space Science Reviews*, 189(1):65–78, 2015. ISSN 1572-9672. doi: 10.1007/s11214-015-0151-1. URL http://dx.doi.org/10.1007/s11214-015-0151-1.

G. Laval and R. Pellat. Particle acceleration by electrostatic waves propagating in an inhomogeneous plasma. *Journal of Geophysical Research*, 75(16):3255–3256, 1970. doi: 10.1029/JA075i016p03255. URL https://agupubs.onlinelibrary.wiley.com/doi/abs/10.1029/JA075i016p03255.

Randall J. LeVeque. *Finite volume methods for hyperbolic problems*. Cambridge texts in applied mathematics. Cambridge University Press, Cambridge, New York, 2002. ISBN 0-521-81087-6. URL http://opac.inria.fr/record=b1100566.

W. Li, R. M. Thorne, J. Bortnik, Y. Nishimura, V. Angelopoulos, L. Chen, J. P. McFadden, and J. W. Bonnell. Global distributions of suprathermal electrons observed on themis and potential mechanisms for access into the plasmasphere. *Journal of Geophysical Research: Space Physics*, 115(A12), 2010. doi: 10.1029/2010JA015687. URL https://agupubs.onlinelibrary.wiley.com/doi/abs/10.1029/2010JA015687.

P. Louarn, J. E. Wahlund, T. Chust, H. Deferaudy, A. Roux, B. Holback, P. O. Dovner, A. I. Eriksson, and G. Holmgren. Observation of kinetic Alfvén waves by the FREJA Spacecraft. *Geophysical Research Letters*, 21(17):1847–1850, AUG 15 1994.

R. L. Lysak and Y. Song. The role of Alfvén waves in the formation of auroral parallel electric fields. In Ohtani, S., Fujii, R., Hesse, M., Lysak, R. L., editor, *Magnetospheric Current Systems*, volume 118 of *Geophysical Monograph Series*, pages 147–155, 2000.

Robert L. Lysak. Feedback instability of the ionospheric resonant cavity. *Journal of Geophysical Research: Space Physics*, 96(A2):1553–1568, 1991. ISSN 2156-2202. doi: 10.1029/90JA02154. URL `http://dx.doi.org/10.1029/90JA02154`.

Robert L. Lysak and William Lotko. On the kinetic dispersion relation for shear Alfvén waves. *Journal of Geophysical Research: Space Physics*, 101(A3):5085–5094, 1996. ISSN 2156-2202. doi: 10.1029/95JA03712. URL `http://dx.doi.org/10.1029/95JA03712`.

Robert L Lysak and Yan Song. Kinetic theory of the alfvén wave acceleration of auroral electrons. *Journal of Geophysical Research D: Atmospheres*, 108(A4), 1 2003. ISSN 0148-0227. doi: 10.1029/2002JA009406.

Schulz M. and L. J. Lanzerotti. *Particle diffusion in the radiation belts*. Springer, New York, 1974.

Richard M Thorne, Binbin Ni, Xin Tao, Richard B Horne, and Nigel Meredith. Scattering by chorus waves as the dominant cause of diffuse aurora precipitation. *Nature*, 467:943–6, 10 2010. doi: 10.1038/nature09467.

R. L. Mace and M. A. Hellberg. A dispersion function for plasmas containing superthermal particles. *Physics of Plasmas*, 2(6):2098–2109, 1995. doi: 10.1063/1.871296. URL `https://doi.org/10.1063/1.871296`.

David M. Malaspina, John R. Wygant, Robert E. Ergun, Geoff D. Reeves, Ruth M. Skoug, and Brian A. Larsen. Electric field structures and waves at plasma boundaries in the inner magnetosphere. *Journal of Geophysical Research: Space Physics*, 120(6):4246–4263, 2015. doi: 10.1002/2015JA021137. URL `https://agupubs.onlinelibrary.wiley.com/doi/abs/10.1002/2015JA021137`.

J. P. McFadden, C. W. Carlson, M. H. Boehm, and T. J. Hallinan. Field-aligned electron flux oscillations that produce flickering aurora. *Journal of Geophysical Research: Space Physics*, 92(A10):11133–11148, 1987. ISSN 2156-2202. doi: 10.1029/JA092iA10p11133. URL `http://dx.doi.org/10.1029/JA092iA10p11133`.

Nigel P. Meredith, Richard B. Horne, and Roger R. Anderson. Substorm dependence of chorus amplitudes: Implications for the acceleration of electrons to relativistic energies. *Journal of Geophysical Research: Space Physics*, 106(A7):13165–13178, 2001. doi: 10.1029/2000JA900156. URL https://agupubs.onlinelibrary.wiley.com/doi/abs/10.1029/2000JA900156.

A. Morioka, Y. Miyoshi, F. Tsuchiya, H. Misawa, T. Sakanoi, K. Yumoto, R. R. Anderson, J. D. Menietti, and E. F. Donovan. Dual structure of auroral acceleration regions at substorm onsets as derived from auroral kilometric radiation spectra. *Journal of Geophysical Research: Space Physics*, 112(A6), 2007. doi: 10.1029/2006JA012186. URL https://agupubs.onlinelibrary.wiley.com/doi/abs/10.1029/2006JA012186.

A. Morioka, Y. Miyoshi, F. Tsuchiya, H. Misawa, K. Yumoto, G. K. Parks, R. R. Anderson, J. D. Menietti, E. F. Donovan, F. Honary, and E. Spanswick. AKR breakup and auroral particle acceleration at substorm onset. *Journal of Geophysical Research: Space Physics*, 113(A9), 2008. doi: 10.1029/2008JA013322. URL https://agupubs.onlinelibrary.wiley.com/doi/abs/10.1029/2008JA013322.

F. Mottez and V. Gnot. Electron acceleration by an alfvnic pulse propagating in an auroral plasma cavity. *Journal of Geophysical Research: Space Physics*, 116(A1), 2011. doi: 10.1029/2010JA016367. URL https://agupubs.onlinelibrary.wiley.com/doi/abs/10.1029/2010JA016367.

Didier Mourenas, Anton Artemyev, Oleksiy Agapitov, V Krasnoselskikh, and F S. Mozer. Very oblique whistler generation by low energy electron streams: Oblique whistler-mode wave generation. *Journal of Geophysical Research: Space Physics*, 120, 04 2015. doi: 10.1002/2015JA021135.

F. S. Mozer, S. D. Bale, J. W. Bonnell, C. C. Chaston, I. Roth, and J. Wygant. Megavolt parallel potentials arising from double-layer streams in the earth's outer radiation belt. *Phys. Rev. Lett.*, 111:235002, Dec 2013. doi: 10.1103/PhysRevLett.111.235002. URL https://link.aps.org/doi/10.1103/PhysRevLett.111.235002.

F. S. Mozer, O. Agapitov, V. Krasnoselskikh, S. Lejosne, G. D. Reeves, and I. Roth. Direct observation of radiation-belt electron acceleration from electron-volt energies to megavolts by nonlinear whistlers. *Phys. Rev. Lett.*, 113:035001, Jul 2014. doi: 10.1103/PhysRevLett.113.035001. URL https://link.aps.org/doi/10.1103/PhysRevLett.113.035001.

F. S. Mozer, O. V. Agapitov, A. Artemyev, J. F. Drake, V. Krasnoselskikh, S. Lejosne, and I. Vasko. Time domain structures: What and where they are, what they do, and

how they are made. *Geophysical Research Letters*, 42(10):3627–3638, 2015. doi: 10.1002/2015GL063946. URL https://agupubs.onlinelibrary.wiley.com/doi/abs/10.1002/2015GL063946.

A. I. Neishtadt. *Hamiltonian systems with three or more degrees of freedom*. Number 533 in NATO ASI Series C. Kluwer Academic, 1999. doi: 10.1063/1.166236.

A I Neishtadt. Averaging, passage through resonances, andcapture into resonance in two-frequency systems. *Russian Mathematical Surveys*, 69(5):771, 2014. URL http://stacks.iop.org/0036-0279/69/i=5/a=771.

Binbin Ni, Richard M. Thorne, Richard B. Horne, Nigel P. Meredith, Yuri Y. Shprits, Lunjin Chen, and Wen Li. Resonant scattering of plasma sheet electrons leading to diffuse auroral precipitation: 1. evaluation for electrostatic electron cyclotron harmonic waves. *Journal of Geophysical Research: Space Physics*, 116(A4), 2011a. doi: 10.1029/2010JA016232. URL https://agupubs.onlinelibrary.wiley.com/doi/abs/10.1029/2010JA016232.

Binbin Ni, Richard M. Thorne, Nigel P. Meredith, Richard B. Horne, and Yuri Y. Shprits. Resonant scattering of plasma sheet electrons leading to diffuse auroral precipitation: 2. evaluation for whistler mode chorus waves. *Journal of Geophysical Research: Space Physics*, 116(A4), 2011b. doi: 10.1029/2010JA016233. URL https://agupubs.onlinelibrary.wiley.com/doi/abs/10.1029/2010JA016233.

Binbin Ni, Jun Liang, Richard M. Thorne, Vassilis Angelopoulos, Richard B. Horne, Marina Kubyshkina, Emma Spanswick, Eric F. Donovan, and Dirk Lummerzheim. Efficient diffuse auroral electron scattering by electrostatic electron cyclotron harmonic waves in the outer magnetosphere: A detailed case study. *Journal of Geophysical Research: Space Physics*, 117(A1), 2012. doi: 10.1029/2011JA017095. URL https://agupubs.onlinelibrary.wiley.com/doi/abs/10.1029/2011JA017095.

Binbin Ni, Jacob Bortnik, Yukitoshi Nishimura, Richard M. Thorne, Wen Li, Vassilis Angelopoulos, Yusuke Ebihara, and Allan T. Weatherwax. Chorus wave scattering responsible for the earth's dayside diffuse auroral precipitation: A detailed case study. *Journal of Geophysical Research: Space Physics*, 119(2):897–908, 2014. doi: 10.1002/2013JA019507. URL https://agupubs.onlinelibrary.wiley.com/doi/abs/10.1002/2013JA019507.

Dwight R. Nicholson. *Introduction to Plasma Theory*. John Wiley and Sons, 1983.

T. G. Northrop. *The adiabatic motion of charged particles*. Interscience Publishers John Wiley and Sons, New York-London-Sydney, 1963.

D. Nunn. Wave-particle interactions in electrostatic waves in an inhomogeneous medium. *Journal of Plasma Physics*, 6(2):291307, 1971. doi: 10.1017/S0022377800006061.

David Nunn. A self-consistent theory of triggered vlf emissions. In B. M. McCormac, editor, *Magnetospheric Physics*, pages 313–321, Dordrecht, 1974. Springer Netherlands. ISBN 978-94-010-2214-9.

A. Olsson, P. Janhunen, J. Hanasz, M. Mogilevsky, S. Perraut, and J. Menietti. Observational study of generation conditions of substorm-associated low-frequency AKR emissions. *Annales Geophysicae*, 22:3571–3582, October 2004. doi: 10.5194/angeo-22-3571-2004.

Thomas O'Neil. Collisionless damping of nonlinear plasma oscillations. *The Physics of Fluids*, 8(12):2255–2262, 1965. doi: 10.1063/1.1761193. URL `https://aip.scitation.org/doi/abs/10.1063/1.1761193`.

George Parks. *Physics of Space Plasmas: an Introduction*. Westview Press, 2003.

G. Paschmann, S. Haaland, and R. Treumann. *Auroral Plasma Physics*. Kluwer Academic Publishers, 2003.

V. Pierrard and J. Lemaire. Lorentzian ion exosphere model. *Journal of Geophysical Research: Space Physics*, 101(A4):7923–7934, 1996. ISSN 2156-2202. doi: 10.1029/95JA03802. URL `http://dx.doi.org/10.1029/95JA03802`.

I Potapenko, C A de Azevedo, and P Sakanaka. Electron heating and acceleration by alfvn waves with varying phase velocity. *Physica Scripta*, 62:486, 03 2006. doi: 10.1238/Physica.Regular.062a00486.

R. Rankin, C. E. J. Watt, and J. C. Samson. Self-consistent wave-particle interactions in dispersive scale long-period field-line-resonances. *Geophysical Research Letters*, 34 (23), 2007. ISSN 1944-8007. doi: 10.1029/2007GL031317. URL `http://dx.doi.org/10.1029/2007GL031317`. L23103.

B. W. Sheeley, M. B. Moldwin, H. K. Rassoul, and R. R. Anderson. An empirical plasmasphere and trough density model: Crres observations. *Journal of Geophysical Research: Space Physics*, 106(A11):25631–25641, 2001. doi: 10.1029/2000JA000286. URL `https://agupubs.onlinelibrary.wiley.com/doi/abs/10.1029/2000JA000286`.

Run Shi, Huixin Liu, A. Yoshikawa, Beichen Zhang, and Binbin Ni. Coupling of electrons and inertial Alfvén waves in the topside ionosphere. *Journal of Geophysical Research: Space Physics*, 118(6):2903–2910, 2013. ISSN 2169-9402. doi: 10.1002/jgra.50355. URL http://dx.doi.org/10.1002/jgra.50355.

D. R. Shkliar. Stochastic motion of relativistic particles in the field of a monochromatic wave. *Zhurnal Eksperimentalnoi i Teoreticheskoi Fiziki*, 80:2272–2282, June 1981.

D. R. Shklyar. On the nature of particle energization via resonant wave-particle interaction in the inhomogeneous magnetospheric plasma. *Annales Geophysicae*, 29(6): 1179–1188, 2011. doi: 10.5194/angeo-29-1179-2011. URL https://www.ann-geophys.net/29/1179/2011/.

David Shklyar and Hiroshi Matsumoto. Oblique whistler-mode waves in the inhomogeneous magnetospheric plasma: Resonant interactions with energetic charged particles. *Surveys in Geophysics*, 30(2):55–104, Apr 2009. ISSN 1573-0956. doi: 10.1007/s10712-009-9061-7. URL https://doi.org/10.1007/s10712-009-9061-7.

M. I. Sitnov, N. A. Tsyganenko, A. Y. Ukhorskiy, and P. C. Brandt. Dynamical data-based modeling of the storm-time geomagnetic field with enhanced spatial resolution. *Journal of Geophysical Research: Space Physics*, 113(A7), 2008. doi: 10.1029/2007JA013003. URL https://agupubs.onlinelibrary.wiley.com/doi/abs/10.1029/2007JA013003.

K. Stasiewicz, P. Bellan, C. Chaston, C. Kletzing, R. Lysak, J. Maggs, O. Pokhotelov, C. Seyler, P. Shukla, L. Stenflo, A. Streltsov, and J.-E. Wahlund. Small Scale Alfvénic Structure in the Aurora. *Space Science Reviews*, 92(3):423–533, May 2000. ISSN 1572-9672. doi: 10.1023/A:1005207202143. URL https://doi.org/10.1023/A:1005207202143.

R. J. Strangeway, R. E. Ergun, C. W. Carlson, J. P. Mcfadden, G. T. Delory, and P. L. Pritchett. Accelerated electrons as the source of Auroral Kilometric Radiation. *Physica and Chemistry of the Earth PART C-Solar-Terrestrial and Planeraty Science*, 26(1-3): 145–149, 2001. doi: 10.1016/S1464-1917(00)00100-8.

Yi-Jiun Su, Samuel T. Jones, Robert E. Ergun, and Scott E. Parker. Modeling of field-aligned electron bursts by dispersive Alfvén waves in the dayside auroral region. *Journal of Geophysical Research: Space Physics*, 109(A11):n/a–n/a, 2004. ISSN 2156-2202. doi: 10.1029/2003JA010344. URL http://dx.doi.org/10.1029/2003JA010344. A11201.

Yi-Jiun Su, R. E. Ergun, S. T. Jones, R. J. Strangeway, C. C. Chaston, S. E. Parker, and J. L. Horwitz. Generation of short-burst radiation through Alfvénic acceleration of auroral electrons. *Journal of Geophysical Research: Space Physics*, 112(A6), 2007. ISSN 2156-2202. doi: 10.1029/2006JA012131. URL `http://dx.doi.org/10.1029/2006JA012131`.

Yi-Jiun Su, Lun Ma, Robert E. Ergun, Philip L. Pritchett, and Charles W. Carlson. Short-burst auroral radiations in Alfvénic acceleration regions: FAST observations. *Journal of Geophysical Research-Space Physics*, 113(A8), Aug 12 2008. doi: 10.1029/2007JA012896.

Danny Summers and Richard M. Thorne. The modified plasma dispersion function. *Physics of Fluids B*, 3(8):1835–1847, 1991. doi: http://dx.doi.org/10.1063/1.859653.

Danny Summers, Yoshiharu Omura, Yu Miyashita, and Dong-Hun Lee. Nonlinear spatiotemporal evolution of whistler mode chorus waves in earth's inner magnetosphere. *Journal of Geophysical Research: Space Physics*, 117(A9), 2012. doi: 10.1029/2012JA017842. URL `https://agupubs.onlinelibrary.wiley.com/doi/abs/10.1029/2012JA017842`.

H. Tanaka, Y. Saito, K. Asamura, S. Ishii, and T. Mukai. High time resolution measurement of multiple electron precipitations with energy-time dispersion in high-latitude part of the cusp region. *Journal of Geophysical Research: Space Physics*, 110(A7):n/a–n/a, 2005. ISSN 2156-2202. doi: 10.1029/2004JA010664. URL `http://dx.doi.org/10.1029/2004JA010664`. A07204.

B. J. Thompson and R. L. Lysak. Electron acceleration by inertial Alfvén waves. *Journal of Geophysical Research*, 101:5359–5370, March 1996. doi: 10.1029/95JA03622.

V. T. Tikhonchuk and R. Rankin. Parallel potential driven by a kinetic Alfvén wave on geomagnetic field lines. *Journal of Geophysical Research-Space Physics*, 107(A7), Jul 2002. doi: 10.1029/2001JA000231.

V. Y. Trakhtengerts, A. G. Demekhov, Y. Hobara, and M. Hayakawa. Phase-bunching effects in triggered vlf emissions: Antenna effect. *Journal of Geophysical Research: Space Physics*, 108(A4), 2003. doi: 10.1029/2002JA009415. URL `https://agupubs.onlinelibrary.wiley.com/doi/abs/10.1029/2002JA009415`.

R. A. Treumann and W. Baumjohann. *Advanced Space Plasma Physics*. Imperial College Press, 1997.

Rudolf A Treumann. Generalized-lorentzian thermodynamics. *Physica Scripta*, 59(3): 204, 1999. URL `http://stacks.iop.org/1402-4896/59/i=3/a=004`.

Rudolf A. Treumann. The electron-cyclotron maser for astrophysical application. *Astronomy and Astrophysics review*, 13(4):229–315, Aug 2006.

N. A. Tsyganenko, H. J. Singer, and J. C. Kasper. Storm-time distortion of the inner magnetosphere: How severe can it get? *Journal of Geophysical Research: Space Physics*, 108(A5), 2003. doi: 10.1029/2002JA009808. URL `https://agupubs.onlinelibrary.wiley.com/doi/abs/10.1029/2002JA009808`.

Bram van Leer. Towards the ultimate conservative difference scheme. ii. monotonicity and conservation combined in a second-order scheme. *Journal of Computational Physics*, 14(4):361 – 370, 1974. doi: http://dx.doi.org/10.1016/0021-9991(74)90019-9.

I. Y. Vasko, O. V. Agapitov, F. S. Mozer, and A. V. Artemyev. Thermal electron acceleration by electric field spikes in the outer radiation belt: Generation of field-aligned pitch angle distributions. *Journal of Geophysical Research: Space Physics*, 120(10):8616–8632, 2015. doi: 10.1002/2015JA021644. URL `https://agupubs.onlinelibrary.wiley.com/doi/abs/10.1002/2015JA021644`.

C. Watt, R. Rankin, and R. Marchand. Kinetic simulations of electron response to shear Alfvén waves in magnetospheric plasmas. *Physics of Plasmas*, 11(4):1277–1284, Apr 2004. doi: 10.1063/1.1647140.

C. E. J. Watt and R. Rankin. Electron acceleration due to inertial Alfvén waves in a non-Maxwellian plasma. *Journal of Geophysical Research: Space Physics*, 112(A4): n/a–n/a, 2007a. ISSN 2156-2202. doi: 10.1029/2006JA011907. URL `http://dx.doi.org/10.1029/2006JA011907`. A04214.

C. E. J. Watt and R. Rankin. Do magnetospheric shear Alfvén waves generate sufficient electron energy flux to power the aurora? *Journal of Geophysical Research: Space Physics*, 115(A7), 2010. doi: 10.1029/2009JA015185.

C. E. J. Watt and R. Rankin. Alfvén Wave Acceleration of Auroral Electrons in Warm Magnetospheric Plasma. *Washington DC American Geophysical Union Geophysical Monograph Series*, 197, 2012. doi: 10.1029/2011GM001171.

C. E. J. Watt, R. Rankin, I. J. Rae, and D. M. Wright. Self-consistent electron acceleration due to inertial Alfvén wave pulses. *Journal of Geophysical Research: Space Physics*, 110(A10), 2005. ISSN 2156-2202. doi: 10.1029/2004JA010877. URL `http://dx.doi.org/10.1029/2004JA010877`. A10S07.

C. E. J. Watt, R. Rankin, I. J. Rae, and D. M. Wright. Inertial Alfvén waves and acceleration of electrons in nonuniform magnetic fields. *Geophysical Research Letters*, 33(2), 2006. ISSN 1944-8007. doi: 10.1029/2005GL024779. URL `http://dx.doi.org/10.1029/2005GL024779`. L02106.

C.E.J. Watt and R. Rankin. Parallel electric fields associated with inertial Alfvén waves. *Planetary and Space Science*, 55(6):714 – 721, 2007b. ISSN 0032-0633. doi: http://dx.doi.org/10.1016/j.pss.2006.04.042. Ultra-Low Frequency Waves in the Magnetosphere Magnetospheric {ULF} Waves.

Clare E. J. Watt and Robert Rankin. Electron trapping in shear Alfvén waves that power the aurora. *Phys. Rev. Lett.*, 102:045002, Jan 2009. doi: 10.1103/PhysRevLett.102.045002.

Puetter R. Whipple E. and Rosenberg M. A two-dimensional, time-dependent, near-earth magnetotail. *Advances in Space Research*, 11:133–142, 1991. doi: 10.1016/0273-1177(91)90024-E.

J. R. Wygant, A. Keiling, C. A. Cattell, M. Johnson, R. L. Lysak, M. Temerin, F. S. Mozer, C. A. Kletzing, J. D. Scudder, W. Peterson, C. T. Russell, G. Parks, M. Brittnacher, G. Germany, and J. Spann. Polar spacecraft based comparisons of intense electric fields and poynting flux near and within the plasma sheet-tail lobe boundary to uvi images: An energy source for the aurora. *Journal of Geophysical Research: Space Physics*, 105(A8):18675–18692, 2000. ISSN 2156-2202. doi: 10.1029/1999JA900500. URL `http://dx.doi.org/10.1029/1999JA900500`.

J. R. Wygant, A. Keiling, C. A. Cattell, R. L. Lysak, M. Temerin, F. S. Mozer, C. A. Kletzing, J. D. Scudder, V. Streltsov, W. Lotko, and C. T. Russell. Evidence for kinetic Alfvén waves and parallel electron energization at 46 RE altitudes in the plasma sheet boundary layer. *Journal of Geophysical Research: Space Physics*, 107(A8):SMP 24–1–SMP 24–15, 2002. ISSN 2156-2202. doi: 10.1029/2001JA900113. URL `http://dx.doi.org/10.1029/2001JA900113`.

A. W. Yau and H. G. James. Cassiope enhanced polar outflow probe (e-pop) mission overview. *Space Science Reviews*, 189(1):3–14, 2015. ISSN 1572-9672. doi: 10.1007/s11214-015-0135-1. URL `http://dx.doi.org/10.1007/s11214-015-0135-1`.

Xiaojia Zhang, Vassilis Angelopoulos, Binbin Ni, Richard M. Thorne, and Richard B. Horne. Extent of ech wave emissions in the earth's magnetotail. *Journal of Geophysical Research: Space Physics*, 119(7):5561–5574, 2014. doi: 10.1002/2014JA019931. URL `https://agupubs.onlinelibrary.wiley.com/doi/abs/10.1002/2014JA019931`.

Appendices

Appendix A

The Fermi Interaction

A.1 Single particle Fermi interaction

Imagine a charged particle moving to the right at a constant rate v_0, with respect to some laboratory reference frame. An electromagnetic wave catches up to the particle while moving also to the right with constant speed $v_w > v_0$ (Figure A.1a). In a frame reference moving with the perturbation, however, the wave looks like an electrostatic field, characterized only by the amplitude of its scalar potential, ϕ_0. A seen by the moving observer, the particle approaches towards the wave with speed $v_0' = v_0 - v_w < 0$ (Figure A.1b). Energy conservation in the wave frame provides the velocity of the particle while under the influence of the wave field,

$$v' = \pm\sqrt{v_0'^2 + \frac{2e\phi}{m}}, \tag{A.1}$$

where the charge is set to $q = -e$, since we are interested in interactions involving electrons, and ϕ represents the potential at the position of the electron. The sign of the potential in (A.1) reveals the nature of the wave-electron interaction: a positive

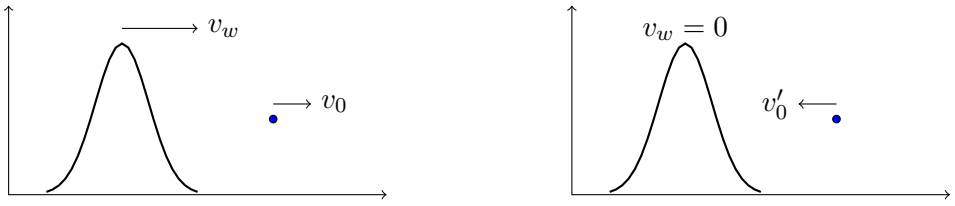

(a) absolute frame (b) wave frame

Figure A.1: A fast wave reaches an electron

potential becomes an attractor for electrons, while a negative potential constitutes a repeller. These two scenarios are to be discussed next using simple arguments of particle motion in a conservative field.

Figure A.2 sketches the potential (left), force and electric field (middle), and energy (right); all of them as a function of the position in the wave frame. A positive (negative) force imply acceleration to the right (left). For a positive potential, the force indicates acceleration towards the position of maximum potential, regardless of where the particle is located inside the spatial domain of the wave. Thus, an electron entering the domain of a wave with spatial extension L from the left with constant speed v_0' increases its velocity until it reaches the center of the wave with a maximum speed of $v'(\phi_0)$. Due to its inertia, the electron moves further to the right into the region where it experiences negative acceleration. From the bottom panel, it is clear that the electron leaves the wave with the same speed it entered. The net effect of the whole interaction consists on a shift in position $\Delta x'$ relative to the position it would have had if there was no wave:

$$\Delta x' = v_0'(t - t_0) - L. \tag{A.2}$$

The time $t - t_0$ it takes for the interaction to take place is a function of the potential and its dimensions:

$$t - t_0 = \int_0^L \frac{dx'}{v'} = \int_0^L \frac{dx'}{\sqrt{v_0'^2 + 2e\phi/m}}. \tag{A.3}$$

Notice that a very similar scenario occurs with an electron that enters the wave from the right. Once under the influence of the wave, its speed increases towards the center of the wave; this gain in momentum causes the particle to overshoot the point of attraction and move into the region of positive acceleration where its speed decreases, to finally abandon the wave at the same speed it entered. In both cases the electrons kinetic energy is always higher than its initial value, which indicates no possibility for resonant interaction; particles interacting with this wave rush and move past it, regardless of initial velocity and orientation.

Consider now the case $\phi(x) < 0$ (Figure A.3). In this case, the force accelerates the particles away from the wave. Two different cases unfold: for initial speeds such that $1/2mv_0'^2 > e\phi_0$, the electron decreases its speed while in the wave domain to a minimum speed of $\sqrt{v_0'^2 - 2e|\phi_0|/m}$, but eventually will move to the other extreme of the wave with final speed equal to its initial speed. If, on the other hand, $1/2mv_0'^2 < e\phi_0$, the electron reaches a turning point where its velocity becomes zero, further motion sees the particle moving back and eventually exiting the wave at the same point it entered with

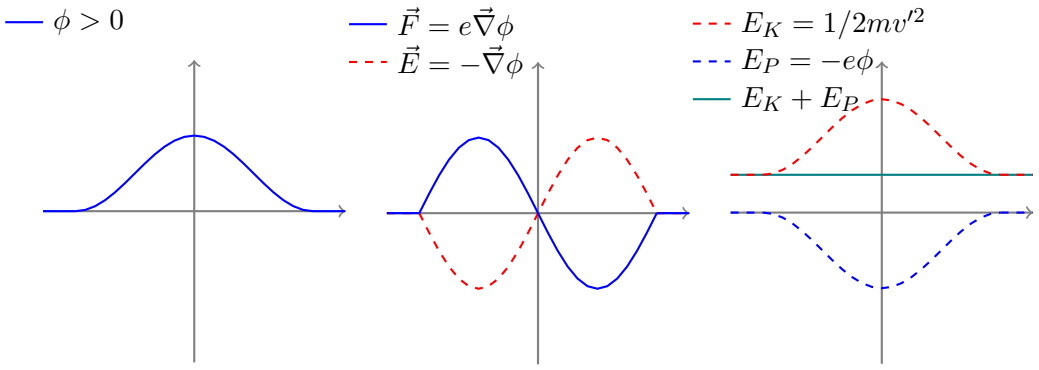

(a) Electrostatic potential (b) Electric field and force (c) Energy

Figure A.2: Electron interaction with positive potential in the wave frame. The particles final velocity is unchanged after interaction

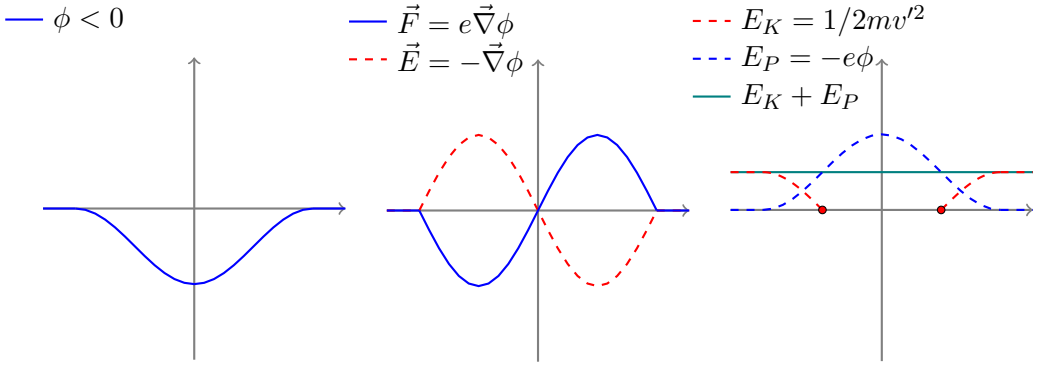

(a) Electrostatic potential (b) Electric field and force (c) Energy

Figure A.3: Electron interaction with negative potential in the wave frame. The particles final velocity changes if its initial energy is lower than the wave potential

final speed $v'_f = -v'_0$. In the rest frame, the speed at which the electron leaves the wave is:

$$v_f = 2v_w - v_0. \tag{A.4}$$

The single special case of initial velocity $v'_0 = \sqrt{2e\phi_0/m}$ causes the electron to sit still at the location of maximum potential. Any other value will drive the particle away from this point.

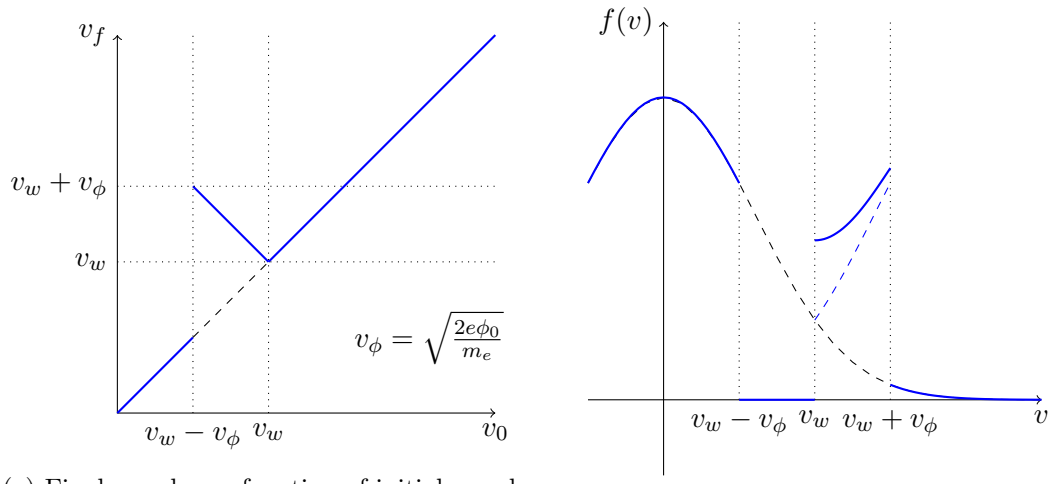

(a) Final speed as a function of initial speed

(b) Electron redistribution

Figure A.4: Speed mapping on a distribution after a Fermi interaction

A.2 Fermi interaction over a distribution of particles

Lets briefly consider the effect of Fermi interactions over a given distribution. From here onwards we consider wave-particle interactions with negative potentials unless otherwise specified. Recall that, even though the potential affects all particles, only electrons whose initial speed in the wave frame is such that

$$0 \leq |v_0'| \leq \sqrt{\frac{2e\phi_0}{m_e}} \tag{A.5}$$

will have net non-zero acceleration. From the point of view of the plasma itself, according to equation (A.4), the condition (A.5) maps electrons with initial speeds:

$$v_w - \sqrt{\frac{2e\phi_0}{m_e}} < v_0 < v_w, \tag{A.6}$$

into the interval:

$$v_w < v_f < v_w + \sqrt{\frac{2e\phi_0}{m_e}}. \tag{A.7}$$

The diagram in Figure A.4 illustrates the mapping of speeds before and after interaction with the wave (left). This mapping advects part of the distribution into forming a beam after interaction (right).

Appendix B

The Corner Transport Upwind method

The following is a summarized description of the modified Upwind Method with high-resolution corrections, for the case where the advection coefficients are divergent-less ($\nabla \cdot v = 0$). The entirety of the ideas, terminology, and the mathematical treatment included here was taken from LeVeque [2002], where the interested reader will find a much more complete discussion and extension of these ideas into more general cases.

The *Upwind Method* belongs to the category of *Finite Volume Methods* (FVM) used to solve problems where conservation laws are enforced. In this context, if the property $q(x,t)$ of the system is conserved, it is possible to obtain its evolution by tracking the flow across each cell boundary and the boundaries of the simulation domain. The Upwind approach is used in advection related problems where the direction of the flow of information is known; exploiting this knowledge leads to a one-sided scheme for $q(x,t)$, instead of a centered one.

While finite differential methods use pointwise discretization, FVM defines piecewise continuous functions with compact support C_i of the extent of the i-th cell size; in this case, discretized quantities represent the cell average value in its domain:

$$Q_i^n \simeq \frac{1}{\Delta x} \int_{C_i} dx\, q(x, t^n). \tag{B.1}$$

Even though the right hand side on equation (B.1) correctly defines the average value of $q(x,t)$ in the interval defined by the limits of the integral, the functional form $q(x,t)$ is not known and instead all we have is a simplified representation, piecewise continuous

and differentiable, $\tilde{q}(x,t)$, which is defined under the conditions:

$$Q_i^n = \frac{1}{\Delta x}\int_{C_i} dx\, \tilde{q}(x,t^n), \tag{B.2}$$

and,

$$\tilde{q}(x_i,t^n) = Q_i^n. \tag{B.3}$$

According to LeVeque [2002], these conditions ensure the approximation is second order accurate provided $q(x,t)$ is a well behaved (continuous and differentiable) function. Equation (B.2) uses the construction $\tilde{q}(x,t)$ to obtain an approximation of the average value for the interval at each iteration.

B.1 Conservation law

Consider a finite one dimensional region subdivided into N cells of equal size Δx. The i-th '*volume*' spans the region $C_i = (x_{i-\frac{1}{2}}, x_{i+\frac{1}{2}})$, where $x_j = j\Delta x$. Assuming $q(x,t)$ follows a conservation law, the rate of change of the amount of $q(x,t)$ inside its domain is given by the fluxes across the boundaries:

$$\frac{d}{dt}\int_{x_{i-\frac{1}{2}}}^{x_{i+\frac{1}{2}}} dx\, q(x,t) = f(q(x_{i-\frac{1}{2}},t)) - f(q(x_{i+\frac{1}{2}},t)), \tag{B.4}$$

each flux $f(q(x,t))$ represents the amount of $q(x,t)$ per unit time transported across any given x. The time integral of equation (B.4), from time t^n to time t^{n+1}, provides the update scheme for $q(x,t)$ in the form:

$$\int_{x_{i-\frac{1}{2}}}^{x_{i+\frac{1}{2}}} dx\, q(x_i,t^{n+1}) = \int_{x_{i-\frac{1}{2}}}^{x_{i+\frac{1}{2}}} dx\, q(x_i,t^n) + \int_{t^n}^{t^{n+1}} dt\, f(q(x_{i-\frac{1}{2}},t)) - \int_{t^n}^{t^{n+1}} dt\, f(q(x_{i+\frac{1}{2}},t)). \tag{B.5}$$

Analogous to the numerical definition for $q(x,t)$, the flow across the cell boundaries is regarded as a time average of the traversing amount of the quantity $q(x,t)$ across any given cell boundary, per unit time,

$$F_{i\pm\frac{1}{2}}^n \simeq \frac{1}{\Delta t}\int_{t^n}^{t^{n+1}} dt\, f(q(x_{i\pm\frac{1}{2}}),t). \tag{B.6}$$

These elements derive into the following numerical algorithm:

$$Q_i^{n+1} = Q_i^n - \frac{\Delta t}{\Delta z}\left(F^n_{i+\frac{1}{2}} - F^n_{i-\frac{1}{2}}\right). \tag{B.7}$$

B.2 Upwind Method for advection in 1D

Before presenting the numerical form of the Vlasov equation that provides the time evolution of the distribution function, let us discuss the main ideas regarding upwind transport over the equation for advection in one dimension:

$$\frac{\partial q(x,t)}{\partial t} + u\frac{\partial q(x,t)}{\partial x} = 0, \tag{B.8}$$

which has the form of the free force Vlasov equation. A typical example of a system obeying this equation involves a liquid flowing through a pipe of constant cross-section A. Suppose the fluid has a tracer within, whose is given by $Aq(x,t)$. In this context, equation (B.4) represents the time variation of the total mass of tracer within positions $x_{i-\frac{1}{2}}$ and $x_{i+\frac{1}{2}}$ along the pipe, which of course depends on the fluxes at the boundaries only, assuming there are no other sources within the pipe section. Characteristic solutions for equation (B.8) have the form $q(x,t) = q(x-ut)$, so the tracers linear density profile simply shifts its position towards the right or left, depending on the sign of u. The amount of tracer that crosses the boundary per unit time, or *flux*, is given by $f(q(x,t)) = uq(x,t)$.

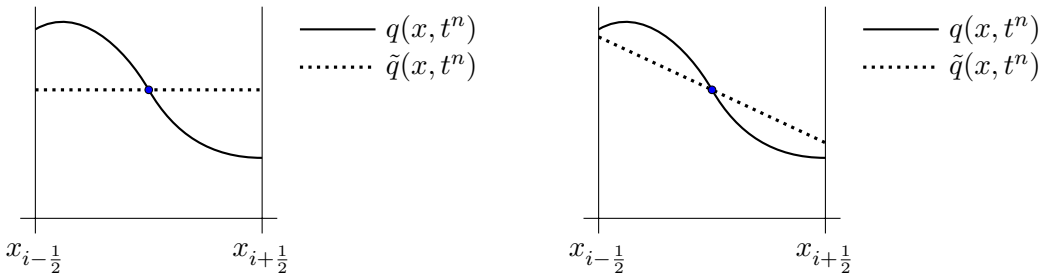

(a) Constant (b) Linear

Figure B.1: Piecewise approximations $\tilde{q}(x,t^n)$

B.2.1 Upwind method for piecewise constant functions

A first order method for (B.8) is obtained by taking $\tilde{q}(x, t^n) = Q_i^n$ (see figure B.1a). Assuming that the flow direction is known, advection becomes one-sided:

$$F_{i+\frac{1}{2}}^n = \begin{cases} uQ_i^n & \text{if } u > 0 \\ uQ_{i+1}^n & \text{if } u < 0. \end{cases} \tag{B.9}$$

This dependence naturally imposes a condition on the numerical scheme in order to ensure conservation at every time step. More specifically, it constrains the velocity of advection, which is to fall within the range:

$$0 \geq |u| \frac{\Delta t}{\Delta x} \geq 1, \tag{B.10}$$

since evidently, advection at higher velocities introduces information coming form non-adjacent cells, which openly contradicts the flux description provided. Substituting (B.9) into equation (B.7) leads to the first order Upwind method for advection:

$$Q_i^{n+1} = \begin{cases} \left(1 - u\frac{\Delta t}{\Delta x}\right) Q_i^n + u\frac{\Delta t}{\Delta x} Q_{i-1}^n & \text{if } u > 0 \\ \left(1 + u\frac{\Delta t}{\Delta x}\right) Q_i^n - u\frac{\Delta t}{\Delta x} Q_{i+1}^n & \text{if } u < 0. \end{cases} \tag{B.11}$$

Notice that (B.11) correctly expresses Q_i^{n+1} as a weighted sum of its previous value and the value of the cell from where the flow proceeds. This situation is illustrated in Figure B.2, showing a hypothetical system where an initial configuration is advected to the right with constant velocity u. After an iteration, each piecewise section moves to the right so that the jump initially at $x_{i-\frac{1}{2}}$ is now at a distance $u\Delta t$ inside the next cell. Each new cell value is computed by averaging the new configuration according to the definition (B.2).

A common implementation in the form of a single upwind formula, valid for any u reads:

$$\begin{aligned} Q_i^{n+1} &= Q_i^n - \frac{\Delta t}{\Delta x}\left(u^- dQ_{i+\frac{1}{2}}^n + u^+ dQ_{i-\frac{1}{2}}^n\right) \\ u^- &= \min(u, 0) \\ u^+ &= \max(u, 0) \\ dQ_j^n &= Q_{j+\frac{1}{2}}^n - Q_{j-\frac{1}{2}}^n \end{aligned} \tag{B.12}$$

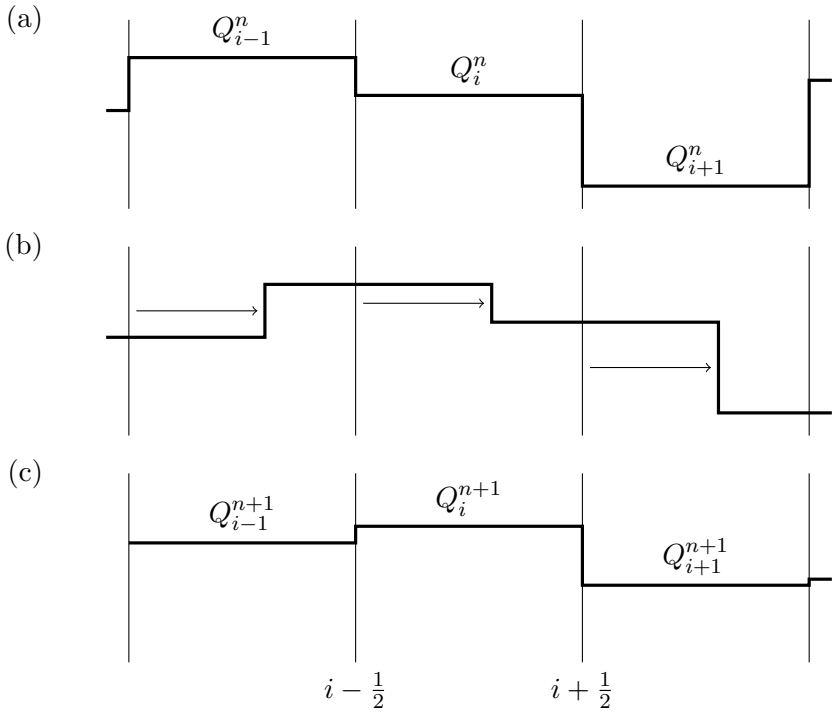

Figure B.2: The upwind method using piecewise constant functions. (a) Initial configuration. (b) After some time Δt these volumes shift to the right by a distance $u\Delta t$. (c) The new values Q_i^{n+1} correspond to the weighted average of Q_{i-1}^n and Q_i^n.

B.2.2 Upwind Method for Piecewise linear functions

The Upwind Method using constant functions (B.11) can be arranged in the form of forward or backward finite differences, depending on the direction of the flow. In any case, this means that the approximation is only first order accurate. Higher order accuracy can be achieved by introducing higher order polynomials in the formulation. Piecewise linear functions complying with the conditions (B.2) and (B.3) have the form

$$\tilde{q}^n(x,t^n) = Q_i^n + \sigma_i^n(x - x_i), \tag{B.13}$$

where

$$x_i = \frac{(x_{i-\frac{1}{2}} + x_{i+\frac{1}{2}})}{2} = x_{i\pm\frac{1}{2}} \mp \frac{\Delta x}{2}. \tag{B.14}$$

Just as in the piecewise constant case shown above, one can calculate the new update by evaluating the shifting according to the characteristic solution, and compute the new average as defined in equation (B.2). Within the DK1D code, however, the update form of the distribution function has been coded in terms of the fluxes across the boundaries, so we are interested in addressing the differencing flux formulation instead. Expressions for the flux are found by integrating $u\tilde{q}(x,t)$ in time at the boundaries, as suggested in equation (B.6),

$$\begin{aligned}
F^n_{i-\frac{1}{2}} &= \frac{1}{\Delta t}\int_{t^n}^{t^{n+1}} dt\, u\tilde{q}^n(x_{i-\frac{1}{2}},t) \\
&= \frac{1}{\Delta t}\int_{t^n}^{t^{n+1}} dt\, u\tilde{q}^n(x_{i-\frac{1}{2}} - u(t-t^n),t^n) \\
&= \begin{cases} \frac{1}{\Delta t}\int_{t^n}^{t^{n+1}} dt\, u\left[Q^n_{i-1} + \sigma^n_{i-1}\left(x_{i-\frac{1}{2}} - u(t-t^n) - x_{i-1}\right)\right] & \text{if } u>0 \\ \frac{1}{\Delta t}\int_{t^n}^{t^{n+1}} dt\, u\left[Q^n_{i} + \sigma^n_{i}\left(x_{i-\frac{1}{2}} - u(t-t^n) - x_{i}\right)\right] & \text{if } u<0 \end{cases} \\
&= \begin{cases} u\left[Q^n_{i-1} + \frac{\sigma^n_{i-1}}{2}(\Delta x - u\Delta t)\right] & \text{if } u>0 \\ u\left[Q^n_{i} - \frac{\sigma^n_{i}}{2}(\Delta x + u\Delta t)\right] & \text{if } u<0 \end{cases}.
\end{aligned} \tag{B.15}$$

Substitution of these expressions into equation (B.7) lead to the following form for the

upwind method:

$$Q_i^{n+1} = \begin{cases} Q_i^n - \dfrac{u\Delta t}{\Delta x}(Q_i^n - Q_{i-1}^n) - \dfrac{u\Delta t}{2}\left(1 - u\dfrac{\Delta t}{\Delta x}\right)(\sigma_i^n - \sigma_{i-1}^n) & \text{if } u > 0 \\ Q_i^n - \dfrac{u\Delta t}{\Delta x}(Q_{i+1}^n - Q_i^n) + \dfrac{u\Delta t}{2}\left(1 + u\dfrac{\Delta t}{\Delta x}\right)(\sigma_{i+1}^n - \sigma_i^n) & \text{if } u < 0 \end{cases}. \quad \text{(B.16)}$$

Notice that the use of linear piecewise functions has simply added a second order correction to the first order upwind formula. The correction term is still undetermined since the slopes have not been defined yet. Different methods usually take advantage of this degree of freedom to set the slopes to some common value,

$$\sigma_i^n = \sigma_{i-1}^n = \frac{\Delta Q_{i-\frac{1}{2}}^n}{\Delta x}, \quad \text{(B.17)}$$

so that the flux formula can be expressed as

$$F_{i-\frac{1}{2}}^n = u^- Q_i^n + u^+ Q_{i-1}^n + \frac{|u|}{2}\left(1 - \frac{|u|\Delta t}{\Delta x}\right)\Delta Q_{i-\frac{1}{2}}^n. \quad \text{(B.18)}$$

Second order methods provide superior accuracy than first order methods in the sense that they follow rapid changes more quickly. In regions of high variability, on the other hand, first order methods react poorly to sudden changes, causing diffusive effects on the solution. However, first order methods have the advantage that their numerical solutions preserve monotonicity, while the introduction of nonzero slopes tends to generate spurious oscillations in regions of rapid change or at sharp discontinuities; such oscillations could grow and eventually become a source of numerical instability. In order to avoid this oscillatory behavior, these high-resolution methods usually apply some *limiter* value to the slope so to enforce local monotonicity, at the expense of allowing some degree of diffusion locally. A standard criteria to ensure monotonicity consists on requiring the method to be *total variation diminishing* (TVD), or,

$$\sum_{i=-\infty}^{\infty} |Q_i^{n+1} - Q_i^{n+1}| \leq \sum_{i=-\infty}^{\infty} |Q_i^n - Q_i^n|. \quad \text{(B.19)}$$

For example, the following definition provides a method which is both TVD and second-order accurate:

$$\sigma_i^n = \text{minmod}\left(\frac{Q_i^n - Q_{i-1}^n}{\Delta x}, \frac{Q_{i+1}^n - Q_i^n}{\Delta x}\right), \quad \text{(B.20)}$$

where the minmod function is defined by,

$$\text{minmod}(a,b) = \begin{cases} a & \text{if } |a| < |b| \text{ and } ab > 0 \\ b & \text{if } |b| < |a| \text{ and } ab > 0 \\ 0 & \text{if } ab < 0. \end{cases} \tag{B.21}$$

This choice of slope selects the lower between the right and left differences, in regions of monotone behavior; slopes with different signs signal a local maximum or minimum, and the slope is assigned a value of zero. Other methods also apply some *limit* to the value of the slope, based on inspection of the surrounding data, in order to minimize undesired behavior.

B.3 Convergence of the Upwind Method

A major concern about the use of numerical methods as differential equation solvers is to ensure that the numerical solution is a good approximation to the real one. We already used a logical/physical argument to introduce the Courant condition (equation B.10). The Courant condition appears naturally in hyperbolic problems. However, the Courant condition is only necessary, but not sufficient, to guarantee the convergence of the numerical solutions.A numerical method is considered *convergent* if the numerical solution at the cell points tends to the analytic solution as $\Delta t \to 0$. One way to establish convergence consists on verifying that the method is both *consistent* and *stable*. The consistency of the numerical solution ensures that the amount of error introduced after a single iteration is small, while stability asserts that the accumulated error of multiple iterations remains bounded to some acceptable level.

Evidently, it is easier to establish consistency than stability. A standard criterion for consistency says that the *local truncation error*, which is defined as:

$$\tau^n = \frac{Q^{n+1} - q^{n+1}}{\Delta t}, \tag{B.22}$$

goes to zero as $\Delta t \to 0$. If the method is proven stable, the local truncation error indicates its global order of accuracy.

Verifying stability, on the other hand, it is far more involved. It is possible to show that the first order Upwind Method is stable given that the Courant condition is satisfied; the demonstration is reasonably uncomplicated (see section 8.3 in Laveque's book), but it is not simple enough as to be included here without falling out of the scope of interest for this investigation. Plus, the proof is not valid for the nonlinear Upwind Method with limiters. As it turns out, stability on a nonlinear Upwind Method can be established

provided that the method is TDV, and that the Courant condition is satisfied.

B.4 Upwind Method in two dimensions

Now let us consider the following advection equation:

$$\frac{\partial q(x,y,t)}{\partial t} + u\frac{\partial q(x,y,t)}{\partial x} + v\frac{\partial q(x,y,t)}{\partial y} = 0, \tag{B.23}$$

for which the characteristic solutions has the form $q(x,y,t) = q(x-ut, y-vt, t)$. Generalization of the Upwind Method for the case of advection in 2 dimensions is fairly straightforward, although not as trivial as to say:

$$\begin{aligned} Q_{ij}^{n+1} = Q_{ij}^{n} &- \frac{\Delta t}{\Delta x}\left[u^{+}(Q_{ij}^{n} - Q_{i-1,j}^{n}) + u^{-}(Q_{i+1,j}^{n} - Q_{ij}^{n})\right] \\ &- \frac{\Delta t}{\Delta y}\left[v^{+}(Q_{ij}^{n} - Q_{i,j-1}^{n}) + v^{-}(Q_{i,j+1}^{n} - Q_{ij}^{n})\right]. \end{aligned} \tag{B.24}$$

Upon close inspection, one notices that this corresponds to uncoupled advection flowing normal to x or y with constant speed u or v, respectively. One recognizes that, in order to obtain a method that correctly models advection in any arbitrary direction, there must be additional terms in the update form for $q(x,y,t)$, to account for flux contributions from diagonally adjacent neighbors (see Figure B.3).

Analogously to the one dimensional case, lets define each finite *volume* as the region within the cell $C_{ij} = (x_{i-\frac{1}{2}}, x_{i+\frac{1}{2}}) \times (y_{j-\frac{1}{2}}, y_{j+\frac{1}{2}})$. We regard the approximate value Q_{ij}^{n} as the cell average of the quantity $q(x,y,t^n)$,

$$Q_{ij}^{n} = \frac{1}{\Delta x \Delta y}\int_{x_{i-\frac{1}{2}}}^{x_{i+\frac{1}{2}}} dx \int_{y_{j-\frac{1}{2}}}^{y_{j+\frac{1}{2}}} dy\, q(x,y,t^n). \tag{B.25}$$

Lets assume $u > 0$ and $v > 0$. Figure B.3a marks the cell sources of inflow into C_{ij}. The Courant condition necessary for stability is established by constraining the flow velocity to less than a cell per time iteration. In this case reads:

$$max\left(\left|\frac{u\Delta t}{\Delta x}\right|, \left|\frac{v\Delta t}{\Delta y}\right|\right) \leq 1. \tag{B.26}$$

Again, the Upwind Method is constructed by:

- defining initial piecewise constant functions $\tilde{q}(x,y,t^n)$ at each cell;
- evolving the solution in time, $\tilde{q}(x,y,t^{n+1}) = \tilde{q}(x-u\Delta t, y-v\Delta t, t^n)$;

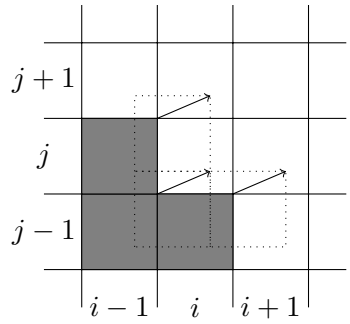

(a) Transverse inflow in 2 dimensions

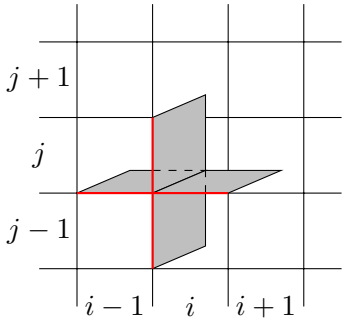

(b) Each transverse flow is proportional to the jump at their corresponding cell boundary (marked red)

Figure B.3: Transverse inflow into cell C_{ij} for the case $u > 0$ and $v > 0$

- evaluating the new average over the cell Q_{ij}^{n+1} through equation (B.25):

$$
\begin{aligned}
Q_{ij}^{n+1} =& \frac{1}{\Delta x \Delta y} \int_{x_{i-\frac{1}{2}}}^{x_{i+\frac{1}{2}}} dx \int_{y_{j-\frac{1}{2}}}^{y_{j+\frac{1}{2}}} dy\, \tilde{q}(x - u\Delta x, y - v\Delta y, t^n) \\
=& \frac{1}{\Delta x \Delta y} \int_{x_{i-\frac{1}{2}}-u\Delta t}^{x_{i+\frac{1}{2}}-u\Delta t} dx \int_{y_{j-\frac{1}{2}}-v\Delta t}^{y_{j+\frac{1}{2}}-v\Delta t} dy\, \tilde{q}(x, y, t^n) \\
=& Q_{ij}^n - \frac{u\Delta t}{\Delta x}(Q_{ij}^n - Q_{i-1,j}^n) - \frac{v\Delta t}{\Delta x}(Q_{ij}^n - Q_{i,j-1}^n) + \\
& \frac{uv}{2}\frac{(\Delta t)^2}{\Delta x \Delta y}\left[(Q_{ij}^n - Q_{i,j-1}^n) - (Q_{i-1,j}^n - Q_{i-1,j-1}^n)\right. \\
& \left. + (Q_{ij}^n - Q_{i-1,j}^n) - (Q_{i,j-1}^n - Q_{i-1,j-1}^n)\right].
\end{aligned}
\tag{B.27}
$$

The first three terms of this expansion reproduce the form (B.24). The additional terms account for diagonally directed fluxes. Figure B.3b marks the boundaries undergoing inflow into C_{ij}. Take for example the interface between cells $C_{i,j-1}$ and C_{ij}. A fraction of the inflow into C_{ij} from this boundary is ultimately advected into cell $C_{i+1,j}$; clearly, the modification to the cell average caused by this fraction must be subtracted, since it does not really contribute to the cell average Q_{ij}^{n+1}, but it has been already included in the third term of volume average. The value of the contribution in this case is equal to $Q_{ij}^n - Q_{i,j-1}^n$, times the fractional part of the area, $1/2uv\Delta t^2$, covered in cell $C_{i+1,j}$; this corresponds to the fourth term in equation (B.27). The remaining three corrections correspond each to one of the other diagonal fluxes.

Let us forget about the restriction $u > 0$ and $v > 0$. To account for fluxes in any

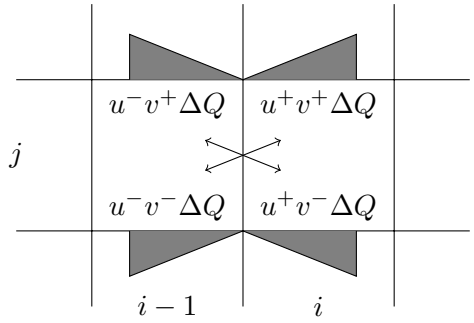

Figure B.4: All possible transverse paths for the jump $\Delta Q_{i-1/2,j} = Q_{ij} - Q_{i-1,j}$. (Taken from [LeVeque, 2002])

arbitrary direction, consider all possible lateral contributions that potentially take place as the vertical jump ΔQ moves transversely (see Figure B.4). There are four possible scenarios for transverse flow, depending on the sign of each velocity component; then four correction terms arise [LeVeque, 2002]:

$$\begin{aligned} G_{i-1,j-\frac{1}{2}} &= -\frac{1}{2}\frac{\Delta t}{\Delta x}v^-u^-(Q_{ij} - Q_{i-1,j}), \\ G_{i-1,j+\frac{1}{2}} &= -\frac{1}{2}\frac{\Delta t}{\Delta x}v^+u^-(Q_{ij} - Q_{i-1,j}), \\ G_{i,j-\frac{1}{2}} &= -\frac{1}{2}\frac{\Delta t}{\Delta x}v^-u^+(Q_{ij} - Q_{i-1,j}), \\ G_{i,j+\frac{1}{2}} &= -\frac{1}{2}\frac{\Delta t}{\Delta x}v^+u^+(Q_{ij} - Q_{i-1,j}). \end{aligned} \tag{B.28}$$

Similar considerations lead to additional terms arising due to the horizontal cell boundaries:

$$\begin{aligned} F_{i-\frac{1}{2},j-1} &= -\frac{1}{2}\frac{\Delta t}{\Delta y}v^-u^-(Q_{ij} - Q_{i,j-1}), \\ F_{i+\frac{1}{2},j-1} &= -\frac{1}{2}\frac{\Delta t}{\Delta y}v^-u^+(Q_{ij} - Q_{i,j-1}), \\ F_{i-\frac{1}{2},j} &= -\frac{1}{2}\frac{\Delta t}{\Delta y}v^+u^-(Q_{ij} - Q_{i,j-1}), \\ F_{i+\frac{1}{2},j} &= -\frac{1}{2}\frac{\Delta t}{\Delta y}v^+u^+(Q_{ij} - Q_{i,j-1}). \end{aligned} \tag{B.29}$$

The corrections just presented correctly describe advection in any direction, yet the method is still first order accurate. For higher order corrections one further update each

of the fluxes as

$$\begin{aligned} F_{i-\frac{1}{2},j} &+= \frac{|u|}{2}\left(1-\frac{\Delta t}{\Delta x}|u|\right)\delta_{i-1/2,j}, \\ G_{i,j-\frac{1}{2}} &+= \frac{|v|}{2}\left(1-\frac{\Delta t}{\Delta y}|v|\right)\delta_{i,j-1/2}. \end{aligned} \tag{B.30}$$

Appendix C

Electron trapping and acceleration by kinetic Alfven waves in the inner magnetosphere

C.1 Abstract

In this paper we study the interaction of kinetic Alfven waves generated near the equatorial plane of the magnetosphere with electrons having initial energies up to ~ 100 eV. Wave-particle interactions are investigated using a theoretical model of trapping into an effective potential generated by the wave parallel electric field and the mirror force acting along geomagnetic field lines. It is demonstrated that waves with an effective potential amplitude on the order of $\sim 100 - 400$ V, and with perpendicular wavelengths on the order of the ion gyroradius, can trap and efficiently accelerate electrons up to energies of several keV. Trapping acceleration corresponds to conservation of the electron magnetic moment and, thus, results in a significant decrease of the electron equatorial pitch-angle with time. Analytical and numerical estimates of the maximum energy and probability of trapping are presented and the application of the proposed model is discussed.

C.2 Introduction

Hot (few keVs) electron populations in Earth's inner magnetosphere play an important role in the generation of whistler waves [e.g., Li et al., 2010; Fu et al., 2014; Mourenas et al., 2015, and references therein] and in scattering electrons into the atmosphere to produce diffusive aurora [e.g., Arnoldy, 1974; Akasofu, 1974]. Besides convection and

(or) substorm injections of hot magnetotail electrons into the inner magnetosphere [e.g., Gabrielse et al., 2012; Ganushkina et al., 2013, and references therein], local acceleration of cold ionospheric electrons represents a promising scenario for formation of hot electron populations. Effective acceleration of cold magnetized electrons is usually provided by wave-particle resonant interactions. In the inner equatorial magnetosphere sub-keV electrons ($\sim$ 100 eV) can resonate with electron cyclotron harmonics [e.g., Horne et al., 2000], upper band chorus waves [e.g., Ni et al., 2011b], very oblique low band chorus waves [Artemyev et al., 2015a], kinetic Alfven waves (KAWs) [e.g., Hasegawa, 1976; Wygant et al., 2002], and broad low frequency electrostatic noise that consists of a mixture of electron holes and double layers [Mozer et al., 2015, and references therein]. Excitation and amplification of wave emissions is also closely related to injections from the magnetotail [Angelopoulos et al., 2002; Ni et al., 2012; Mozer et al., 2014; Malaspina et al., 2015; Ergun et al., 2015]. Scattering of sub-keV electrons by upper band chorus and electron cyclotron waves mainly results in precipitation, while parallel electric fields of very oblique low band chorus waves, KAWs, and electrostatic noise, can effectively accelerate electrons along magnetic field lines.

Phase velocities of very oblique low band chorus waves are comparable with thermal electron velocities for electron energies between 100-1000 eV, and thus Landau resonance interaction is possible [Artemyev et al., 2012]. In contrast, the phase velocity of KAWs is too low at the equatorial region around L-shells $6-9$ to allow these waves undergo Landau resonance with $\sim$ 100 eV electrons [situation is different for aurora region where high amplitude of Alfven velocity becomes comparable with thermal electron energy running the Landau resonance interaction, see, e.g., Chaston et al., 2000, 2002b]. However, the amplitude of the wave potential for KAWs is large enough to effectively expand the range of resonance velocities. Although a full understanding of the interaction between KAWs and electrons remains unclear, but parallel electric fields are known to play an important role [Kletzing et al., 2003; Damiano and Wright, 2005; Chaston et al., 2008; Chaston et al., 2012; Watt et al., 2004, 2005, 2006]. The magnitude of parallel electric fields in KAWs can be many times larger in the plasma sheet than above the ionosphere [Watt and Rankin, 2009] and can drive wave-particle interactions via at least three mechanisms: diffusive-like electron heating [e.g., Hasegawa and Mima, 1978; Potapenko et al., 2006; Tikhonchuk and Rankin, 2002; Lysak and Song, 2003], acceleration due to reflection of electrons from the wave potential wall [Kletzing and Torbert, 1994], and possible electron trapping. The later mechanism was proposed by Hasegawa and Mima [1976] for soliton-like KAW trapping of electrons into a potential well formed by parallel electric fields. This classical trapping effect is significantly modified in the case of inhomogeneous plasma [Laval and Pellat, 1970; Karpman and Shklyar, 1972] and

magnetic field gradients [Nunn, 1971; Karpman et al., 1974].

Wave propagation along dipole magnetic field lines away from the equatorial plane has two effects on electrons: 1) the competition of the wave parallel electric field and mirror force can generate an effective potential well for trapped electrons, and 2) trapped particles moving with the wave velocity along the spatially growing magnetic field are accelerated due to conservation of the first adiabatic invariant (magnetic moment). This mechanism of acceleration works well for very oblique whistler waves [Artemyev et al., 2012] and for electrostatic double layers [Artemyev et al., 2014]. Recent numerical modelling [Watt and Rankin, 2009, 2010] suggests that a similar mechanism can be realised in a system with KAWs. Moreover, modern spacecraft observations reveal an abundance of such waves in the equatorial inner magnetosphere [Chaston et al., 2014; Ergun et al., 2015] where they are correlated with the presence of low frequency electrostatic noise [Mozer et al., 2013, 2015; Malaspina et al., 2015]. Thus, detailed parametric investigation of sub-keV electron trapping and acceleration by KAWs represents an interesting and important problem.

In this paper we generalize the approach proposed by Artemyev et al. [2014] to account for electron interactions with KAWs having a finite transverse scale on the order of the ion gyroradius. We propose a new theoretical model describing electron trapping by KAWs and estimate the maximum energy that can be gained by trapped electrons.

C.3 Electron trapping and acceleration

Superthermal electrons can efficiently interact with intense KAW having a pronounced parallel electric field component. Such fields do not significantly perturb the electron gyromotion and, thus, the first adiabatic invariant (magnetic moment) is conserved. In this case, Landau resonance $k_\parallel v_\parallel = \omega$ between waves with frequency ω and electrons moving with the parallel velocity $v_\parallel$ should be considered. Resonance implies that the wave parallel phase velocity $\omega/k_\parallel \sim v_A$ is approximately the same magnitude as the electron thermal velocity (v_A is the Alfven velocity). Around L-shell ~ 9 the Alfven speed v_A amplitude is generally less than about 2000 km/s, while electron thermal velocities (for energy $50-500$ eV) are about 4000-13000 km/s. Therefore, the resonant condition $k_\parallel v_\parallel = \omega$ cannot be easily satisfied. However, the presence of a parallel electric field provides an efficient widening of the resonance region [e.g., Karney, 1978], making resonance more favorable: $v_\parallel \in [\omega/k_\parallel \pm \sqrt{eE_\parallel/m_e k_\parallel}]$ with m_e and e the electron mass and charge, respectively. For scalar potential amplitudes $\Phi_0 \sim E_\parallel/k_\parallel \sim 100 - 400$ V the resonant condition can be satisfied easily for electrons with energies up to 550 eV. Electrons in this

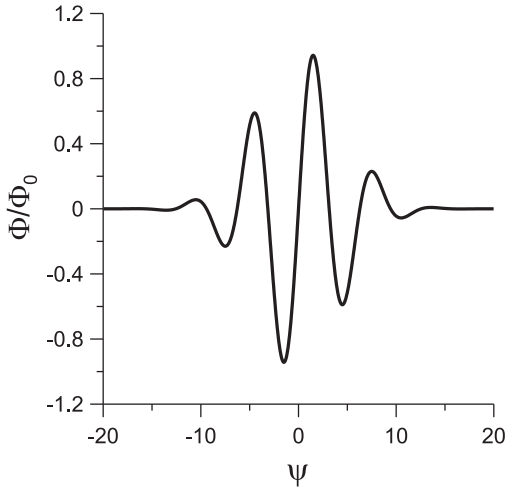

Figure C.1: The assumed shape of the kinetic Alfven wavepacket. The effective scalar potential is shown).

energy range are consequently trapped by waves into Landau resonance, and are able to reach higher latitudes than they normally do. As they move along field lines conserving their magnetic moment they are efficiently accelerated [see examples of such acceleration mechanism in Artemyev et al., 2012, 2014]. The efficiency of electron trapping and acceleration by parallel eletric fields of KAWs during this intercation is estimated below.

In our analysis the effects of transverse components of the wave electric field are neglected (see Discussion) and only parallel electron motion is considered. The wave parallel electric field is described by an effective scalar potential Φ that includes contributions from the electric scalar potential and the parallel component of the magnetic vector potential (see Appendix A). The amplitude of the effective potential is Φ_0, while the wave dispersion relation provides the function $k_{\|}(z)$, where z is the field aligned coordinate (see Eq. (C.6) in Appendix A). The corresponding wave phase ψ is

$$\psi = \int^{z} k_{\|}(z')dz' - \omega t + const. \tag{C.1}$$

The shape of the wave packet shown in Fig. C.1 includes variations over a few wave periods [in agreement with numerical models, e.g., Watt and Rankin, 2009].

C.3.1 Equations of motion

The geomagnetic topology characteristic of the inner magnetosphere will be considered to be a curvature-free dipole magnetic field $B(\lambda) = B_{eq}b(\lambda)$ [Bell, 1984] with a plasma

density defined by $n_e(\lambda) = n_{eq}\cos^{\ell}\lambda$ where index $\ell = -5$ is taken from the empirical model presented by Denton et al. [2006] for L-shell$\sim 6-7$. The relation between the field aligned coordinate and magnetic latitude is given by: $dz = R_0\sqrt{1+3\sin^2\lambda}\cos\lambda$ and $R_0 = R_E L$, while the equatorial value of the plasma density n_{eq} is given by the Sheeley et al. [2001] model. The main deviation of magnetic field configuration from the dipole field at $L \sim 6-9$ (the L-shell range considered in this study) corresponds to the near-equatorial region where currents of hot injected ions can significantly deform the magnetic field lines [see, e.g., Tsyganenko et al., 2003]. We explain a possible role of such magnetic field reconfiguration for KAW interaction with electrons in Discussion.

We introduce the dimensionless spatial coordinate $s = z/R_0$ and normalized time coordinate $t \to tv_{A,eq}/R_0$, where $v_{A,eq}$ is the equatorial Alfven speed. The corresponding Hamiltonian of electrons includes three terms: the electron kinetic energy corresponding to the motion along magnetic field lines $m_e v^2/2$ (where $v = \dot{s}$), the electron kinetic energy corresponding to the gyrorotation $\mu B(s)$ (where μ is the electron magnetic moment), and the potential energy $\sim \Phi$ [see gyroaveraged equations of motion in Northrop, 1963]. The dimensionless form of this Hamiltonian can be written as

$$H = \frac{1}{2}v^2 + h\sin^2\alpha_{eq,0}b(s) - \phi_0 w(s)F(\psi), \tag{C.2}$$

where $\alpha_{eq,0}$ is equatorial initial pitch-angle, and the function $F(\psi) = \Phi/\Phi_0$ is shown in Fig. C.1. The function $w(s)$ is determined by the dispersion relation (see Eq. C.10 in Appendix), $\alpha_{eq,0}$ is the initial equatorial pitch-angle, $h \approx 60(E_e/100\text{eV})(L/9)^2$, E_e is the initial electron energy, and $\phi_0 \approx 60(\Phi_0/100\text{V})(L/9)^2$. The initial dimensionless particle energy (in absence of waves) is h, while the dimensionless phase (C.1) is defined by:

$$\psi = \chi\left(\int^{s} K(s')ds' - t\right), \tag{C.3}$$

where $K(s)$ is given by Eq. (C.7), $\chi \approx 250(2\text{s}/T)(L/9)^2$, and T is the wave period (see Appendix A). For all calculations in this paper we use $L = 9$. However, as Eq. (C.2) shows, both factors h and ϕ_0 depend on L similarly. Thus, change of the L-shell corresponds to multiplication of the initial energy $\sim v^2$ on factor $(9/L)^2$.

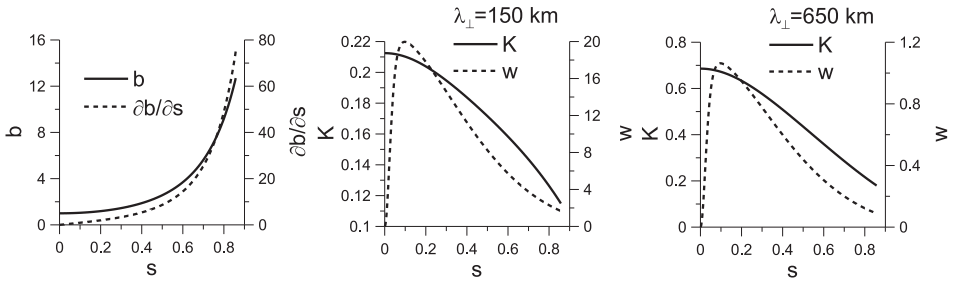

Figure C.2: Profiles of functions $b(s)$, $\partial b(s)/\partial s$, $K(s)$, and $w(s)$.

The equations of motion corresponding to the Hamiltonian (C.2) is defined by,

$$\begin{aligned} \ddot{s} &= -h\sin^2\alpha_{eq,0}\frac{\partial b}{\partial s} + \phi_0\frac{\partial w}{\partial s}F + \phi_0\chi K w\frac{\partial F}{\partial \psi} \\ &\approx -h\sin^2\alpha_{eq,0}\frac{\partial b}{\partial s} + \phi_0\chi K w\frac{\partial F}{\partial \psi} \\ \dot{\psi} &= \chi\left(K\dot{s}-1\right) \end{aligned} \tag{C.4}$$

where we have taken into account that $\chi \gg 1$. Profiles of functions $b(s)$, $\partial b(s)/\partial s$, $K(s)$, and $w(s)$ are shown in Fig. C.2. Spacecraft observations in the equatorial magnetotail suggest that KAWs have a significant amplitude of electrostatic field $\sim 10-100$ mV/m, while $k_\perp/k_\parallel$ ratio is within the range $10-100$ [e.g., Chaston et al., 2012, 2014]. Thus, almost all observed electric field corresponds to the transverse (relative to the background magnetic field) component. Using the KAW dispersion $k_\perp\rho_s \sim 1$ [Hasegawa, 1976] with the ion acoustic gyroradius $\rho_s \sim 50-100$ km (for $L \sim 7-9$, hot ion temperature $\sim 1-10$ keV and hot electron temperature $0.1-3$ keV [e.g., Denton et al., 2005]), one can estimate the scalar potential amplitude as $\Phi_0 \sim 200-400$ V. The corresponding parallel electric field is about ~ 1 mV/m [see, e.g., Watt and Rankin, 2012; Chaston et al., 2012]. Thus, through the paper we consider $\Phi_0 \in [100, 400]$ V and $\lambda_\perp = 2\pi/k_\perp \in [150, 650]$ km.

C.3.2 Test particle trajectories

To demonstrate the effect of charged particle trapping and acceleration we numerically integrate Eq. (C.4) for different values of initial electron energy and transverse wavelength $\lambda_\perp$ (see dispersion relation and description of wave model in Appendix A).

Four examples of particle trajectories are presented in Fig. C.3. The top panels show particle trajectories in the phase plane (s, v) where $v = \dot{s}$. Initially, electrons move along closed trajectories shown by grey small circles. This motion corresponds to electron bounce oscillations between mirror points. On each bounce period, electrons

pass through the resonance region with $\dot{\psi} = 0$ (or $v \approx 1/K \pm \sqrt{\phi_0/\chi}$). The corresponding resonant position s_{res} of electrons can be determined from energy conservation in absence of waves: $b(s_{res}) = (2h - K^{-2})/(2h \sin^2 \alpha_{eq,0})$. As $h \sim 60$ for 100 eV electrons, s_{res} is located very close to the mirror point s_{mir} defined by the equation $b(s_{mir}) = 1/\sin^2 \alpha_{eq,0}$. When the wave approaches to s_{res}, electrons can be trapped into the effective potential well. This potential well corresponds to the competition of two forces acting on particles: the wave electric field $\sim \phi_0 \chi K w F'$ compensates the mirror force $\sim h \sin^2 \alpha_{eq,0} b'$. Thus, the mirror force does not decrease the particle parallel velocity, and the trapped particle can move with the wave. Trapping is possible only if this effective potential expands [more precisely, if the area filled by trapped particles in the phase plane increases, see detailed description of the trapping process in Artemyev et al., 2010, 2012; Neishtadt, 2014]. The wave model described in Appendix A assumes that the wave amplitude (scalar potential) grows within $|\lambda| < 5^\circ$ region near the magnetic equator. At $|\lambda| > 5^\circ$ waves propagate with a constant scalar potential amplitude and all variation of wave amplitude corresponds to wave dispersion (see Eq.(C.10) in Appendix A). Thus, only electrons with large enough equatorial pitch-angles (i.e. with small $s_{res} \sim s_{mir}$) can be trapped. For instance, four almost equatorial electrons shown in Fig. C.3 become trapped and start moving with the wave. The trapped motion (shown by black color) corresponds to electron transport to higher latitudes (larger s) with the resonant velocity $\sim 1/K$. Electron trapped motion corresponds to fast oscillations of wave phase ψ around a resonant value (while $\dot{\psi}$ oscillates around zero). The frequency of these oscillations $\sim \sqrt{\phi_0 \chi}$ is high [e.g., Artemyev et al., 2012], and electrons make a lot of oscillations within the effective potential. In the phase plane $(\psi, \dot{\psi})$ these oscillations can be shown as a quasi-periodic electron motion (see Fig. C.4).

During the transport of trapped electrons to high latitudes, the electron energy increases as $\sim h \sin^2 \alpha_{eq,0} b(s)$, while the mirror force $\sim h \sin^2 \alpha_{eq,0} b'$ becomes stronger. When electrons reach the position s^* with $h \sin^2 \alpha_{eq,0} b'(s^*) \approx \phi_0 \chi K(s^*) w(s^*) \max F'$ (i.e. the mirror force becomes equal to the wave electric field force), the effective potential vanishes and electrons escape from the resonance [a more accurate definition of the escape coordinate can be found in Arnold V. I. and Neishtadt, 2006]. After escape, electrons start moving along closed trajectories (bounce oscillations) with larger radius (see grey circles in Fig. C.3, top panels).

Trapping motion corresponds to two effects: electron acceleration (see middle row of panels in Fig. C.3) and the decrease of electron equatorial pitch-angle α_{eq} (see bottom row of panels in Fig. C.3). The later processes is due to electron transport by the wave to high latitudes. Electrons escape in the vicinity of their new mirror points $\sim s^*$ with an energy $H_{fin} \sim h \sin^2 \alpha_{eq,0} b(s^*)$ and velocity $v^* \sim 1/K(s^*)$. Thus, a new

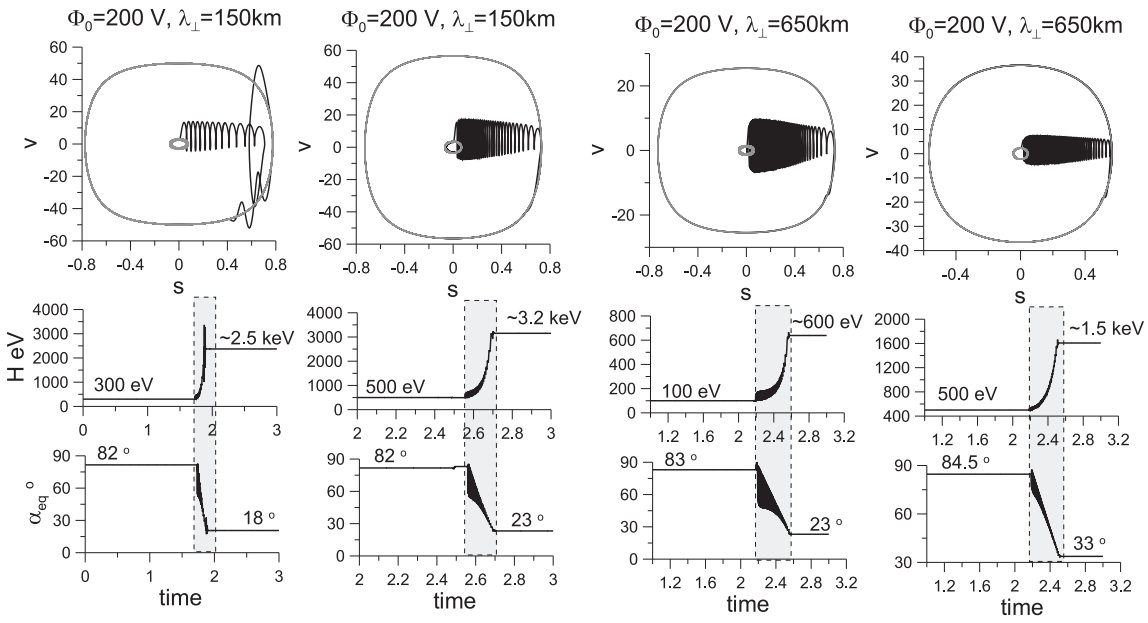

Figure C.3: Four examples of particle trajectories in (s, v) plane (top panels). Grey fragments of trajectories show particle bounce oscillations before trapping and after escape from the resonant. Middle and bottom panes show evolution of particle energy and equatorial pitch-angle. Grey color shows the time interval of trapping particle motion.

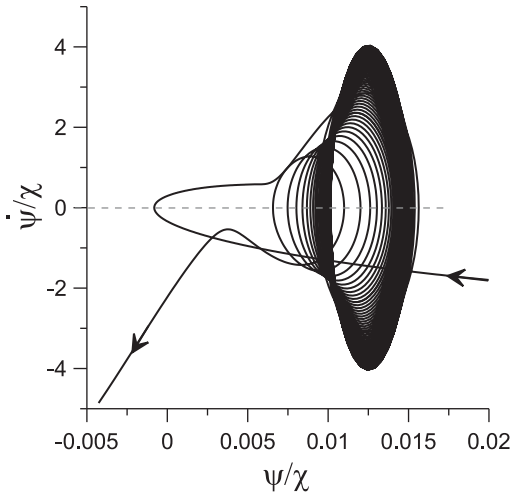

Figure C.4: Particle trajectory in the plane $(\psi, \dot{\psi})$. Only fragment of trapped motion is shown.

equatorial pitch-angle can be calculated as $\sin^2\alpha_{eq} = (1-\cos^2\alpha^*)/b(s^*)$ with $\cos\alpha^* = v^*/\sqrt{2H_{fin}} = (h\sin^2\alpha_{eq,0}K^2(s^*)b(s^*))^{-1/2}$. For large enough s^* we have $\sin^2\alpha_{eq} \approx 1/b(s^*) \ll \sin\alpha^2_{eq,0} \sim 1$, i.e. we can write the ratio $\sin\alpha_{eq}/\sin\alpha_{eq,0} \approx \sqrt{E_e/H_{fin}}$ where E_e is an initial electron energy. Therefore, electron trapping results in particle acceleration and transport to lower equatorial pitch-angle range. Both processes are very effective: electrons shown in Fig. C.3 gain several hundreds of eV and electron pitch-angles decreases down to $\sim 20^\circ - 30^\circ$.

C.3.3 Probability of trapping and maximum energies

Figure C.3 shows that trapped electrons can be effectively accelerated by the wave. However, the trapping is a probabilistic process [Neishtadt, 1999; Arnold V. I. and Neishtadt, 2006], i.e. only a part of resonant particles can be trapped by waves. The ratio of trapped particles to the whole population of resonant particles can be called a "probability of trapping". This probability can be determined analytically or numerically [see examples in Shkliar, 1981; Artemyev et al., 2013]. The probability characterizes the efficiency of the acceleration mechanism and, thus, represents the important system parameter. We use the following approach to derive the probability. For a particular value of the initial energy E_e we consider an ensemble of 10^4 particles with a uniform distribution of initial pitch-angles α_{eq} and uniform initial distribution along magnetic field lines. We run a single wave packet (see Fig. C.2) and numerically integrate particle trajectories. When wave packet reach latitude $\lambda \sim 45^\circ$ we stop numerical integration and collect the final energy spectra. All particles with the final energy $H_{fin} > 1.5E_e$ are assumed to be accelerated due to the trapping mechanism (to exclude the effect of the particle acceleration due to reflection we consider only $H_{fin} > 300$ eV, see Discussion for more details). The probability of trapping is defined as a ratio of trapped (and accelerated) particles to the initial number of particles.

Figure C.5(left panel) shows profiles of the probability of trapping as a function of initial electron energy E_e. For $\lambda_\perp = 650$ km the maximum of probability of trapping corresponds to the initial energies $E_e \sim 150-300$ eV. Depending on the wave amplitude Φ_0, 15-40% of resonant particles become trapped and accelerated up to averaged energies ~ 500 eV (see right panel in Fig. C.5). The probability of trapping decreases with the increase of E_e for $E_e > 300$ eV. As an example, the most accelerated particles with $E_e \sim 500$ eV are trapped with a probability $< 20\%$. A low level of probability of trapping for $E_e < 150$ eV is due to our criterion of the final energy $H_{fin} > 300$ eV. Small probability of trapping of energetic electrons with $E_e \sim 500$ eV corresponds to large difference between an electron thermal velocity (~ 13000 km/s) and resonant velocity

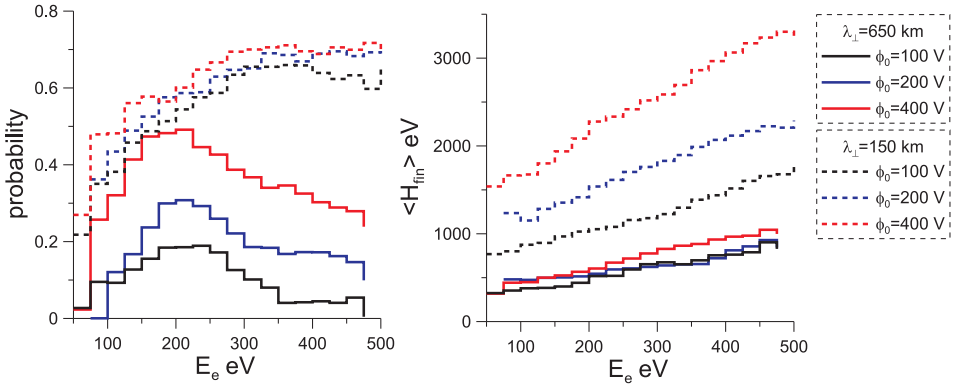

Figure C.5: The left panel shows the probability of trapping as a function of the initial energy E_e. The right panel shows the average energies gained by trapped particles.

(i.e. Alfven speed < 2000 km/s). Thus, only small population of particles can be trapped. The situation changes for waves with $\lambda_\perp = 150$ km. In this case, the wave electric field is significantly stronger (see Appendix A) and the range of resonant velocities becomes wide owing to factor $\sim \sqrt{E_\parallel/k_\parallel}$ [Karney, 1978]. As a result, even energetic electrons with $E_e \sim 500$ eV becomes trapped with a probability $\sim 60 - 70\%$. These electrons are accelerated up to few keVs on average (see right panel in Fig. C.5). The expansion of the resonant region in velocity ($\sim \sqrt{E_\parallel/k_\parallel}$) space results also to expansion of the resonant region in the coordinate space (i.e. along magnetic field lines) [e.g., Artemyev et al., 2010]. Thus, even particles located initially at some distance from the equatorial plane can be trapped. These two effects (expansion of the velocity and coordinate resonant ranges) result in the significant increase of the probability of trapping.

KAWs accelerate trapped electrons, transporting them up to the escape position s^* defined by equation $h \sin^2 \alpha_{eq,0} b'(s^*) \approx \phi_0 \chi K(s^*) w(s^*)$. Moreover, to be trapped electrons should have the resonant velocity in the vicinity of the equatorial plane where wave amplitude increases: $\sqrt{2h} \cos \alpha_{eq,0} \approx 1/K(0)$. Thus, we can combine these two equations to derive the single equation for s^*:

$$\frac{1}{K(s^*)w(s^*)} \left.\frac{\partial b}{\partial s}\right|_{s^*} = \frac{2\phi_0 \chi}{2h - K^{-2}(0)} \tag{C.5}$$

Solution of Eq. (C.5) gives s^* as a function of $E_e = h$. Thus, we can substitute this solution to equation for the final energy $H_{fin} \approx h \sin^2 \alpha_{eq,0} b(s^*) = (2h - K^{-2}(0)) b(s^*)/2$ and obtain the maximum energy gained by trapped electrons. Figure C.6 presents this maximum energy as a function of initial energy for three values of Φ_0 and two values of transverse wave length $\lambda_\perp$. The maximum energy is about two times larger than the

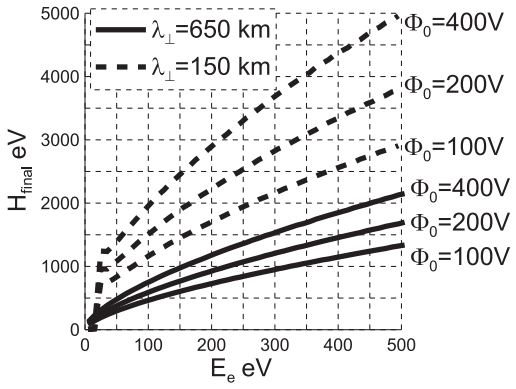

Figure C.6: Maximum of energy gained by trapped particles.

average energy shown in Fig. C.5 (right panel).

C.4 Discussion

We have focused in this paper on electron acceleration produced by trapping in an effective wave potential, and have not considered Fermi acceleration [Bryant et al., 1991; Kletzing and Torbert, 1994]. It is known that cold electrons with thermal velocity lower than (or about) the wave phase velocity can interact with the moving parallel electric field of a KAW in a manner similar to a ball interacting with a moving wall. Simple reflection of electrons from such a *wall* results in an energy gain about $\sim 2mv_A^2$. In the case of a large amplitude KAW scalar potential, reflected electrons can gain energy $\sim mv_A\sqrt{e\Phi_0/m}$ [see description of this acceleration mechanism for electron interaction with double layers in Vasko et al., 2015]. The maximum energy of reflected electrons is consequently less than 100 eV (for $\Phi_0 < 400$ V). Therefore, Fermi acceleration can be responsible for heating of cold ionospheric electrons (< 10 eV) by KAWs, but cannot produce easily a keV population.

One limitation of our analysis is that we have not taken into account the effect of transverse electric field components of KAWs. Although the transverse components are much larger than the parallel one [e.g., Watt and Rankin, 2012, and references therein], these components can significantly perturb electron motion only in two cases: provided the cyclotron resonant condition is satisfied, or if the effect of finite electron gyroradius ρ_e becomes important. The cyclotron resonance condition is $v_\parallel = (\omega - \Omega_c)/k_\parallel$, where Ω_c is electron cyclotron frequency [M. and Lanzerotti, 1974]. The corresponding electron energy is significantly larger than a typical hot electron temperature, i.e. this resonance is unavailable for thermal electrons. The second effect of strong electric field gradients

[when a spatial scale of electric field becomes comparable with the electron gyroraidus, see Balikhin et al., 1993] requires $\lambda_\perp \sim \rho_e$. This condition cannot be satisfied for KAW with $\lambda_\perp \sim \rho_s$ where ρ_s is an ion acoustical scale (see Appendix A and Hasegawa [1976]). Thus, transverse electric field components can be neglected from consideration as an effective acceleration mechanism.

To simplify analytical estimates and numerical model we use the dipole approximation for the background magnetic field. However, for night-side magnetosphere at $L \sim 6-9$ the magnetic field configuration can be substantially deformed by currents of hot ions injected from the plasmasheet [Tsyganenko et al., 2003; Sitnov et al., 2008]. Such deformation results in decrease of the equatorial magnetic field B_{eq} and stretching of magnetic field lines. Thus, the equatorial energy of resonant particles $\sim v_{A,eq}^2 \sim B_{eq}^2$ can be significantly decreased. The final energy of accelerated electrons is defined by the position where electrons escape from the resonance at high latitudes. In this region deformations of magnetic field are insignificant [Tsyganenko et al., 2003; Sitnov et al., 2008]. Therefore, for the deformed magnetic field configuration one can expect the trapping of colder electrons, but the acceleration efficiency (the final energies) should be the same as for the dipole magnetic field. The escape position s^* given by Eq. (C.5) depends on $K(s)$ function including the variation of the plasma density along magnetic field lines (see Eq. (C.7) in Appendix A). We use the model of the plasma density variation $n_e \sim \cos^{-5}\lambda$ presented by Denton et al. [2006]. However, this model is well justified only for $L \leq 7$. The stronger variation of n_e with magnetic latitude λ should result in larger s^* and, thus, leads to the stronger electron acceleration. Quantitative estimates of this effect requires more detailed models of $n_e(\lambda)$.

Our calculations have shown that trapping of sub-keV electrons by KAWs results in an acceleration up to few keV, with a corresponding decrease of the equatorial pitch-angle. Thus, trapped and accelerated electrons should form predominantly field aligned distributions or even beams. Subsequent relaxation of these beams should lead to excitation of electrostatic structures [e.g., electron holes and double layers, see modelling in Gnot et al., 2004; Mottez and Gnot, 2011] and very oblique whistler waves [e.g., Mourenas et al., 2015]. This process naturally represents energy cascading from large (ion) scales corresponding to KAWs, to smaller (electron) scales of double layers and whistler waves. Indeed, Mozer et al. [2014] and Malaspina et al. [2015] show that intensification of electrostatic structures is strongly related to plasma injections bringing into the inner magnetosphere a wide spectrum of KAWs [Chaston et al., 2014; Ergun et al., 2015].

Figure C.5 demonstrates that the electron probability of trapping can become very large (close to 80%) in certain cases. This strongly nonlinear regime should cause strong damping of KAWs by the large population of electrons that are trapped and accelerated.

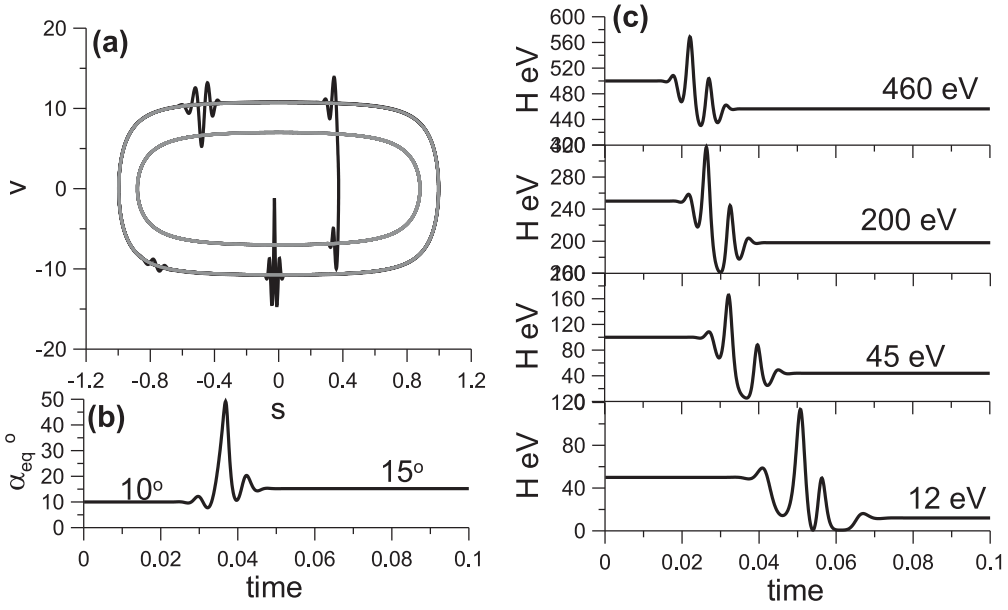

Figure C.7: Panels (a) and (b) show an example of charged particle trajectory and the corresponding jump of the equatorial pitch-angle. Grey fragments of the trajectory show particle bounce oscillations before and after interaction with KAW. Panels (c) show several examples of jump of particle energy for different values of initial energy.

However, regular detection of strong KAWs by spacecraft [e.g., Wygant et al., 2002; Chaston et al., 2014] points to a mechanism responsible for wave amplification. One possibility is due to the competition of effects of trapped and transient particles in the system with nonlinear wave-particle interaction [e.g., Shklyar, 2011]. Indeed, the acceleration of trapped particles can be compensated by noticeable deceleration of a much larger amount of transient particles scattered by the wave electric field. Particles loosing energy due to interaction with KAW will move ahead of the wave and reflect from the scalar potential with a velocity decrease [see the similar mechanism of particle deceleration due to interaction with electrostatic double layers Vasko et al., 2015]. Figure C.7 shows an example of transient particle trajectory reflecting from the wave potential with a loss of energy. Particles with different initial energy lose the same energy ~ 40 eV corresponding to $\sim mv_A\sqrt{e\Phi_0/m}$ [see Vasko et al., 2015]. In the self-consistent system this energy should be transferred to waves and can be spent for acceleration of trapped particles. Thus, for calculation of the nonlinear evolution of the amplitude of KAWs one should estimate both nonlinear currents of trapped and transient electrons [see the similar estimates for whistler waves in Shklyar and Matsumoto, 2009; Demekhov, 2011; Summers et al., 2012]. We leave this problem for further publications.

Two important properties of electron acceleration by KAWs can be considered in light of our analysis: formation of field aligned electron population in the region of plasma injection where most intense KAWs are observed [Chaston et al., 2014; Ergun et al., 2015], and effective acceleration of sub-keV electrons up to keV energies. The trapping mechanism we have discussed can potentially explain the formation of electron beams (or, at least, streams with almost absent gradient of the parallel velocity distribution function) with peak parallel velocity $\sim (5-30)\cdot 10^3$ km/s. To demonstrate this we numerically integrate 10^6 trajectories and plot in Fig. C.8 the final velocity distribution for field aligned electrons ($\alpha_{eq} < 30^\circ$). One can distinguish from the figure a beam-like population of accelerated electrons with average parallel velocities $\sim$ 7000 km/s. The initial pitch-angle distribution is uniform, while the final pitch-angle distribution contains the maximum in the small pitch-angle range $\alpha_{eq} < 30^\circ$ corresponding to the accelerated electron population. This population is generated by a combination of particle reflection from the potential wall of KAWs [see description of this mechanism of acceleration in Bryant et al., 1991; Kletzing and Torbert, 1994; Vasko et al., 2015], and electron trapping and acceleration by KAWs. For L-shell $\sim 6-9$ the equatorial phase velocity of low band parallel chorus waves is about $\sim 5000-10000$ km/s [e.g., Kennel and Petschek, 1966]. Thus, the accelerated field aligned beam should be very unstable relative to the generation of whistler waves. This regime of generation is similar to triggered whistler wave emission [e.g., Nunn, 1974; Trakhtengerts et al., 2003]. Therefore, we suggest that particle trapping can produce high-amplitude KAW-shape electron beams with substantial source of free energy, while secondary instability of such beams can result in efficient generation of whistler waves in the region of plasma injection. This scenario is generally confirmed by statistically higher amplitudes of whistler waves observed in the nigh-side inner magnetosphere [Meredith et al., 2001; Agapitov et al., 1974].

Although, we demonstrate the rapid acceleration of sub-keV electrons up to several keVs and transport of these electrons to small pitch-angle range, we should admit that the proposed model cannot alone describe the formation of electron population precipitating into atmosphere and corresponding to diffusive aurora. Indeed, final energies of accelerated particles are exactly in the range aurora electron energies, but their pitch-angles being rather small are still quite far from the loss-cone. Thus, the proposed mechanism of electron acceleration can be responsible for formation of aurora electron (small pitch-angles, keV-energies) population, which should be further transported to loss-cone by some high-latitude mechanisms. Alternatively, electrons accelerated by KAW can be further scattered into the loss-cone by chorus waves [M Thorne et al., 2010; Ni et al., 2014] or electron cyclotron waves [Ni et al., 2011a; Zhang et al., 2014].

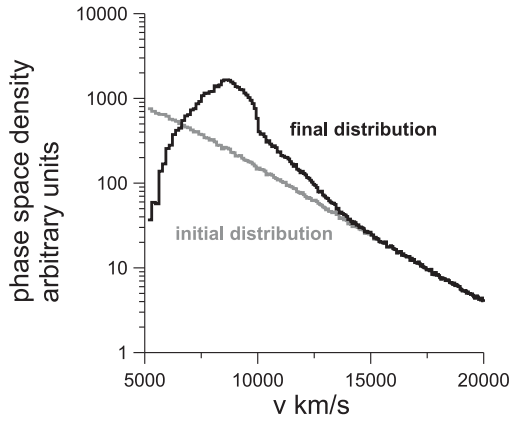

Figure C.8: Velocity distributions of field aligned electrons ($\alpha_{eq} < 30^\circ$). Initial distribution is shown by grey color, while the final (after interaction with KAW) distribution is shown by black color.

C.5 Conclusions

We have considered a nonlinear mechanism of sub-keV electron acceleration by high-amplitude KAWs propagating away from the equatorial region. Our main results can be summarize as:

1. The parallel electric field of KAWs and the mirror force acting on electrons in an inhomogeneous magnetic field form an effective potential well for electron trapping and acceleration along magnetic field lines.

2. Trapped electrons can be transported by KAWs up to high latitudes ($\lambda \sim 40^\circ$) with a corresponding energy gain up to several keV.

3. Acceleration of trapped electrons corresponds to a rapid decrease of the electron equatorial pitch-angle: almost equatorial electrons with $\alpha_{eq} \sim 80^\circ$ become field aligned with $\alpha_{eq} < 30^\circ$ during a single trapping event.

4. Large amplitude of wave electrostatic potential significantly expands the range of electron velocity resonantly interacting with KAWs: even electrons with ~ 500 eV can be trapped and accelerated.

Appendix C.6: model description

To model kinetic Alfven wave propagating away from the equatorial plane we use the dispersion relation provided by Hasegawa [1976]:

$$\omega = k_{\|} v_A \sqrt{1 + k_{\perp}^2 \rho_s^2 \left(1 + T_i/T_e\right)} \tag{C.6}$$

where $v_A = B(\lambda)/\sqrt{4\pi n_e(\lambda) m_i}$ is an Alfven velocity, $\rho_s = \sqrt{2T_e m_i}c/eB(\lambda)$ is an ion acoustic scale, $k_{\|}$ and $k_{\perp}$ are components of wave vector. Dispersion relation (C.6) was derived for plasma beta (ratio of plasma and magnetic field pressures) larger than the electron to ion mass ratio. For $L = 6.6$ (geostationary orbit) the conservative estimate of the plasma beta gives $\sim 0.1 - 0.2$ (for hot proton density $\sim 1 - 2$ cm^{-3} and hot proton temperature $\sim 1 - 10$ keV [see Denton et al., 2005]). Thus, Eq. (C.6) can be applied to describe KAW dispersion at $L > 6.6$ (the equatorial plasma beta generally increases with L).

Due to absence of a reliable information about ion and electron temperature variation along magnetic field lines, throughout the paper we consider the constant ion and electron temperatures $T_e = 100$ eV, $T_i = 1000$ eV. This approximation corresponds to the assumption of particle temperature isotropy and Maxwell distributions [see, e.g., Whipple E. and M., 1991]. The wave frequency is $\omega = 2\pi/2$s. To model variations of the magnetic field $B(\lambda)$ and electron density $n(\lambda)$ with the magnetic latitude λ we use the dipole model and Denton et al. [2006] model with $n_e = n_{eq}\cos^{-5}(\lambda)$, while the equatorial value of n_{eq} is provided by Sheeley et al. [2001]. We introduce the equatorial perpendicular wave number $\lambda_{\perp}$ and use the approximation $k_{\perp} = (2\pi/\lambda_{\perp})\sqrt{B(\lambda)/B_{eq}}$ [see Watt and Rankin, 2012, and references therein]. Thus, Eq. (C.6) can be rewritten as: $k_{\|} = (R_0\omega/v_{A,eq})K(\lambda)$ where

$$K(\lambda) = \frac{1}{b(\lambda)}\sqrt{\frac{n_e(\lambda)}{n_{eq}}}\left(1 + \frac{\kappa^2}{b(\lambda)}\right)^{-1/2} \tag{C.7}$$

$b(\lambda) = B(\lambda)/B_{eq}$, $v_{A,eq}$ is an equatorial value of Alfven velocity, $R_0 = R_E L$ is a scale of magnetic field inhomogeneity, $\kappa = 2\pi\sqrt{2T_e m_i}c\sqrt{1 + T_i/T_e}/\lambda_{\perp}eB_{eq}$. We also use dimensionless parameter $\chi = R_0\omega/v_{A,eq} \approx 250(2\text{s}/T)(L/9)^2$ and $T = 2$ s is a wave period.

In the kinetic Alfven wave the approximate relation between parallel component of the vector potential $A_{\|}$ and scalar potential φ can be written in following form [see, e.g., Watt and Rankin, 2010]:

$$\frac{\partial A_{\|}}{\partial z} = -\frac{c}{v_A^2}\frac{\partial \varphi}{\partial t} \tag{C.8}$$

where $z = R_0 \int \sqrt{1+3\sin^2\lambda}\cos\lambda d\lambda$ is a field aligned coordinate. Assuming, that φ and $A_\parallel$ depend on phase $\psi = \int^z k_\parallel dz - \omega t$ we solve Eq. (C.8): $A_\parallel = c\omega\varphi/k_\parallel v_A^2$. Thus, the total parallel electric field can be written as:

$$E_\parallel = -\frac{\partial\varphi}{\partial z} - \frac{1}{c}\frac{\partial A_\parallel}{\partial t} = -k_\parallel\left(1 - \frac{\omega^2}{k_\parallel^2 v_A^2}\right)\varphi = k_\parallel k_\perp^2\rho_s^2\left(1+T_i/T_e\right)\varphi \tag{C.9}$$

We introduce the generalized potential $\Phi = -\Phi_0 w(z) f(\psi)$ and write $E_\parallel = -k_\parallel\Phi = -\partial\Phi/\partial z$ with

$$w(z) = g(z)k_\perp^2\rho_s^2\left(1+T_i/T_e\right) = \kappa^2 g(z)/b(z) \tag{C.10}$$

where function $g(z)$ defines the growth of the scalar potential from zero value up to an amplitude Φ_0. We use $g(z)$ corresponding to the monotonical increase of Φ within 5° near the equatorial plane. For $|\lambda| > 5^\circ$ function g is equal to one.